

**KINEMATIC DESIGN AND ANALYSIS OF  
DEPLOYABLE VAULT AND PSEUDO-DOME  
STRUCTURES BASED ON ORIGAMI  
TECHNIQUES**

**A Thesis Submitted to  
The Graduate School of Engineering and Sciences of  
İzmir Institute of Technology  
In Partial Fulfillment of the Requirements for the Degree of**

**DOCTOR OF PHILOSOPHY**

**in Architecture**

**by  
Andrée Sonad KARAVELİ KARTAL**

**July 2017  
İZMİR**

We approve the thesis of **Andrée Sonad KARAVELİ KARTAL**

**Examining Committee Members:**

---

**Assoc. Prof. Dr. Koray KORKMAZ**

Department of Architecture, Izmir Institute of Technology

---

**Assoc. Prof. Dr. Gökhan KİPER**

Department of Mechanical Engineering, Izmir Institute of Technology

---

**Assoc. Prof. Dr. M. Emre İLAL**

Department of Architecture, Izmir Institute of Technology

---

**Assoc. Prof. Dr. A. Vefa ORHON**

Department of Architecture, Dokuz Eylül University

---

**Assist. Prof. Dr. Özgür KİLİT**

Department of Industrial Design, Yaşar University

**21 July 2017**

---

**Assoc. Prof. Dr. Koray KORKMAZ**

Supervisor, Department of Architecture  
Izmir Institute of Technology

---

**Assoc. Prof. Dr. Şeniz ÇIKIŞ**

Head of the Department of Architecture

---

**Prof. Dr. Aysun SOFUOĞLU**

Dean of the Graduate School of  
Engineering and Sciences

## ACKNOWLEDGMENTS

My interest in this field of origami as a structure came from one of my professors at EPFL, Hans Ulrich Buri who at that time was working on his dissertation. It has been an inspirational encounter for me that rekindled my origami interest and led to this dissertation. So I would like to express my gratitude to Prof. Buri for this encounter.

I would like to thank everyone who contributed in making this process an exciting and enriching experience: I would like to express my gratitude to my supervisor Assoc. Prof. Dr. Koray Korkmaz for his continuous guidance, support and especially his patience toward me throughout this study. I would like to thank the members of my thesis committee: Assoc. Prof. Dr. M. Emre İlal, for his support, observations and feedbacks from on the subject of architectural design. Assoc. Prof. Dr. Gökhan Kiper for his support, insightful comments and evaluations on the subjects of mechanical engineering and the help he extended to me during my crisis.

I would also like to thank all my ex-colleagues and friends that picked me up when I was lost and supported me through hard times.

My mom, Maguy, and my husband, Halit, deserve special thanks for their continuous encouragement, patience, unconditional support, love and friendship.

# ABSTRACT

## KINEMATIC DESIGN AND ANALYSIS OF DEPLOYABLE VAULT AND PSEUDO-DOME STRUCTURES BASED ON ORIGAMI TECHNIQUES

In recent years a need for more adaptable and flexible structures have been observed due to the changing spatial and functional needs. One of the solutions for an adaptable space in architecture is deployable structures. These kinds of structures provide flexible solutions to the functional and spatial necessities of an environment. There are different kinds of deployable structures such as bar and foldable plate structures, membrane, inflatable, cable/strut etc.

This study presents a method of designing a pseudo-dome flat-foldable and deployable plate structure (rigid origami) based on origami patterns that have a polar rotation deployment axis. To achieve this objective, first a method of designing flat-foldable and linearly deployed barrel vault structures have been created by analyzing their geometrical properties. This analysis along with a workspace analysis provided knowledge on the geometrical relations between the cross-sections and deployment parameters. These relations allowed the design of a flat-foldable rigid origami structure based on the geometry of the cross-section using a pattern-generator.

The method of using a pattern-generator to create an origami pattern has been modified to achieve a polar rotated deployable pseudo-dome structure. The design method allows the designer to calculate all the relevant parameters to create an origami structure by modifying three parameters for barrel vault foldable structures and two parameters for pseudo-dome structures. The created origami pattern is then transformed to a foldable deployable plate structure with the intended design requirements. The design processes for both design methods have been explained with case studies.

# ÖZET

## ORİGAMİ TEKNİKLERİ TEMEL ALINARAK AÇILIR KAPANIR TONOZ VE KUBBEMİSİ STRÜKTÜRLERİN KİNEMATİK TASARIMI VE ANALİZİ

Son yıllarda mimarlık alanında değişim gösteren mekânsal ve fonksiyonel gereklilikler, esnek ve uyarlanabilen strüktürlere ihtiyaç duyulmasına neden olmuştur. Mimarlıkta uyarlanabilir mekânlara çözümlerden bir tanesi açılır-kapanır (katlanabilir) strüktürlerdir. Bu tür strüktürler çevre nedeni ile ihtiyaç duyulan fonksiyonel ve mekânsal gereksinimlere esnek çözümler sunmaktadır. Açılır-kapanır strüktürler çubuk veya plakalardan oluşabilmektedir.

Bu çalışma merkezi dönme eksenini etrafında açılan, yassı-katlanabilir (flat-foldable) açılır kapanır düzlemsel -rijit origami- bir kubbemsi strüktür için bir tasarım yöntemi sunmaktadır. Bu amaca ulaşmak için önce çizgisel eksen ile açılan, yassı-katlanabilir açılır kapanır düzlemsel beşik tonoz strüktürlerin geometrik özellikleri incelenmiştir. Bu analiz ve çalışma alanı analizleri sayesinde strüktürün arakesit ve açılma parametreleri arasındaki bağıntılar ortaya çıkmıştır. Bu bağıntılar, arakesit geometrisi temel alınarak oluşturulan örüntü-üretici (pattern-generator) kullanılarak yassı-katlanabilir rijit origami strüktürlerin tasarımını sağlamıştır.

Origami örüntüsü yaratmak için kullanılan örüntü-üretici yöntemi merkezi açılım dönme eksenini oluşması için geliştirilmiştir. Tasarım yöntemi tasarımcının beşik tonoz strüktürler için üç, kubbemsi strüktürler için ise iki parametreyi değiştirerek origami örüntüsünü oluşturmak için gerekli tüm parametrelerin hesaplanmasını sağlamaktadır. Belirlenmiş parametreler tarafından oluşturulan origami örüntüsü, uygulamanın gereklilikleri doğrultusunda açılır-kapanır plaka strüktüre dönüştürülmektedir. Çalışmanın sonunda her iki yöntemin tasarım süreci birer örnek inceleme ile sunulmaktadır.

# TABLE OF CONTENT

LIST OF FIGURES.....	ix
LIST OF TABLES .....	xviii
CHAPTER 1. INTRODUCTION.....	1
1.1. Aim and Scope of the Research. ....	2
1.2. Outline of the Thesis. ....	2
CHAPTER 2. REVIEW OF PREVIOUS WORK. ....	4
2.1. History of Origami. ....	4
2.2. Origami Classification. ....	8
2.3. Origami Terminology.....	15
2.4. Origami Theorems.....	17
2.4.1. Huzita-Justin Axioms.....	18
2.4.2. Flat Foldability.....	18
2.5. Origami Applications. ....	25
2.5.1. Origami Structures. ....	25
2.5.2. Deployable Structures. ....	28
2.5.2.1. Fold and Pattern Types .....	30
2.5.2.2. Kinematics of Origami Inspired Mechanisms .....	39
CHAPTER 3. RIGID ORIGAMI BARREL VAULT STRUCTURES .....	44
3.1. Single Centered Barrel Vaults. ....	45
3.1.1. Geometrical Properties. ....	45
3.1.1.1. Final Folded State.....	45
3.1.1.2. Partially Folded State.....	48
3.1.1.3. Initial State, MV-Pattern.....	53
3.1.1.4. Conclusion .....	56
3.1.2. Workspace Analysis .....	59
3.1.2.1. Depth.....	59
3.1.2.2. Span and Height .....	62
3.1.2.3. Volume.....	67

3.1.3. Mobility Analysis .....	70
3.1.3.1. Triangular Patterns .....	72
3.1.3.1.1. Six Segmented Pattern .....	72
3.1.3.1.2. Five Segmented Pattern.....	75
3.1.3.2. Trapezoidal Patterns .....	79
3.1.4. Conclusion .....	86
3.2. Double Centered Barrel Vaults .....	87
3.2.1. Geometrical Properties .....	88
3.2.1.1. Final Folded State.....	88
3.2.1.2. Partially Folded State.....	92
3.2.1.3. Initial State, MV-Pattern.....	95
3.2.1.4. Conclusion .....	98
3.2.2. Workspace Analysis .....	101
3.2.2.1. Depth.....	102
3.2.2.2. Span and Height .....	102
3.2.2.3. Volume.....	106
3.2.3. Mobility Analysis .....	109
3.2.3.1. Triangular Patterns .....	109
3.2.3.2. Trapezoidal Patterns .....	116
3.2.4. Conclusion .....	121
3.3. Conclusion .....	122
CHAPTER 4. DEPLOYABLE PSEUDO-DOME STRUCTURES .....	123
4.1. Segmentation.....	123
4.2. Geometrical Analysis .....	126
4.2.1. Final Folded State and Initial State .....	127
4.2.2. Partially State .....	132
4.2.3. Conclusion .....	137
4.3. Workspace Analysis .....	144
4.3.1. Height, Span and Coverage Area .....	150
4.3.2. Volume .....	155
4.4. Mobility Analysis .....	157
4.4.1. Double Row Patterns.....	158
4.4.2. 3- Rows Patterns .....	160

4.4.3. 4- Rows Patterns .....	163
4.4.4. 5- Rows Patterns .....	166
4.5. Conclusion .....	171
CHAPTER 5. CASE STUDIES.....	172
5.1. Case Study 1.....	172
5.1.1. Step 1 – Parameters Calculations.....	173
5.1.2. Step 2 – MV-Pattern Creation.....	175
5.1.3. Step 2 – Dimensions of the Created Pattern .....	178
5.1.4. Conclusion .....	183
5.2. Case Study 2.....	184
5.2.1. Step 1 – Parameters Calculations.....	184
5.2.2. Step 2 – MV-Pattern Creation.....	188
5.2.3. Step 2 – Dimensions of the Created Pattern .....	190
5.2.4. Conclusion .....	195
CHAPTER 6. CONCLUSION.....	197
BIBLIOGRPHY .....	203
APPENDICES	
APPENDIX A. SINGLE CENTERED RIGID ORIGAMI BARREL	
VAULT CALCULATION SHEET .....	214
APPENDIX B. SINGLE CENTERED RIGID ORIGAMI BARREL	
VAULT PATTERN AND KINEMATIC DIAGRAMS .....	215
APPENDIX C. DOUBLE CENTERED RIGID ORIGAMI BARREL	
VAULT CALCULATION SHEET .....	230
APPENDIX D. DOUBLE CENTERED RIGID ORIGAMI BARREL	
VAULT PATTERN AND KINEMATIC DIAGRAMS .....	231
APPENDIX E. PSEUDO-DOME RIGID ORIGAMI CALCULATION	
SHEET (PATTERN).....	242
APPENDIX F. PSEUDO-DOME RIGID ORIGAMI CALCULATION	
SHEET (COMPLEMENTARY PATTERN) .....	243



# LIST OF FIGURES

<b><u>Figure</u></b>	<b><u>Page</u></b>
Figure 2.1. Mecho (female, left) and Ocho (male, middle). Noshi (right) .....	5
Figure 2.2. Page from Sembazuru Orikata.....	6
Figure 2.3. European traditional origami models .....	7
Figure 2.4. Mountain and Valley folds – drawn by the author .....	15
Figure 2.5. (a) CP of the traditional crane origami, (b) the MV-Pattern of the same model – drawn by the author .....	16
Figure 2.6. (a) MV-P initial state, (b) partially folded state, and (c) final folded state. Dotted lines represent hidden lines – drawn by the author .....	16
Figure 2.7. Huzita-Justin Axioms.....	18
Figure 2.8. (a) traditional crane MV-Pattern, (b) closer view of the central vertex of the traditional crane - drawn by the author .....	20
Figure 2.9. (a) CP-1 (b) CP-2. Both CPs are not globally flat-foldable .....	21
Figure 2.10. CP-1 – (a) MV-assignment done for the purpose (b) degree of the angles. Dashed dot lines are mountain folds and dashed lines are valley folds. – redrawn by the author.....	22
Figure 2.11. CP-2 - (a) MV-assignment done for the purpose (b) degree of the angles. Dashed dot lines are mountain folds and dashed lines are valley folds. – redrawn by the author .....	23
Figure 2.12. Noncrossing condition. Central vertex of the traditional crane MV-Pattern left, non-crossing representation of the folded central vertex on the right - drawn by the author.....	24
Figure 2.13. (a) Linear folded plate structures (b) Radial folded plate structure (c) Spatial folded plate structure.....	26
Figure 2.14. (a) Temporary chapel for the Deaconesses of St-Loup, (b) The US Air Force Academy Chapel, Colorado, (c) The Church St. Paulus, Germany .	27
Figure 2.15. (a) Diamatic folded plate dome, (b) Origami dome and (c) Hexagonal Dome .....	27
Figure 2.16. (a) Al Bahr Tower Façade Detail, (c) Kiefer Technic Showroom.....	27
Figure 2.17. (a) Origami pattern (b) Bar structure (c) Rigid origami structure .....	28

Figure 2.18. (a) De Temmerman’s Foldable Mobile Shelter (b) Tachi’s Rigid origami structure.....	29
Figure 2.19. Oricrete creation process.....	30
Figure 2.20. (a) Parallel fold and (b) Reverse fold - redrawn based on Buri .....	31
Figure 2.21. Pattern generation by Stavric and Wiltsche. ....	32
Figure 2.22. Pattern creation by Jackson .....	33
Figure 2.23. Miura-ori pattern / Herringbone pattern.....	34
Figure 2.24. Yoshimura pattern / Diamond pattern.....	35
Figure 2.25. Quadrilateral pattern .....	36
Figure 2.26. Nojima’s (a) non-inclined quadrilateral pattern (b) inclined quadrilateral pattern.....	37
Figure 2.27. Water Bomb pattern.....	37
Figure 2.28. Variation of Resch’s pattern.....	38
Figure 2.29. Resch patterns by Tachi (a) Variations of Resch’s pattern (b) freeform shapes of patterns.....	38
Figure 2.30. Deployment motion of patterns by Schimme et al .....	40
Figure 2.31. Origami inspired mechanisms. ....	41
Figure 2.32. Spherical joints (a) 4R spherical linkage (b) 6R spherical linkage—drawn by the author.....	42
Figure 2.33. Joints (a) Zero-thickness model (b) Axis-shift method (c)Tapered panels (d) Membrane folds method (e) Offset panel technique (f) Rolling joints connection method .....	43
Figure 3.1. (a) Horseshoe arch and (b) Semicircle arch parameters’ representations. Bold dashed lines: <i>pattern-generators</i> .....	46
Figure 3.2. 3 segments semicircle arch, 4 segments, 6 segments, 9 segments semicircle arches (from left to right). ....	46
Figure 3.3. Single row CP and the parameters for the six segmented semicircle arch.....	48
Figure 3.4. (a) Elevation and (b) double row CP of a rigid origami barrel vault structure with 6 segments, created using the maximum value of $h$ .....	49
Figure 3.5. Vertexes $v_1^4$ and $v_2^6$ ’s parameters .....	50
Figure 3.6. Vertex $v_3^6$ ‘s parameters. ....	50
Figure 3.7. Relation between angles $\mu$ and $\lambda$ with $\sigma$ for an $n:6, r:2$ semicircle arch....	53
Figure 3.8. Unfolded crease pattern for the six segmented semicircle arch. ....	54

Figure 3.9. MV-Pattern created by using maximum value of $h$ for a $n$ : 6, semicircle arch. Triangular pattern (Yoshimura pattern).....	55
Figure 3.10. MV-Pattern created by using $h$ as 0,104 m, for a $n$ : 6, semicircle arch. Trapezoidal pattern .....	56
Figure 3.11. Triangular pattern rigid origami horseshoe 200° barrel vault tested on FreeformOrigami software. ....	57
Figure 3.12. Trapezoidal pattern rigid origami horseshoe 200° barrel vault tested on FreeformOrigami software. ....	58
Figure 3.13. Rearranged triangular pattern rigid origami horseshoe 200° barrel vault tested on FreeformOrigami software .....	58
Figure 3.14. Models of trapezoidal pattern (left) and triangular pattern (right) for a semicircular cross-section .....	58
Figure 3.15. Models of trapezoidal pattern (left) and triangular pattern (right) for a horseshoe cross-section. ....	59
Figure 3.16. $r$ : 6m $n$ :8 $\Omega$ :220 horseshoe arch motion - xz-plane (left) and yz-plane (right) .....	59
Figure 3.17. Side view showing the relation between inclination angle $\sigma$ and depth. Dashed lines are the <i>pattern-generator</i> , bold full lines are the section lines .....	60
Figure 3.18. Relation between the inclination angles $\sigma$ and the total depth, $TD_I$ of a 10 row single centered barrel vault pattern .....	61
Figure 3.19. (left) Horseshoe arch <i>pattern-generator</i> with even and odd number segments, (right) Semicircle arch <i>pattern-generator</i> with even and odd number of segments .....	62
Figure 3.20. Parameters for (above) Horseshoe 200 arch <i>pattern-generator</i> with even number of segments, (below) Horseshoe 200 arch <i>pattern-generator</i> with odd number of segments.....	64
Figure 3.21. Relation between the inclination angle and the span of a horseshoe arch $r$ : 4 $n$ : 6 $\Omega$ : 200.....	65
Figure 3.22. Relation between the inclination angle and the height of a horseshoe arch $r$ : 4 $n$ : 6 $\Omega$ : 200.....	66
Figure 3.23. Single centered barrel vaults' volume parameters.....	68

Figure 3.24. Single centered <i>pattern-generator</i> positions according to the inclination angle values (1) 10°, (2) 50°, and (3) 90° during folding process. ....	68
Figure 3.25. Relation between the inclination angle and the volume of a horseshoe arch $r: 4 \ n: 6 \ \Omega: 200$ . ....	70
Figure 3.26. Element of structural group.....	72
Figure 3.27. Triangular double row semicircle arch $r:3 \ n:6 \ \Omega:180^\circ$ (a) crease pattern (b) kinematic diagram .....	73
Figure 3.28. Triangular 3-row semicircle arch $r:3 \ n:6 \ \Omega:180^\circ$ (a) crease pattern (b) kinematic diagram .....	74
Figure 3.29. Triangular four rows semicircle arch $r:3 \ n:6 \ \Omega:180^\circ$ (a) crease pattern (b) kinematic diagram .....	75
Figure 3.30. Triangular double row semicircle arch $r:3 \ n:5 \ \Omega:180^\circ$ (a) crease pattern (b) kinematic diagram .....	76
Figure 3.31. Triangular three rows semicircle arch $r:3 \ n:5 \ \Omega:180^\circ$ (a) crease pattern (b) kinematic diagram .....	77
Figure 3.32. Triangular four rows semicircle arch $r:3 \ n:5 \ \Omega:180^\circ$ (a) crease pattern (b) kinematic diagram .....	78
Figure 3.33. Trapezoidal double row semicircle arch $r:2 \ n:6 \ \Omega:180^\circ$ (a) crease pattern (b) kinematic diagram .....	80
Figure 3.34. Modified Trapezoidal double row semicircle arch $r:2 \ n:6 \ \Omega:180^\circ$ pattern kinematic diagram. ....	81
Figure 3.35. Trapezoidal three rows semicircle arch $r:2 \ n:6 \ \Omega:180^\circ$ (a) crease pattern (b) kinematic diagram .....	82
Figure 3.36. Modified Trapezoidal three rows semicircle arch $r:2 \ n:6 \ \Omega:180^\circ$ pattern kinematic diagram. ....	82
Figure 3.37. Trapezoidal four rows semicircle arch $r:2 \ n:6 \ \Omega:180^\circ$ (a) crease pattern (b) kinematic diagram .....	83
Figure 3.38. Modified Trapezoidal four rows semicircle arch $r:2 \ n:6 \ \Omega:180^\circ$ pattern kinematic diagram. ....	84
Figure 3.39. Parameters for (a) Pointed Equilateral arch, (b) Lancet arch, and (c) Obtuse arch. Bold dashed lines: <i>pattern-generators</i> .....	89
Figure 3.40. Different lancet arches. ....	90
Figure 3.41. Single row crease pattern and the parameters for six segmented pointed equilateral arch. ....	92

Figure 3.42. (a) Elevation and (b) MV-Pattern of a six segmented obtuse arch, created using maximum value of $h_l$ .....	93
Figure 3.43. Vertexes $v_1^4, v_2^6, v_3^4$ and $v_4^4$ 's parameters.....	94
Figure 3.44. Relation between bending angles and inclination angle $\sigma$ for a $n_T: 6$ $r: 3 a:2$ obtuse arch .....	95
Figure 3.45. Unfolded crease pattern for the six segmented obtuse arch .....	96
Figure 3.46. MV-Pattern created by using maximum value of $h$ for a $n_T: 6$ , obtuse arch. Triangular pattern.....	97
Figure 3.47. MV-Pattern created by using value of $h$ as 0,08 m for a $n_T: 6$ , obtuse arch. Triangular pattern.....	98
Figure 3.48. Triangular pattern rigid origami obtuse barrel vault tested on Freeform-Origami software.....	100
Figure 3.49. Trapezoidal pattern rigid origami obtuse barrel vault tested on Freeform-Origami software .....	100
Figure 3.50. Rearranged triangular pattern rigid origami obtuse barrel vault tested on Freeform-Origami software.....	101
Figure 3.51. Model of trapezoidal pattern (left) and triangular pattern (right) for an obtuse barrel vault.....	101
Figure 3.52. Relation between the inclination angles $\sigma$ and the total depth, $TD_l$ of a 10 row double centered barrel vault pattern. ....	102
Figure 3.53. Lancet, Pointed equilateral and Obtuse arches' development with $n:3$ and $n_T:6$ .....	103
Figure 3.54. Parameters for Obtuse arch's pattern-generator with $n:3$ and $n_T:6$ .....	104
Figure 3.55. Relation between the inclination angle $\sigma$ and the span $S$ of an obtuse arch $r: 4$ m, $a: 2$ m, and $n: 3$ .....	105
Figure 3.56. Relation between the inclination angle $\sigma$ and the height $H$ of an obtuse arch $r: 4$ m, $a: 2$ m, and $n: 3$ .....	106
Figure 3.57. Double centered barrel vaults' volume parameters .....	107
Figure 3.58. Relation between the inclination angle $\sigma$ and the volume $V$ of an obtuse arch $r: 4$ m, $a: 2$ m, and $n: 3$ .....	108
Figure 3.59. Triangular double row obtuse arch $n:3 n_T:6$ (a) crease pattern (b) kinematic diagram .....	110
Figure 3.60. Modified triangular double row obtuse arch $n:3 n_T:6$ pattern's kinematic diagram.....	110

Figure 3.61. Triangular 3 row obtuse arch $n:3$ $n_T:6$ (a) crease pattern (b) kinematic diagram. ....	111
Figure 3.62. Modified triangular 3 row obtuse arch $n:3$ $n_T:6$ pattern's kinematic diagram.....	112
Figure 3.63. Triangular 4 row obtuse arch $n:3$ $n_T:6$ (a) crease pattern (b) kinematic diagram. ....	113
Figure 3.64. Modified triangular four rows obtuse arch $n:3$ $n_T:6$ pattern's kinematic diagram.....	114
Figure 3.65. Trapezoidal double row obtuse arch $n:3$ $n_T:6$ (a) crease pattern (b) kinematic diagram. ....	116
Figure 3.66. Modified trapezoidal double row obtuse arch $n:3$ $n_T:6$ pattern's kinematic diagram.....	117
Figure 3.67. Trapezoidal 3 row obtuse arch $n:3$ $n_T:6$ (a) crease pattern (b) kinematic diagram. ....	117
Figure 3.68. Modified trapezoidal 3 row obtuse arch $n:3$ $n_T:6$ pattern's kinematic diagram.....	118
Figure 3.69. Trapezoidal 4 row obtuse arch $n:3$ $n_T:6$ (a) crease pattern (b) kinematic diagram. ....	118
Figure 3.70. Modified trapezoidal 4 row obtuse arch $n:3$ $n_T:6$ pattern's kinematic diagram.....	119
Figure 4.1. Dome creation methods (a) Polar rotation of a semicircle along the x-axis (b) Polar rotation of a quarter of a circle around z-axis.....	124
Figure 4.2. Segmentation of an arc by 3, 4, 5, 6, 7, and 8; and the top view of the segmented domes .....	125
Figure 4.3. Parameters of the cross-section of a pseudo-dome $r: 5m$ , $n: 4$ , $\theta_I: 9^\circ$ .....	128
Figure 4.4. Parameters of (a) the final folded state and (b) the crease pattern, for a dome with $r: 5m$ , $n: 4$ , $\theta_I: 9^\circ$ .....	129
Figure 4.5. MV-Pattern for a dome with $r: 5m$ , $n: 5$ , $\theta_I: 6^\circ$ .....	132
Figure 4.6. Parameters of a partially folded state of a dome with $r: 5m$ , $n: 5$ , $\theta_I: 6^\circ$ . 134	
Figure 4.7. Relation between the bending angles and inclination angle for a dome $r: 5m$ , $n: 5$ , $\theta_I: 6^\circ$ .....	137
Figure 4.8. (a) $r: 5m$ , $n: 4$ , $\theta_I: 9^\circ$ Pattern (b) $r: 5m$ , $n: 4$ , $\theta_I: 6^\circ$ Overlapping Pattern (c) $r: 5m$ , $n: 4$ , $\theta_I: 12^\circ$ Complementary Pattern .....	138
Figure 4.9. $r: 5m$ , $n: 5$ , $\theta_I: 6^\circ$ Pattern's simulation in RigidOrigami software.....	142

Figure 4.10. Model of $n$ : 4 pseudo-dome created with shift-axis method.....	142
Figure 4.11. $r$ : 5m, $n$ : 5, $\theta_I$ : 6° Pattern. Red line: generator-line, Blue line: cut line, Green lines: cut lines.....	143
Figure 4.12. $r$ : 5m, $n$ : 5, $\theta_I$ : 6° Pattern with cut lines' simulation in RigidOrigami software.....	143
Figure 4.13. Pattern-generator's motion during folding process of a pseudo-dome cross-section .....	144
Figure 4.14. Parameters for pseudo-dome pattern-generator with $r$ : 5m, $n$ : 5, $\theta_I$ : 6°..	146
Figure 4.15. Parameters for a pseudo-dome .....	148
Figure 4.16. Height, Span and Coverage Area illustration for a $n$ : 5 and $\sigma$ : 40° pseudo-dome.....	151
Figure 4.17. The relation between the inclination angle $\sigma$ and the height $H$ during the folding process of a pseudo-dome $r$ : 5m, $n$ : 4, and $\theta_I$ : 9°.....	152
Figure 4.18. The relation between the inclination angle $\sigma$ and the span $S$ during the folding process of a pseudo-dome $r$ : 5m, $n$ : 4, and $\theta_I$ : 9°.....	153
Figure 4.19. The relation between the inclination angle $\sigma$ and the coverage area $A_c$ during the folding process of a pseudo-dome $r$ : 5m, $n$ : 4, and $\theta_I$ : 9°.....	154
Figure 4.20. Pattern-generator's motion during folding process of a pseudo-dome cross-section. Inclination angle values 90°, 60°, 30°, 10° and 0° from the initial state to final folded state.....	155
Figure 4.21. Parameters for the volume calculations of a pseudo-dome.....	156
Figure 4.22. The relation between the inclination angle $\sigma$ and the volume $V$ during the folding process of a pseudo-dome $r$ : 5m, $n$ : 4, and $\theta_I$ : 9°.....	157
Figure 4.23. $r$ : 5m, $n$ : 3, $\theta_I$ : 15° double row (a) crease pattern and (b) kinematic diagram.....	158
Figure 4.24. $r$ : 5m, $n$ : 4, $\theta_I$ : 9° double row (a) crease pattern and (b) kinematic diagram .....	159
Figure 4.25. $r$ : 5m, $n$ : 5, $\theta_I$ : 6° double row (a) crease pattern and (b) kinematic diagram.....	159
Figure 4.26. $r$ : 5m, $n$ : 3, $\theta_I$ : 15° three rows (a) crease pattern, (b) kinematic diagram, and the (c) modified kinematic diagram .....	160
Figure 4.27. $r$ : 5m, $n$ : 4, $\theta_I$ : 9° three rows (a) crease pattern, (b) kinematic diagram, and the (c) modified kinematic diagram .....	161

Figure 4.28. $r: 5\text{m}$ , $n: 5$ , $\theta_I: 6^\circ$ three rows (a) crease pattern, (b) kinematic diagram, and the (c) modified kinematic diagram .....	162
Figure 4.29. $r: 5\text{m}$ , $n: 3$ , $\theta_I: 15^\circ$ four rows (a) crease pattern, (b) kinematic diagram, and the (c) modified kinematic diagram. ....	163
Figure 4.30. $r: 5\text{m}$ , $n: 4$ , $\theta_I: 9^\circ$ four rows (a) crease pattern, (b) kinematic diagram, and the (c) modified kinematic diagram .....	164
Figure 4.31. $r: 5\text{m}$ , $n: 5$ , $\theta_I: 6^\circ$ four rows (a) crease pattern, (b) kinematic diagram, and the (c) modified kinematic diagram .....	165
Figure 4.32. $r: 5\text{m}$ , $n: 3$ , $\theta_I: 15^\circ$ five rows (a) crease pattern, (b) kinematic diagram, and the (c) modified kinematic diagram .....	166
Figure 4.33. $r: 5\text{m}$ , $n: 4$ , $\theta_I: 9^\circ$ five rows (a) crease pattern, (b) kinematic diagram, and the (c) modified kinematic diagram .....	167
Figure 4.34. $r: 5\text{m}$ , $n: 5$ , $\theta_I: 6^\circ$ five rows (a) crease pattern, (b) kinematic diagram, and the (c) modified kinematic diagram .....	168
Figure 5.1. Design Parameters for double centered barrel vaults .....	176
Figure 5.2. Pattern's drawing steps .....	177
Figure 5.3. Increasing single row .....	177
Figure 5.4. MV-Patterns and their final folded states.....	178
Figure 5.5. Span changes for an obtuse barrel vault with $n: 4$ , $r: 6\text{m}$ , and $a: 3\text{m}$ . ....	179
Figure 5.6. Height changes for an obtuse barrel vault with $n: 4$ , $r: 6\text{m}$ , and $a: 3\text{m}$ ...	180
Figure 5.7. Depth changes for an obtuse barrel vault with $n: 4$ , $r: 6\text{m}$ , and $a: 3\text{m}$ ...	181
Figure 5.8. Volume changes for an obtuse barrel vault with $n: 4$ , $r: 6\text{m}$ , and $a: 3\text{m}$ . ...	181
Figure 5.9. Deployable Obtuse Barrel Vault structure with $n: 4$ , $r: 6\text{m}$ , $a: 3\text{m}$ and $\sigma: 40^\circ$ .....	182
Figure 5.10. Deployable Obtuse Barrel Vault structure with $n: 4$ , $r: 6\text{m}$ , $a: 3\text{m}$ and $\sigma: 40^\circ$ , $\sigma: 55^\circ$ , and $\sigma: 70^\circ$ . ....	182
Figure 5.11. Design Parameters for semi-pseudo-dome.....	188
Figure 5.12. Pattern's drawing steps .....	189
Figure 5.13. Pattern's row multiplication and MV-Pattern .....	190
Figure 5.14. Semi-pseudo-dome pattern with $r: 5\text{m}$ , $n: 6$ , and $R_T: 82$ .....	191
Figure 5.15. Inclination angle $\sigma$ and Central angle $\rho_T$ relation for a semi-pseudo-dome with $r: 5\text{m}$ , $n: 6$ , and $R_T: 82$ .....	192
Figure 5.16. Height changes for a semi-pseudo-dome with $r: 5\text{m}$ , $n: 6$ , and $R_T: 82$ ...	193
Figure 5.17. Span changes for a semi-pseudo-dome with $r: 5\text{m}$ , $n: 6$ , and $R_T: 82$ . ....	193



Figure 5.18. Coverage area changes for a semi-pseudo-dome with $r$ : 5m, $n$ : 6, and $R_T$ : 82.....	194
Figure 5.19. Volume changes for a semi-pseudo-dome with $r$ : 5m, $n$ : 6, and $R_T$ : 82.....	194
Figure 5.20. Deployable Semi-pseudo-dome structure with $r$ : 5m, $n$ : 6, $R_T$ : 82, and $\sigma$ : 60° .....	195

## LIST OF TABLES

<u>Table</u>	<u>Page</u>
Table 2.1. Origami Family Tree by David Mitchel .....	9
Table 2.2. Origami Classifications and architectural speculation by Lee and Leounis	10
Table 2.3. Systematization attempt of origami art by Oksana Chorna. ....	11
Table 2.4. Origami Classification done by the author.....	14
Table 3.1. Maximum and minimum values of the angles $\mu$ , $\lambda'$ , $\varphi$ , and $\sigma$ .....	52
Table 3.2. Parameters for $r: 2, n: 6$ semicircle and $r: 2, n: 5$ horseshoe $200^\circ$ arches .	54
Table 3.3. Number of degree-4 and degree-6 vertexes on triangular patterns.....	55
Table 3.4. Number of degree-4 vertexes on trapezoidal patterns .....	55
Table 3.5. Parameter of figure 3.23 for a horseshoe arch $n:6 r:4 \Omega:200 R_n:10$ .....	69
Table 3.6. Single centered triangular pattern mobility analysis with different number of segments and rows .....	79
Table 3.7. Single centered trapezoidal pattern mobility analysis with different number of segments and rows .....	85
Table 3.8. Single centered modified trapezoidal pattern mobility analysis with different number of segments and rows.....	86
Table 3.9. Maximum and minimum values of the angles $\mu_1, \mu_2, \lambda', \varphi$ , and $\sigma$ .....	94
Table 3.10. Parameters for Obtuse, Pointed Equilateral, and Lancet arches.....	96
Table 3.11. Number of vertexes on triangular patterns.....	97
Table 3.12. Number of vertexes on trapezoidal patterns.....	97
Table 3.13. Double centered triangular pattern mobility analysis with different number of segments and rows. ....	115
Table 3.14. Double centered modified triangular pattern mobility analysis with different number of segments and rows.....	115
Table 3.15. Double centered trapezoidal pattern mobility analysis with different number of segments and rows. ....	120
Table 3.16. Double centered modified triangular pattern mobility analysis with different number of segments and rows.....	120
Table 4.1. Parameters for a $r: 5m n: 5$ and $\theta_I: 6^\circ$ rigid origami dome pattern.....	131
Table 4.2. Maximum and minimum values of the angles $\mu$ , $\varphi$ , and $\sigma$ for a Pseudo-dome pattern.....	136

Table 4.3.	Conditions for selecting and calculating the total number of rows $R_T$ ....	154
Table 4.4.	Pseudo-dome pattern mobility analysis with different number of segments and rows.....	169
Table 4.5.	Pseudo-dome modified pattern mobility analysis with different number of segments and rows.....	170
Table 5.1.	Design Parameters for Obtuse arch cross-sectioned rigid origami barrel vault.....	175
Table 5.2.	Design Parameters for semi-pseudo-dome deployable structure. ....	188

# CHAPTER 1

## INTRODUCTION

Origami is a Japanese word which means “folding paper”. Paper folding is an ancient art, which is believed to have developed simultaneously in eastern and western civilizations (Hatori, 2011; Lister, 2005b). The art of paper folding has evolved rapidly starting from the end of 19th century. Today origami is not only a primarily field of art, but also a topic in research of mathematics, engineering and architecture (Fei & Sujan, 2013).

In the field of engineering and architecture the application of origami’s geometrical properties are studied under two main topics: folded plate structures and deployable structures. Folded plate structures have the static advantage created by the geometrical principle of the origami pattern allowing its application with different construction materials like timber and steel (Buri & Weinand, 2008).

In recent years; the need for a more flexible space organization has risen in architecture, leading to researches in the field of kinetic architecture. The kinetic properties (developability and flat-foldability) of certain origami patterns allow the design of a multitude of different deployable structures. There are different kinds of deployable structures within the field of kinetic architecture which use origami principles; the most studied kinds are bar structures created with scissor mechanisms and textiles allowing structures to be light weighted, deployable and transportable (Thrall & Quaglia, 2014; De Temmerman et al, 2007b). There are also foldable plate structures, called rigid origami (Tachi, 2009b), created with rigid materials allowing the structure to still be deployable and transportable but also more resistant and durable. The use of an origami principle is different for both types of structures: the bar structures uses the crease lines as bars and the vertexes as the joints of the mechanism, while the rigid origami structures uses the crease lines as joints and the polygons as rigid material to create the mechanism.

This research proposes a novel design method for a pseudo-dome deployable, developable and flat-foldable structure based on the geometrical principles of an origami pattern. In this study, first, the Yoshimura pattern, also named diamond pattern, is geometrically analyzed to determine the parameters required to design a barrel vault

deployable rigid origami structure with different arch types as cross-sections. Then a geometrical method to create a pseudo-dome structure has been demonstrated based on the study conducted on the barrel vault rigid origami structures. Furthermore the mobility calculations, for both barrel vault and pseudo-dome rigid origami structures, are provided to give insight to the deployability of the structure.

The results of this study allows the designer to manipulate the parameters according to the needs of the designed space for both the barrel vault structures and pseudo-dome structures.

## **1.1. Aim and Scope of the Research**

Many different rigid origami designs have been proposed based on different origami patterns, like Miura-ori, Yoshimura, and Waterbomb patterns. Many of these researches are concentrated on the linearly deployed, single curvature structures, like barrel vaults and tubular structures. Few studies are conducted on structures with double curvature that deploy radially, like domes. One of the reasons for this is the complexity of designing a pattern that allows both flat-foldability and developability.

The aim of this research is to propose a novel method of designing pseudo-dome rigid origami structures that is flat-foldable and developable and also provide insight on the movement during the deployment process and the mobility of the created pattern. To achieve this objective an analysis of barrel vaults with different cross-sections will be conducted which shares similarities with dome structures. The design process starts by the choice of suitable geometrical parameters, follows by a workspace analysis, and end with a mobility analysis to understand the kinematics of the created pattern.

A brief history and classification of origami is also presented to be able to understand and determine which types of patterns are used in this research. A review is presented on the previous studies about origami inspired deployable structures, alongside the theorems and principles used in the design of these structures.

## **1.2. Outline of the Thesis**

The second chapter begins with a presentation of the history of origami starting from eastern origins to the present applications of this art, then follows a classification

of origami types, created by the author, to identify the types of patterns that will be used within the context of this research. The origami terminology and the mathematic theorems about folding are given. The chapter ends with a review about general origami applications where origami inspired applications, deployable structures, fold types, pattern creation methods, patterns used in the research fields, and mechanisms are presented.

The third chapter is divided into two sections: single centered and double centered barrel vaults. Single centered barrel vaults have semicircle and horseshoe arches as cross-sections, double centered barrel vaults have pointed equilateral, pointed obtuse and lancet arches. For both section a method of designing a MV-Pattern is presented under the geometrical properties title, where geometrical properties and the relations between parameters are explained. It is followed by the workspace analysis where the properties of the deployable structure, like the span, height, and volume, are put in relation with other parameters. Each section end with a mobility analysis that provide insight to the kinematics of the pattern created.

The fourth chapter presents a novel method of creating a flat-foldable developable pseudo-dome rigid origami deployable structure. A segmentation method is presented in the first section allowing the design of the MV-Pattern. It is followed by a geometrical analysis which explains each step of the design of the pattern and the relation between the parameters. The chapter continues with a workspace analysis where the structure's motion is analyzed during its folding process. Analysis reveals the relation between the parameters and the structure's properties. This chapter ends with a mobility analysis allowing to understand the changes of kinematic properties when the design parameters changes.

The fifth chapter presents two case studies where the design steps for specific emplacements are presented. The first case study is the design of a barrel vault rigid origami structure over an archeological site, which will provide cover when needed. The second case study is the design of a semi-pseudo-dome rigid origami structure to be used as a concert enclosure.

The sixth chapter concludes the study by discussing the possible further studies and an evaluation of the proposed method.

## CHAPTER 2

### REVIEW OF PREVIOUS WORKS

This chapter presents the history of origami, a classification of types of origami and a section about the terminology and theorems about folding. It is followed by origami application section where a review is given about deployable structures, rigid origami, a general presentation of most used origami patterns in this field, and a brief review on studies on the mechanism of rigid origami structures.

#### 2.1. History of Origami

The word “origami” is a Japanese word composed of two different roots, the verb “Oru” (折る) which means “to fold” and “kami” (紙) which means “paper”. There are different views about the origins of origami, some believe that its “invention” coincides with the invention of paper in 105 A.D. in China by an officer of the imperial court T’sai Lun, while others believe that it originates in the Heian period (794-185) in Japan. But there are also different views about the invention of the origami’s medium: paper. Hatori argues that the invention of paper (bark paper) dates back to 5000 B.C. to Meso-America, Hawaii and Southeast Asia (Hatori, History of Origami in the East and West before Interfusion, 2011). The papyrus paper which is believed to have been invented around 3000 B.C., is also a kind of paper used by ancient Egyptians (Lister, 2005a). To be able to determine the origins of the creation of paper a precise definition of it is required.

However, it is known that the knowledge of paper making travelled from China to Japan in 610 A.D. via Korea thanks to a Buddhist monk. Chinese traders transmitted the knowledge to Central Asia. In 751 A.D. Arabs occupying Samarkand took Chinese paper makers as hostages and learned the craft (Smith, 2005). Paper making was introduced to Egypt during the 10th century and from there it spreaded to Spain in the 12th century and to Italy during the 13th century (Smith, 2005).

As mentioned before the origins of paper folding are ambiguous, some attribute it to Chinese funerary art (Kenneway, 1987; Smith, 2005) where papers were folded to replicate the objects that should have been buried with people. This Chinese tradition of

replacing paper folded objects with real ones emerged from the increasing grave robbing theft (Kenneway, 1987). Others attribute the origin of origami to Japanese ceremonial wrappers (Hatori, History of Origami in the East and West before Interfusion, 2011), and finally some others to ancient Egypt map folding of papyrus paper (Lister, 2005a). David Lister believes that the most ancient example of paper folding dates from around 1150 B.C., an old Egyptian map found in the Nubian Desert which has a folding style resembling today's road maps (Lister, 2005a).

It is believed that the art of folding paper emerged simultaneously in the West and East. There are contradictory views about in which period, origami emerged in Japan. Some believe that folding started right after the introduction of paper in Japan during the 6th century (Kenneway, 1987). Others believe that folding ceremonial wrappers are part of samurai warrior's etiquette, which goes back to Muramochi period (1333-1573) (Hatori, History of Origami in the East and West before Interfusion, 2011). And there are also those believing that origami originates from the Heian period (794–1185) based on an anecdote from Abe no Seimei (Hatori, History of Origami in the East and West before Interfusion, 2011). Whether folding paper started during the Edo period or Muramochi period one thing is an accepted knowledge: the first origami examples had a ceremonial purpose. “Ocho Mecho” which are wrappers for sake bottles representing male and female butterflies, and “Noshi” which are ornaments attached to gifts, are examples of ceremonial origami which also had a religious purpose (Figure 2.1).

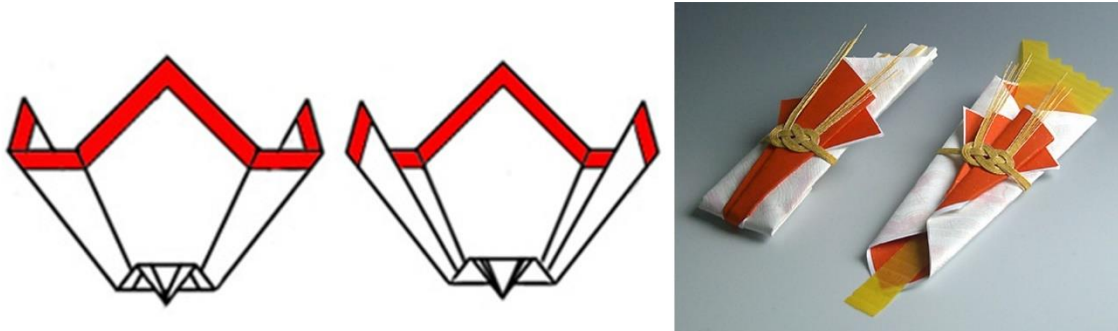


Figure 2.1. Mecho (female, left) and Ocho (male, middle) (Source: Origami resource center (n.d.). Noshi (right) (Source: Abranera (2012)).

It is believed that there existed also an “utilitarian paper folding” between the ceremonial folds and recreational paper folding (Lister, 2005b). “Tato” which is a small paper container and paper “medicine balls” are examples to this style of origami (Lister, 2005b). By the Edo period (1603–1868), the paper folding had become recreational as



well as ceremonial. It was a part of the Japanese oral culture transmitted from mother to daughter (Kenneway, 1987). Sadatake Ise detailed thirteen different wrapping methods, ceremonial origami models, in his book “Tsutsumi-no Ki” published in 1764 (Smith, 2005). The first written instructions, for recreational purposes, appeared in Akisato Rito’s “Sembazuru Orikata” (thousand crane folding) in 1797 (Smith, 2005; Lister, 2005b) (Figure 2.2). During the same year another book “Chushingura Oritaka” appeared. According to Lister these two books represent a division between two different types of origami, one is for adults with complex models requiring cutting, the other for children with almost no cutting (Lister, 2005b).

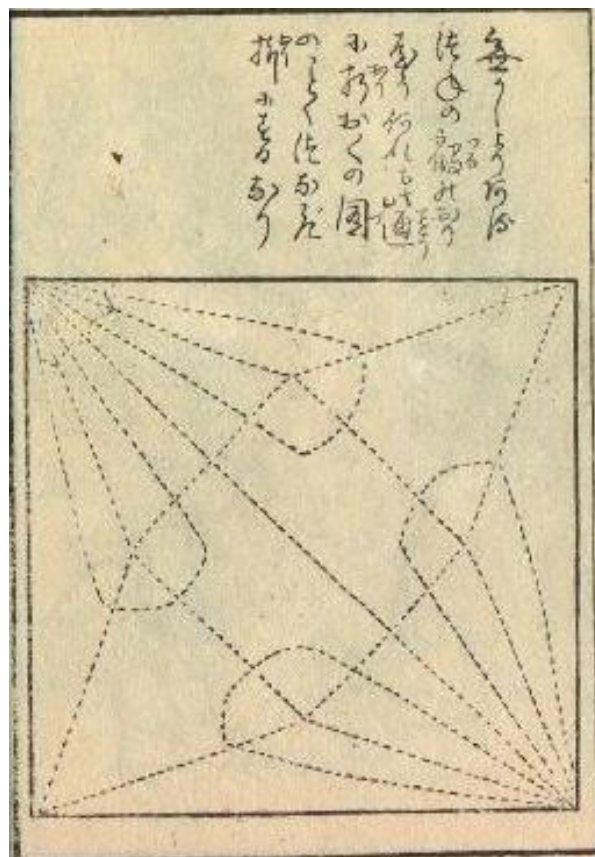


Figure 2.2. Page from Sembazuru Orikata.  
(Source: Sembazuru Orikata, 1797)

Another book appeared in 1801 titled “Toryu Orikatachi Taizen” (Encyclopedia of Contemporary Origami) written by Hokyū Ogani (Smith, 2005). A more broad compilation was published in 1845 by Adachi Kazuyuki titled “Kayara-gusa” (Hatori, History of Origami in the East and West before Interfusion, 2011).

In western civilizations at the beginning, as in Japan, origami was used for religious purposes: baptismal certificates are examples of ceremonial origami from 17th and 18th centuries (Hatori, History of Origami in the East and West before Interfusion, 2011). In the play “the Duchess of Malfi” by Webster there is evidence of the origami model of paper fly-trap known today as “water bomb” (Lister, 2005b). During the 19th century the recreational origami model known in Spanish as “pajarita” and “cocotte” in French appeared (Lister, 2005b), it can also be considered as a typical model of western origami (Hatori, History of Origami in the East and West before Interfusion, 2011) (Figure 2.3).

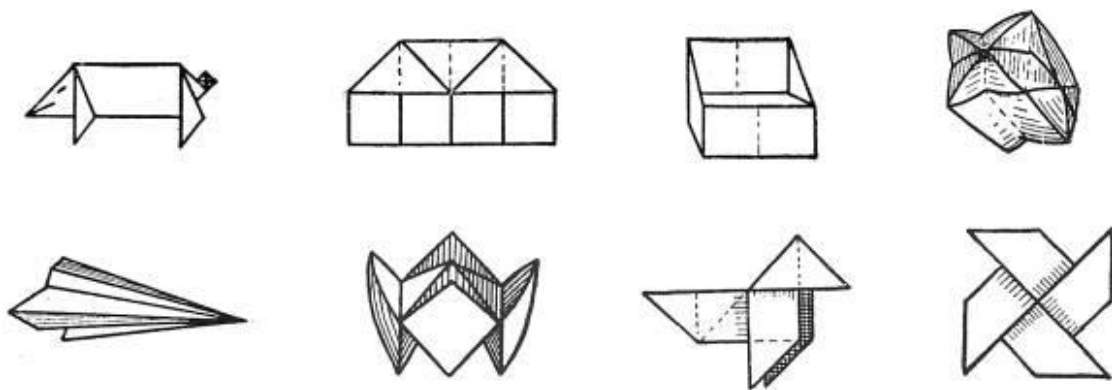


Figure 2.3. European traditional origami models (starting from left top corner; pig, house, sofa, waterbomb (balloon), paper plane (arrow), salt cellar, pajarita or cocotte, and windmill (Source: Hatori, 2011, p. 7).

Around the middle of 19th century, the founder of the first modern kindergarten, Friedrich Wilhelm August Froebel, introduced origami as an “occupation” to his educational system (Hatori, History of Origami in the East and West before Interfusion, 2011). This educational system introduced three different foldings, the first, “Folds of Truth” is a way of teaching mathematics, the second “Folds of Life” is a recreational folding of objects, and animals, the third “Folds of Beauty” is a decorative patterns (Lister, 1998).

The analysis of the Japanese and European origami models shows an important difference between the crease patterns: while Japanese models’ crease patterns have arbitrary angles, European models use square grids (Hatori, History of Origami in the East and West before Interfusion, 2011; Lister, 2005b). Based on these differences, both Hatori (Hatori, History of Origami in the East and West before Interfusion, 2011) and

Lister (Lister, 2005b) believe that origami developed independently in Eastern and Western civilizations.

With the end of the self-imposed isolation around the end of the 19th century (1870) Japanese conjurers travelled around to world bringing traditional Japanese origami models with them (Lister, 2005b). Around the same time Froebel's kindergarten educational system was introduced to Japan which led to the blending of the two different folding styles (Lister, 1998).

Starting from the creation of paper till around 1950, there was a handful of designs of origami figurines because it was mostly an oral tradition. In 1955 the exhibition of paper folding in Amsterdam by Akira Yoshizawa marks the "beginning of modern origami" (Lister, 2005c). Around the same time Yoshizawa also created a set of simple symbols - diagrams - that "transcends language boundaries" (Lang, 2003, p. 4), allowing the worldwide spread of the art. Slowly origami societies started to open around the world the first one being the Origami Center in New York in 1958 by Lillian Oppenheimer (Lister, 2005b). According to Lister, Oppenheimer named the paper folding art as "origami" to differentiate it from paper craft (Lister, n.d.).

During the last sixty years, origami developed rapidly and, with the help of new computer based design methods, figurines became more complex and realistic. The art of paper folding became more than figurine design; today alongside new classical origami models we can observe new geometrical types, like modular origami, tessellation and Golden Venture Folding (3D origami), which is presumed to be an ancient type of paper folding from China. But the principles behind the paper folding art intrigued scientists, primarily the mathematicians, which led to a second field occupied with origami. Today we can not only see different type of artistic origami but also different applications of the folding principals in both the fields of architecture and engineering (rigid origami, foldable structures), and biomedical research (origami stent) (Fei & Sujun, 2013).

## **2.2. Origami Classification**

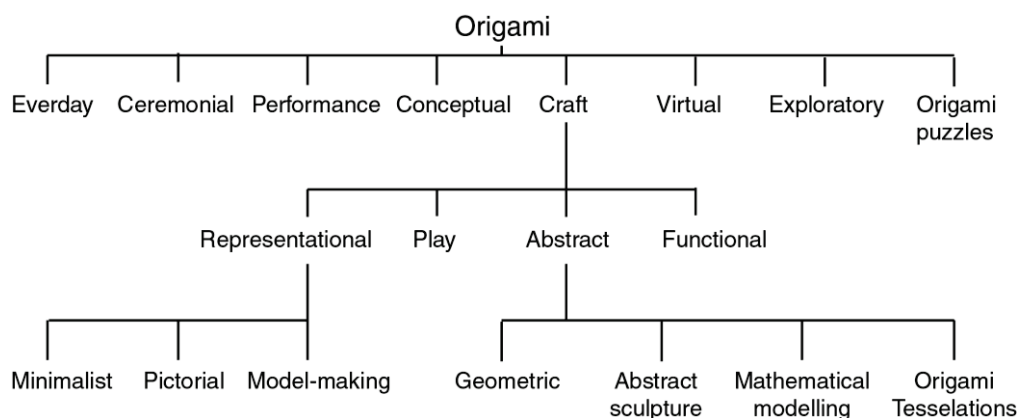
It is difficult to classify all the existing types of origami firstly because it is difficult to access to all origami models made around the world and secondly, it is an art form which has developed rapidly in recent years and has become a focal point for mathematicians, engineers, and architects as well as for many other science fields.

Some attempts have been made by different authors like David Mitchell (Mitchell, n.d.), Oksana Chorna (Chorna, 2012), Lee and Leounis (Lee & Leounis, 2011) to classify different types of origami.

Mitchell differentiates the origami styles not by their folding techniques, but by whether the paper is folded or designed. There are different kind of origami designers, some, like Eric Joisel improvise, create their model while folding (Gould, 2008) while others like Robert J. Lang design the pattern to achieve a desired model (Lang, 2008). The origami family tree (Mitchell, n.d.) is primarily divided into eight different styles. As seen in the Table 2.1, craft origami can be divided into four: representational, play, abstract, and functional origami. The representational origami deals with, the representation of animals, humans and objects. In representational origami field some designers try to reach a perfect representation of the modeled animal with all its detail, while some designers seek a close resemblance. In play origami, models should function as a toy. In functional origami, models must have a utility, like gift boxes or ornaments. In abstract origami, models have geometric qualities.

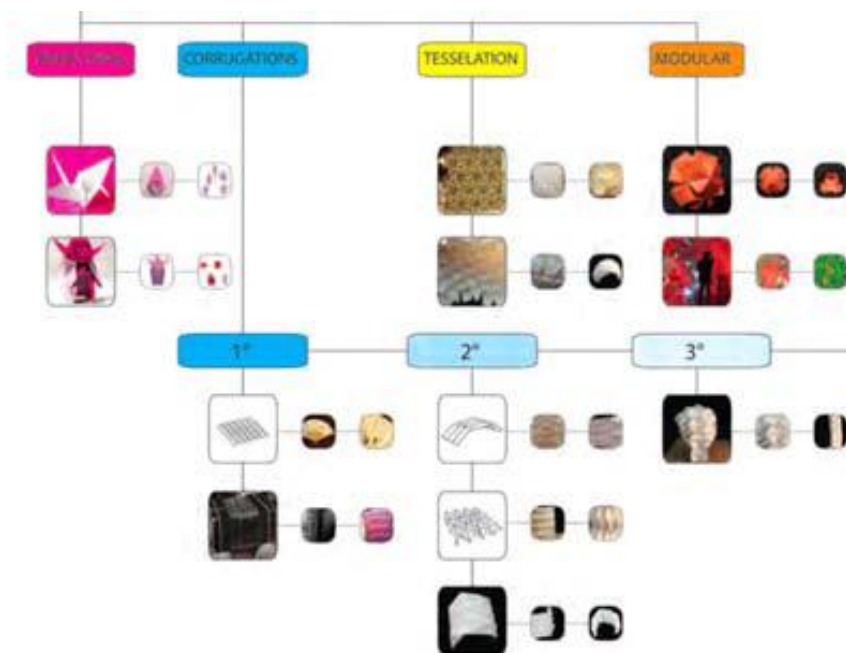
The patterns used in most architectural and engineering studies fall under the abstract origami models. The abstract origami models can be divided into four: geometric origami, abstract sculpture, mathematical modelling, and origami tessellations. Geometric origami, are models that replicate geometric forms. These models can be created by a single sheet of paper or multiple sheets. Abstract sculpture, is a style that pursues an aesthetic appeal. Mathematical Modelling, is folding tiles or polyhedra (Mitchell, n.d.). Origami Tessellations, is the style where multi-layered models are created with the help of the twist folding technique.

Table 2.1. Origami Family Tree by David Mitchell.  
(Redrawn based on source: Mitchell, n.d.)



According to Lee and Leounis (Lee & Leounis, 2011), origami can be classified under four main types: (1) traditional origami, (2) corrugations, (3) tessellation, and (4) modular (Table 2.2). Figurative models like the crane are under the title of traditional origami while models with geometric pattern are under the corrugation title. The third type, tessellation, is divided into as 2D and 3D tessellations. The final type, modular origami, is origami models created by using multiple modules.

Table 2.2. Origami Classifications and architectural speculation by Lee and Leounis. (Source: Lee & Leounis, 2011)



In the third classification Chorna, from the point of view of art history, tried to analyze different styles and types, to determine different criteria to be able to classify origami models, and according to the criteria detected, to be able to establish origami as an art (Table 2.3) (Chorna, 2012).

Chorna defines ten different types of origami: conventional origami, plastic origami, origami tessellations, pleat origami, Tachi's origami (3D Origami), origami corrugations, curvilinear origami, crumpling origami, synthesized origami and modular origami. She subdivides origami tessellation and modular origami into two-dimensional and three-dimensional tessellations and homomodular and heteromodular respectively (Chorna, 2012). She also categorizes them according to their genres - animalistic, portrait, still life, teratological, geometrical and other -, to their content and function - applied, easel and monumental -, to their spacing - open or closed -, to their historical

features - whether the author is known or unknown -, and finally as an analogy to miniature (Chorna, 2012).

Table 2.3: Systematization attempt of origami art by Chorna.  
(Source: Chorna, 2012)

	Conventional origami	Plastic origami	Origami Tessellations	Panel Origami	Tachi's origami	Origami Corrugations	Continual origami	Crumpling origami	Other origami	Synthesized origami	Modular origami		
			Two-dimensional	Three-dimensional							Heteromodular	Heteromodular	
to historical features	Traditional												
	Author's												
to its opening	Opened												
	Closed												
to its content and its function	Monumental												
	Exact												
	Applied												
analogy to miniature	Mini origami												
	Aesthetic												
	Portrait												
to genres	Still life												
	Translogical												
	Geometric												
Others													

In this new attempt of classification, the four main types by Lee and Leounis (Lee & Leounis, 2011) are used but they are subdivided into categories based on their folding technique - folding and wet folding - for traditional origami, or based on their final form - two-dimensional or three-dimensional - for origami tessellation, and corrugations. And modular origami is subdivided based on the modules - homomodular and heteromodular - used in the creation of the model.

The properties of four different types of origami can be classified under three main titles: sheet number, patterns, and movement. Origami models can be differentiated by the number of sheets they are using while creating a model; the sheet number property under this definition can be subdivided into single sheet and multiple sheet usage (Table 2.4). As

it has been pointed out by Lister in his study of origami history, there are different kinds of crease patterns used (Lister, 2005b). Crease patterns are the second property suggested for this classification which is subdivided as geometric patterns and grid patterns. A generalization has been made under the title of geometric patterns, which classifies patterns with mixed patterns - grid and radial together - under this title. Some are central while others have multiple central dispersions. The grid patterns are then subdivided into tessellation patterns and corrugation patterns. The last property is movement which differentiates whether the origami model is designed to be static or kinetic.

Animal, plant and human figurine origami models alongside utilitarian ones, like containers, are placed under the title of traditional origami. A volumetric division has not been proposed for traditional origami but it should be pointed out that some are two-dimensional, which means they are flat-folded, while others are three dimensional models, like containers. The difference between the subcategories of folding and wet folding lies in the ‘how’ the paper is used, and ‘how’ it is folded to achieve the final model. Folding refers to the models folded with sharp edges while wet folding refers to curved/smooth edge folding which is achieved by moistening the paper before starting the folding process. The wet folding technique has been developed by Akira Yoshizawa (Lister, 2005c). The unwritten rule of pure origami defines that the model has to be achieved only by folding, using glue or cutting paper are unacceptable. In traditional origami, most of the models are pure origami thus they are created using of a single paper. There are other figurine models where we can see the use of two or three pieces of paper in the creation. Most of the crease patterns have radial properties, but as indicated before, it is not possible to locate and categorize all the existing origami models. Some traditional models like the flapping bird or seller origami models, designed as toys or entertainment purpose, are kinetic models. The world known traditional crane model or the pajarita models are static origami models.

“Origami tessellations are geometric designs folded from a single sheet of paper, creating a repeating pattern of shapes from folded pleats and twists.” (Gjerde, 2009). Tessellation can also be described as a tiling of a surface using one or more polygons with no overlaps or gaps between them. There are two types of origami tessellations: the first one is the two-dimensional ones where the pattern is created by folding, twisting and locking the paper, which make the model a static one, and the second type is the three-dimensional ones where the paper is folded and twisted but not locked. Models like Reschs’s pattern (Tachi, 2013), and Huffman’s patterns (Davis et al., 2013) are

example to three-dimensional tessellations, where the models expands and retracts when force is applied. Two-dimensional tessellations' final states are flat surfaces but the three-dimensional tessellations have thickness in all three directions. Thus it can be said that in this subdivision the models do not create volume but are different in being planar or non-planar surfaces. This volumetric subdivision can also be noticed in the classification by (Chorna, 2012). The patterns for both types of tessellations, are tessellation patterns under the grid pattern category. In both types regular and irregular tessellation patterns can be observed.

On the other hand, modular origami is subdivided into two parts: homomodular and heteromodular (Chorna, 2012). Homomodular origami models are composed of a single unit folded the same way, while heteromodular origamis are composed of different units folded differently. Both homomodular and heteromodular are subdivided according to their volumetric properties. The three-dimensional homomodular origamis are again subdivided into polyhedral and 3D origami, the later one being a Chinese folding technique of a single triangular module, also known as Golden Venture Folding. As the name suggests, the final model of all the models under this category use multiple number of sheets. Two-dimensional homomodular origami models are created when multiple planar modules are interlocked to create a surface, like origami quilts. Polyhedra created by multiple modules fell under the three-dimensional homomodular or heteromodular origami models depending on the module used. In the book “Modular Origami Polyhedra”, there are examples of the creation of polyhedrons using homomodels, like a 30-module dodecahedron (Simon, Arnstein, & Gurkewitz, 1999). Patterns of this type of origami models fell under radial patterns, but it should be pointed out that, especially for polyhedra creations, modules are geometrically created to form, when interlocked, a specific angle required for the vertex or edge of the polyhedron. There are few examples of kinetic modular origami; flexibola and curlicue, both can be seen in Table 2.4.

“Origami Corrugation” is a technique of alternating mountain and valley folds in an arrangement that allows movement in a folded model” (Lee & Leounis, 2011). Corrugations are also subdivided into two volumetric properties. The two-dimensional origami models in this type have thickness in z-direction - Miura-ori pattern - but do not create a volume, while the three-dimensional corrugated origami models – Yoshimura pattern - final state creates volumes.



Table 2.4. Origami Classification done by the author.  
 (Sources: Wet folding, Dreamer (Dinh, n.d.), Christmas tree (Guarnieri, 2010), all other are folded by author.)

		NUMBER of SHEET		CREASE PATTERNS			MOVEMENT	
		SINGLE	MULTIPLE	GEOMETRIC PATTERNS	GRID PATTERNS		STATIC	KINETIC
					TESSELLATION	CORRUGATION		
MODULAR ORIGAMI	HETEROMODULAR	3D						
		2D						
	HOMOMODULAR	3D						
		POLYHEDRON						
		3D-ORIGAMI						
		2D						
ORIGAMI CORRUGATION	3D							
	2D							
ORIGAMI TESSELLATION	3D							
	2D							
TRADITIONAL ORIGAMI	WET FOLDING							
	FOLDING							

There are various models of origami making difficult to create a classification but patterns used in this study need to be placed within this vast universe of origami. Corrugated origami with three-dimensional properties are patterns used in this study to create foldable and deployable structures.

### 2.3. Origami Terminology

Starting from the medium of origami, the paper is defined as a *flat surface*; it is the *initial state* before starting the folding process. The next step is to fold the *crease* which can be defined as a line segment (Demaine & O'Rourke, 2007) or a trace left after the paper is folded and unfolded. There are two different ways to create a crease *mountain fold* and *valley fold* (Figure 2.4) which “can be considered as dual to each other” (Dureisseix, 2012). Generally the mountain fold is represented by dash-dot-dash line while valley fold is represented as a dashed line (Lang, 2004). But origami designers have their own system of representing the types of folds which is generally explained in their books.

Origami models vary from one-fold models (Jackson, 2011) to complex models composed of multiple creases. *Crease pattern* [CP] is the network of creases on the surface of the paper. The designation of which creases will be mountain fold or valley fold is called *mountain-valley assignment* [MV-assignment] and when CP and MV-assignment are represented together the network of the creases became a *mountain-valley pattern* [MV-Pattern] (Demaine & O'Rourke, 2007). Some creases are created to be used as references for other creases, these *reference creases* are left as solid lines in the MV-Pattern of the origami model. For example, the diagonal drawn from the right top corner to the left bottom corner on the MV-Pattern of the traditional crane (Figure 2.5b) is a reference crease.

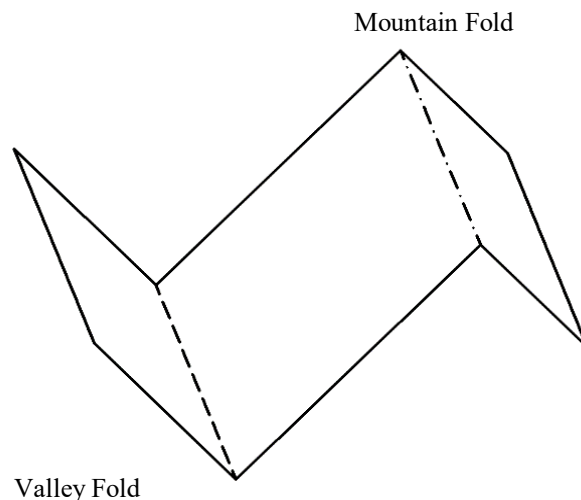


Figure 2.4. Mountain and Valley folds – drawn by the author.

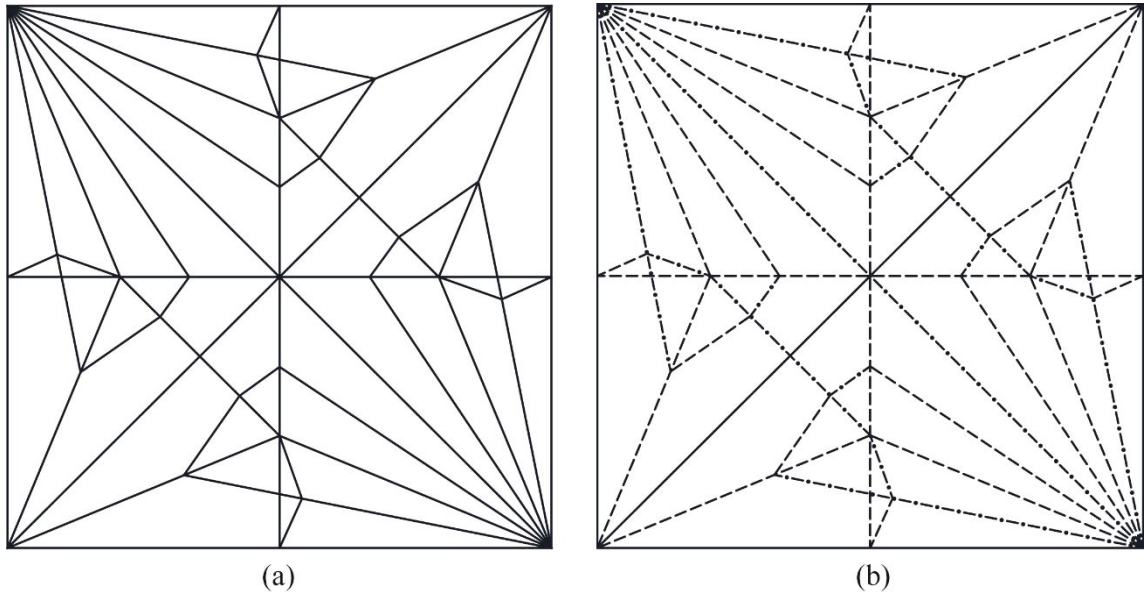


Figure 2.5. (a) CP of the traditional crane origami, (b) the MV-Pattern of the same model– drawn by the author.

During the creation of an origami model there is a motion which starts from the flat surface and end as a folded model. The model starts as a plane [flat surface] called *initial state* (Figure 2.6a) and when the model is finished it reaches its *final folded state* (Figure 2.6c) (Demaine & O'Rourke, 2007, p. 169); between these two states there is the *partially folded state* (Figure 2.6b), which is important while designing an origami inspired kinetic structure.

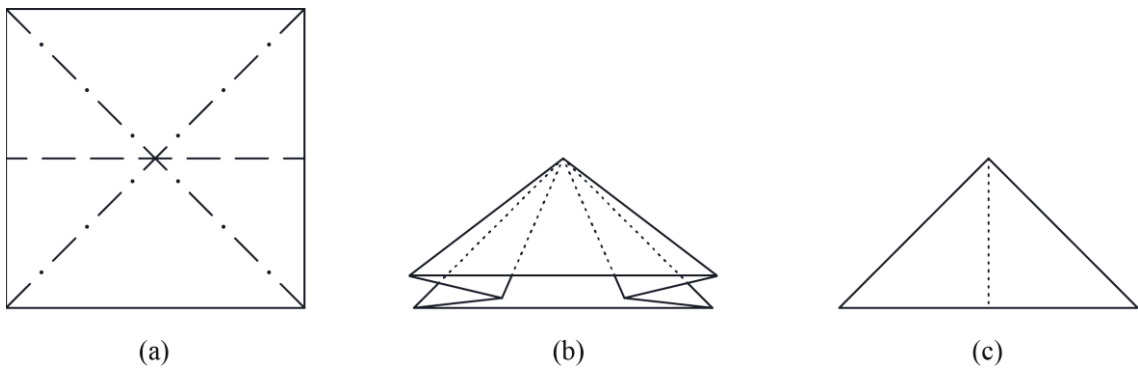


Figure 2.6. (a) MV-P initial state, (b) partially folded state, and (c) final folded state. Dotted lines represent hidden lines – drawn by the author.

The intersection of two or more creases in the interior of the surface is called a *vertex*. The vertexes are named according to the number of edges or plates joining to form that particular vertexes, as an example a vertex created by four edges coming

together is called a *4-edge vertex* (Buri H. , Origami - Folded Plate Structures, 2010) or a *degree-4 vertex* (Weisstein). In this study the annotation to precise the type of vertexes will be  $v^k$  and read as *degree-k vertex*, where  $k$  is the number of edges coming together to form the vertex; thus a degree-4 vertex will be annotated as  $v^4$  and a degree-6 vertex as  $v^6$ .

*Flat-foldable* is a model that can be folded flat on the ground without adding new creases, in other words the final folded state of the model can be put between the pages of a closed book. The question of flat-foldability is studied under two angles: the first is the *local flat-foldability*, LF-F, which regards the flat-foldability of a single vertex on a MV-Pattern. The second is the *global flat-foldability*, GF-F, which considers the flat-foldability of the whole model. While there are theorems like the Kawasaki-Justin theorem or the Maekawa theorem for local flat-foldability, the question of global flat-foldability is still unsolved (Demaine & O'Rourke, 2007, p. 170; Hull T. , 2002).

In the field of engineering and architecture the term *developable surface* refers to a surface which can be open completely to a flat surface. And the term *non-developable surface* means that when the structure is completely unfolded the surface is not flat (Gattas & You, 2013; Gioia, Dureisseix, Motro, & Maurin, Design and Analysis of a Foldable/Unfoldable Corrugated Architectural Curved Envelop, 2012). In the same fields of study the word *rigid-origami* (Tachi, 2010b) is used as reference to origami inspired structures created by plates with thickness (Tachi, 2011). Most of the engineering or/and architectural studies on this subject assume the deployable structure uses perfect hinges, while the thickness of the plates is neglected (Gattas & You, 2013; Gioia, Dureisseix, Motro, & Maurin, Design and Analysis of a Foldable/Unfoldable Corrugated Architectural Curved Envelop, 2012).

## 2.4. Origami Theorems

There are different theorems on origami. The first one is Huzita-Justin axioms which define how lines can be drawn using points and lines. The other theorems presented in this section are on the *flat-foldability* conditions of single vertexes, LF-F, of patterns and guidelines that can be used to create a globally foldable, GF-F MV-Pattern.

## 2.4.1. Huzita-Justin Axioms

Huzita’s axioms “describes a set of six basic ways of defining a single fold by aligning various combinations of existing points, lines, and the fold line itself” (Lang, 2003b).

The seventh axiom was described by Hatori (Alperin & Lang, 2009), but later it has been found that all the seven axioms had already been presented by Jacques Justin in 1989. That is the reason of the name Huzita-Justin axioms (Lang, 2003b; Alperin & Lang, 2009). These axioms describe how to create a crease by the combination of points and lines (Figure 2.7).

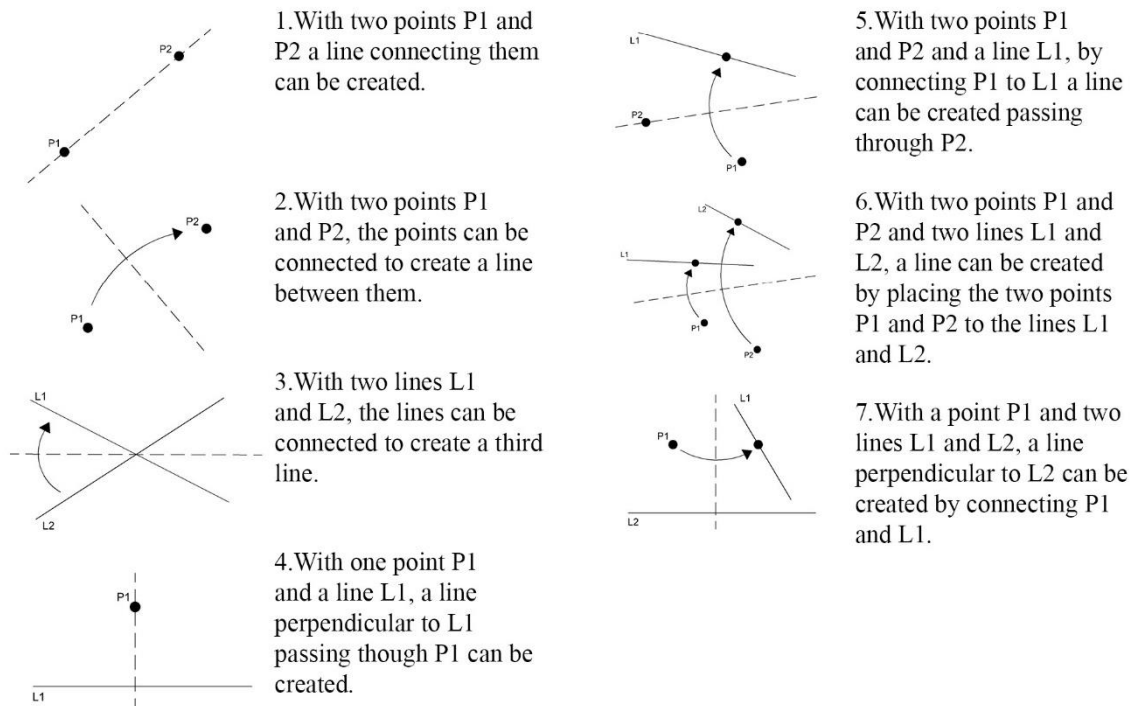


Figure 2.7. Huzita-Justin Axioms drawn by the author based on representation from Alperin and Lang. (Source: (Alperin and Lang, 2009))

## 2.4.2. Flat Foldability

As explained before, a model is flat-foldable when its final folded state is flat. LF-F is the flat-foldability condition of a single vertex on the surface of a CP while the GF-F is the general flat-foldability condition of the CP. There are two theorems regarding the LF-F and two methods/guidelines to achieve a GF-F model.

### **Local Flat-Foldability, LF-F**

There are two theorems on LF-F: the Maekawa theorem, the Kawasaki-Justin theorem. Both are explained and described in the analysis of the central vertex of the crane's MV-Pattern, which is a flat-folded pattern.

#### **Maekawa's Theorem**

The theorem is based on the number of mountain folds and valley folds connected to a single vertex. The value of the subtraction of number of mountain folds and valley folds should be absolute 2 for the vertex to be flat-foldable (eq. (2.1)). For this condition to be satisfied the number of crease lines that are connecting to the vertex needs to be of an even number (Mitani, 2011).

$$|M - V| = 2 \quad (2.1)$$

When the central vertex of the traditional crane pattern (Figure 2.8a) is analyzed and eq. (2.1) is applied, it is proven that the degree-6 vertex is flat-foldable. L are the lines connected to the vertex and the M or V denotes whether the line is mountain or valley fold. L1 and L4 are mountain folds and L2, L3, L5, and L6 are valley folds (Figure 2.8b).

$$|2 - 4| = 2 \quad (2.2)$$

#### **Kawasaki-Justin Theorem**

Kawasaki-Justin theorem approach is based on the value of the angles surrounding a single vertex. For a vertex to be flat-foldable the sum of alternating angles has to be  $180^\circ$  (Figure 2.9). But there are some crease patterns where each vertex are flat-foldable based on this equation that do not fold flat globally, some examples of these type of patterns will be analyzed in the section about GF-F.

$$\alpha_1 + \alpha_3 + \alpha_5 + \dots + \alpha_{2n-1} = \alpha_2 + \alpha_4 + \alpha_6 + \dots + \alpha_{2n} = 180^\circ \quad (2.3)$$

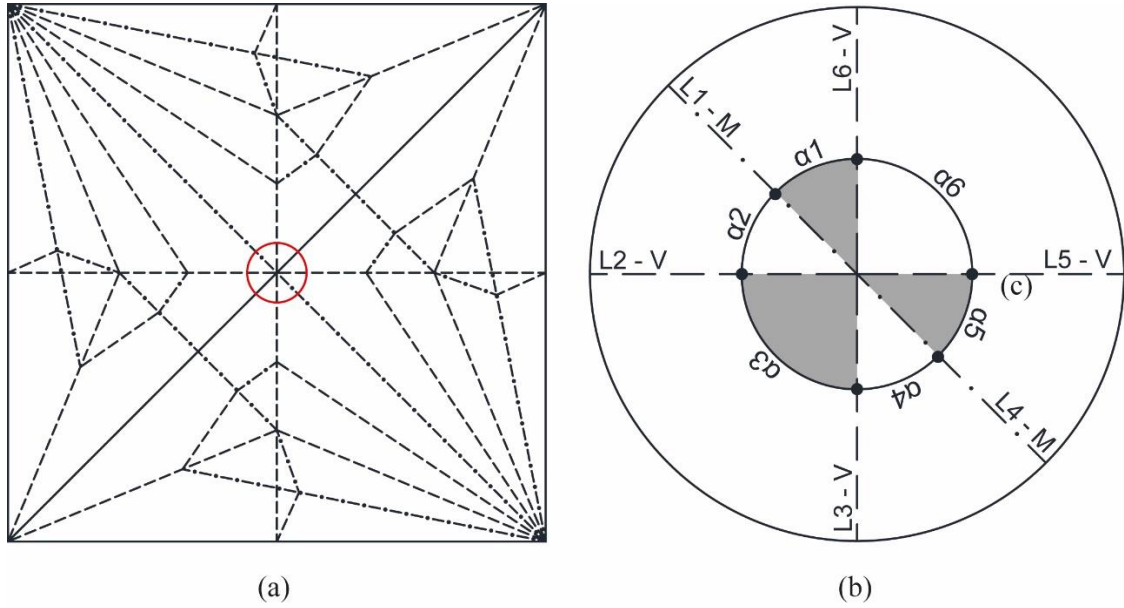


Figure 2.8. (a) traditional crane MV-Pattern, (b) closer view of the central vertex of the traditional crane - drawn by the author.

The central vertex of a traditional crane MV-Pattern is again used to test the theorem (Figure 2.8). The central vertex is flat-foldable based on both Maekawa and Kawasaki-Justin theorems.

$$\alpha_1 = 45^\circ \quad \alpha_2 = 45^\circ \quad \alpha_3 = 90^\circ \quad (2.4)$$

$$\alpha_4 = 45^\circ \quad \alpha_5 = 45^\circ \quad \alpha_6 = 90^\circ \quad (2.5)$$

$$45^\circ + 90^\circ + 45^\circ = 45^\circ + 45^\circ + 90^\circ = 180^\circ. \quad (2.6)$$

From this, it can be assumed that all sector angles sum to  $360^\circ$  ( $2\pi$ ) which can also be defined as the *developability* condition (Gioia et al., 2012). If the sum of all the angles surrounding a vertex is more or less than  $360^\circ$  then that model is *non-developable* because it cannot open flat without a gap or overlap.

### Global Flat-Foldability

As described before, a flat-foldable model is when the final folded state can be closed (neglecting the thickness of the paper) flat without adding new creases or cuts. If the final model is flat then the CP is *globally flat-foldable*. The conditions for GF-F have not been mathematically described yet (Hull T. , 2002; Demaine & O'Rourke, 2007, p. 170). There are CPs and MV-Patterns that satisfy Kawasaki-Justin and

Maekawa theorems but are not globally flat-foldable (Hull T. , 2002). Figure 2.9 presents two different CPs that satisfy the LF-F condition but do not satisfy the global flat-foldability because, when patterns are folded, the surfaces cross each other creating an obstacle to accomplish the folding motion. Both CP's vertexes are analyzed and calculated according to local flat-foldability theorems.

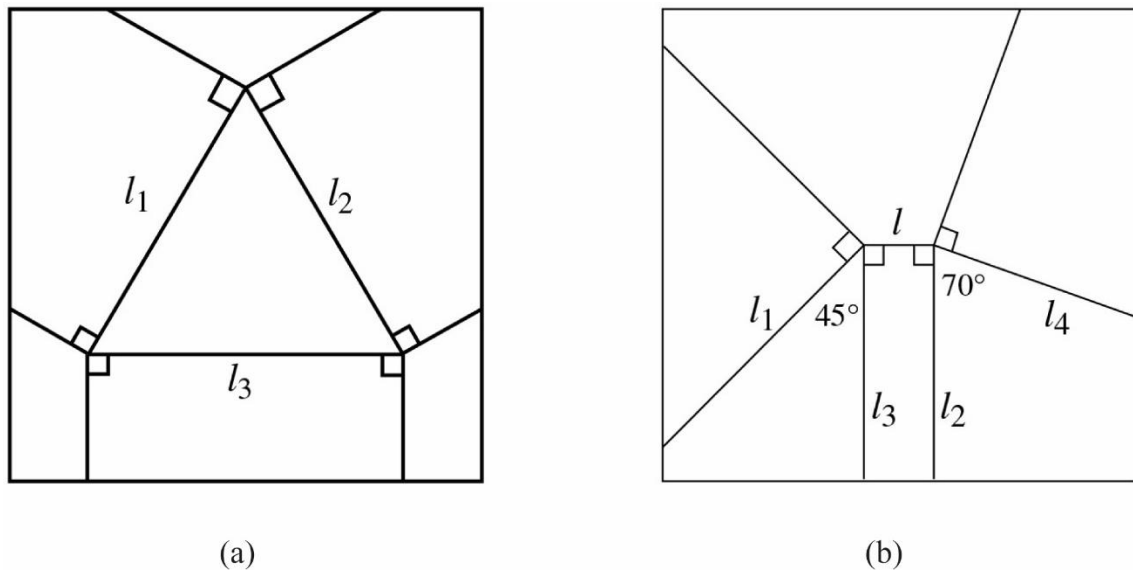


Figure 2.9. (a) CP-1 (b) CP-2. Both CPs are not globally flat-foldable.  
(Source: Hull, 2002)

The first analysis has been conducted on the CP-1 of Figure 2.9. First, each vertex is calculated according to both Maekawa theorem and Kawasaki-Justin Theorem to verify the local flat-foldability condition (Figure 2.10).

Maekawa Theorem: for a vertex to be flat-foldable, the value of the subtraction of mountain folds and valley folds should be  $\pm 2$  as stated in eq. (2.1) (Figure 2.10a). All vertex equations satisfy the condition of Maekawa theorem but when the model is folded it can be observed that the paper does not fold flat because the surfaces cross each other.

$$\text{Vertex a : } 3M - 1V = 2 \quad (2.7)$$

$$\text{Vertex b : } 3M - 1V = 2 \quad (2.8)$$

$$\text{Vertex c : } 3M - 1V = 2 \quad (2.9)$$



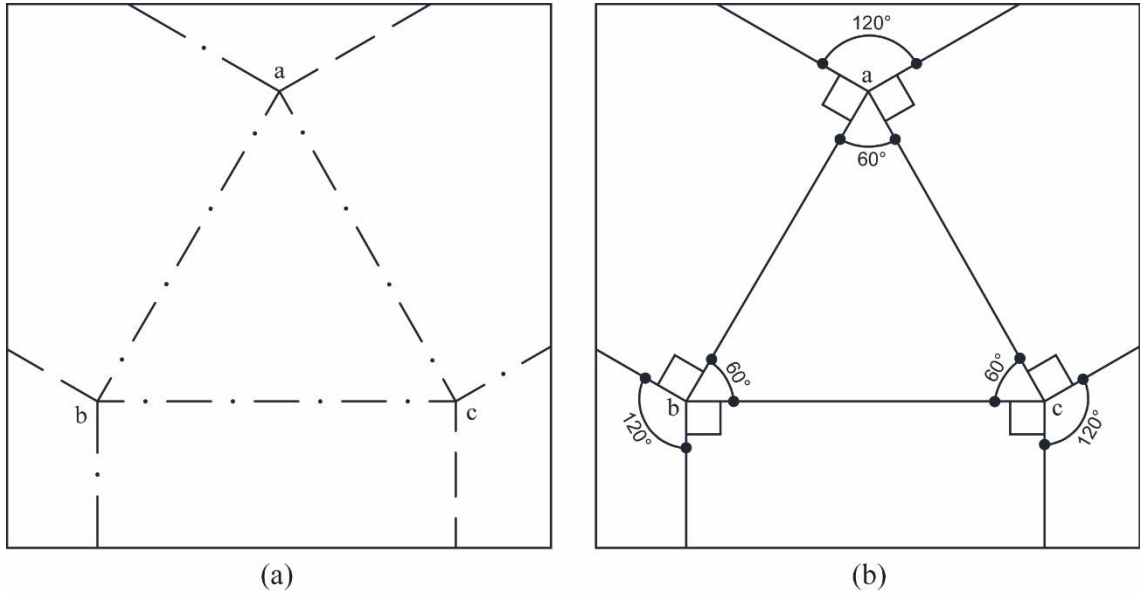


Figure 2.10. CP-1 – (a) MV-assignment done for the purpose (b) degree of the angles. Dashed dot lines are mountain folds and dashed lines are valley folds – redrawn by the author.

Kawasaki-Justin Theorem: for the vertex to be flat-foldable the sum of alternating angles has to be  $180^\circ$ , eq. (2.3) (Figure 2.10b). All vertex equations satisfy the Kawasaki-Justin condition but again the paper is not flat-foldable.

$$\text{Vertex a : } 120^\circ + 60^\circ = 90^\circ + 90^\circ = 180^\circ \quad (2.10)$$

$$\text{Vertex b : } 120^\circ + 60^\circ = 90^\circ + 90^\circ = 180^\circ \quad (2.11)$$

$$\text{Vertex c : } 120^\circ + 60^\circ = 90^\circ + 90^\circ = 180^\circ \quad (2.12)$$

The second analysis has been conducted on CP-2 in Figure 2.9b to verify the local flat-foldability of the CP using both LF-F theorems.

Maekawa Theorem: for a vertex to be flat-foldable the value of the subtraction of mountain folds and valley folds should be  $\pm 2$  as stated in eq. (2.1) (Figure 2.11a). All vertex equations satisfy the condition of Maekawa theorem but the model does not fold flat.

$$\text{Vertex a : } 3M - 1V = 2 \quad (2.13)$$

$$\text{Vertex b : } 3M - 1V = 2 \quad (2.14)$$

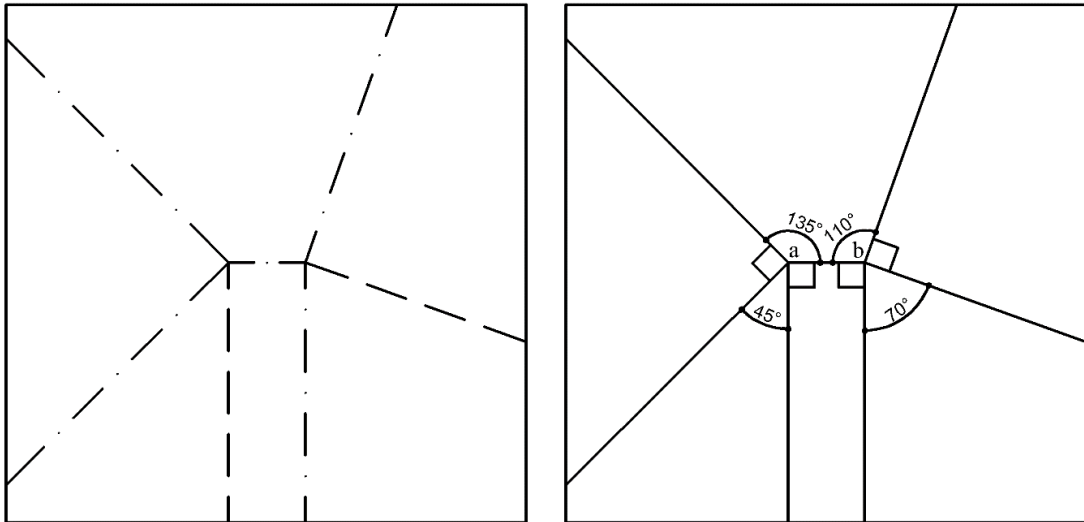


Figure 2.11. CP-2 - (a) MV-assignment done for the purpose (b) degree of the angles. Dashed dot lines are mountain folds and dashed lines are valley folds – redrawn by the author.

Kawasaki-Justin Theorem: for the vertex to be flat-foldable the sum of alternating angles has to be  $180^\circ$ , eq. (2.3) (Figure 2.11b). All vertex equations satisfy the Kawasaki-Justin condition but again the paper is not flat-foldable.

$$\text{Vertex a : } 135^\circ + 45^\circ = 90^\circ + 90^\circ = 180^\circ \quad (2.15)$$

$$\text{Vertex b : } 110^\circ + 70^\circ = 90^\circ + 90^\circ = 180^\circ \quad (2.16)$$

Both CPs on Figure 2.9 are locally flat-foldable for each of their vertexes but not globally flat-foldable. Even though global flat-foldability has not been stated yet mathematically, Schneider (Schneider, 2004) and Mitani (Mitani, 2011) offers methods for creating globally flat-foldable CP by satisfying precise conditions.

Schneider describes the required conditions for flat-foldable crease pattern as (Schneider, 2004):

- “1. All crease lines must be straight line segments.
2. All interior vertices in the crease pattern must be of even degree.
3. At each interior vertex, the sum of every other angle must be  $180^\circ$
4. There must exist a superposition ordering function that does not violate the non-crossing condition.”

Schneider’s first condition specifies that all creases should be straight lines, not curved, for the model to fold flat. The second and third conditions defines the Kawasaki-Justin theorem where alternating angles sum needs to be  $180^\circ$ . The last

condition defines a folding order so that the planes do not intersect in any given state of the folding, also defined as the *noncrossing condition* by Justin (Hull T. , 2002, p. 33). For the *noncrossing condition* to be satisfied, a folding sequence and order is required so that the folded planes do not intersect with each other. Figure 2.12 illustrates the noncrossing condition achieved at the central vertex of the crane MV-Pattern.

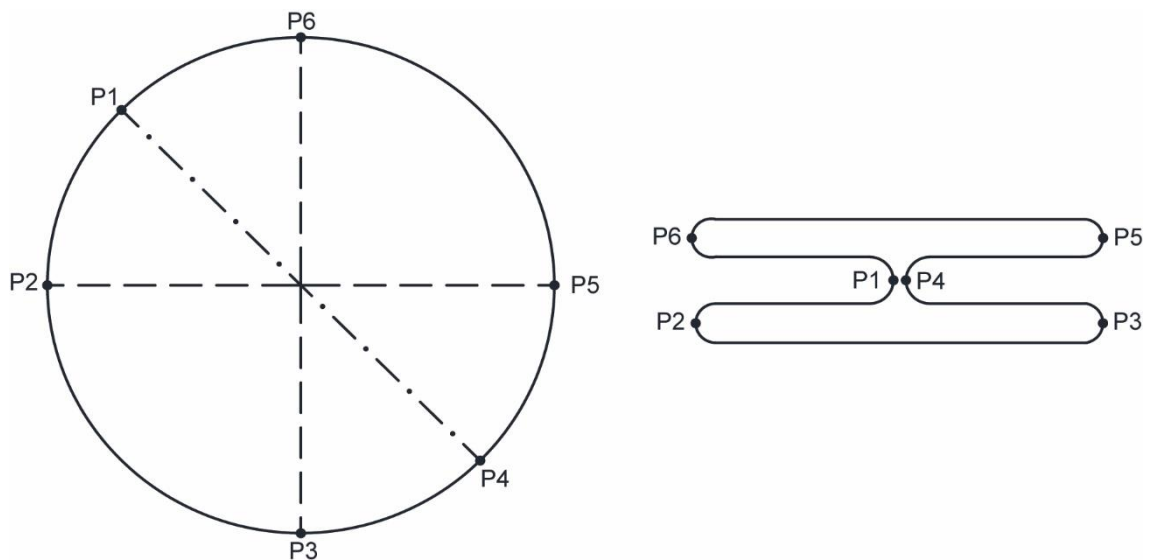


Figure 2.12. Noncrossing condition. Central vertex of the traditional crane MV-Pattern left, non-crossing representation of the folded central vertex on the right - drawn by the author.

Mitani offers a numerical optimization method to design globally flat-foldable crease patterns (Mitani, 2011). He offers two conditions, which are Maekawa and Kawasaki-Justin theorems, followed by a five step method (Mitani, 2011):

“Condition 1.1. The number of lines connecting to a single inner vertex is even.

Condition 1.2. The sums of alternating angles are 180 degrees.

Step 1. Place vertices on edges and inside a sheet of paper.

Step 2. Generate lines that connect two vertices.

Step 3. Adjust the number of lines so that condition 1.1 is satisfied.

Step 4. Move the positions of the vertices so that condition 1.2 is satisfied.

Step 5. Validate that the pattern is globally flat foldable.”

These conditions allow the creation of a globally flat-foldable origami CP where, the MV-Pattern still needs to be folded physically or digitally to control the GF-F. Because it is not mathematically proven after the creation of the CP and the MV-Assignment has been done based on the theorems explained above.

## 2.5. Origami Applications

Origami is still an art form growing rapidly and in the last decade a rise in the use of its principles has been observed in various fields of study due to the advances on computer sciences which transformed origami into a science subject. Origami principles have been used in industrial design to create both foldable and static furniture (Rogers) and also to create packages with both functional and/or decorative purposes. Examples of origami principles can also be found in fashion industries using cloth or textile (De Ruysser, 2014; Dureisseix, 2012).

Origami principles can be found in many forms from the smallest scale as a stent graph (Kuribayashi et al., 2006) in biomedical disciplines to a larger scale structure. In space applications, origami principles can be found in form of a lunar base, solar panels, and foldable telescopic lens (Fei & Sujan, 2013; Dureisseix, 2012; Gruber et al., 2007). In robotics, origami can be found as a self-folding structure (Peraza-Hernandez, Hartl, Malak Jr, & Lagoudas, 2014; Gray, Zeichner, Yim, & Kumar, 2011) or as *oribotis* which has a commanded folding and unfolding process (Gardiner, 2009). In automotive industries, its principles are used to design airbags (Cromvik & Eriksson, 2009).

Other engineering applications are in material design as a morphing sandwich structure (Gattas & You, 2014; Gattas & You, 2015), a sandwich trusscore panels for sound insulation (Ishida, Morimura, & Hagiwara, 2014), a sandwich core material (Klett & Drechsler, 2011), a metamaterial (cellular materials) which is deployable and flat-foldable in two directions and stiff in one direction (Cheung, Tachi, Calisch, & Miura, Origami Interleaved Tube Cellular Materials, 2014).

### 2.5.1. Origami Structures

Applications and studies are also conducted in the fields of architecture, and engineering in correlation with each other. In recent years, architectural needs have changed; more flexible forms are required to fit to the new functional needs which can be provided by an origami CP generating both structural properties and spatial qualities to a space. The form generated by an origami CP produces spatial structures, kinetic or static, that can be altered by modifications to the CP, which provides designers with a tool to accomplish various spatial forms (Gönenç Sorguç, Hagiwara, & Arslan Selçuk,

2009). Searches toward new adaptable forms in architecture led to the creation of deployable and kinetic structures using origami principles. According to Schenk, structures inspired by origami can be classified under three different types: (1) folded plate structure, (2) deployable structures and (3) transformable/kinetic structures (Schenk, 2012).

Folded plate structures are static applications of origami principles and can be constructed with different materials like timber, glass alongside concrete and metal composite sheets. According to Sekularac et al. folded plate structures can be divided in three types based on their load transmission and direction of relying (Figure 2.13): linear, radial and spatial folded plate structures (Sekularac, Ivanovic Sekularac, & Ciric Tovarovic, 2012). While most seen architectural examples are linear (Figure 2.14) and radial folded plate structures (Figure 2.15), a combination of two of these types can also be constructed. The Church St. Paulus, Neuss, in Germany is an example of the combination of linear and central folded plate structures (Figure 2.14 (c)).

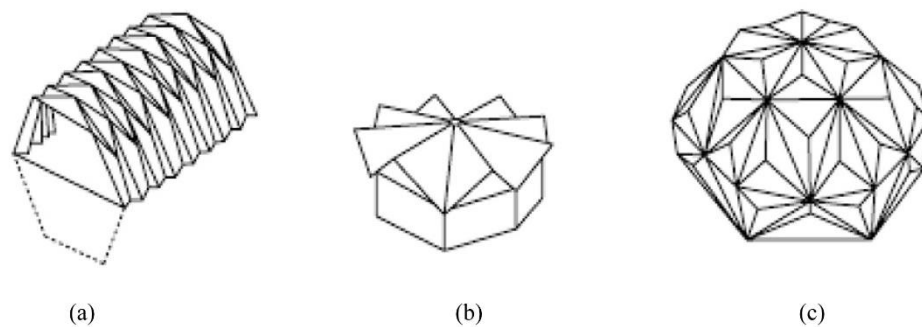


Figure 2.13. (a) Linear folded plate structures (b) Radial folded plate structure (c) Spatial folded plate structure (Source: Sekularac, Ivanovic Sekularac, & Ciric Tovarovic, 2012).

Geodesic domes can be considered as spatial folded plate structures even though they are generally classified as shell structures. But there are no constructed architectural examples of domes created based on origami principles, only research examples are available. Falk et al. presented a form of exploration for folded plate domes based on timber where “Using a combination of geometry generation and performance optimization, parameters of folds, depth of folds, height of dome and the effect of perforations on structural efficiency, interior lighting and acoustics are explored” (Falk, Von Buelow, & Khodadadi, 2015) (Figure 2.15(a)). There is another ongoing research, an initiative, on origami domes called *flexidome*, consisting in

creating domes using origami principles lead by Dr. Susan Taylor, Mr. Andrew Clancy and Mr. Colm Moore (Flexidome, n.d.) (Figure 2.15(b)).

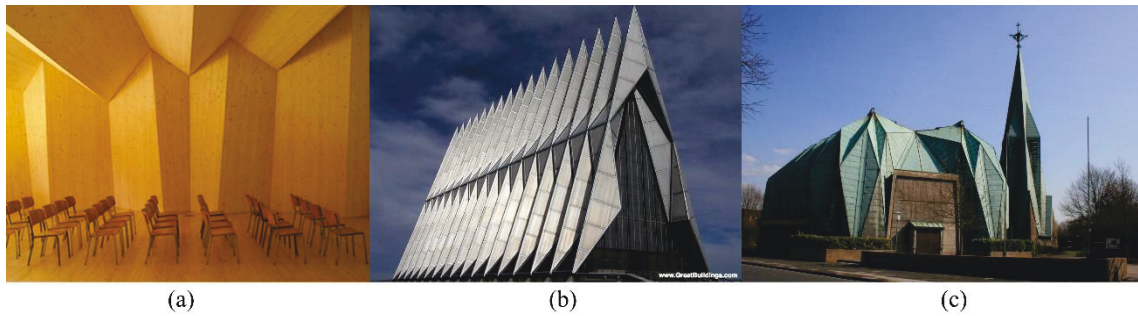


Figure 2.14. (a) Temporary chapel for the Deaconesses of St-Loup (Source: Keller, 2008), (b) The US Air Force Academy Chapel, Colorado (Source: Highsmith, 2007), (c) The Church St. Paulus, Germany (Source: Limburg, 2012).

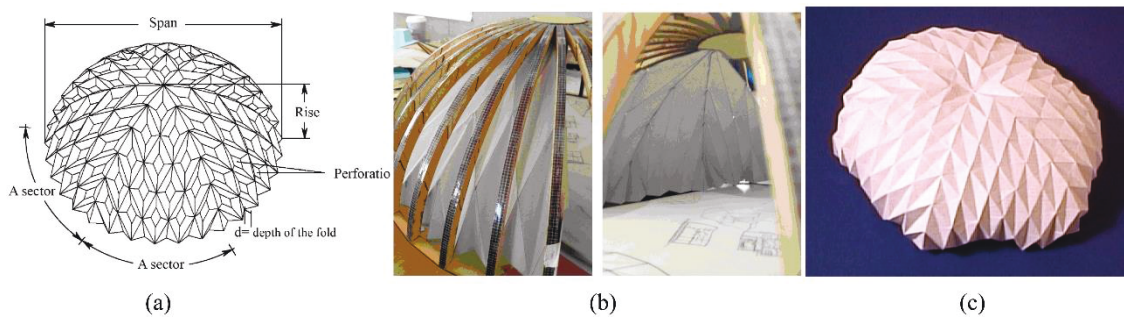


Figure 2.15. (a) Diametric folded plate dome (Source: Falk, Von Buelow, & Khodadadi, 2015), (b) Origami dome (Source: Flexidome, 2012) and (c) Hexagonal Dome (Source: Sierra, 2006).

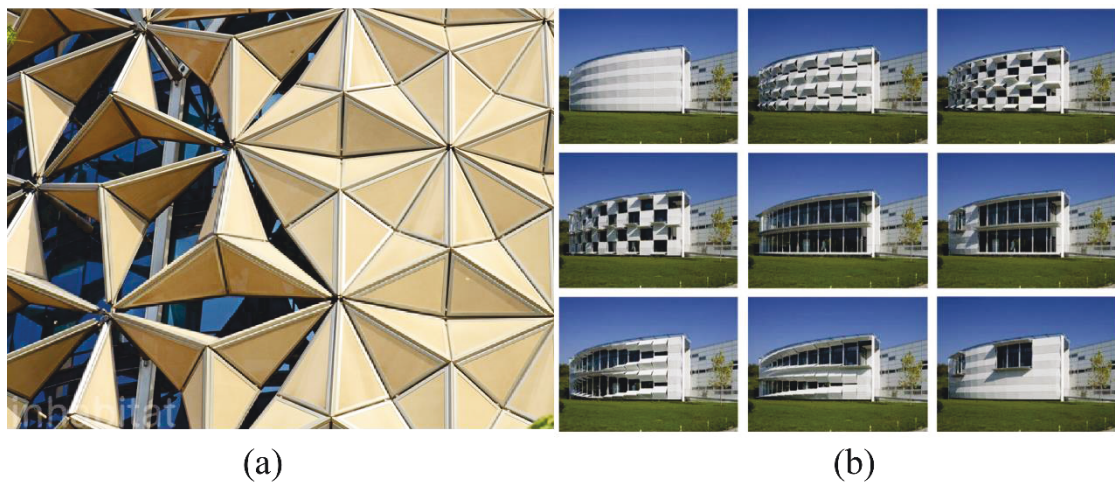


Figure 2.16. (a) Al Bahr Tower Façade Detail (Source: Laylin, 2014) and (b) Kiefer Technic Showroom (Source: Ott, 2007).

Transformable and/or kinetic structures are planar applications, like façades, of origami principles. Their application can be a foldable/deployable plate façades like Al Bahr Towers' façades (Figure 2.16(a)) and Kiefer Technic Showroom (2.16(b)).

## 2.5.2. Deployable Structures

Deployable structures utilizing the origami principles can be analyzed under two types: the bar structures and foldable plate structures, the latter can also be called rigid origami. In rigid bar structures [pin-jointed bar framework] the creases are replaced by bars and vertices by joints (Figure 2.17(b)). According to Tachi “*Rigid-foldable origami (or rigid origami) is a piecewise linear origami that is continuously transformable along its folds without deformation by bending or folding of any facet. Therefore, rigid origami can realize a deployment mechanism using stiff panels and hinges, which has advantages for various engineering purposes, especially for designs of kinetic architecture.*” (Tachi, 2011). In rigid origami the creases are replaced by hinges and the polygons by a rigid material (Figure 2.17(c)). Applications like De Temmerman's foldable mobile shelter system is an example of the bar structures (Figure 2.18 (a)), while Tachi's rigid origami (Figure 2.18(b)) is a foldable plate structure example for deployable architecture. According to Tachi, deployable and transformable structures that are rigid-foldable and flat-foldable have the following advantages from an architectural point of view.

- “1. The existence of a collapsed state enables compact packaging of the structure.
  2. The synchronized complex folding motion produced by constrained rotational hinges can be controlled with simple manipulation.
  3. The transformation mechanism that does not rely on the flexibility of materials can be made out of thick rigid panels and hinges.
  4. The watertightness of the surface maintained throughout the transformation is potentially suitable for the envelope of a space, a partition, and the façade of a building.”
- (Tachi, 2010a)

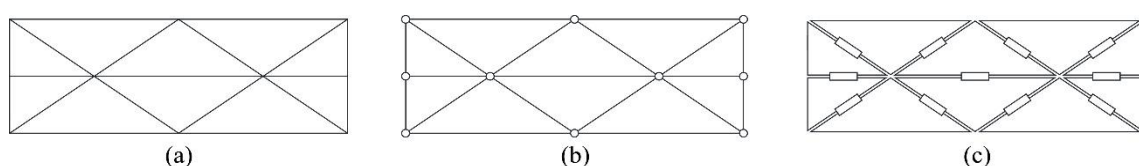


Figure 2.17. (a) Origami pattern (b) Bar structure (c) Rigid origami structure

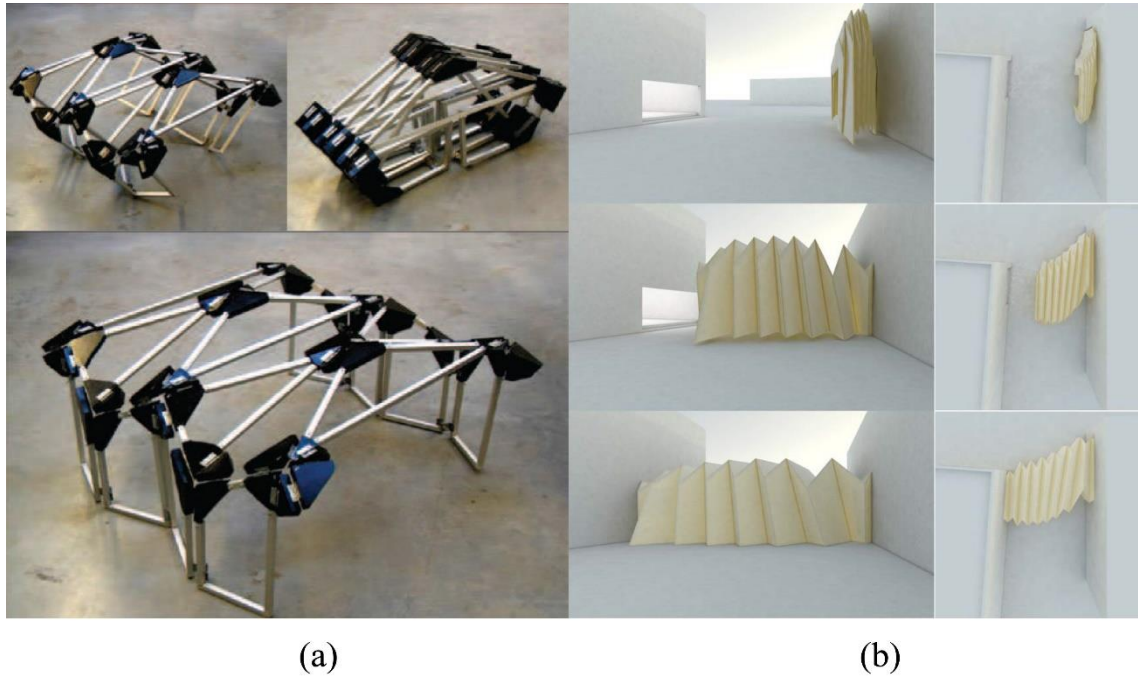


Figure 2.18. (a) De Temmerman's Foldable Mobile Shelter (Source: De Temmerman et al., 2007b) (b) Tachi's Rigid origami structure (Source: Tachi, 2010b).

In contrast to folded plate structures, deployable structures, whether they are bar or foldable plate structures are generally small scaled applications, like emergency shelters (Thrall & Quaglia, 2014) (Figure 2.18(a)) due to the complexity of the application. Research conducted on origami-inspired deployable structures are mostly based on pure geometry which makes the real life application difficult. The thickness of the material is one of the difficulties to consider while designing an origami-inspired foldable plate structure. Another difficulty is, as the scale increases, the kinematics and the structural behaviors, like load bearing, becomes more complex to calculate and to realize. Oricrete (Figure 2.19) is an example that approaches these problems with a different perspective. Concrete is cast on a reinforced fabric with spacers placed as crease lines of the pattern, once the concrete is hardened the spacers are removed and the structure is folded to its shape; once the desired shape is obtained, the fold lines are fixed by filling them with epoxy grout (Chudoba, van der Woerd, & Hegger, 2014a; Chudoba, van der Woerd, & Hegger, 2014b; Lebée, 2015). This method renders the creation of multiple spatial folded plate structures such as barrel vaults and domes. This structure type can be called a developable structure till it reaches its intended 3D form, and its joints are fixed at which point it has been transformed into a folded plate structure.



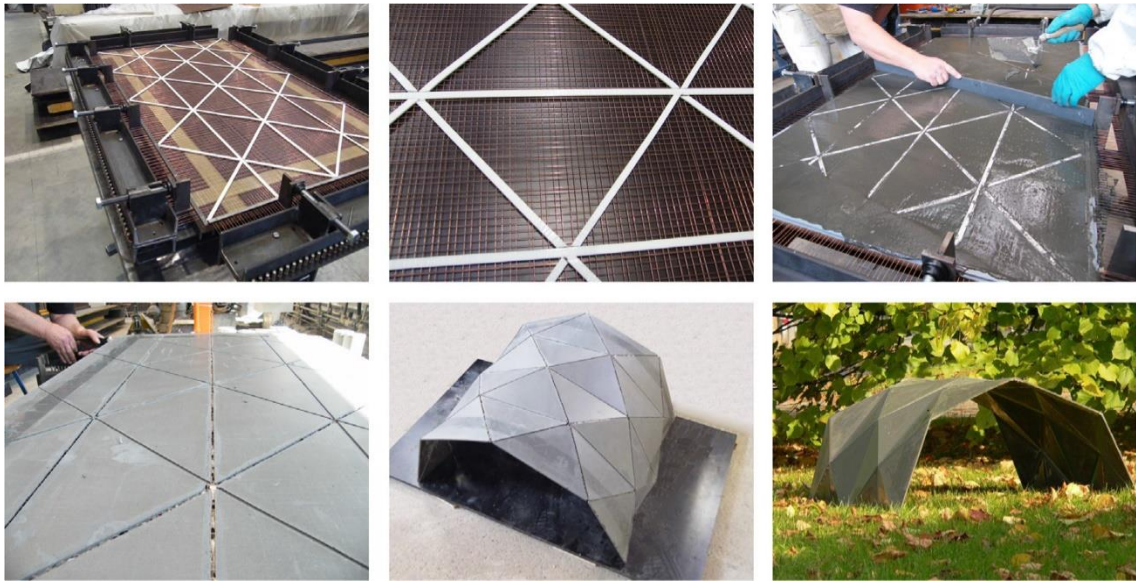


Figure 2.19. Oricrete creation process.  
(Source: Chudoba R. et al., 2014a)

### 2.5.2.1. Fold and Pattern Types

There are two basic fold types that can be observed in patterns used in architectural and engineering applications. The first is the *parallel fold* where parallel lines are alternated folding of mountain and valley creating an accordion like form (Figure 2.20(a)); the second is the *reverse fold* which is created by reversing the direction of a mountain fold to a valley fold by creating a vertex, adding 2 diagonal mountain, as in this example (Figure 2.20(b)) or valley fold. According to Buri (Buri, 2010) the angle  $\beta$  is in close relation with the fold angle  $\delta$  and the angle  $\alpha$  between the main fold and the diagonal line.

At the initial state of the fold, when it is deployed both the fold angle  $\delta$  and the dihedral angle  $\beta$  are equal to  $180^\circ$ . At the final folded state where the fold angle  $\delta$  is equal to  $0^\circ$ , the dihedral angle  $\beta$  is equal to  $180^\circ$  minus 2 times the angle  $\alpha$  (eq. (2.17)) (Buri & Weinand, 2008).

$$\beta = 180^\circ - 2\alpha \quad (2.17)$$

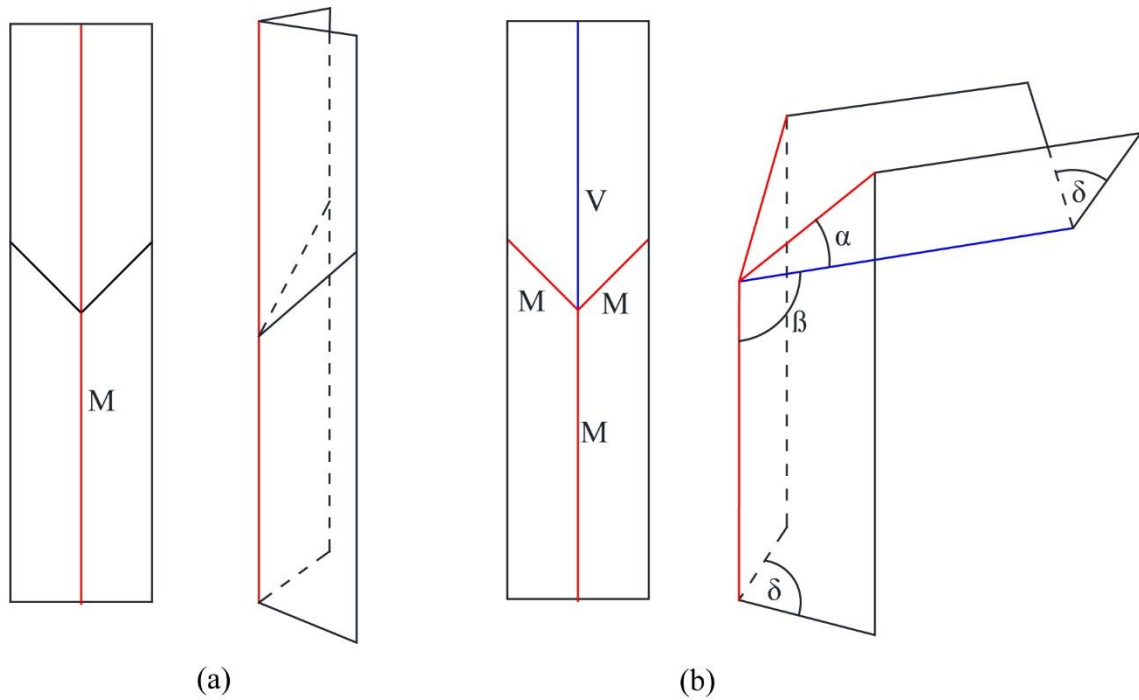


Figure 2.20. (a) Parallel fold and (b) Reverse fold - redrawn based on Buri.  
(Source: Buri H. , 2010)

This relation between angles is used to create the CP using a generator line - *generatrix* (Buri, 2010). The application of this method can be observed in the study of rigid folding structures by Stavric and Wiltsche (Stavric & Wiltsche, Investigations on Quadrilateral Patterns for Rigid Folding Structure, 2013). In this study the curved cross-section generatrix controls polygons to approximate the curve's shape. Then the dihedral angle  $\beta$  is calculated for each vertex, and then based on the formula presented by Buri, the angles  $\alpha$  are calculated (Figure 2.21) (Stavric & Wiltsche, Investigations on Quadrilateral Patterns for Rigid Folding Structure, 2013).

According to Buri and Weinand using the combination of parallel folds and reverse folds patterns like Yoshimura and Miura-ori and patterns can be created (Buri & Weinand, 2008).

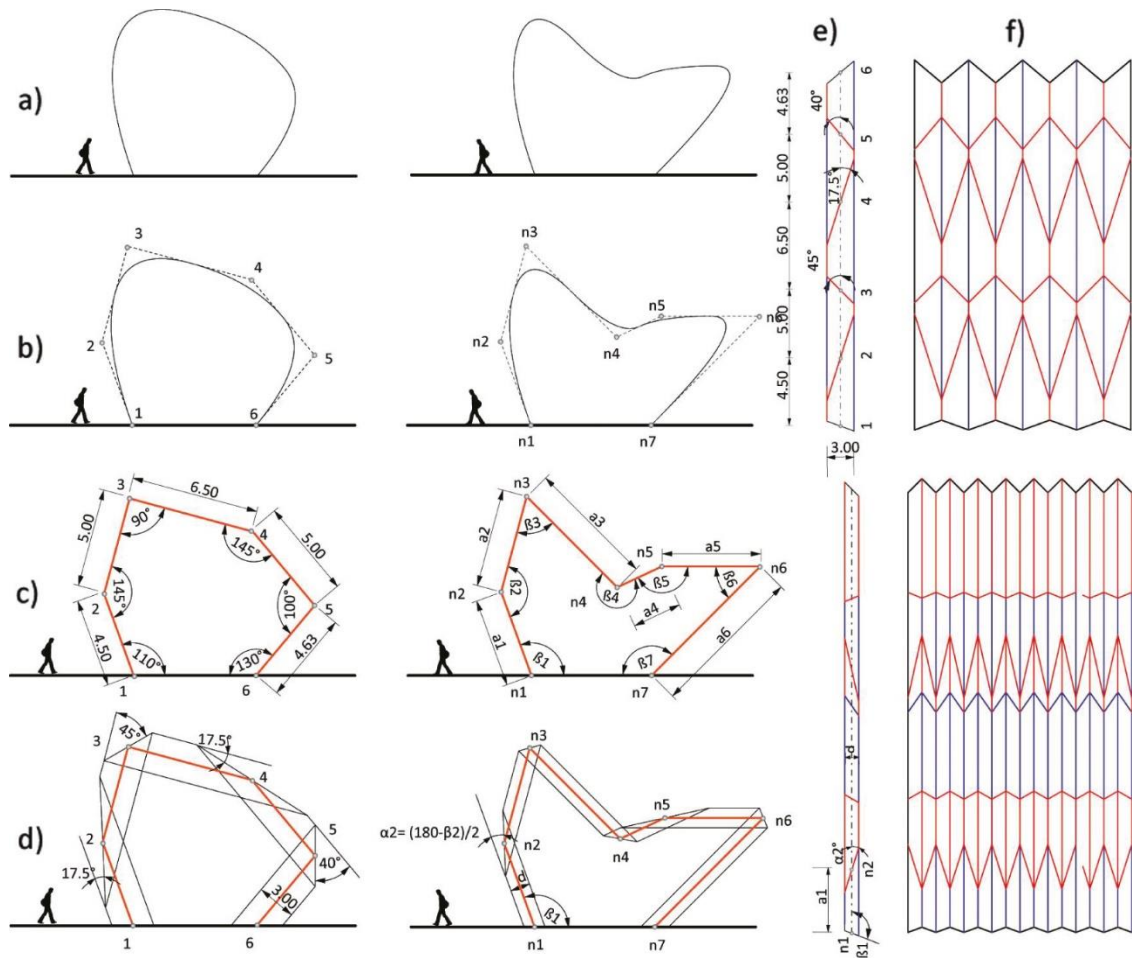


Figure 2.21. Pattern generation by Stavric and Wiltsche.  
 (Source:Stavric & Wiltsche, 2013)

Another method of generating patterns has been presented by Jackson (Jackson, 2011); corrugated patterns can be created by the simple congruence transformations [translation, rotation, reflection, glide reflection] (Figure 2.22). A single unit is repeated using congruence transformation to create the CP. The design and transformations applied define the CP and then the MV-assignment is done, which gives the MV-Pattern. Patterns created using the Jackson's method are developable but some of them may not be flat-foldable like the example of rotation (Figure 2.22). However, patterns created using Buri's method can be considered as flat-foldable because they are created by the desired cross-section.

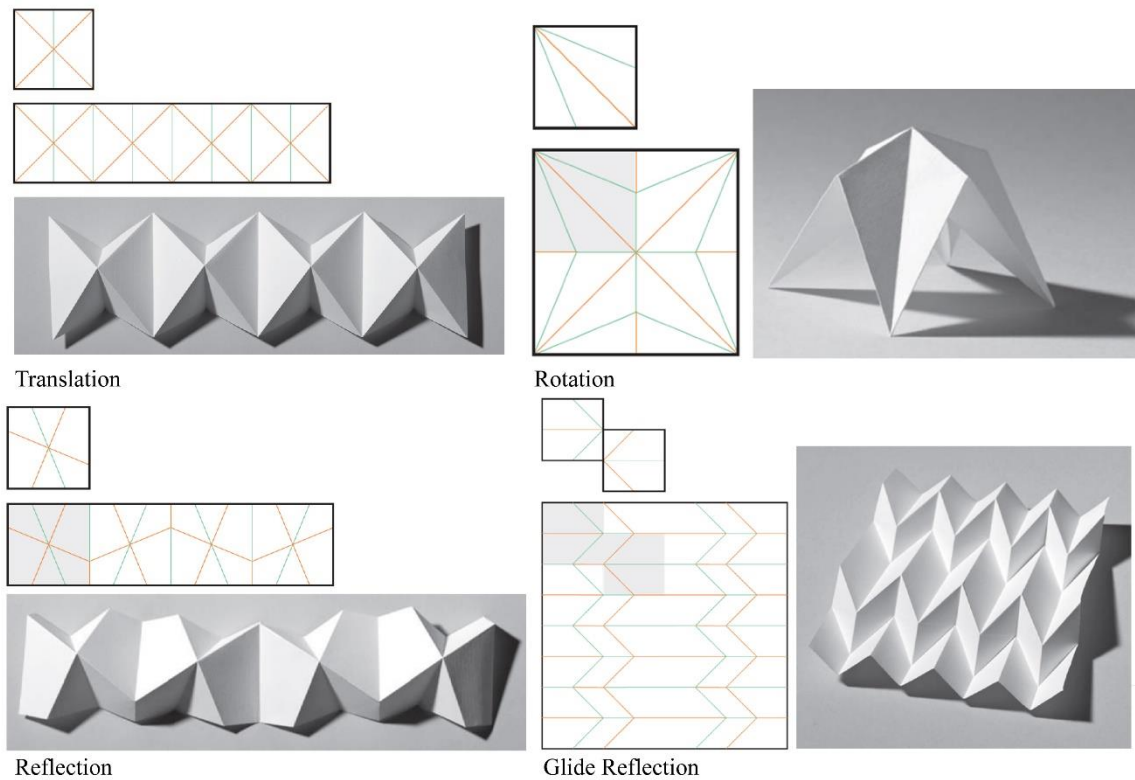


Figure 2.22. Pattern creation by Jackson.  
(Source: Jackson, 2011)

There are many existing patterns that can be designed by following the presented methods, but in engineering and architecture some corrugated patterns are used more than others because of their properties.

Most studied corrugated patterns are: Miura-ori, Yoshimura/Diamond, Quadrilateral, Water Bomb, and Ron Resch 3D tessellation patterns. Tessellation can be described as a tiling of a surface using one or more polygons with no overlaps or gaps between them. According to Lee and Leounis corrugation in origami “is a technique of alternating mountain and valley folds in an arrangement that allows movement in a folded model” (Lee & Leounis, 2011).

### **Miura-ori Pattern**

Miura-ori pattern, also called Herringbone pattern (Buri, 2010; Stavric & Wiltsche, 2013) (Figure2.23), created by Miura for solar panels, is a flat-foldable pattern. It is a quadrilateral pattern where there are 4 crease lines meeting in a vertex (degree-4 vertex). Miura-ori pattern - originally called developable double corrugation (DDC) - designed by Koryo Miura is one of the most studied and analyzed origami

pattern in engineering, architecture and mathematics (Miura, 2009). According to Miura the reason behind this intense research on this pattern is the deployability property:

- It is deployed simultaneously in orthogonal directions and is homogeneous in each direction.
- It possesses a single degree of freedom of motion no matter how large the array.
- Its deployment and retraction follow the same path.” (Miura, 2009)



Figure 2.23. Miura-ori pattern / Herringbone pattern – drawn based on (Source: Miura, 2009) and folded by the author.

Gattas alternated the pattern using a piecewise geometry method to create derivative patterns which allows the construction of different forms (Gattas & You, 2013b). The different patterns created by this method can connect with each other to respond to various needs in architecture. But some of the derivated patterns created are not developable, they do not fully open to become a flat surface (Gattas, Wu, & You, 2013a) . Gioia et al. proposed “*foldable corrugated meshes*” of non-developable foldable /unfoldable surfaces based on Miura-ori pattern to create corrugated architectural curved envelops (Gioia et al., 2012). Tachi, analyzed and generalized rigid foldable quadrilateral mesh origami to be able to create a free-formed developable, flat-foldable, and rigid-foldable patterns (Tachi, 2009b). Schenk and Guest, proposed a folded textured sheet for structural applications based on Miura-ori and Eggbox patterns (Schenk & Guest, 2011). Cai et al. (Cai et al., 2015) studied the geometry and motion of pyramidal deployable structures inspired by leaf’s movement which shows similarities to the Miura-ori pattern.

### **Yoshimura Pattern**

Yoshimura pattern also called Diamond pattern, (Buri, 2010; Stavric & Wiltsche, 2013) is a triangular pattern where six crease lines are joined in a vertex (degree-6

vertex). Yoshimura pattern is also called triangular pattern due to its polygon's shapes. Yoshimura pattern (Figure 2.24) has been developed by Yoshimura who observed thin cylinder's behavior when exposed to compression forces (Miura & Tachi, 2010). It is a developable pattern with multiple degree of freedom (DOF). The diamond shape of the CP allows a cylindrical shape to emerge. This shape allows the creation of vault-like structures when the CP is modified to the need of the form.

The geometrical analysis of this particular pattern has been presented by Foster and Krishnakumar (Foster & Krishnakumar, 1986/87) and expanded by Tonon (Tonon, 1991) who presented the creation of a variety of forms such as barrel vaults and surfaces with double-curvature. This method did not particularly present patterns that are developable and/or flat-foldable and/or deployable. By modifying this method De Temmerman proposed barrel vaults and dome-like circular shaped deployable bar structures (De Temmerman, 2007a) and foldable plate emergency shelter structures (De Temmerman et al., 2007b). The structure's pattern is created by congruent triangular modules, which can be divided into two to create the edge modules. In the method created by De Temmerman, the parameters required to create a deployable, flat-foldable pattern are the number of triangular plates in the span, the number of half-modules and the apex angle of triangular module. Cai et al. (Cai et al., 2016b) presented a motion analysis of regular and irregular Yoshimura pattern based barrel vault, which also presented a geometric analysis of a single unit. The method used in this research is also an adaptation of the geometrical principles proposed by both Tonon and De Temmerman.



Figure 2.24. Yoshimura pattern / Diamond pattern – drawn and folded by the author.

### **Quadrilateral patterns**

Quadrilateral patterns, also called reverse fold frame (Schramme, Boegle, & Ortolano Gonzalez, 2015), are corrugated patterns composed of tetragons (Figure 2.25).

Miura-ori is also a quadrilateral pattern but, because of its properties demonstrated by Miura (Miura, 2009), it has been differentiated from other patterns. These patterns have degree-4 vertexes and their unit's shapes varies from parallelogram to trapezoids. Nojima (Nojima, 2002) presented multiple quadrilateral patterns to fold cylinders. In this study the way of positioning the major fold line of a pattern changes the deployment motion. When modules are multiplied along an inclined major fold line the final model has a spiral shape (Figure 2.26(b)), but if the modules are multiplied along a non-inclined major fold line the final model becomes a cylinder (Figure 2.26(a)). The same properties are presented for triangular patterns (Nojima, 2002).

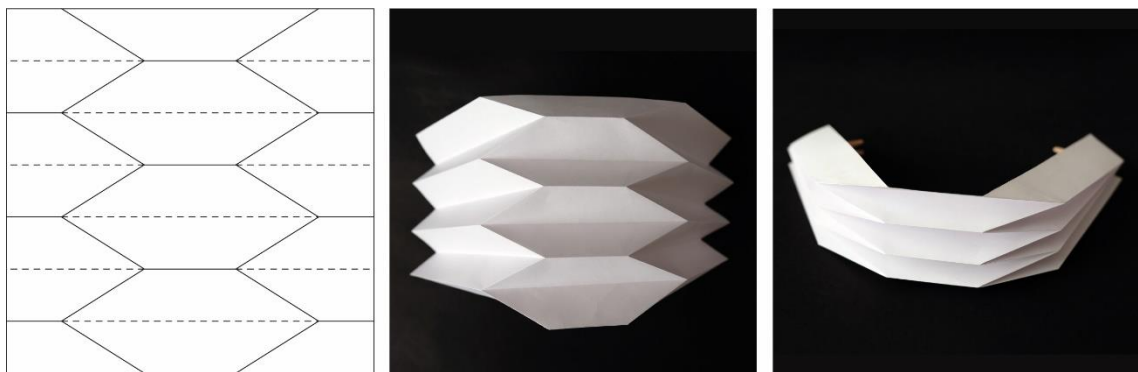


Figure 2.25. Quadrilateral pattern – drawn and folded by the author.

There are multiple examples of tubular/prismatic structures created with quadrilateral patterns. Tachi (Tachi, 2009e) presented a cylindrical deployable structure with thick material and single degree of freedom using quadrilateral patterns. Miura and Tachi (Miura & Tachi, 2010) presented a family of collapsible and rigid-foldable cylindrical polyhedra. Liu et al. (Liu, Lv, Chen, & Lu, 2016) also presented deployable tubular structures using quadrilateral patterns. Lee and Gattas (Lee & Gattas, 2016) presented new accordion-type shelters with structural stability and stiffness using quadrilateral patterns. All designed shelters are deployable but not all types are flat-foldable.

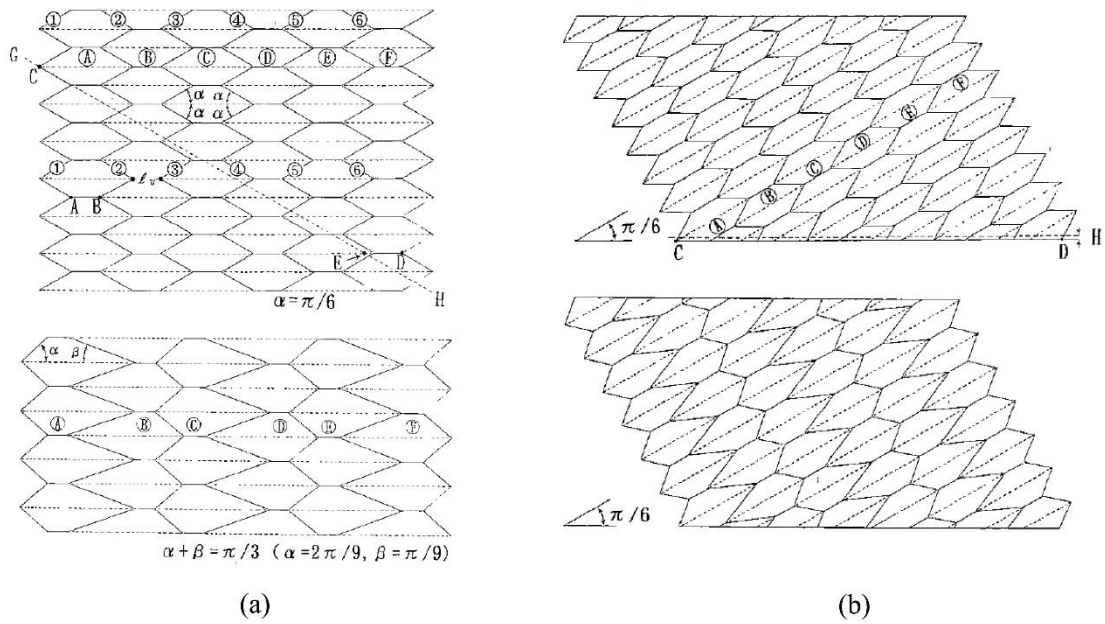


Figure 2.26. Nojima's (a) non-inclined quadrilateral pattern (b) inclined quadrilateral pattern (Source: Nojima, 2002).

### Water Bomb Pattern

Water bomb pattern (Figure 2.27) is also a corrugated pattern created by Shuzo Fujimoto, which is flat-foldable and developable. Compared to Miura-ori pattern, this CP is more flexible because it possesses multiple DOF (degree of freedom). This pattern is a triangular pattern, where the triangles vary in size, consisting of both degree-4 vertexes and degree-6 vertexes. Origami stent is the applied example of this pattern (Kuribayashi, et al., 2006). Parametric design and a structural analysis has been conducted on this pattern for rigid foldable origami structures by Curletto and Gambarotta (Curletto & Gambarotta, 2015).



Figure 2.27. Water Bomb pattern – drawn and folded by the author.



### Resch's 3D Tessellation pattern

Ron Resch pattern is a 3 dimensional tessellation with multiple DOF and flexible. The pattern is tessellated by different types of triangles. This pattern is developable but not flat-foldable. The final folded stage allows the creation of a smooth surface and creates a freeform structures because of its flexibility. Tachi (Tachi, 2013) created new origami tessellations (Figure 2.29(a)) and also proposed designing free-form structures (Figure 2.29(b)) by generalizing the Resch's pattern. Freeform shapes can be created using the method of generalization presented by Tachi with tessellated origami patterns. Figure 2.28 presents one of the variation of Resch pattern, consisting of triangles and squares joining at degree-5 vertexes and degree-8 vertexes.



Figure 2.28. Variation of Resch's pattern – drawn and folded by the author.

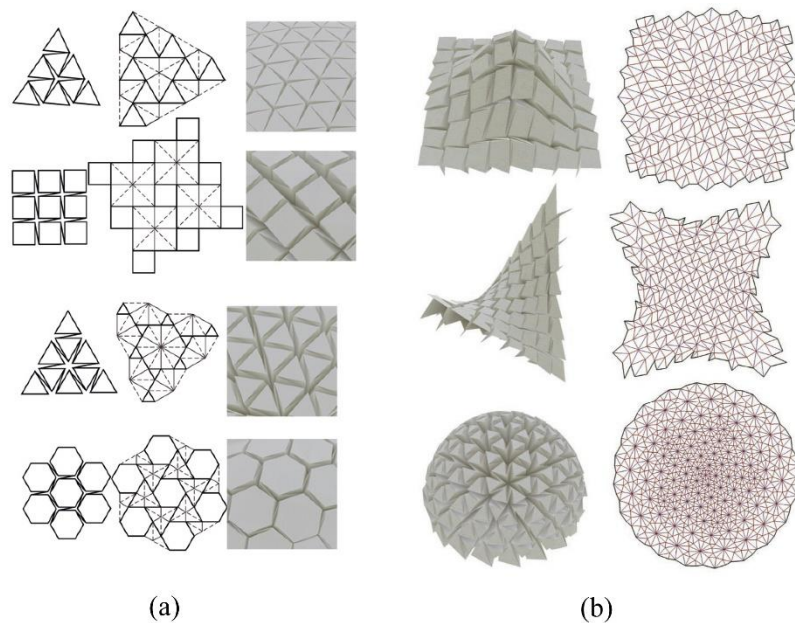


Figure 2.29. Resch patterns by Tachi (a) Variations of Resch's pattern (b) freeform shapes of patterns. (Source: Tachi, 2013).

### 2.5.2.2. Kinematics of Origami-inspired Mechanisms

All these patterns have their own deployment direction during a folding process which has been catalogued by Schramme et al. (Schramme, Boegle, & Ortolano Gonzalez, 2015). According to Schramme et al. there are three directions of deployment for origami patterns: translational, rotational and a combination of both (Schramme, Boegle, & Ortolano Gonzalez, 2015) (Figure 2.30). According to this study; Miura-ori has a bi-directional deployment with translational motion, Yoshimura patterns, referred as Diamond pattern, have a combination of translational and rotational motion during the folding process, Quadrilateral patterns, depending on the tessellation of the pattern can be translational like eggbox pattern or a combination of translational and rotational like herringbone and reverse fold frame patterns during their folding process. Resch's pattern can have different types of motion (translational and/or spherical bending) because of multitude of degree of freedom. This study also reveals that Yoshimura pattern can have a different deployment motion: axial bending which demonstrates that the pattern has multiple degree of freedom.

These presented motions are due to a mechanism existing in these patterns allowing the movement. It should be stated that even though developable and flat-foldable patterns are considered as structures from an architectural point of view, they are mechanisms because of their continuous movement starting from the initial state to their final folded state (Lebée, 2015).

Greenberg et al. (Greenberg et al., 2011) using graph theory observed that origami inspired mechanisms contained interconnected linkages forming a network of loops (Figure 2.31). Depending on the pattern the origami inspired mechanisms showed to be composed of interconnected 6-bar spherical linkages systems or 4-bar spherical linkage systems.








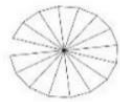



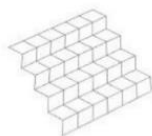
















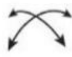




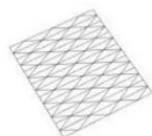


Fold-Pattern	Motion	Folding Angle		
		0	$\pi/2$	$\pi$
Longitudinal (parallel)	Longitudinal 			
Longitudinal (radial)	Polar rotation 			
Miura	Translation 			
Eggbox	Translation 			
Reverse fold frame	Translation / Rotation 			
Herringbone (alteration)	Translation / Rotation 			
Resch	Translation 			
	Bending (spherical) 			
Diamond	Translation / Rotation 			
	Bending (axial) 			

Figure 2.30. Deployment motion of patterns by Schimme et al.  
(Source: Schramme, Boegle, & Ortolano Gonzalez, 2015)

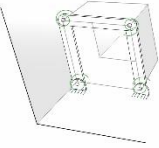
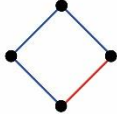
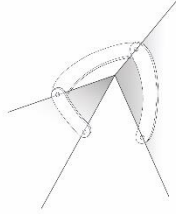
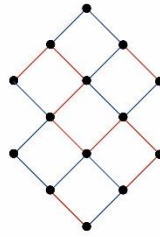
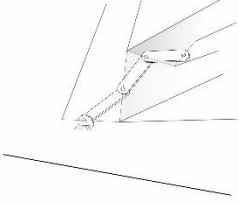
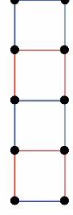
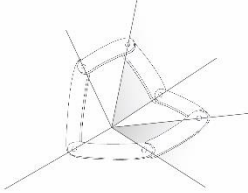
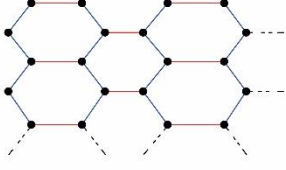
Kinematic Representation	Graph	Kinematic Representation	Graph
			
1. Four-Bar Double Slit		3. Square Twist	
			
2. 45-degree-fold Twisting Mechanism		4. Water Bomb Base Tessellation	

Figure 2.31. Origami inspired mechanisms (Source:Greenberg, Gong, Magleby, & Howell, 2011) – graphs redrawn by author based on (Greenberg, Gong, Magleby, & Howell, Identifying Links Between Origami and Compliant Mechanisms, 2011, p. 222).

The number of loops in a mechanism are calculated using Euler’s equation (eq.(2.18)): where  $L$  stands for the number of loops,  $j$  for the number of joints, and  $l$  for the number of links.

$$L = j - l + 1 \quad (2.18)$$

Origami patterns are a network of crease lines and vertexes, and in rigid origami crease lines are replaced by hinges which allows only rotational movement  $\textcircled{R}$  (Cai et al., 2016a), making a degree-4 vertex, a spherical 4R linkage (Figure 2.32(a)) and a degree-6 vertex, a spherical 6R linkage (Figure 2.32(b)). According to Schulze et al. (Schulze, Guest, & Fowler, 2014) a “mechanical linkage is called *body-hinge structure* if every joint of the linkage is a hinge”. These vertexes regardless of their degree, are assumed to be the central point of a spherical linkage making the pattern an assembly of spherical loops (Bowen et al., 2013; Greenberg , 2011).

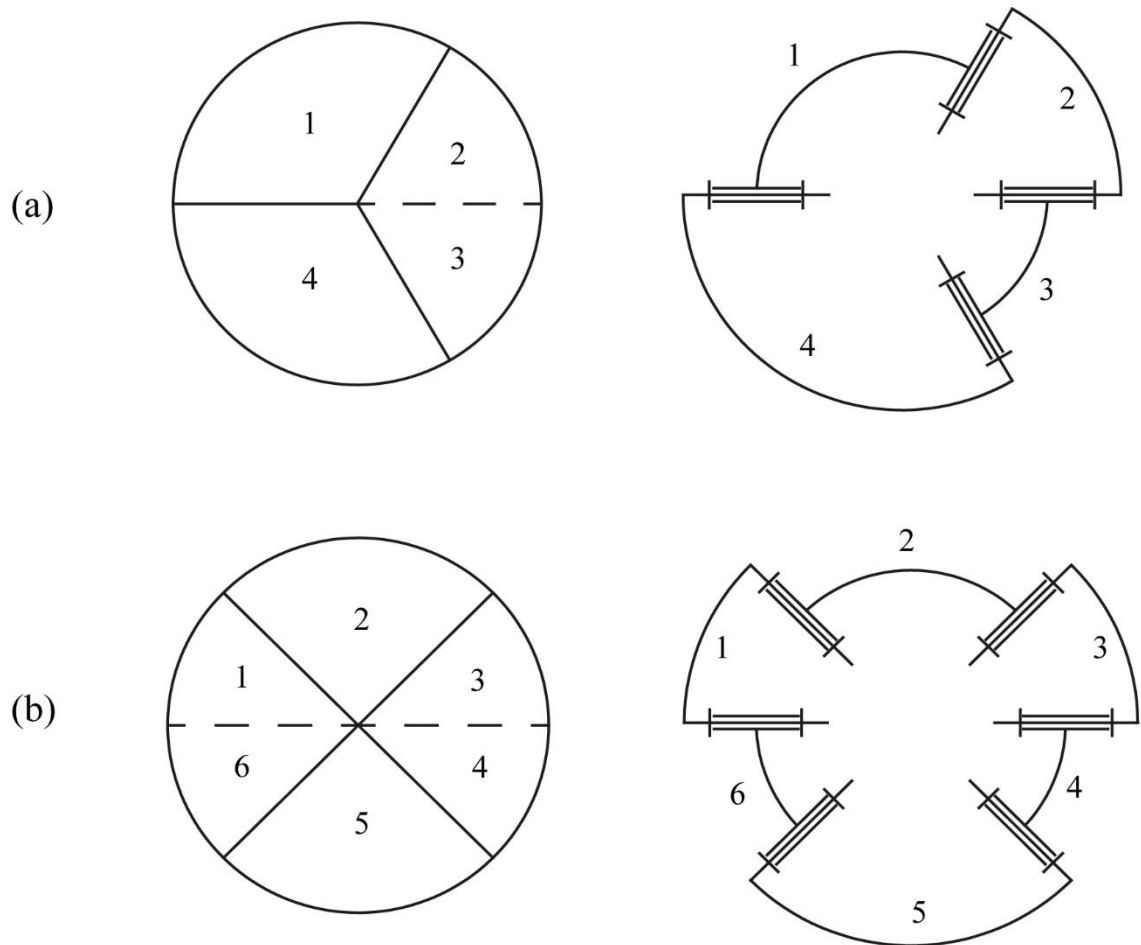


Figure 2.32. Spherical joints (a) 4R spherical linkage (b) 6R spherical linkage - drawn by the author.

Rigid origami deployable structures are often modeled with zero thickness and perfect hinges which causes a problem when an application is required. The material, which should stay stable during the folding process requires to have a thickness which may change the panel's dimensions or the placement of the hinges (Figure 2.33(b)) or the joints' properties like in Figure 2.33f where the joints are rolling joints not hinges (Cai, 2016c). Tachi's study about thick origami (Tachi, 2011) presented two flat-foldable models: the axis-shift method (Figure 2.33(b)) where the joints were placed in different locations and tapered method (Figure 2.33(c)) where the material geometry have been tapered so that the mechanism closes. Edmondson et al. also proposed two other methods to compensate the thickness problem in rigid origami structures (Figure 2.33(d)(e)).

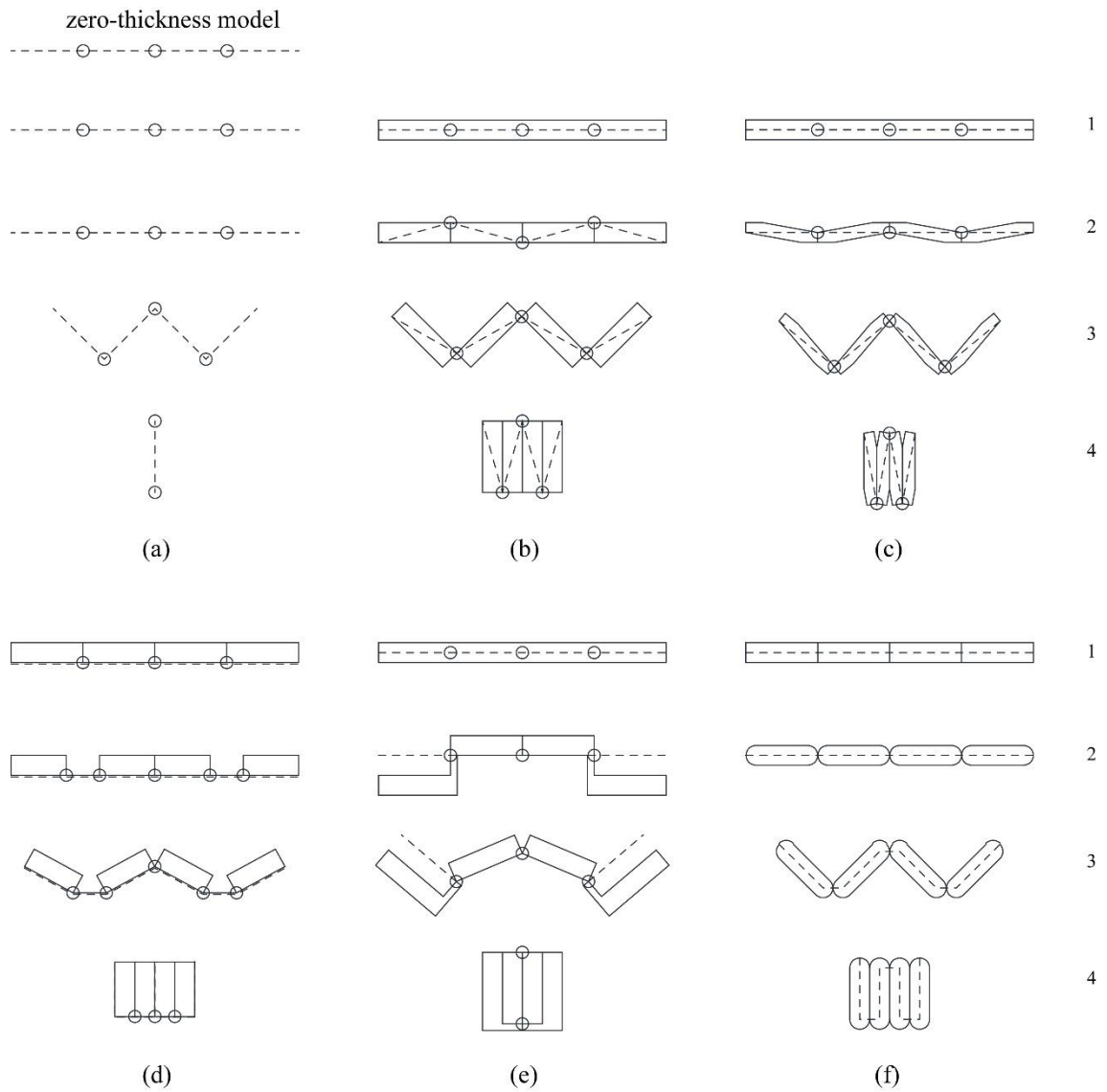


Figure 2.33. Joints (a) Zero-thickness model (b) Axis-shift method (Source: Tachi, 2011) (c) Tapered panels (Source: Tachi, 2011) (d) Membrane folds method (Source: Edmondson et al., 2014) (e) Offset panel technique (Source: Edmondson et al., 2014) (f) Rolling joints connection method (Source: Cai, 2016c) - redrawn by the author based on the sources.

## CHAPTER 3

### RIGID ORIGAMI BARREL VAULT STRUCTURES

The MV-Pattern creation of a foldable plate structure can be generated from the cross-section of the selected geometry, based on a geometrical relation proved by Buri (Buri, 2010). In Buri's dissertation we can observe that a MV-Pattern can be generated by a single line called "*generatrix*" (Buri, 2010). This method is also observed in the study of Stavric and Wiltsche, where a convex and concave *generatrix* was used to generate a folding pattern for rigid folding structures (Stavric & Wiltsche, 2013).

In this study the method of using a generator line "*generatrix*" is applied to create MV-Patterns for some types of foldable barrel vaults with different cross-section. The generator line is referred to as *pattern-generator* in this study. Various types of arches, as the cross-section of the foldable barrel vault, has been selected to demonstrate different parameters that affect the creation of a crease pattern.

In this chapter geometrical properties of different arch types, used as cross-section, are analyzed. Five types of arches have been selected for this study, they can be grouped under two categories: single centered arches and double centered arches.

Single centered arches are the semicircle and the horseshoe arches. Their geometrical properties have been analyzed and because they share common properties their parameters have been combined. Double centered arches, which are pointed equilateral, pointed obtuse, and lancet arches, also have common geometrical properties.

Firstly geometrical properties are analyzed for both categories, starting from the final folded state, partially folded state and initial state which defines the design parameters. Secondly a workspace analysis is carried on to understand the relation between the folding angles and the height, span, and depth of the foldable barrel vault. And then a mobility analysis is carried out to understand the mechanism of the foldable barrel vault structures. Finally a conclusion about each category is presented.

### 3.1. Single Centered Barrel Vaults

Single centered arches are created by a single circled cross section. There are different types of single centered arches but only the semicircle arch and horseshoe arch types are analyzed in this section of the study. The difference between the arches is defined by the value of the central angle  $\Omega$ .

In this section first geometrical properties of single centered rigid origami barrel vault structures are analyzed starting with the final folded state, followed by the partially folded state and then an MV-Pattern is created using the calculated parameters. Secondly a workspace analysis is conducted and finally a mobility analysis is presented.

#### 3.1.1. Geometrical Properties

This section presents the geometrical properties of single centered arches, and the required parameters to create a MV-Pattern. The pattern is created by reverse engineering. The process starts with the final folded state, continues with the partially folded state and ends with the creation MV-Pattern based on the parameters, which is the initial state.

##### 3.1.1.1. Final Folded State

The creation of a single centered folded plate structure starts by defining a radius  $r$ , the segment number  $n$ , and the value of the central angle  $\Omega$ . Figure 3.1 represents the parameters of both horseshoe (Figure 3.1a) and semicircle (Figure 3.1b). The central angle  $\Omega$  defines whether the cross section arch will be semicircle or horseshoe. If the central angle is equal to  $180^\circ$  the arch is a semicircle arch, but if the value of the central angle exceeds  $180^\circ$  then it becomes a horseshoe arch. The horseshoe arch is named according to the value of the central angle, for example Horseshoe  $200^\circ$  arch.

The radius defines the height and width of the structure, and as the number of segments increases an approximation to a curve shape is reached as it can be observed in Figure 3.2. The *pattern-generator* is created by dividing the circle into equal segments.



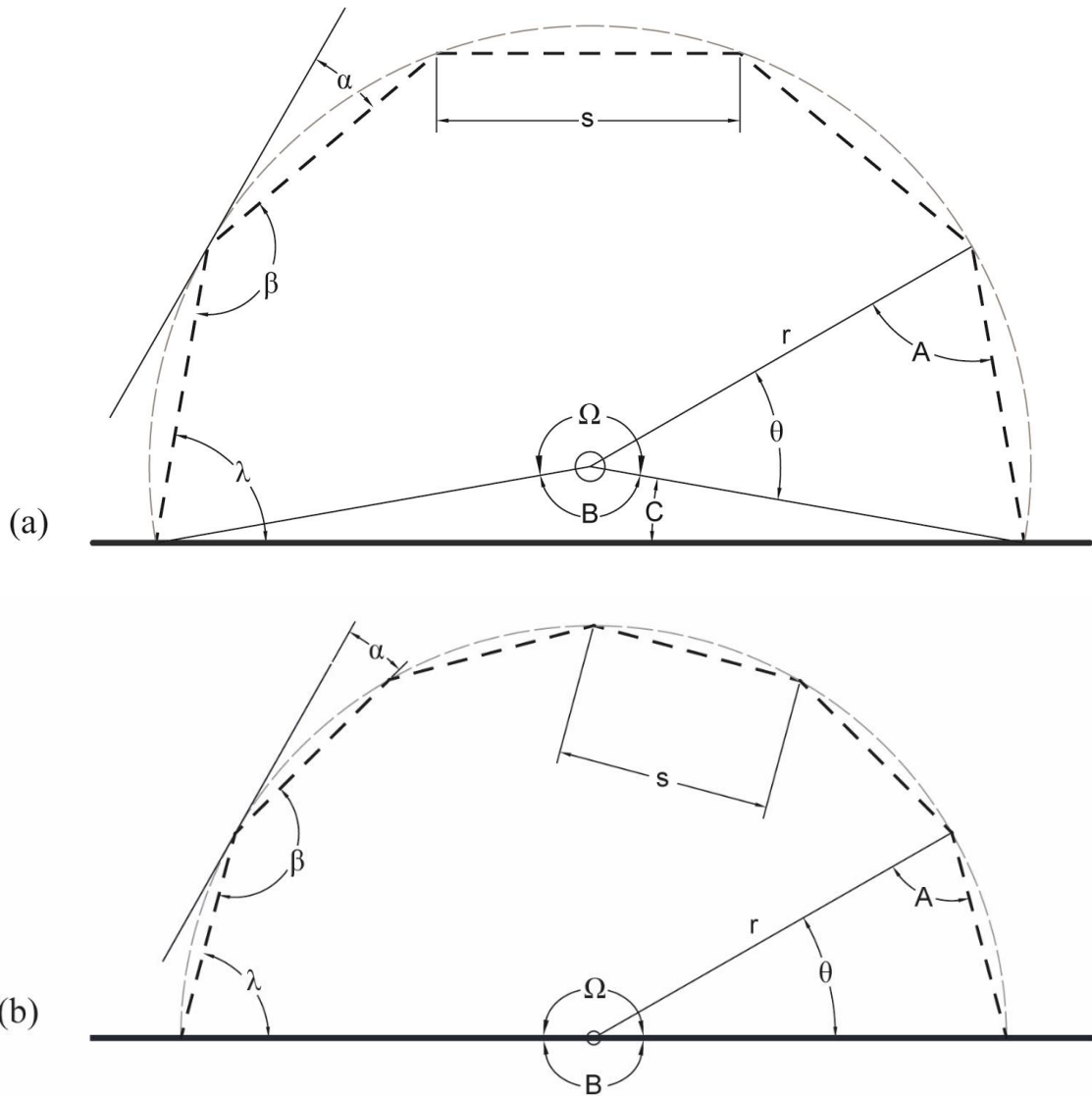


Figure 3.1. (a) Horseshoe arch and (b) Semicircle arch parameters' representations. Bold dashed lines: *pattern-generators*

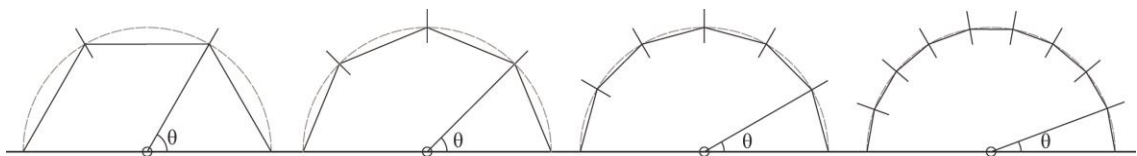


Figure 3.2: 3 segments, 4 segments, 6 segments, 9 segments semicircle arches (from left to right).

The required parameters to be able to create the crease pattern is the length of the *pattern-generator*  $s_t$ , the folding angle  $\alpha$ , and the edge angle  $\lambda$ . After defining the values of the parameters;  $r$ ,  $n$ , and  $\Omega$ , the first step is to calculate segments' angle  $\theta$  using eq. (3.1).

$$\theta = \frac{\Omega}{n} \quad (3.1)$$

Then using the value of the segment's angle, the length of a segment  $s$  can be calculated using eq. (3.2).

$$s = 2r \sin\left(\frac{\theta}{2}\right) \quad (3.2)$$

The length of the *pattern-generator*  $s_t$  can be calculated by multiplying the segment's length with the number of segments (eq. (3.3)).

$$s_t = n \cdot s \quad (3.3)$$

The interior angle  $\beta$  of the *pattern-generator* need to be calculated alongside the edge angle  $\lambda$ . To be able to calculate these two angles,  $\hat{A}$ ,  $\hat{B}$ , and  $\hat{C}$  angles need to be calculated. The angle  $\hat{A}$  is one of the base angles of an isosceles triangle thus calculated using eq. (3.4). And the angle  $\hat{B}$  is the complementary angle of the central angle which is calculated using eq. (3.5).

$$\hat{A} = \frac{\pi - \theta}{2} \quad (3.4)$$

$$\hat{B} = 2\pi - \Omega \quad (3.5)$$

The angle  $\hat{C}$  is one of the base angles of an isosceles triangle thus calculated using eq. (3.6). It should be stated that this angle is equal to zero for a selected central angle equal to  $\pi$ .

$$\hat{C} = \frac{\pi - B}{2} \quad (3.6)$$

To be able to calculate angle  $\beta$  the calculation for regular polygon need to be applied: the radii of the circumference circle of a regular polygon bisect the interior angles. Thus we can calculate angle  $\beta$  by multiplying angle  $\hat{A}$  by 2 (eq. (3.7)).

$$\beta = 2\hat{A} = 2 \cdot \left(\frac{\pi - \theta}{2}\right) = \pi - \theta \quad (3.7)$$

The edge angle  $\lambda$  can be calculated by the addition of angles  $\hat{A}$  and  $\hat{C}$  (eq. (3.8)). This calculation presents the value of the edge angle at its final folded state.

$$\lambda = \hat{A} + \hat{C} \quad (3.8)$$

The fold angle  $\alpha$  depends on the angle  $\beta$  (Buri, 2010; Stavric & Wiltsche, 2013). The equation to calculate the angle  $\alpha$  is;

$$\alpha = \frac{\pi - \beta}{2} \quad (3.9)$$

The last value is the height of a single row  $2h$ , which is the multiplication of the half-row's height  $h$  (eq. (3.10)) with two. Figure 3.3 shows how the parameters are used in the creation of a single row of a crease pattern. Figure 3.4 shows the final folded state of a semicircle folded plate structure.

$$h = \tan \alpha \left( \frac{s}{2} \right) \quad (3.10)$$

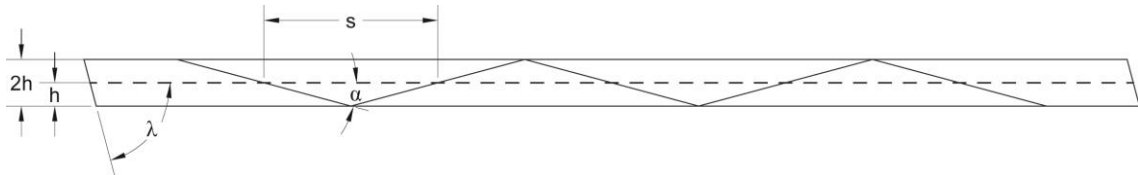


Figure 3.3. Single row CP and the parameters for the six segmented semicircle arch.

### 3.1.1.2. Partially Folded State

The second step in understanding the geometrical properties of a single centered foldable barrel vault is to define the relations between the parameters while the pattern is moving from its initial state to its final folded state. The vertex points of the *pattern-generator* does not coincide with the vertexes of the crease pattern when the final folded state of a single crease pattern row (Figure 3.4) is analyzed. The pattern-generator line in Figure 3.4 has 5 vertexes while the final folded state has 6 vertexes. The final folded state of a semicircle rigid origami barrel vault has been created with the parameters  $r$ :  $2 \text{ m } n$ :  $6 \Omega$ :  $180^\circ$  to demonstrate the geometrical relations on each vertexes (Figure 3.4).

The interior angle  $\beta$  is in relation with the folding angle  $\alpha$ , as the value of the angle  $\beta$  decreases the value of  $\alpha$  increases (eq. (3.9)) and vice versa. Similar relation can be observed, while the pattern moves from the initial state to the final folded state, between the folding angle  $\alpha$  and the angle  $\lambda'$  (eq. (3.11)) and also the bending angle  $\mu$  (eq. (3.12)) (Figure 3.5).

As it can be observed in Figure 3.4 the vertexes  $v_1$  and  $v_6$  are degree-4 vertexes,  $v^4$  and vertexes from  $v_2$  to  $v_5$  are degree-6 vertexes,  $v^6$ . A reverse fold as explained in section 2.3 (Origami Terminology) is a degree-4 vertex, same as vertexes  $v_1^4$  and  $v_6^4$ . The calculation of the degree-4 vertexes' bending angle  $\lambda'$  on both vertexes  $v_1^4$  and  $v_6^4$  is perform using eq. (3.11) provided by the research of Buri (Buri, 2010, pp. 72-76).

$$\lambda' = \pi - 2\alpha \quad (3.11)$$

The work of Buri (Buri, 2010) has been extended to be able to calculate the bending angle  $\mu$  for degree-6 vertexes. In  $v^6$  the bending angle  $\mu$  is in relation with more than two fold angle, as it is in reverse fold (eq. (3.11)). There are four fold angles  $\alpha$  that defines the bending angle thus the equation is modified accordingly (eq. (3.12)).

$$\mu = \pi - 4\alpha \quad (3.12)$$

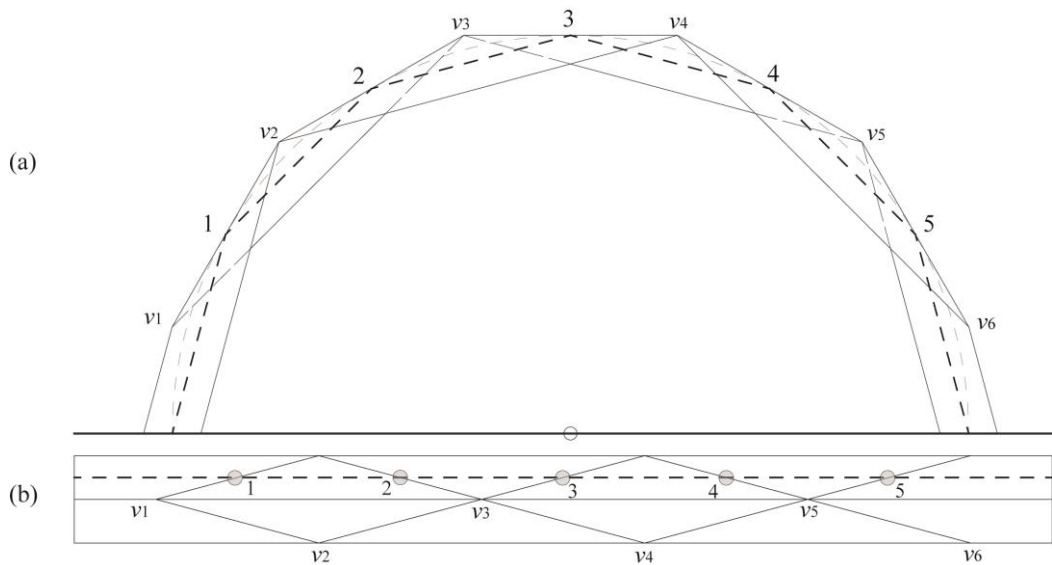


Figure 3.4. (a) Elevation and (b) double row CP of a rigid origami barrel vault structure with 6 segments, created using the maximum value of  $h$ .

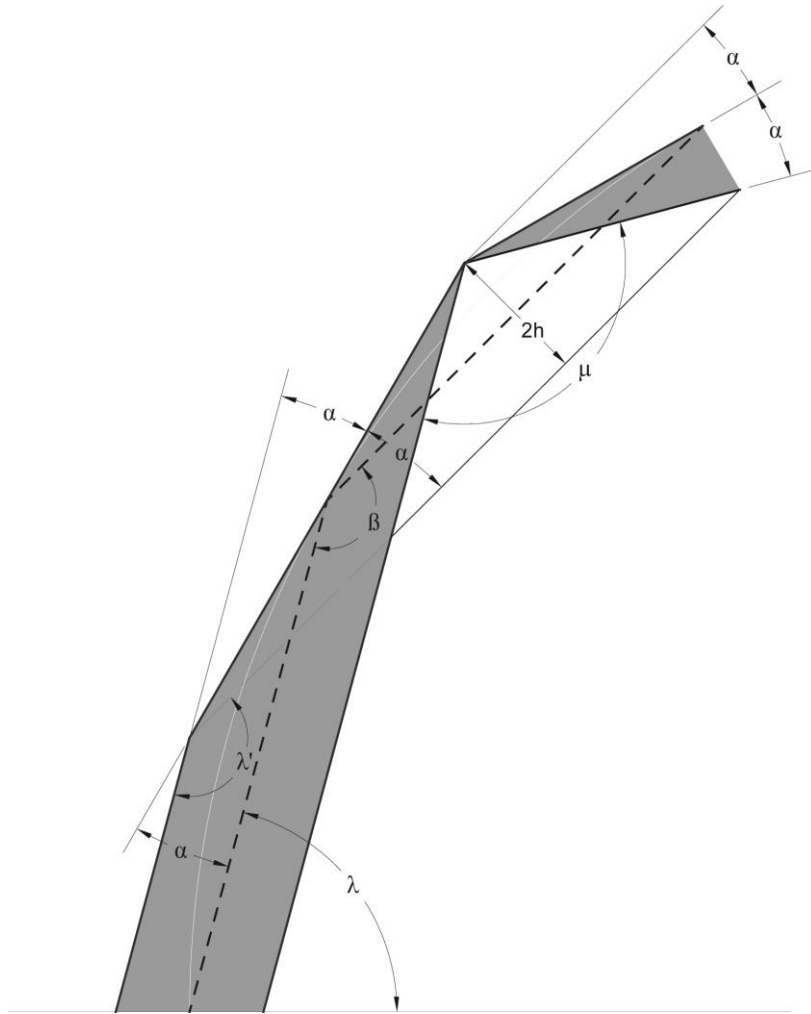


Figure 3.5. Vertexes  $v_1^4$  and  $v_2^6$ 's parameters.

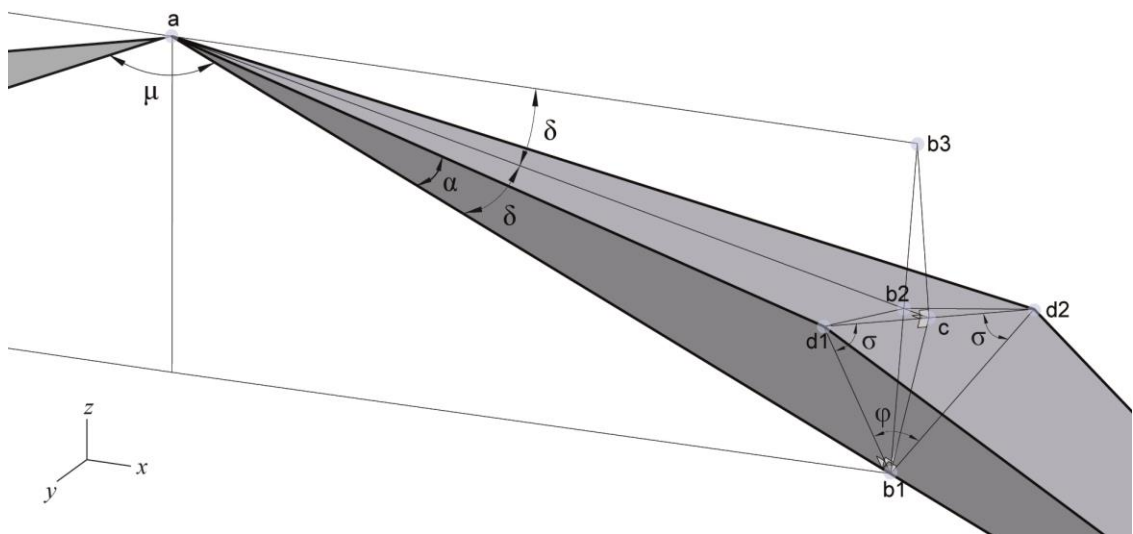


Figure 3.6. Vertex  $v_3^6$ 's parameters.

As it can be observed in Figure 3.4 the vertexes are not on the same line thus point  $a$  is  $v_3^6$  and  $d_1$  is  $v_4^6$  in Figure 3.6.

The bending angle  $\mu$  depends on the dihedral angle  $\varphi$ . As the dihedral angle's value increases toward the value  $\pi$  the bending angle's value also increases. On the initial state of the crease pattern both angles are equal to  $\pi$ . The isosceles triangle  $\Delta d_1 b_1 d_2$  demonstrate the relation between the dihedral angle  $\varphi$  and the inclination angle  $\sigma$ , as the dihedral angle increases both inclination angles decreases. In Figure 3.6 the line  $ab_3$  is the initial place of the crease line which moves toward the position  $ab_1$  which creates an  $xz$ -plane. The line  $ac$  is the bisector of the angle  $b_3 a b_1$  creating two equal angles  $\delta$ . The angle  $\delta$  is the projected angle of the folding angle  $\alpha$  on to the  $xz$ -plane. Eq. (3.12) can be modified by substituting the folding angle  $\alpha$  by its projected angle  $\delta$  (eq. (3.13)).

The relation between the angles can be explained as follows:

$$\mu = \pi - 4\delta \quad (3.13)$$

$$\delta = \tan^{-1}\left(\frac{cb_1}{ab_1}\right) \quad (3.14)$$

$$cb_1 = \sin \sigma \cdot d_1 b_1 \quad (3.15)$$

$$ab_1 = \frac{d_1 b_1}{\tan \alpha} \quad (3.16)$$

Substituting eqs. (3.15) and (3.16) in eq. (3.14), eq. (3.14) becomes:

$$\delta = \tan^{-1}\left(\frac{\sin \sigma \cdot d_1 b_1 \cdot \tan \alpha}{d_1 b_1}\right) = \tan^{-1}(\sin \sigma \cdot \tan \alpha) \quad (3.17)$$

Substituting eq. (3.17) in eq. (3.13) the relation becomes:

$$\mu = \pi - 4 \tan^{-1}(\sin \sigma \cdot \tan \alpha) \quad (3.18)$$

The same relation exists on  $v^4$  where the bending angle  $\lambda'$  is given by eq. (3.19) based on the relation in eq. (3.11) (Buri, 2010, p. 76).

$$\lambda' = \pi - 2 \tan^{-1}(\sin \sigma \cdot \tan \alpha) \quad (3.19)$$

Both types of vertexes have two positions; initial state and final folded state, which are considered as the limits of the crease pattern. The dihedral angle  $\varphi$  initial state

is equal to  $\pi$  because the pattern is flat and as the pattern closes the value decreases to its final folded state where it is equal to 0 (zero). The isosceles triangle  $\Delta d_1 b_1 d_2$  defines the limits for the inclination angles  $\sigma$  as:  $\sigma_{min} = 0$  for the initial state and  $\sigma_{max} = \pi/2$  for the final folded state. The relation between the dihedral angle  $\varphi$  and the inclination angles  $\sigma$  can be defined as;

$$\varphi = \pi - 2\sigma \quad (3.20)$$

The association of the angles of degree-6 vertexes,  $v^6$  in their initial and final folded state can be described as: for  $\sigma = 0$  eq. (3.21) for the initial state and for  $\sigma = \pi/2$  eq. (3.22) for the final folded state.

$$\mu_{min} = \pi - 4 \tan^{-1}(\sin \sigma \cdot \tan \alpha) = \pi \quad (3.21)$$

$$\mu_{max} = \pi - 4 \tan^{-1}(\sin \sigma \cdot \tan \alpha) = \pi - 4\alpha \quad (3.22)$$

For the degree-4 vertexes',  $v^4$  bending angle  $\lambda'$  ( $v_1$  and  $v_6$ ) the relation can be described as: for  $\sigma = 0$  eq. (3.23) for the initial state and for  $\sigma = \pi/2$  eq. (3.24) for the final folded state (Buri, 2010, p. 76).

$$\lambda'_{min} = \pi - 2 \tan^{-1}(\sin \sigma \cdot \tan \alpha) = \pi \quad (3.23)$$

$$\lambda'_{max} = \pi - 2 \tan^{-1}(\sin \sigma \cdot \tan \alpha) = \pi - 2\alpha \quad (3.24)$$

Table 3.1 presents all the values of the  $v^4$  bending angle  $\lambda'$ ,  $v^6$  angle  $\mu$ , dihedral angle  $\varphi$ , and inclination angle  $\sigma$  for their initial and final folded states.

Table 3.1. Maximum and minimum values of the angles  $\mu$ ,  $\lambda'$ ,  $\varphi$ , and  $\sigma$ .

angles	Initial state (min)	Final folded state (max)
$\mu$ ( $v^6$ bending angle)	$\pi$	$\pi - 4\alpha$
$\lambda'$ ( $v^4$ bending angle)	$\pi$	$\pi - 2\alpha$
$\varphi$ (dihedral angle)	$\pi$	0
$\sigma$ (inclination angle)	0	$\pi/2$

The required partially folded state for  $v^6$  can be obtained either by defining the value of the dihedral angle  $\varphi$ , and then using eq. (3.20) the inclination angle  $\sigma$  can be solved, and finally substituted in eq. (3.18) to be able to calculate the bending angle  $\mu$ . Or by defining the value of the inclination angle  $\sigma$  and substituted in eq. (3.18) to calculate the bending angle. Figure 3.7 shows the relation between the inclination angle and both bending angles for a semicircle arch with 6 segment and a radius of 2 m. As the inclination angle increases the bending angles decreases to reach their final folded state.

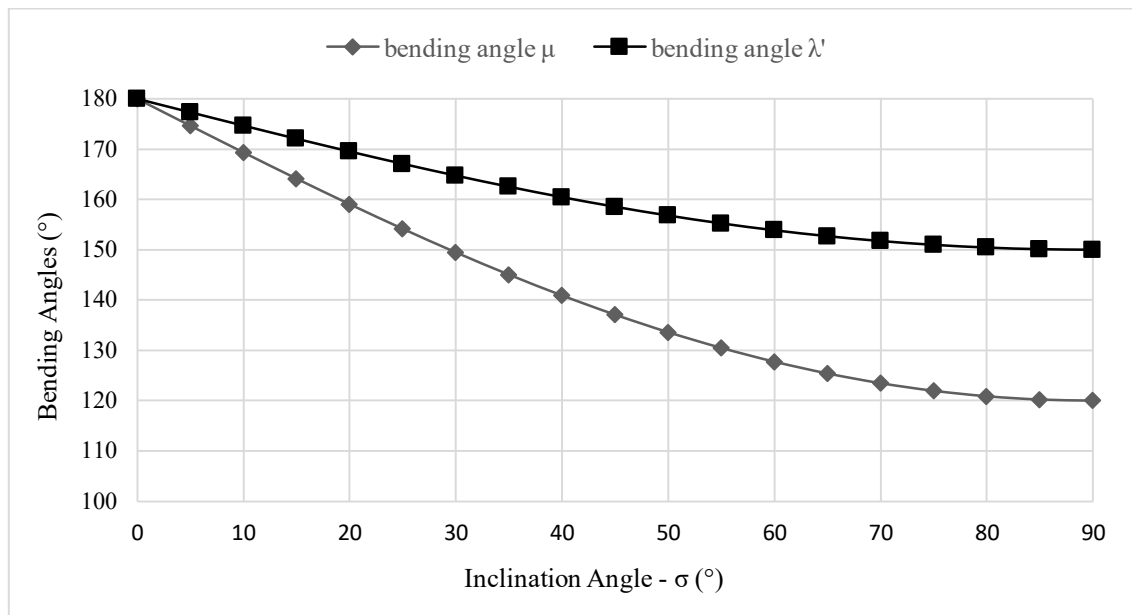


Figure 3.7. Relation between angles  $\mu$  and  $\lambda$  with  $\sigma$  for an  $n:6$ ,  $r:2$  semicircle arch.

### 3.1.1.3. Initial State, MV-Pattern

In this step, based on the calculated parameters, a single row of a CP is created. As presented in the previous step, the required parameters to be able to draw a single chain are the folding angle  $\alpha$ , the edge angle  $\lambda$  and the total length of the *pattern-generator*  $s_t$ . Table 3.2 shows all the parameters calculated in the previous step for a six segmented 2 m radius semicircle arch, and for a horseshoe 200° arch with five segments and 2 m radius.

The lines A and B in Figure 3.8 are parallel to the pattern-generator and the distance between the *pattern-generator* and the lines is defined by the parameter  $h$ . The distance between lines A and B is the total height of a single row  $2h$ . The value for the parameter  $h$  can be changed for the creation of a different CP. If the maximum value of



the  $h$  is used to create  $2h$  the CP will be a triangular pattern where edge vertexes are  $v^4$  but all others are  $v^6$ , but if a smaller value of  $h$  is used then the pattern will be a trapezoidal pattern where all vertexes are  $v^4$ .

Table 3.2. Parameters for  $r: 2, n: 6$  semicircle and  $r: 2, n: 5$  horseshoe  $200^\circ$  arches.

	$r$ (m)	$n$	$\Omega^\circ$	$\theta^\circ$	$s$ (m)	$s_r$ (m)	$\hat{A}^\circ$
Semicircle	2	6	180	30	1,035	6,21	75
Horseshoe	2	5	200	40	1,368	6,84	70
	$\hat{B}^\circ$	$\hat{C}^\circ$	$\beta^\circ$	$\lambda^\circ$	$\alpha^\circ$	$h$ (m)	$2h$ (m)
Semicircle	180	0	150	75	15	0,138	0,277
Horseshoe	160	10	140	80	20	0,248	0,497

The crease line created by the folding angle  $\alpha$  is placed on the edge of the first segment and then extended to both lines A and B. Assuming line 1 is placed first to the end of the first segment, to be able to create a convex form using reverse fold the second line 2 need to be placed in the opposite direction of line 1, as a reflection, and so on for the third, fourth and fifth lines. Lines 6 and 7 are placed based on the edge angle  $\lambda$ . Both lines 6 and 7 need to have the same direction with the adjacent lines if the structure needs to touch the ground from the edges.

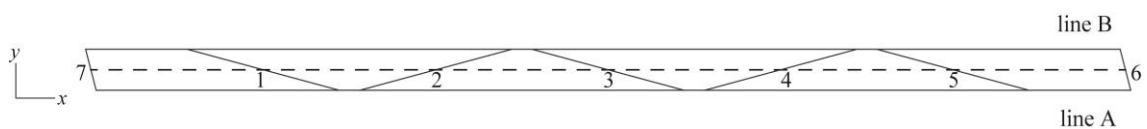


Figure 3.8. Unfolded crease pattern for the six segmented semicircle arch.

The reproduction of the row into a pattern is done by a simple congruence transformation: reflection by the line B, then the two rows together is translated in  $y$ -direction (Figures 3.9 and 3.10).

The created pattern needs an application of MV-Assignment to be applied to create the MV-Pattern. The MV-Pattern is applied based on Maekawa's theorem where the difference of the number of mountain folds and valley folds should be equal to 2 at each vertex (Figures 3.9 and 3.10). For both figures full lines are mountain folds and dashed lines are valley folds.

The triangular pattern has both  $v^4$  and  $v^6$  (Figure 3.9). As it can be observed in Figure 3.9 for a single row the number of vertexes are equal to the number of segments  $n$ . As the number of segments increases the number of vertexes also increases, but only the number of  $v^6$  increases because the  $v^4$  are only positioned in the edge of the single row, and the additional segment does not change the conditions of the pattern.

Table 3.3. Number of degree-4 and degree-6 vertexes on triangular patterns.

$n$	$v^4$	$v^6$	$v$ total
3	2	1	3
4	2	2	4
5	2	3	5
6	2	4	6

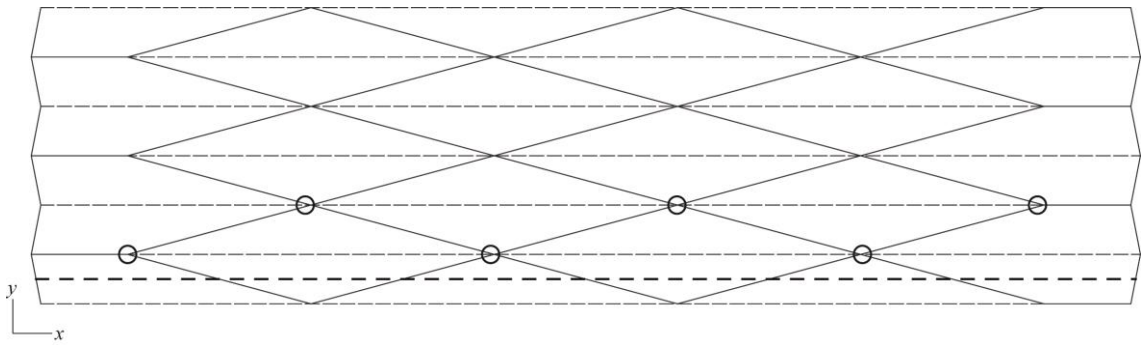


Figure 3.9. MV-Pattern created by using maximum value of  $h$  for a  $n$ : 6, semicircle arch. Triangular pattern (Yoshimura pattern)

The trapezoidal pattern has only  $v^4$  (Figure 3.10). As it can be observed in figure 3.10 for a single row the number of vertexes are not equal to the number of segments  $n$ , as it is in the triangular pattern. Because the maximum value of  $h$  has not been used, the diagonal lines created using the folding angle  $\alpha$  do not intersect on the edge, thus no  $v^6$  is created which leads to an all  $v^4$  CP. The relation between the number of segments and the number of vertexes can be observed in Table 3.4.

Table 3.4. Number of degree-4 vertexes on trapezoidal patterns.

$n$	$v^4$	$v^6$	$v$ total
3	4	0	4
4	6	0	6
5	8	0	8
6	10	0	10

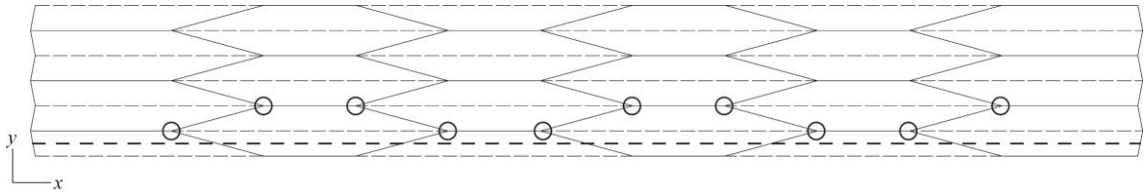


Figure 3.10. MV-Pattern created by using  $h$  as 0,104 m, for a  $n$ : 6, semicircle arch. Trapezoidal pattern

### 3.1.1.4. Conclusion

In this section rules and limitations are discussed. While creating a pattern, some parameters need to be specified by the designer: the radius  $r$ , the number of segments  $n$  which defines the approximation of the form of the structure, and the central angle  $\Omega$  which defines the type of arch required. The properties of these parameters are discussed together with the rigid foldability of the patterns created using the method of creation. The rigid foldability of the created MV-Pattern has been tested on both Rigid Origami Simulator and Freeform Origami softwares created by Tachi (Tachi, 2009a; Tachi, 2009c).

It should also be stated that the process of creating a crease pattern and assigning mountain and valley folds to the crease lines do not differ for a semicircle arch barrel vault MV-Pattern and Horseshoe arch barrel vault MV-Pattern.

If the structure needs to have a temporary stop point while reaching the final flat-folded state, the inclination angle  $\sigma$  needs to be specified by the designer. Also the edge angle  $\lambda$  needs to be recalculated so that the edges touch the ground at the desired dihedral angle.

Height of a single row: The value of  $2h$  has been calculated as the maximum value for the parameter which allows its manipulation. All values under the maximum value of  $h$  will create a trapezoidal pattern (Figure 3.10) while the use of maximum height for  $h$  will create a triangular pattern which has similarities with Yoshimura pattern (Figure 3.9).

Central angle  $\Omega$ : the value of the central angle defines the type of arch that will be used as the cross-section of a rigid origami folded plate structure.

If  $\Omega = \pi$  Semicircle cross-section

If  $2\pi > \Omega > \pi$  Horseshoe cross-section

All single centered arches' trapezoidal and triangular MV-Patterns' rigid foldability have been tested on Rigid Origami Simulator (Tachi, 2009c), and all created patterns have folded without problems. Same patterns have been tested on the Freeform Origami software (Tachi, 2009a); in this software, while all pattern flat-folded without deformation, the software suggested additional creases to the pattern created, which can be observed on Figures 3.11 and 3.12 as gray lines.

When the suggested grey lines are applied to the triangular MV-Pattern the pattern become composed of  $\nu^6$ , as it can be observed in Figure 3.13. As it can be observed while the dimensions do not change the form of the parts that touches, the ground change both in form and in geometry.

Both trapezoidal and triangular MV-Patterns are developable and flat-foldable if the medium is assumed a surface with no thickness. Models using thick cardboard have been created to be able to understand the changes suggested by the Freeform Origami software. Models have showed that  $\nu^4$  do not flat folds without tearing the material while the  $\nu^6$  folds flat without resistance with axis-shift method (Figures 3.14 and 3.15).

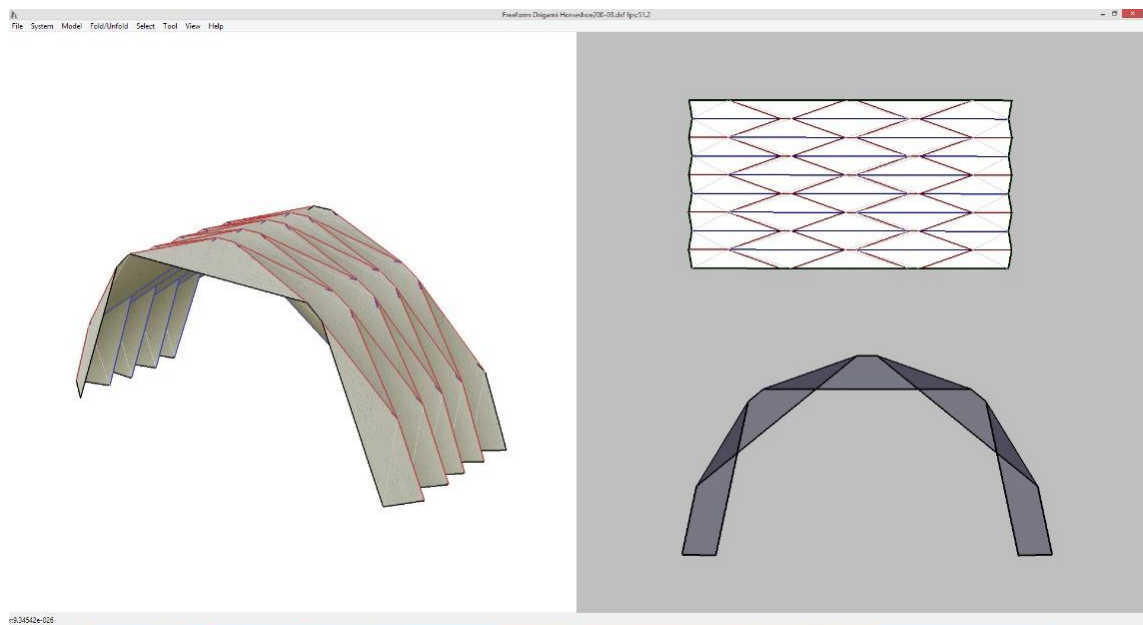


Figure 3.11. Triangular pattern rigid origami horseshoe 200° barrel vault tested on FreeformOrigami software (Tachi, 2009a).

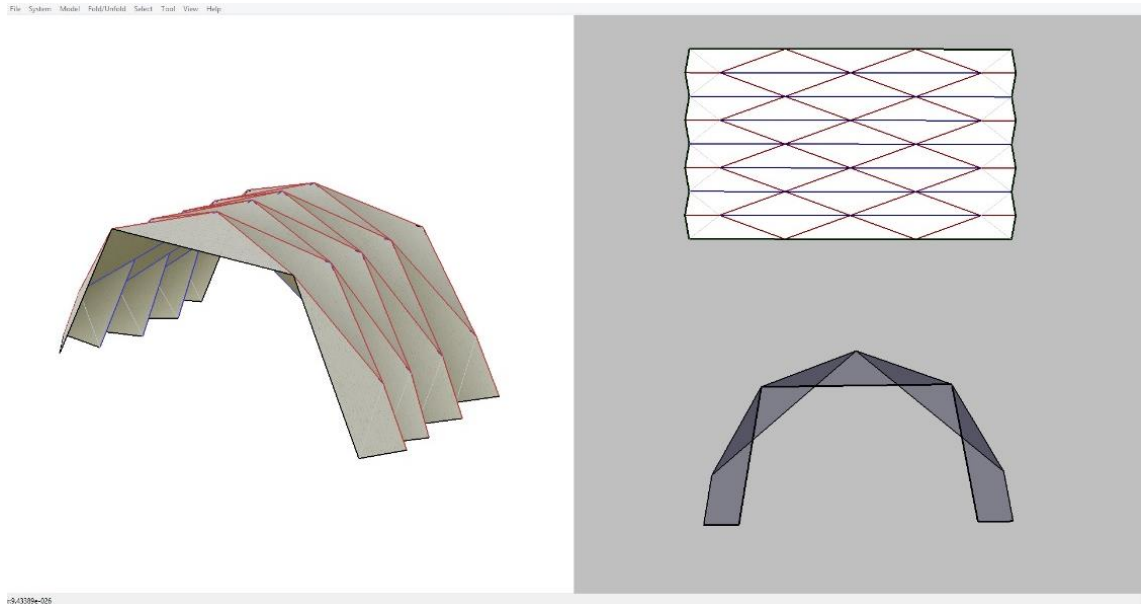


Figure 3.12. Trapezoidal pattern rigid origami horseshoe 200° barrel vault tested on FreeformOrigami software (Tachi, 2009a).

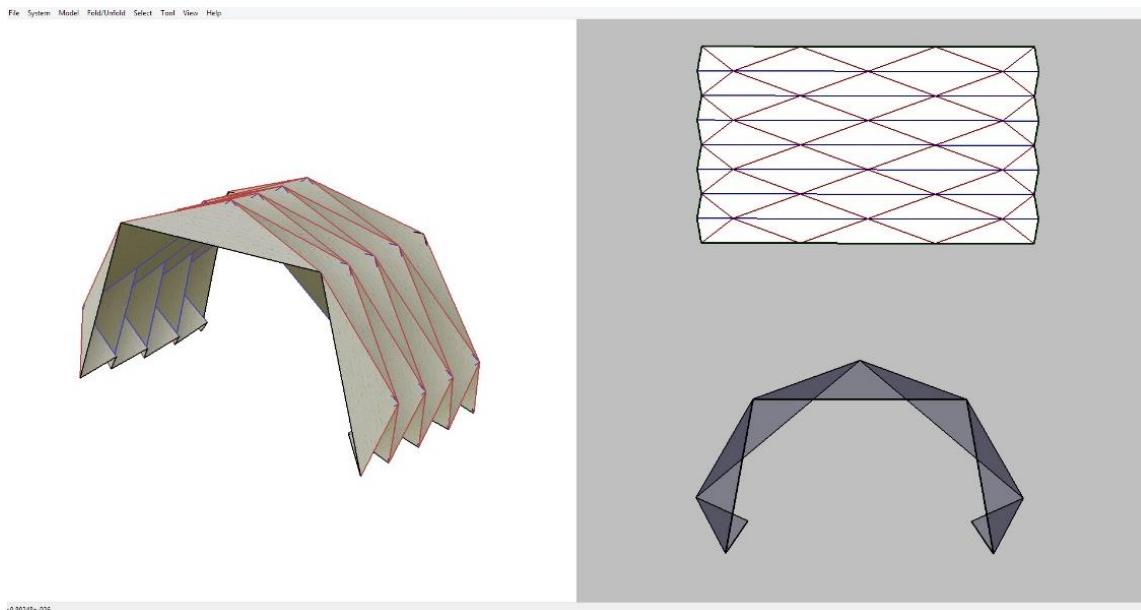


Figure 3.13. Rearranged triangular pattern rigid origami horseshoe 200° barrel vault tested on FreeformOrigami software (Tachi, 2009a).

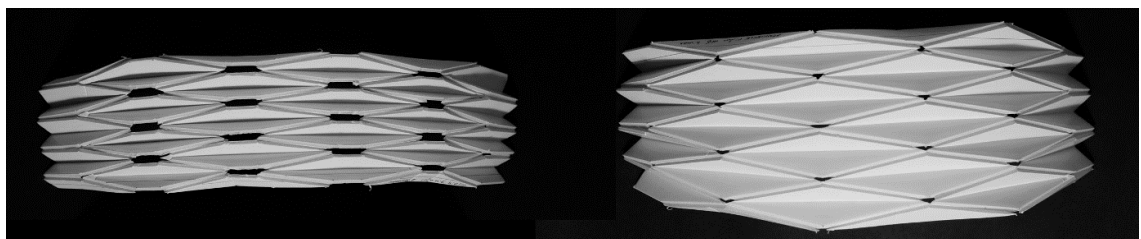


Figure 3.14. Models of trapezoidal pattern (left) and triangular pattern (right) for a semicircular cross-section.

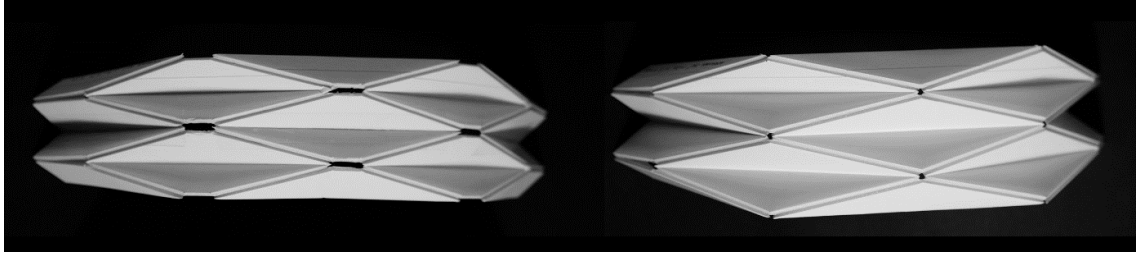


Figure 3.15. Models of trapezoidal pattern (left) and triangular pattern (right) for a horseshoe cross-section.

### 3.1.2. Workspace Analysis

The workspace analysis is first carried by analyzing the geometrical properties of the depth and then followed by the analysis of the span and height based on the cross-section of the rigid origami barrel vault structure. Both arch types demonstrated translational and rotational motion while folding (Figure 3.16). While the structure takes its single centered final folded state its depth and span decreases, but the height increases.

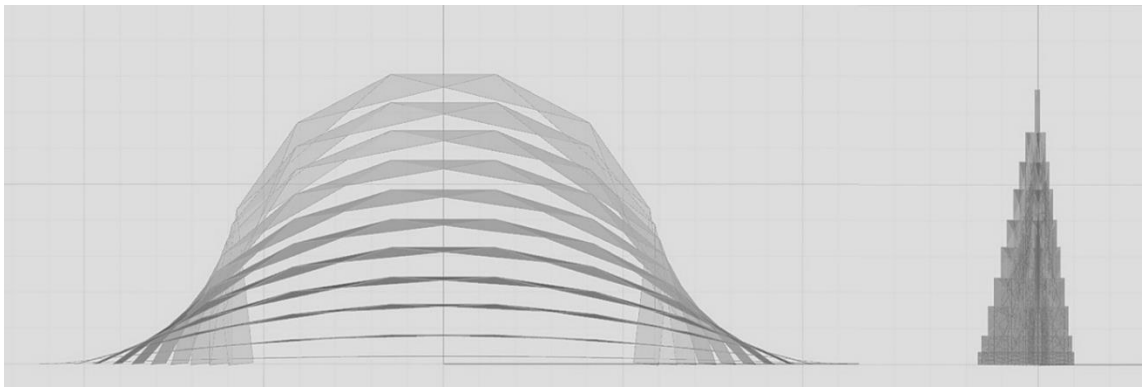


Figure 3.16.  $r: 6m$   $n:8$   $\Omega:220$  horseshoe arch motion - xz-plane (left) and yz-plane (right).

#### 3.1.2.1. Depth

The relation between the inclination angle  $\sigma$  and the depth can be explained by analyzing the vertexes. As it has been stated before in the partially folded state of the pattern, the inclination angle  $\sigma$  is equal to zero, and the dihedral angle  $\varphi$  is equal to  $\pi$  (Table 3.1). The depth of the mechanism depends on the number of rows  $R_n$  used to

create the pattern. The calculations start with a double row where the relation between the inclination angle and distance between two vertexes is analyzed. The lines  $d_1b_1$  and  $d_2b_1$  and are equal to the height of the pattern  $2h$ :  $d_1b_1 = d_2b_1 = 2h$  (Figure 3.17).

The depth of the pattern depends on the length of line  $d_1d_2$  named  $D_l$ , which in turn depends on the inclination angle  $\sigma$ . The relation is as the follows, based on the isosceles triangle rule:

$$D_l = 2 \cdot (2h) \cdot \cos \sigma \quad (3.25)$$

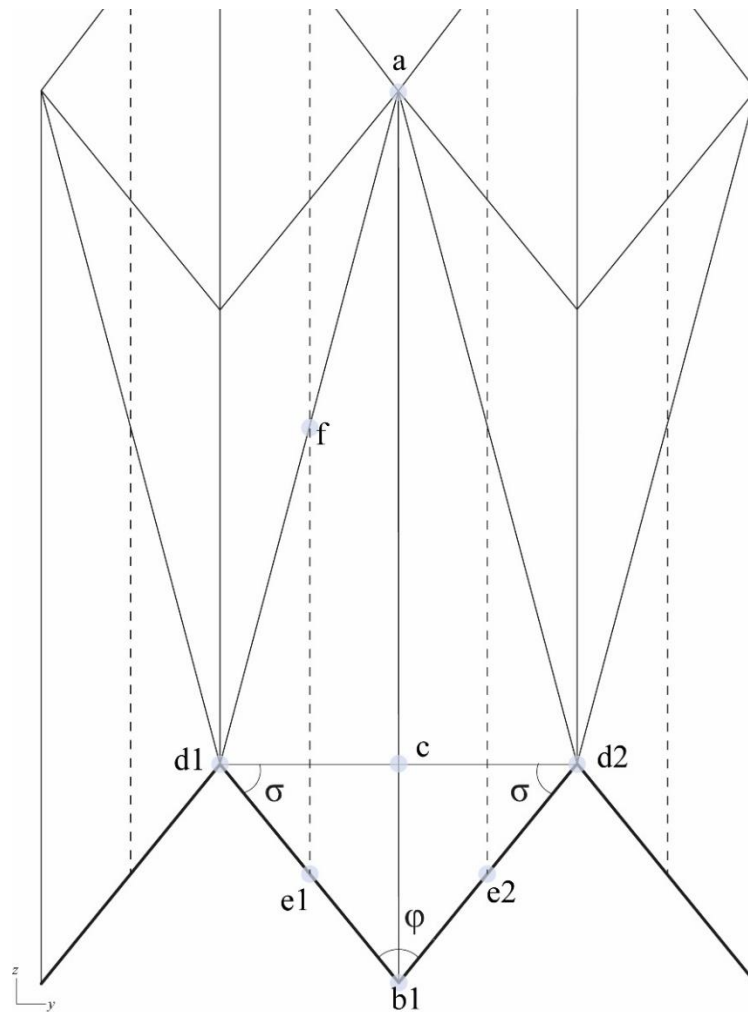


Figure 3.17. Side view showing the relation between inclination angle  $\sigma$  and depth. Dashed lines are the *pattern-generator*, bold full lines are the section lines.

As stated before, values of the inclination angle  $\sigma$  are  $\sigma_{min} = 0$  for the initial state and  $\sigma_{max} = \pi/2$  for the final folded state. As the distance  $D_l$  increases the value of the inclination angle decreases and thus the distance  $D_l$  is equal to:

$$D_{lmax} = 2 \cdot (2h) \cdot \cos \sigma_{min} = 4h \quad (3.26)$$

and

$$D_{lmin} = 2 \cdot (2h) \cdot \cos \sigma_{max} = 0 \quad (3.27)$$

The total depth  $TD_l$  depends on the number of rows  $R_n$  in a pattern and the distance  $D_l$  calculated by eq. (3.28).  $D_l$  is the distance between two rows so, to be able to calculate the value for each additional row, the value of  $D_l$  is divided by 2.

$$TD_l = \frac{D_l}{2} \cdot R_n \quad (3.28)$$

Substituting eq (3.25) in eq (3.28), the relation between the inclination angle and the total depth is obtained:

$$TD_l = 2h \cdot \cos \sigma \cdot R_n \quad (3.29)$$

The relation between the inclination angle and the total depth of a horseshoe  $n: 8$   $r: 6$  m,  $\Omega: 220^\circ$  pattern with 10 rows and  $2h: 0,697$ m can be observed in Figure 3.18 where, as the inclination angle increases, the total depth decreases.

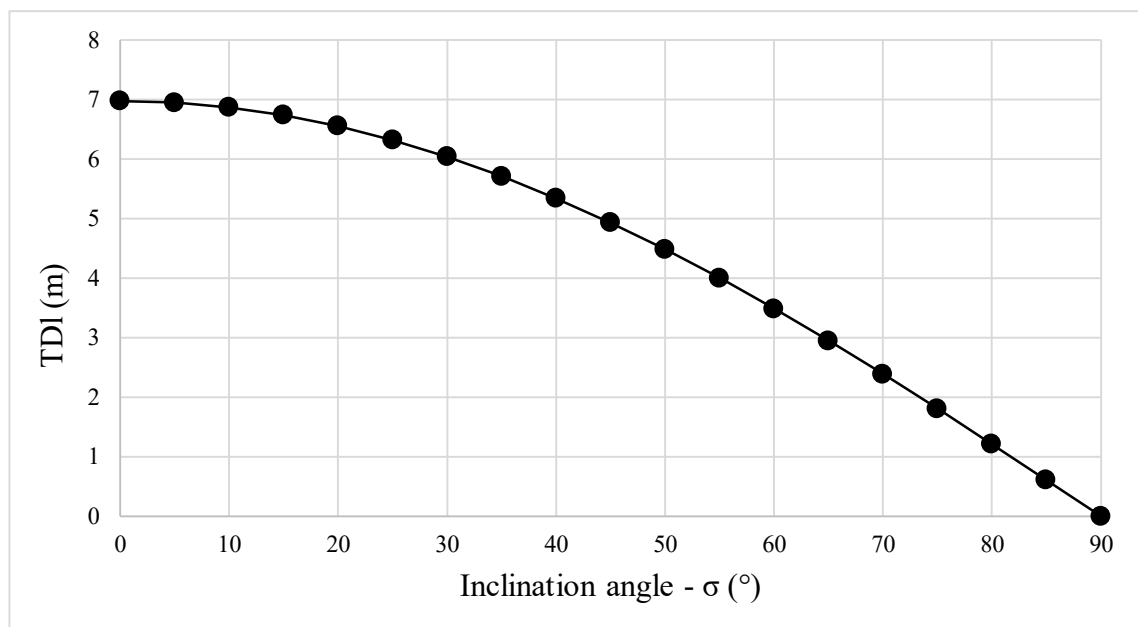


Figure 3.18. Relation between the inclination angles  $\sigma$  and the total depth,  $TD_l$  of a 10 row single centered barrel vault pattern.



### 3.1.2.2. Span and Height

The span and height are affected by the cross-section of the type of the rigid origami barrel vault. The geometrical analysis is carried out on the *pattern-generator*'s properties during the folding process. The central point of the *pattern-generator* line has been fixed to be able to calculate the span and height differences occurring during the process. As it can be observed in Figure 3.19 as the MV-pattern folds the central point of the structures changes, the value of the inclination angle  $\sigma$  are:  $0^\circ$ ,  $10^\circ$ ,  $30^\circ$ ,  $50^\circ$ ,  $70^\circ$ ,  $90^\circ$ , where  $90^\circ$  is the final folded state of the MV-Pattern. Changes occurring to the span and the height are analyzed in this section in relation to the inclination angle  $\sigma$ . To carry the analysis, some parameters' properties need to be put in relation with the inclination angle  $\sigma$ . These parameters are denoted with a  $d$  next to them to differentiate them (Figure 3.20). The calculations differs when the number of segment  $n$  is an even or odd number thus span and height for even numbers are denoted  $S_E$  and  $H_E$  and  $S_O$  and  $H_O$  for odd numbers.

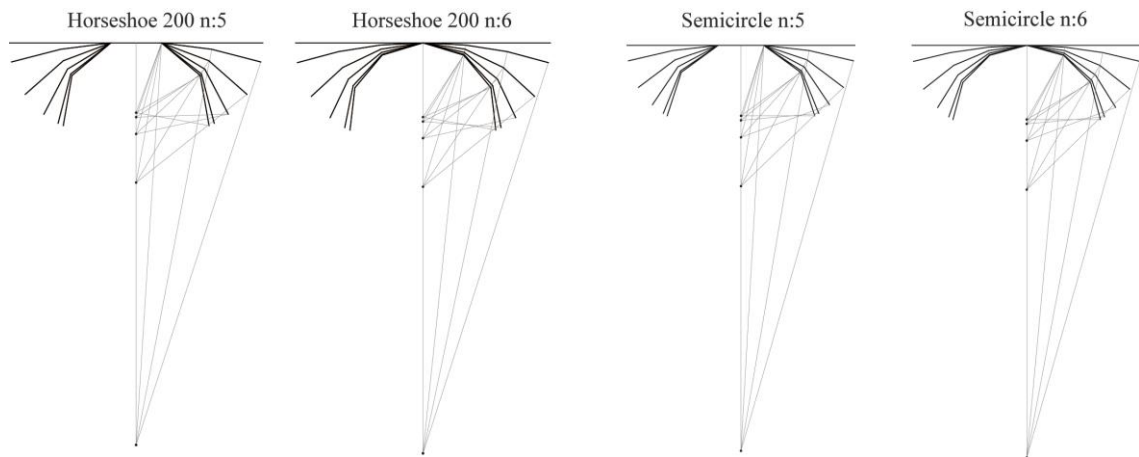


Figure 3.19. (left) Horseshoe arch *pattern-generator* with even and odd number segments, (right) Semicircle arch *pattern-generator* with even and odd number of segments.

Parameters required to calculate the span  $S$  and height  $H$  are the segments' angle during the development process  $\theta_d$  and the angle  $\delta$  - projected angle of the folding angle  $\alpha$ . Both parameters need to be in relation with the inclination angle  $\sigma$  to be able to calculate the differences of span and height during the development process. The relation between the projected angle  $\delta$  and inclination angle  $\sigma$  has already been explained in eq. (3.17).

$$\delta = \tan^{-1}\left(\frac{\sin \sigma \cdot d_1 b_1 \cdot \tan \alpha}{d_1 b_1}\right) = \tan^{-1}(\sin \sigma \cdot \tan \alpha) \quad (3.17)$$

The relation of the segments' angle  $\theta_d$  can be explained by expanding the geometrical relations presented in the previous section where eq. (3.7) is the value of the interior angle  $\beta$  in relation to segment's angle  $\theta$ , and eq. (3.9) where the relation of the folding angle  $\alpha$  with the interior angle  $\beta$  is presented. By substituting eq. (3.7) in eq. (3.9) a relation between the folding angle  $\alpha$  and segments' angle  $\theta$  can be achieved eq. (3.30).

$$\alpha = \frac{\pi - \beta}{2} = \frac{\pi - (\pi - \theta)}{2} = \frac{\theta}{2} \quad \theta = 2\alpha \quad (3.30)$$

Because the angle  $\delta$  is the projected angle of the folding angle  $\alpha$  and defines the relation between the inclination angle  $\sigma$  and the folding angle  $\alpha$ , the eq. (3.30) can be modified to calculate the value of the segments' angle during the development process  $\theta_d$  (eq. (3.31)) by substituting the folding angle  $\alpha$  by its projected angle  $\delta$ .

$$\theta_d = 2\delta \quad (3.31)$$

In Figure 3.20 the parameters for both even and odd numbered horseshoe arch with central angle equal  $200^\circ$  can be observed. The *pattern-generator* noted as **1** is the final folded state where the inclination angle  $\sigma$  is equal to  $90^\circ$ , and the number **2** is the position of the pattern-generator when the inclination angle is equal to  $30^\circ$ . The central point of the *pattern-generator* is assumed fixed in order to calculate both the span and height of the rigid origami barrel vaults.

Span: The span is calculated by adding each segments' length projected to the x-axis  $s_{d1}$  for both types of arches. The calculations differ if the number of segment is an even or odd number.

Starting from the apex, for even numbered segmented arches, the deployment starts with the projected angle  $\delta$  and with each segment the angle increases by the segments' angle  $\theta_d$ . Thus, the segment's projected length is calculated using eq. (3.32) where  $i$  is equal to 0 (zero) for the first segment, 1 for the second, 2 for the third, and so on.

$$s_{Ed1} = s \cdot \cos(\delta + i\theta_d) \quad (3.32)$$

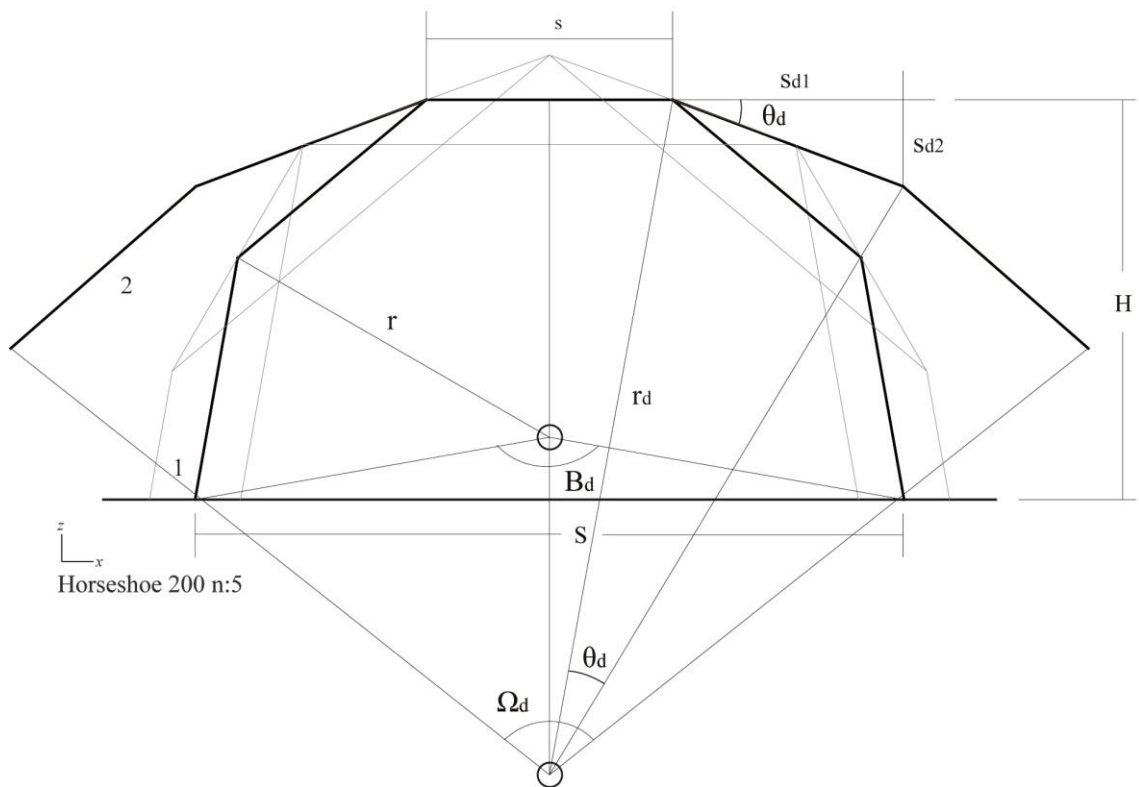
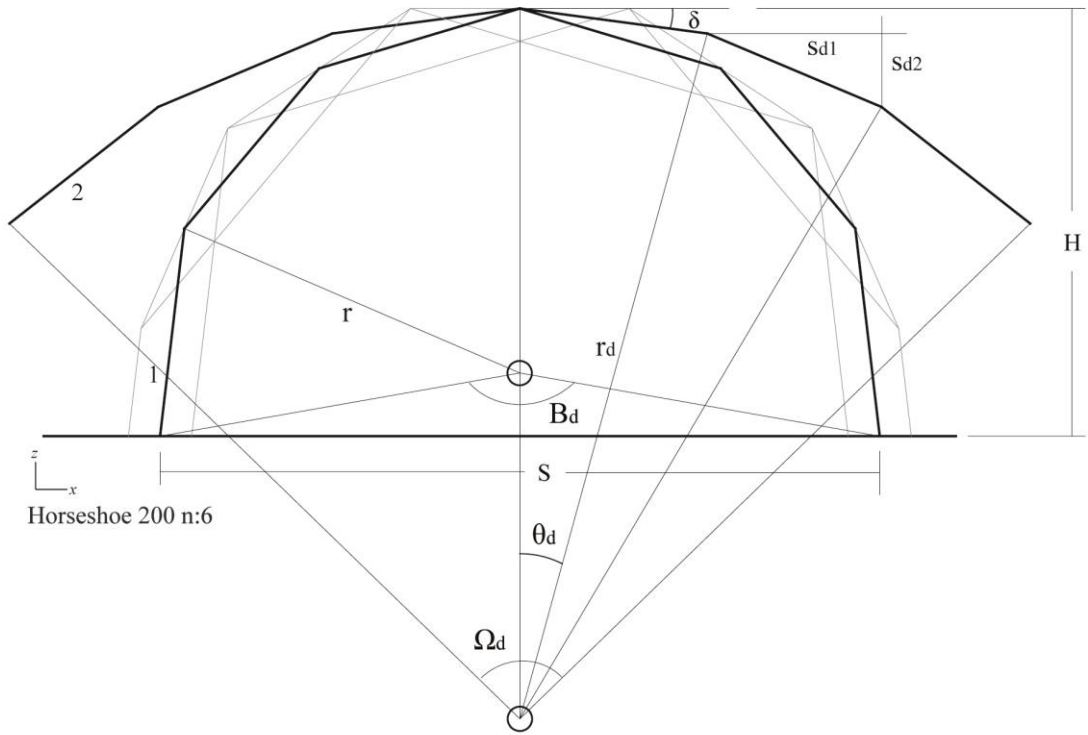


Figure 3.20. Parameters for (above) Horseshoe 200 arch *pattern-generator* with even number of segments, (below) Horseshoe 200 arch *pattern-generator* with odd number of segments.

For patterns with an odd number of segments, which can be observed in Figure 3.20, calculation start from the central point of the pattern-generator and not the apex. The folding starts with the segments' angle  $\theta_d$  and with each segment the angle increases by the value of the angle  $\theta_d$ . The projected segment's length is calculated using eq. (3.33).

$$s_{Od1} = s \cdot \cos(i\theta_d) \quad (3.33)$$

The span for both types of single centered arches are calculated by eq. (3.34) for even numbered segments and by eq (3.35) for odd numbered segments. For the even numbered arch the sum of the segments' projected length is multiplied by 2 to have the total span of the arch. For the odd numbered arch, a segment's length  $s$  is added to the sum of the projected lengths.

$$S_E = 2s(\sum_{i=0}^{n/2} \cos(\delta + i\theta_d)) \quad (3.34)$$

$$S_O = s + 2s(\sum_{i=1}^{n-1/2} \cos(i\theta_d)) \quad (3.35)$$

The required parameters to calculate the span are the projected angle  $\delta$  and the segments' angle in development process  $\theta_d$ . Figure 3.21 shows the relation between the inclination and the span. As the inclination angle increases the span decreases. The maximum span of the pattern is obtained in its initial state.

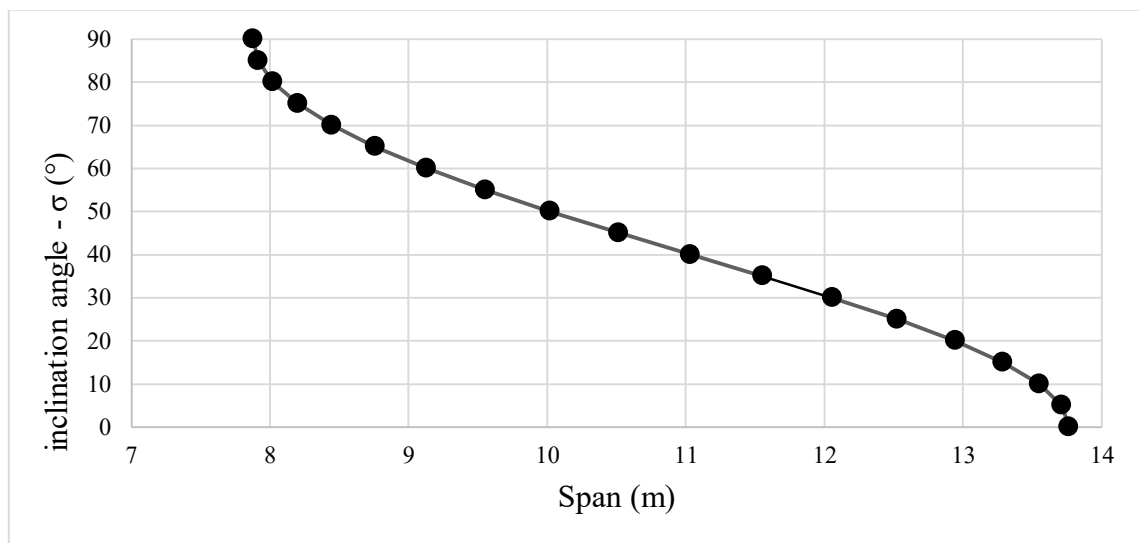


Figure 3.21. Relation between the inclination angle and the span of a horseshoe arch  $r$ :  
 $4 n: 6 \Omega: 200$ .

Height: The height is calculated by adding each segments' length projected to the z-axis  $s_{d2}$  for both types of arches, eq. (3.36) and eq. (3.37) again the calculations differs if the segment number  $n$  is an even or odd number.

$$s_{Ed2} = s \cdot \sin(\delta + i\theta_d) \quad (3.36)$$

$$s_{Od2} = s \cdot \sin(i\theta_d) \quad (3.37)$$

As it was with the span calculations each projected segments length  $s_{d2}$  is added to each other resulting in the eq. (3.38) for an even numbered arch, and eq. (3.39) for an even numbered arch.

$$H_E = s \left( \sum_{i=0}^{n/2} \sin(\delta + i\theta_d) \right) \quad (3.38)$$

$$H_O = s \left( \sum_{i=1}^{n-1/2} \sin(i\theta_d) \right) \quad (3.39)$$

The required parameters to calculate the height are the same as the span. Figure 3.22 shows the relation between the inclination angle  $\sigma$  and the height  $H$ . As the inclination angle increases, the height increases too.

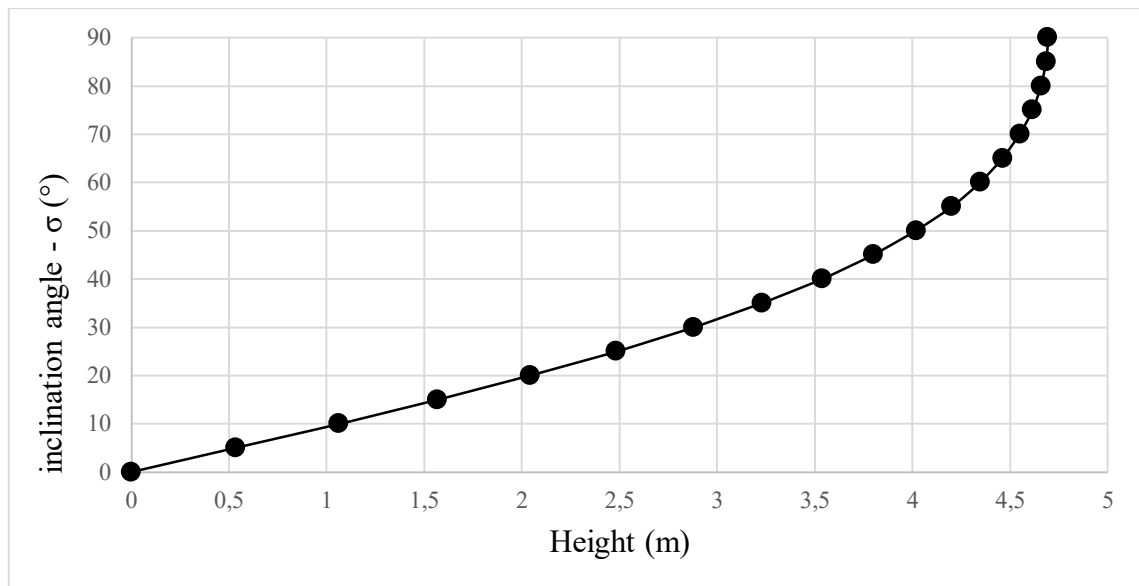


Figure 3.22. Relation between the inclination angle and the height of a horseshoe arch  
 $r: 4 \ n: 6 \ \Omega: 200$ .

### 3.1.2.3. Volume

The volume is calculated by multiplying the cross-section area with the total depth  $\mathbf{TD}_l$  (eq. (3.29)). Calculations for the volume are conducted using the arc of the pattern-generator. To be able to calculate the area of the cross-section changes occurring to the central angle's  $\Omega_d$ , its complementary angle's  $B_d$  and radius  $r_d$  during the deployment are required. All these angles have a relation with the inclination angle which will lead to the relation between the inclination angle  $\sigma$  and the volume  $\mathbf{V}$ .

The radius during the deployment is calculated by the following equation.

$$r_d = \frac{s}{2 \sin\left(\frac{\theta_d}{2}\right)} \quad (3.40)$$

The central angle  $\Omega_d$  is calculated by multiplying the number of segment  $n$  with the deployment state segments' angle  $\theta_d$  (eq. (3.41)). The value of the segment's angle has been calculated using eq. (3.31).

$$\Omega_d = \theta_d \cdot n \quad (3.41)$$

The complementary angle  $B_d$  of the central angle is calculated with the following equation:

$$B_d = 2\pi - \Omega_d \quad (3.42)$$

The area is calculated by the segment area equation which is valid for a central angle value equal or less than  $\pi$  ( $=<\pi$ ) which present a problem when the cross-section is a horseshoe arch. For the semicircular cross-section the following equation is used to calculate the area:

$$Area = \frac{1}{2} r_d^2 (\Omega_d - \sin(\Omega_d)) \quad (3.43)$$

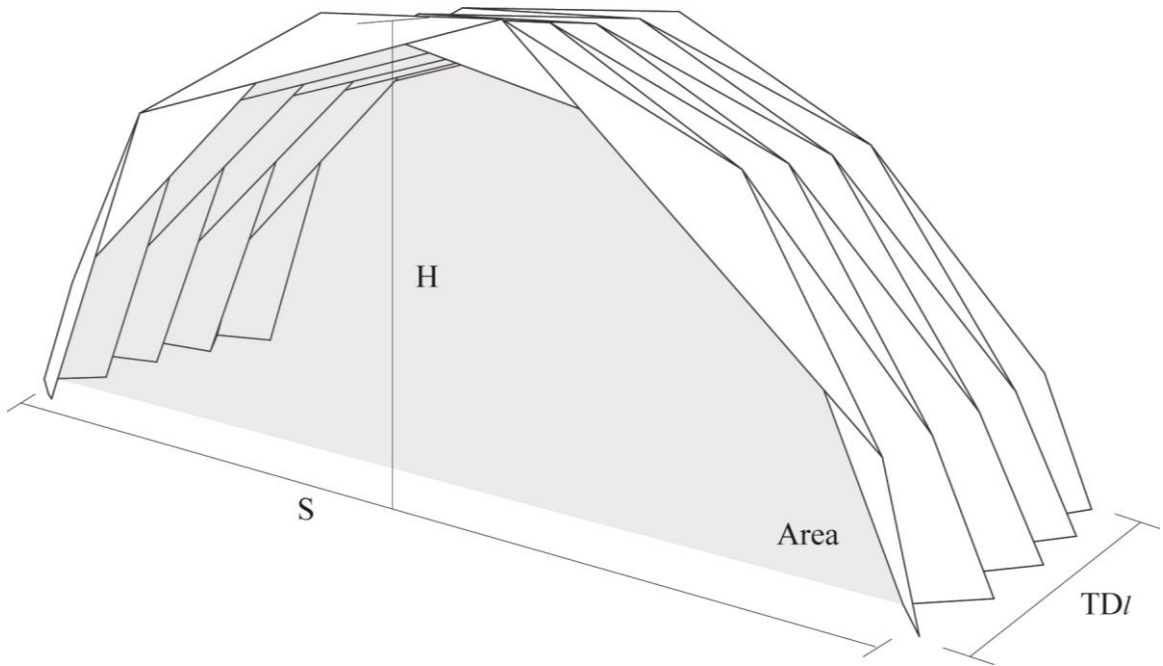


Figure 3.23. Single centered barrel vaults' volume parameters.

The center point of the arch moves during the deployment process as it has been showed in Figure 3.19, for horseshoe arches, after a certain point, the central angle's value becomes more than  $\pi$  (Figure 3.24 situation 3). In these cases the area of the cross-section is calculated by subtracting the sector area by the circle's area (eq. (3.44)).

$$Area_H = \pi r_d^2 - \frac{1}{2} r_d^2 (B_d - \sin(B_d)) = r_d^2 \left( \pi - \left( \frac{B_d - \sin(B_d)}{2} \right) \right) \quad (3.44)$$

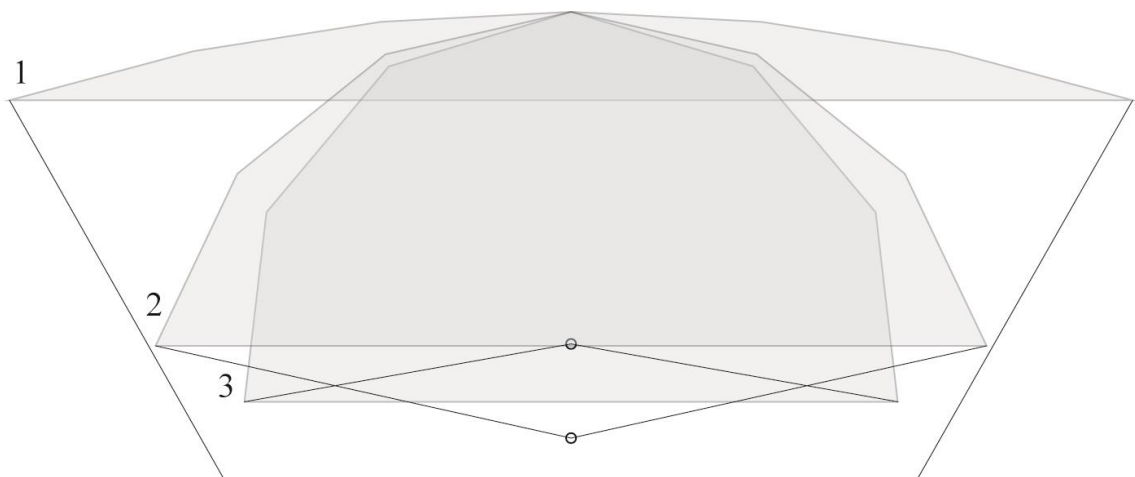


Figure 3.24. Single centered *pattern-generator* positions according to the inclination angle values (1) 10°, (2) 50°, and (3) 90° during folding process.

These changes appear during the deployment process; for this problem a solution has been incorporated in a Microsoft Excel 2013® calculation sheet (Appendix A).

The volume  $V$  is calculated with the following equations depending on the condition.

$$\text{If } \Omega_d \leq \pi \quad V = TD_l \cdot Area \quad (3.45)$$

$$\text{If } \Omega_d > \pi \quad V = TD_l \cdot Area_H \quad (3.46)$$

Table 3.5. Parameter of figure 3.23 for a horseshoe arch  $n:6$   $r:4$   $\Omega:200$   $R_n:10$

horseshoe n:6 r:4 $\Omega:200$						
$\sigma$ (°)	$\Omega_d$ (°)	$B_d$ (°)	$r_d$ (m)	Area (m <sup>2</sup> )	$TD_l$ (m)	V (m <sup>3</sup> )
0	0,00	360,00	0,00	0,00	6,87	0,00
5	17,94	342,06	43,98	4,92	6,84	33,67
10	35,71	324,29	22,10	9,66	6,76	65,37
15	53,17	306,83	14,85	14,07	6,64	93,32
20	70,16	289,84	11,26	18,00	6,45	116,20
25	86,53	273,47	9,14	21,39	6,23	133,15
30	102,16	257,84	7,75	24,19	5,95	143,87
35	116,92	243,08	6,78	26,40	5,63	148,55
40	130,71	229,29	6,07	28,07	5,26	147,72
45	143,43	216,57	5,54	29,27	4,86	142,15
50	155,00	205,00	5,13	30,06	4,42	132,73
55	165,35	194,65	4,82	30,54	3,94	120,33
60	174,42	185,58	4,57	30,79	3,43	105,74
65	182,17	177,83	4,38	30,87	2,90	89,63
70	188,55	171,45	4,24	30,86	2,35	72,51
75	193,55	166,45	4,13	30,80	1,78	54,76
80	197,13	162,87	4,06	30,73	1,19	36,66
85	199,28	160,72	4,01	30,68	0,60	18,37
90	200,00	160,00	4,00	30,66	0,00	0,00

Table 3.5 presents the values of a horseshoe arch with  $n:4$ ,  $r:4$ ,  $\Omega:200$  and 10 rows. The condition presented occurs when the inclination angle  $\sigma$  increases from  $60^\circ$  to  $65^\circ$  and the central angle's value surpasses the condition:  $\Omega_d \leq \pi$  for the volumetric calculations made using eq. (3.45). After this point eq. (3.46) is used for the area calculations. Figure 3.25 represent the data presented in Table 3.5. As it can be observed as the inclination increases the volume increases rapidly till reaching its peak when the inclination angle's value is around  $35^\circ$ . From its peak as the inclination angle



increases the volume of the barrel vault shows a slow decreases until it reaches its final folded state where the volume is equal to zero.

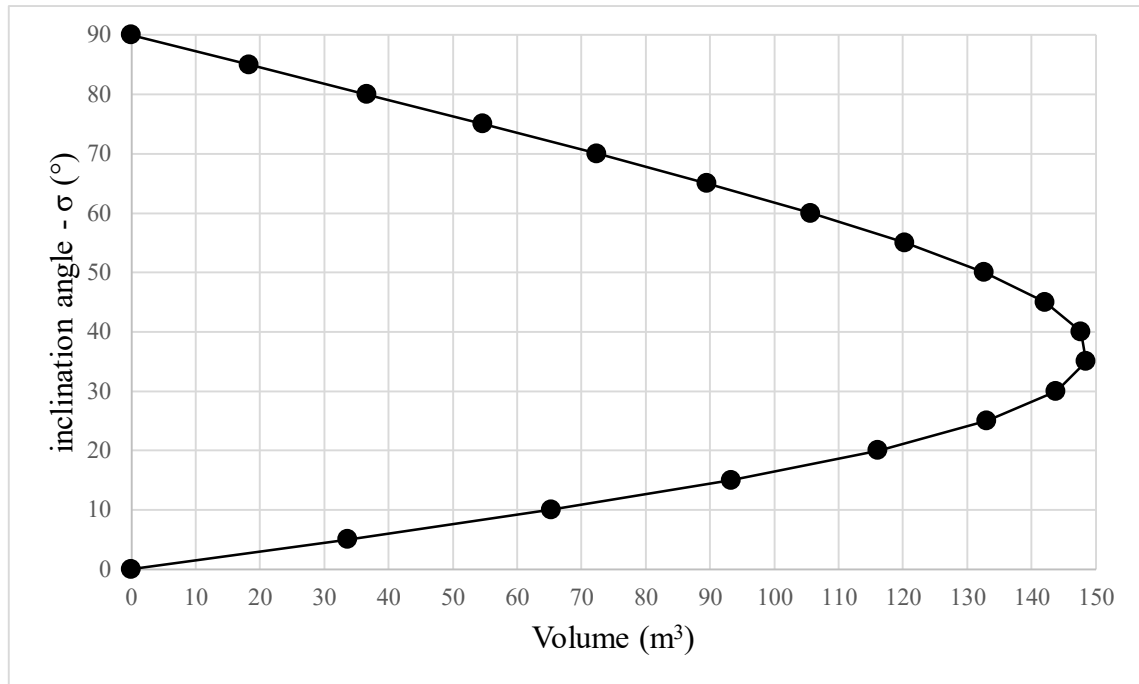


Figure 3.25. Relation between the inclination angle and the volume of a horseshoe arch  $r: 4 n: 6 \Omega: 200$ .

### 3.1.3. Mobility Analysis

Rigid origami barrel vault plate structures are obtained by the cross-section of the desired shape and designed with the required parameters of the geometrical properties of the selected cross-section arch type. This section only analyses the mobility of the single centered arch types. Rigid origami structures are considered as a mechanism, constructed by rigid panels and revolute joints allow motion. As discussed in previous chapters (2.5.2.2.) the origami-inspired structures are comprise of spherical loops.

As it will be demonstrated, that when the kinematic diagram of a pattern is analyzed, both triangular and trapezoidal patterns are comprised of multiple loops. To be able to calculate the number of independent loops Euler's equation (eq. (3.47)) is used, where  $L$  stands for the number of loops,  $j$  for the number of joints, and  $l$  for the number of links.

$$L = j - l + 1 \quad (3.47)$$

A rigid body in space has six parameters that allows motion: three coordinates [x, y, and z] and three angles that define the rigid body's position and orientation in space. When the movement of a rigid body is restricted, it becomes part of a subspace where the motion has been restricted by one or multiple constraints (Selvi, 2012). Spherical mechanisms used in rigid origami foldable structures have three constraints, thus  $\lambda = 3$ . When multiple subspaces are combined (Alizade et al., 2014) the number of the new subspace can be calculated by the eq. (3.48) presented by (Selvi, 2012, p. 52). The number of subspaces combined is  $n$ .

$$\lambda_{combined} = \sum_{k=1}^n \lambda_k + (1 - n) \quad (3.48)$$

This section analyses the mobility of the created patterns using the Freudenstein and Alizade's equation (eq.3.49):

$$M_{nr} = \sum_{i=1}^j fi - \sum_{k=1}^L \lambda_k + q - j_p \quad (3.49)$$

where  $M$  is the mobility,  $nr$  is the number of segments and rows in a pattern,  $fi$  is the degree of freedom for  $i^{th}$  kinematic pair,  $\lambda_k$  is the degree of spaces or subspaces of  $k^{th}$  loop,  $q$  is the number of excessive links, and  $j_p$  is the number of passive joints. Since all joints are revolute joints (2.5.2.2.) in origami mechanisms, and there are no excessive links or passive joints the eq. (3.49) can be defined as:

$$M_{nr} = \sum_{i=1}^j fi - \sum_{k=1}^L \lambda_k \quad (3.50)$$

The patterns are analyzed first by calculating the number of independent loops using the Euler's equation (eq.(3.47)), then their mobility is calculated using the eq. (3.50), finally the mobility is verified by the properties of structural group. "Structural (Assur) group: Smallest kinematic chain which when added to, or subtracted from, a mechanism results in a mechanism that has the same mobility as the original mechanism." (IFTtoMM online dictionary). Basic elements of structural groups can be observed in figure 3.26. As one of the elements is added to a mechanism the mobility do not changes.

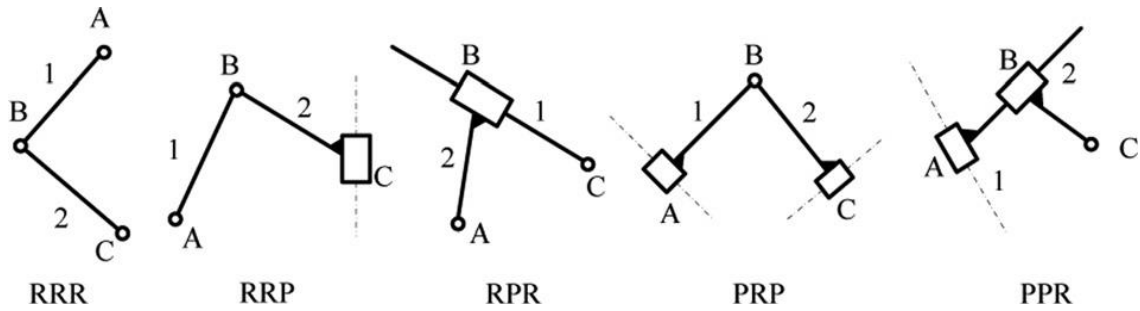


Figure 3.26. Element of structural group.  
(Source: Li & Dai, 2012, p. 2)

The analysis starts with a double row of a six segmented pattern, then a single row is added for each step to understand the mobility of the pattern. Since the row is created with parameters, the pattern can grow in a single direction, so the pattern has only additional rows and not columns. The number of segments is a parameter that is specified by the designer to calculate all other parameters and even though it can be perceived as a change in the number of columns in a pattern, in this study it is not referred as such.

### 3.1.3.1. Triangular Pattern

In this section the mobility analysis is done first for a triangular pattern ( $h$ : max), with 6 segments and 5 segments. Multiple tables are presented to further understand the mobility calculations, and their kinematic diagrams.

#### 3.1.3.1.1. Six Segmented Pattern

Double row: First the crease pattern with the numbers of panels is presented, and then the kinematic diagram with numbering for each link and joints are presented. As it can be observed from Figure 3.27, in a double row of a crease pattern there are twelve panels which can be considered as links. There are 14 joints for 12 links.

The number of independent loops,  $L_{62}$  is calculated using eq. (3.47):  $L_{62} = 14 - 12 + 1 = 3$ , there are 3 loops for a double row triangular pattern. The first loop is a 4-bar spherical mechanism, and loops 2 and 3 are 6-bar spherical mechanisms. For all three loops  $\lambda = 3$  because all the joints' axis meet at a central point. The

mobility calculation for the double row pattern  $M_{62}$  is made by substituting the number of joints and loops to eq. (3.50);

For 14 revolute joints and three  $\lambda = 3$  loops the mobility is equal to 5:  
 $M_{62} = 14 - (3 \cdot 3) = 5$ .

Rigid origami deployable structures are often modeled with zero thickness and perfect hinges which causes a problem when an application is required. The material, which should stay stable during the folding process requires to have a thickness which may change the panel's dimensions or the placement of the hinges (Figure 2.33(b)) or the joints' properties like in Figure 2.33f where the joints are rolling joints not hinges (Cai, 2016c). Tachi's study about thick origami (Tachi, 2011) presented two flat-foldable models: the axis-shift method (Figure 2.33(b)) where the joints were placed in different locations and tapered method (Figure 2.33(c)) where the material geometry have been tapered so that the mechanism closes. Edmondson et al. also proposed two other methods to compensate the thickness problem in rigid origami structures (Figure 2.33(d)(e)).

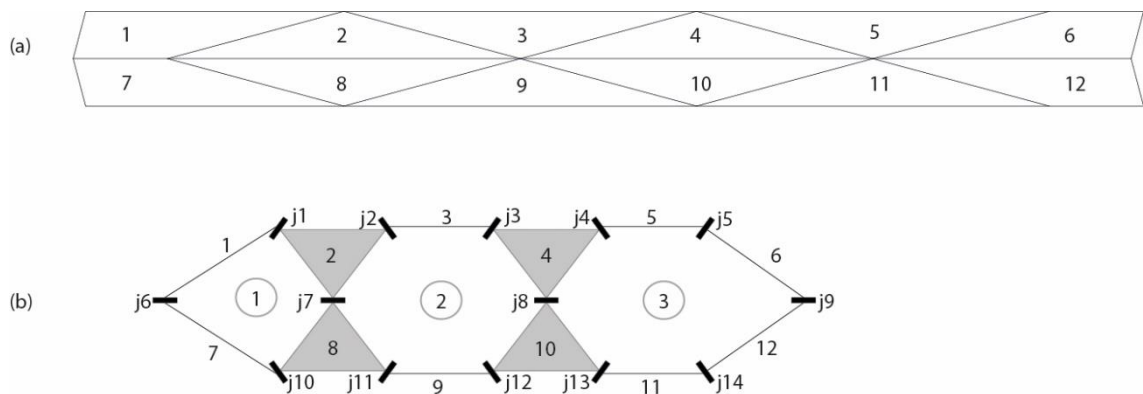


Figure 3.27. Triangular double row semicircle arch  $r:3$   $n:6$   $\Omega:180^\circ$  (a) crease pattern (b) kinematic diagram.

The result can be verified by the properties of structural group; a loops of a 4-bar mechanism has a mobility of 1. To preserve the mobility when a second loop is added, 2 more links need to be added because it is a loop of  $\lambda = 3$ . But as it can be observed in Figure 3.27, the second loop introduces 4 new links, because only 2 new links were sufficient, the additional 2 links increases the mobility to 3. Then a third loop adds 4

new links to the structural group, again increasing the mobility by 2 to 5. Thus the equation is verified.

3 Rows: A third row is added to the double row crease pattern, which means that 6 new links and 9 new joints are added to the mechanism, up to 18 links and 23 joints (Figure 3.28). Three new loops are also added with a new row, calculated using eq. (3.47):  $L_{63} = 23 - 18 + 1 = 6$ . With the third row, two 6-bar spherical loop and one 4-bar loop are added. The mobility calculation for a 3-row six segments pattern  $M_{63}$  is calculated using eq. (3.50):  $M_{63} = 23 - (6 \cdot 3) = 5$ . For 23 joints and six  $\lambda = 3$  loops the mobility is again equal to 5.

The mobility does not change when a new row is introduced to the mechanism. As stated before, to preserve the mobility within a structural group of  $\lambda = 3$ , 2 new links need to be added (Figure 3.28). The 4<sup>th</sup> loop introduces 2 more links [17 and 18] which preserves the mobility. The 5<sup>th</sup> loop introduces again 2 more links and not 4 more links like in the double row because the links 9, 10, 11 and 17 are already part of the structural group; so the mobility is again preserved. The last loop, like the 5<sup>th</sup> loop adds 2 more links [13 and 14] which preserve the mobility. Even after a new row is introduced, the mobility is still equal to 5.

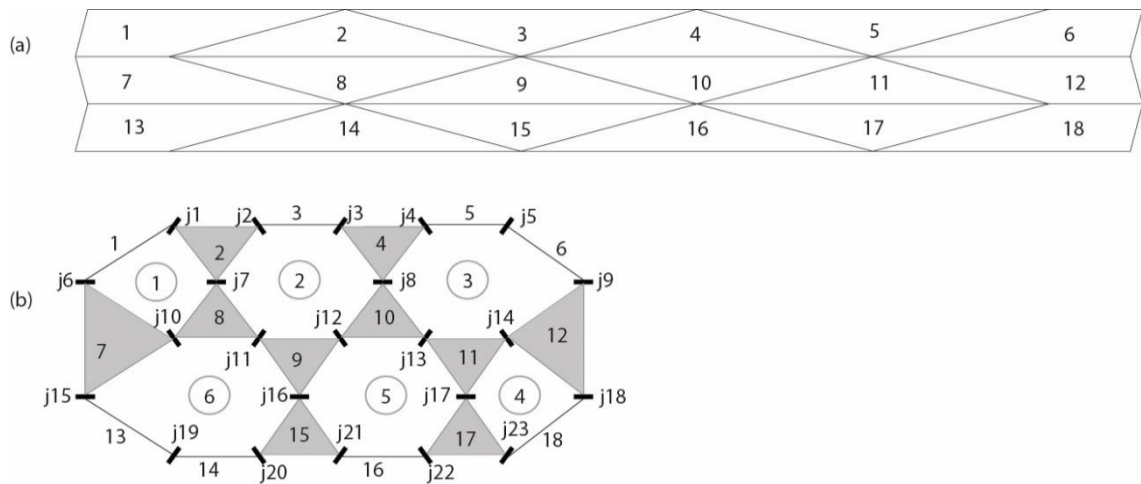


Figure 3.28. Triangular 3-row semicircle arch  $r:3$   $n:6$   $\Omega:180^\circ$  (a) crease pattern (b) kinematic diagram.

4 Rows: One more row is added to the 3-row pattern, that is again 6 new links and 9 new joints are added to the mechanism, increasing the number of joints to 32 and

the number of links to 24 (Figure 3.29). 3 new loops are added to the mechanism increasing the total number of loops to 9:  $L_{64} = 32 - 24 + 1 = 9$ .

The mobility is still equal to 5:  $M_{64} = 32 - (9 \cdot 3) = 5$ . after a new row is added, making a 4-row pattern. 7<sup>th</sup> loop adds two more links [19 and 20] to the mechanism preserving the mobility. The 8<sup>th</sup> and 9<sup>th</sup> loops also added 2 new links each; links 21 and 22 for the 8<sup>th</sup> loop, and links 23 and 24 for the 9<sup>th</sup> loop. The properties of structural groups confirms the calculations.

For a pattern with 6 segments each time a row is added, the mobility is constant and equal to 5. Each row adds 6 new links, 9 new joints, and 3 new loops with  $\lambda = 3$  spherical loops. (Table 3.6).

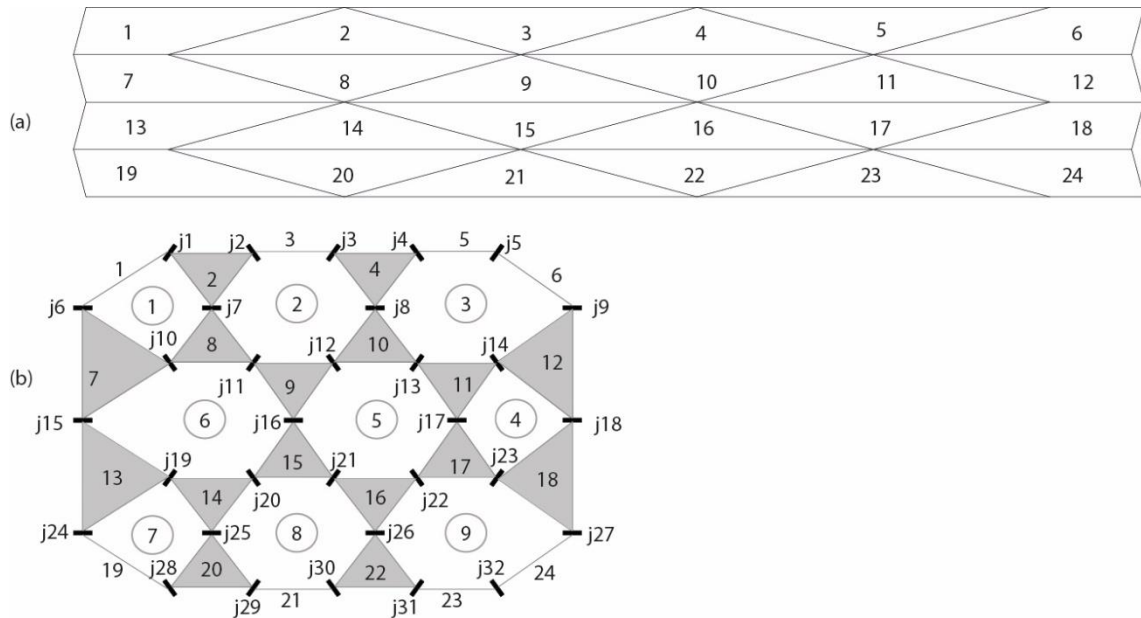


Figure 3.29. Triangular four rows semicircle arch  $r:3$   $n:6$   $\Omega:180^\circ$  (a) crease pattern (b) kinematic diagram.

### 3.1.3.1.2. Five Segmented Pattern

Double row: Patterns created by 5 segments and 6 segments are compared to understand the difference in their mobility values. In double row the six segmented pattern have a 4-bar loop and two 6-bar loops, and as it has been stated with each row a 4-bar loop and two 6-bar loops are added. In double row, the 5 segments pattern has three loops, as the 6 segmented pattern, but they are composed of two 4-bar loops and

one 6-bar loop (Figure 3.30):  $L_{52} = 12 - 10 + 1 = 3$ , which creates the difference between the numbers of joints and links. The mobility is equal to 3:  $M_{52} = 12 - (3 \cdot 3) = 5$ .

The result can again be verified by the properties of structural group: a loop of a 4-bar mechanism has a mobility of 1. When a 2<sup>nd</sup> loop, a 6-bar loop, is added 2 additional links are introduced to the structural group which changes the mobility to 3. Till here the calculations are the same as the 6-segment double row. But when a 3<sup>rd</sup> loop added to the mechanism the mobility is preserved because only 2 new links are added [5 and 10] (Figure 3.30). The mobility of a 5- segments double row triangular pattern is equal to 3.

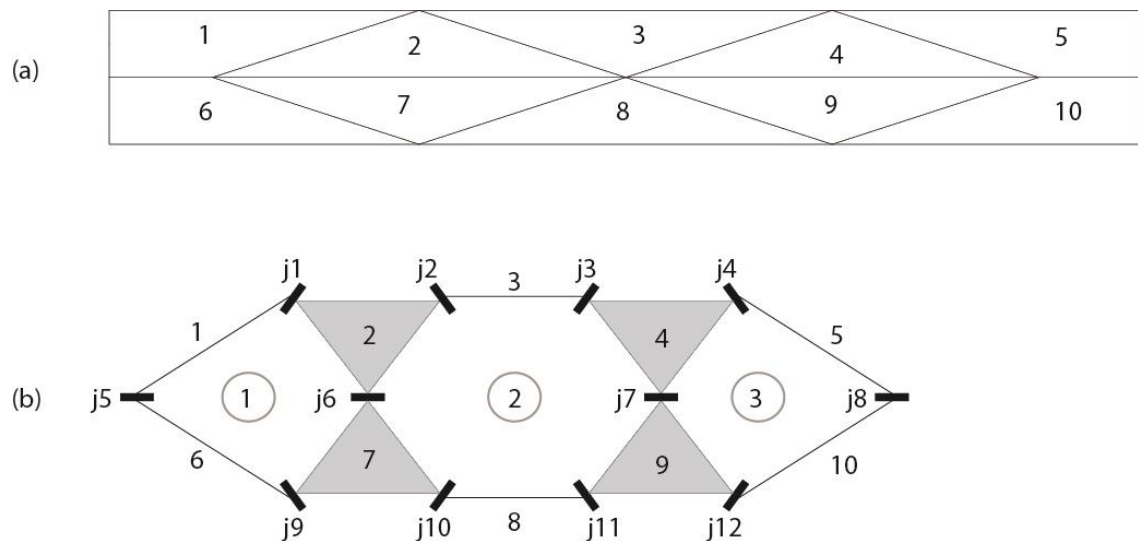


Figure 3.30. Triangular double row semicircle arch  $r:3$   $n:5$   $\Omega:180^\circ$  (a) crease pattern (b) kinematic diagram.

3 Rows: When a third row is added, instead of adding one 6-bar loop and two 4-bar loops, following the same logic observed in 6-segment pattern, a new row only adds two 6-bar loops. A 5 segments pattern with three rows has 5 loops,  $L_{53} = 19 - 15 + 1 = 5$ , while the 6 segments pattern have 6 loops (Figure 3.31).

The 4<sup>th</sup> loop adds 3 new links. Two links [14 and 15] are required to preserve the mobility thus one link [13] is additional and increases the mobility to 4. The 5<sup>th</sup> loop adds two new links [11 and 12] therefore preserve the mobility equal to 4:  $M_{53} = 19 - (5 \cdot 3) = 4$ .

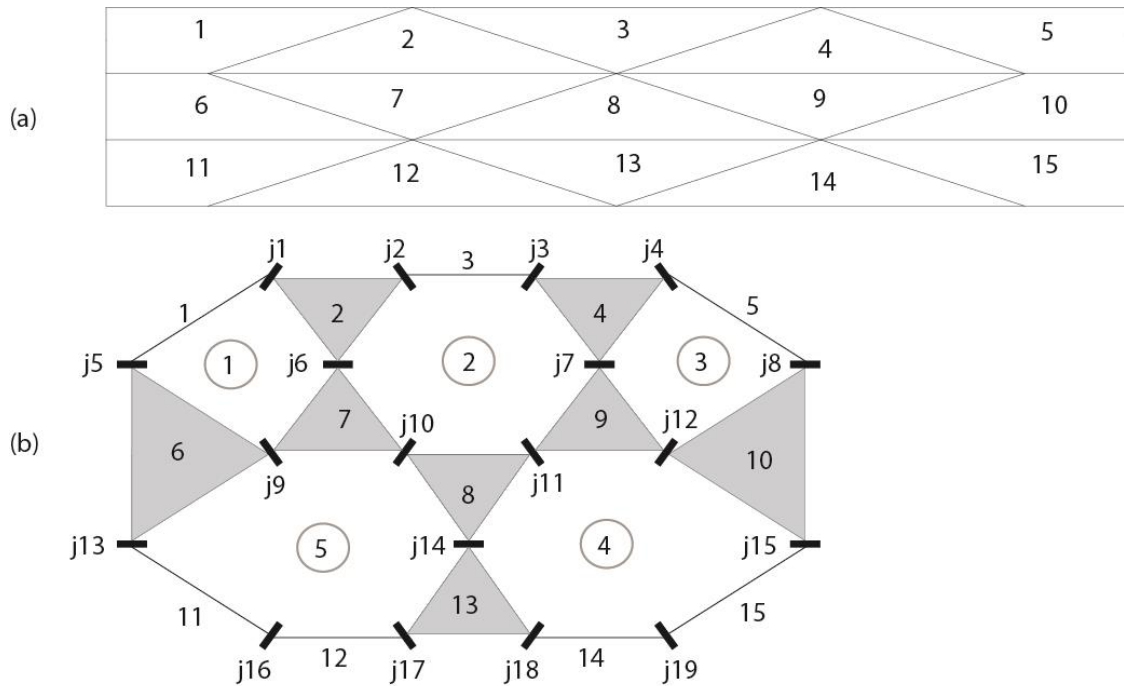


Figure 3.31. Triangular three rows semicircle arch  $r:3$   $n:5$   $\Omega:180^\circ$  (a) crease pattern (b) kinematic diagram.

4 Rows: the 4<sup>th</sup> row adds 3 more loops to the mechanism. It adds two more 4-bar loops and a 6-bar loop adding up a total of 5 new links and 8 new joints (Figure 3.32). There are 8 loops calculated using eq. (3.47):  $L_{54} = 27 - 20 + 1 = 8$  and the mobility is equal to 3:  $M_{54} = 27 - (8 \cdot 3) = 3$ .

The 6<sup>th</sup> loop adds two new links [16 and 17] preserving the mobility equal to 4. The 7<sup>th</sup> loop adds two links [18 and 19] therefore preserve the mobility. The 8<sup>th</sup> loop adds only one new link [20] which is one less link than required to preserve the mobility, thus the mobility decreases by one, making the mobility equal to 3. Therefore, the result of the equation is verified.



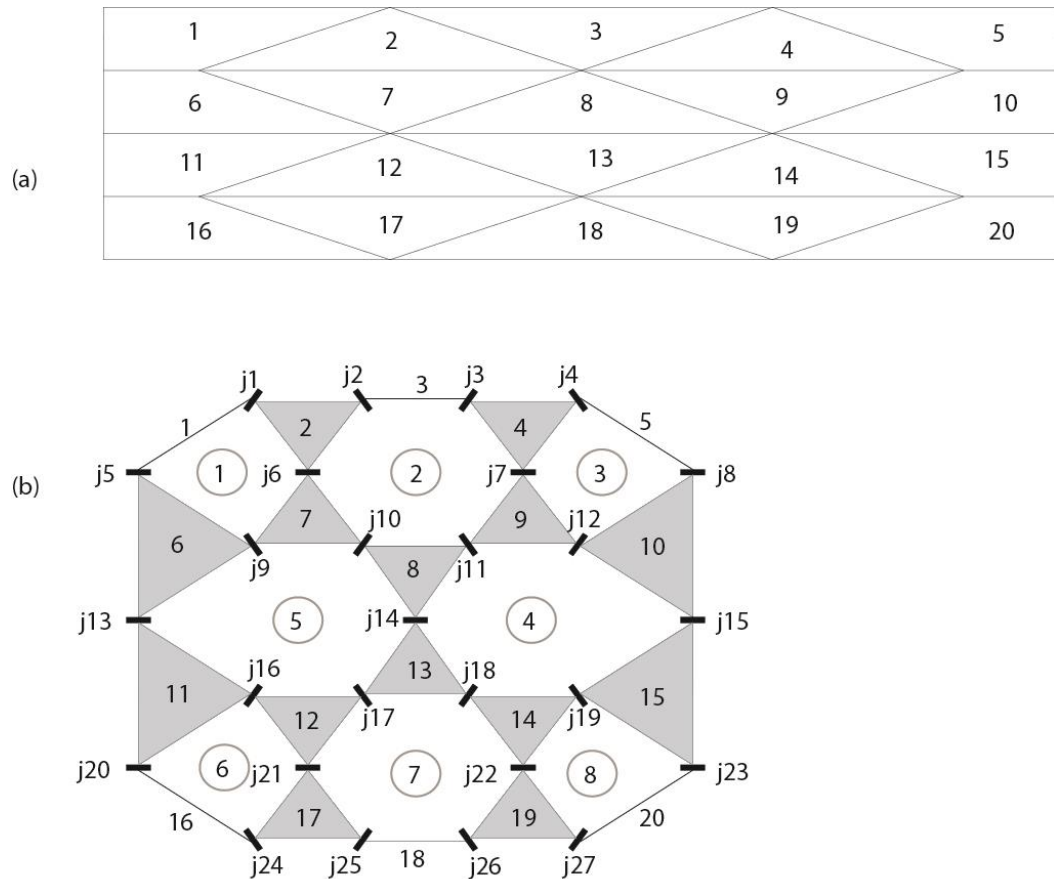


Figure 3.32. Triangular four rows semicircle arch  $r:3$   $n:5$   $\Omega:180^\circ$  (a) crease pattern (b) kinematic diagram.

The approximation of the arch is defined by the number of the segments  $n$ , it is divided, thus the mobility analysis has been extended to observe if there are differences when the segment number changes. As it can be observed in table 3.6 when the segment number is an odd number the mobility changes and it is not constant when there is an even numbered segments.

Table 3.6 presents the mobility calculations of patterns with different segments. When patterns with 6 and 4 segments are analyzed in the Table 3.6 it can be deduced that pattern with even number of segments the mobility is constantly preserved with each row. But when patterns with odd number of segments are analyzed it can be observed that the mobility is irregular. The irregularity have an order depending on the number of rows.

Table 3.6. Single centered triangular pattern mobility analysis with different number of segments and rows.

r:3 $\Omega$ :180 h: max Triangular Pattern																	
# of segment	2 Row			3 Row			4 Row			5 Row			6 Row			increased by	
n:3	# links	6			9			12			15			18			(+3)
	# joints	7			11			16			20			25			(+4) to odd (+5) to even
	# loops	T	$\lambda=3$	$\lambda=5$	T	$\lambda=3$	$\lambda=5$	T	$\lambda=3$	$\lambda=5$	T	$\lambda=3$	$\lambda=5$	T	$\lambda=3$	$\lambda=5$	(+1) to odd (+2) to even
		2	2	0	3	3	0	5	5	0	6	6	0	8	8	0	
M	1			2			1			2			1			(+1) to odd (-1) to even	
n:4	# links	8			12			16			20			24			(+4)
	# joints	9			15			21			27			33			(+6)
	# loops	T	$\lambda=3$	$\lambda=5$	T	$\lambda=3$	$\lambda=5$	T	$\lambda=3$	$\lambda=5$	T	$\lambda=3$	$\lambda=5$	T	$\lambda=3$	$\lambda=5$	(+2)
		2	2	0	4	4	0	6	6	0	8	8	0	10	10	0	
M	3			3			3			3			3			0	
n:5	# links	10			15			20			25			30			(+5)
	# joints	12			19			27			34			42			(+7) to odd (+8) to even
	# loops	T	$\lambda=3$	$\lambda=5$	T	$\lambda=3$	$\lambda=5$	T	$\lambda=3$	$\lambda=5$	T	$\lambda=3$	$\lambda=5$	T	$\lambda=3$	$\lambda=5$	(+2) to odd (+3) to even
		3	3	0	5	5	0	8	8	0	10	10	0	13	13	0	
M	3			4			3			4			3			(+1) to odd (-1) to even	
n:6	# links	12			18			24			30			36			(+6)
	# joints	14			23			32			41			50			(+9)
	# loops	T	$\lambda=3$	$\lambda=5$	T	$\lambda=3$	$\lambda=5$	T	$\lambda=3$	$\lambda=5$	T	$\lambda=3$	$\lambda=5$	T	$\lambda=3$	$\lambda=5$	(+3)
		3	3	0	6	6	0	9	9	0	12	12	0	15	15	0	
M	5			5			5			5			5			0	
n:7	# links	14			21			28			35			42			(+7)
	# joints	17			27			38			48			59			(+10) to odd (+11) to even
	# loops	T	$\lambda=3$	$\lambda=5$	T	$\lambda=3$	$\lambda=5$	T	$\lambda=3$	$\lambda=5$	T	$\lambda=3$	$\lambda=5$	T	$\lambda=3$	$\lambda=5$	(+3) to odd (+4) to even
		4	4	0	7	7	0	11	11	0	14	14	0	18	18	0	
M	5			6			5			6			5			(+1) to odd (-1) to even	

### 3.1.3.2. Trapezoidal Pattern

In this section trapezoidal pattern (h: 0.1m) created for a rigid foldable semicircle cross-sectioned barrel vault are analyzed. Six segmented crease pattern is analyzed; because the model tears during the folding process a different analysis has been conducted as an attempt to modify the pattern along with each row's analysis. The analysis for an odd number of segments has not been presented because mobility calculations showed that there was no significant difference with the analysis of the

triangular pattern. But for a deeper understanding of mobility in trapezoidal patterns a table has been presented with different number of segments.

Double row: The number of links is equal to the triangular pattern but the number of joints increase from 14 to 16 (Figure 3.33). The number of loops,  $L_{62T}$  for the trapezoidal pattern is calculated using eq. (3.47):  $L_{62T} = 16 - 12 + 1 = 5$ , so for a double row trapezoidal pattern there are 5 loops. All loops are 4-bar spherical loops, because all the joints axis meet at a central point for all five loops,  $\lambda = 3$ .

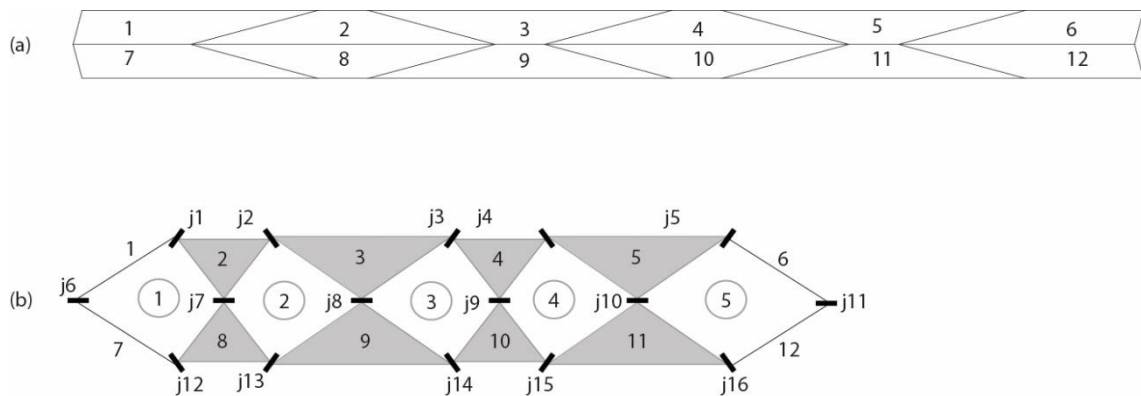


Figure 3.33. Trapezoidal double row semicircle arch  $r:2$   $n:6$   $\Omega:180^\circ$  (a) crease pattern (b) kinematic diagram.

The result can be verified by the properties of the structural group, a loop of a 4-bar linkage has a mobility of 1:  $M_{62T} = 16 - (5 \cdot 3) = 1$ . When a 2<sup>nd</sup> loop is added to preserve the mobility, 2 more links need to be added because it is a loop of  $\lambda = 3$ . Each new loop add 2 additional links thus the mobility does not change and the equation is verified.

Joints where tears appeared during the folding process of the physical model have been removed. Joints 8 and 10 are removed from the mechanism, creating a mechanism with 3 loops (Figure 3.34). The new loops' subspace number needs to be calculated using the eq. (3.48), where two  $\lambda = 3$  mechanism are joined:  $\lambda = (3 + 3) + (1 - 2) = 5$ .

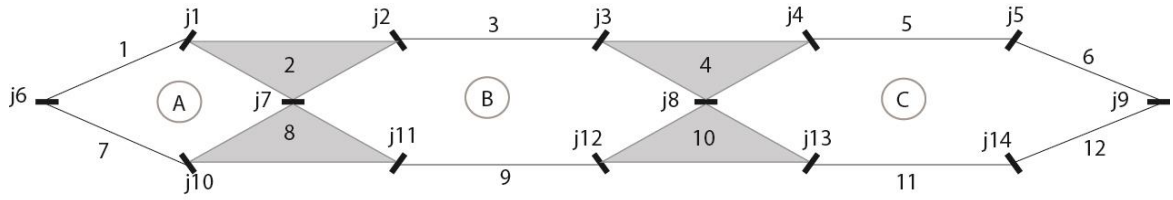


Figure 3.34. Modified Trapezoidal double row semicircle arch  $r:2$   $n:6$   $\Omega:180^\circ$  pattern kinematic diagram.

The new loop B is created by the combination of loops 2 and 3 and its subspace number is  $\lambda = 5$ . The second new loop C is a combination of loops 4 and 5 and its subspace number is as calculated  $\lambda = 5$ . The new obtained 6-bar loop is called the double spherical linkage (Bennett, 1905).

For a double row modified pattern the mobility is equal to 1 when calculated using eq. (3.50):  $M_{62TM} = 16 - ((1 \cdot 3) + (2 \cdot 5)) = 1$ .

The removal of these joints does not modify the mobility of the pattern. The properties of the structural group need to be reanalyzed since the modified mechanism is a mixture of  $\lambda = 3$  and  $\lambda = 5$  loops. The 1<sup>st</sup> loop A is a  $\lambda = 3$  4-bar loop with mobility 1. To preserve the mobility with loops that have  $\lambda = 5$  a structural group with 4 new links is required. So, the mobility is preserved because the new loop B introduces 4 new links [3, 4, 10, and 9] to the structural group. The last loop C also introduces 4 new links [5, 6, 12, and 11] again preserving the mobility as 1.

3 Rows: A third row is added to the double row crease pattern, that means 6 new links and 11 new joints are added to the mechanism. As it can be observed the additional row adds 5 more loops (Figure 3.35).

There are 10 loops:  $L_{63T} = 27 - 18 + 1 = 10$ .

The double row's mobility is equal to 1 as calculated, but with an additional row the mobility decreased to -3:  $M_{63T} = 27 - (10 \cdot 3) = -3$ . The structural group properties need to be analyzed to understand the new value of mobility. The 6<sup>th</sup> loop is added with 2 new links [18 and 17] preserving the mobility. The 7<sup>th</sup> loop only adds 1 new link to the structural group which decreases the mobility to 0. Each of the following loops, that is the 8<sup>th</sup>, 9<sup>th</sup> and 10<sup>th</sup>; introduce 1 new link instead of 2 new links each, which decreased the mobility to -3, creating an overconstrained mechanism.

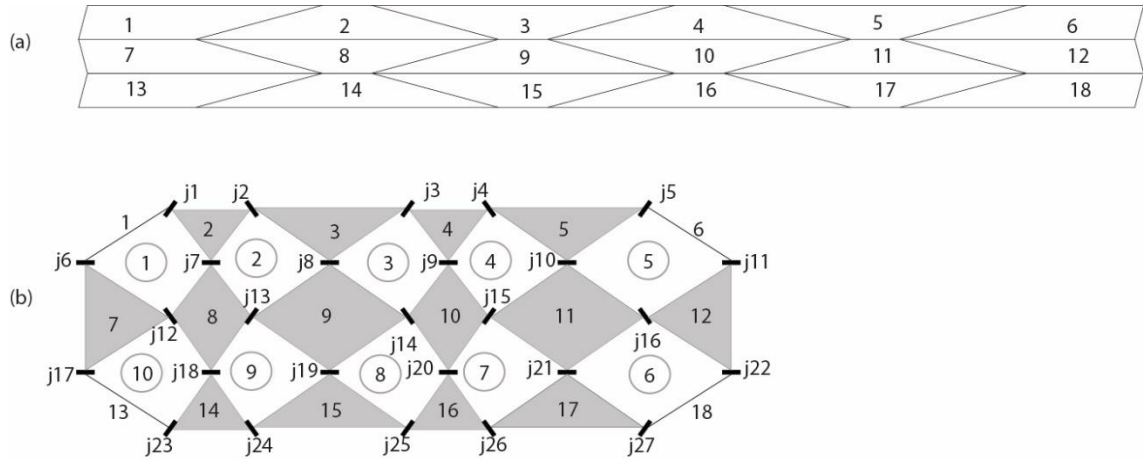


Figure 3.35. Trapezoidal three rows semicircle arch  $r:2$   $n:6$   $\Omega:180^\circ$  (a) crease pattern (b) kinematic diagram.

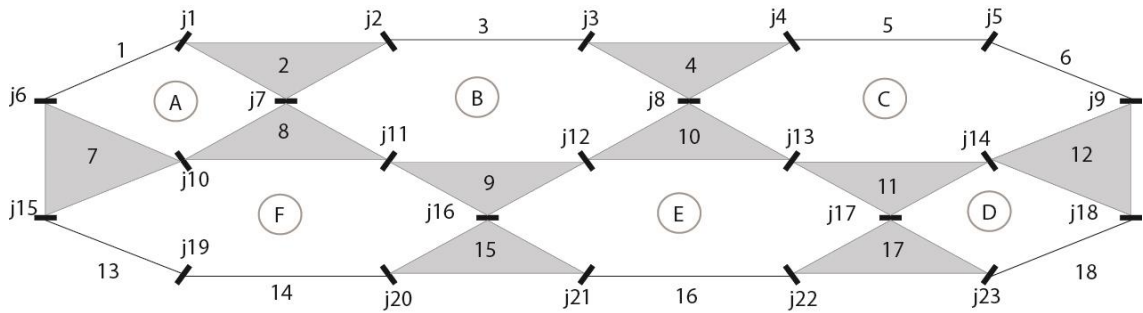


Figure 3.36. Modified Trapezoidal three rows semicircle arch  $r:2$   $n:6$   $\Omega:180^\circ$  pattern kinematic diagram.

As it was with the double row pattern some creases tear during the folding process of the model. Additional to the joints [8 and 10] removed before, the joints 18 and 20 are also removed from the mechanism. This creates a total of 6 loops in the mechanism instead of 10, but as before, when the specified joints are removed the loops [B, C, F, and E] subspace number becomes  $\lambda = 5$  instead of  $\lambda = 3$ , calculated with the eq. (3.48). (Figure 3.36)

The mobility of the modified pattern is equal:  $M_{63TM} = 23 - ((2 \cdot 3) + (4 \cdot 5)) = -3$ .

The value of the mobility does not change from the original trapezoid pattern. When the structural group is analyzed the additional loop D has a  $\lambda = 3$  subspace which requires additional 2 links to preserve the mobility which is satisfied by the addition of links 18 and 17. On the other hand the loops E and F have  $\lambda = 5$  and as stated before for such mechanisms, additional 4 links are required to preserve mobility. Both loop E

and loop F adds 2 links each [15 and 16 for loop E, 13 and 14 for loop F], instead of adding 4 links each which decreases the mobility to -3, confirming the equation.

4 Rows: One new row is added to the 3-row pattern, which adds 6 new links and 11 new joints to the mechanism. As it can be observed, the addition row adds 5 new loops that are 4-bar spherical loops (Figure 3.37).

The 3-row pattern had 10 loops: and -3 mobility, the new loop introduced to the structural group, loop number 11, adds 2 new links [19 and 20]. The number of loops is 15:  $L_{64T} = 38 - 24 + 1 = 15$ , and mobility is equal to -7:  $M_{64T} = 38 - (15 \cdot 3) = -7$ . After this loop each loops add 1 new link instead of 2 new links to the structural group, thus the value of the mobility became; -7, same value calculated as  $M_{64T}$ .

The joints removed from this pattern are joints; 8, 10, 18, 20, 30, and 32. By their removal the number of loops decreases to 9 (Figure 3.38). The new loops B, C, F, E, H and I are  $\lambda = 5$  mechanisms (Table 3.8).

The mobility of the modified pattern is equal:  $M_{64TM} = 32 - ((3 \cdot 3) + (6 \cdot 5)) = -7$ .

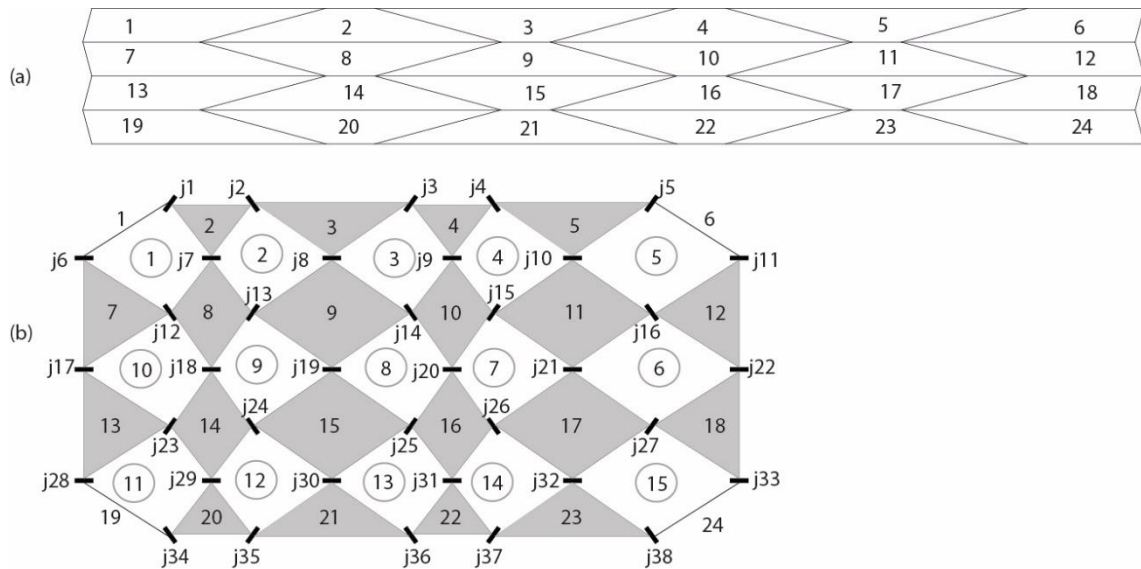


Figure 3.37. Trapezoidal four rows semicircle arch  $r:2$   $n:6$   $Q:180^\circ$  (a) crease pattern (b) kinematic diagram.

The first loop G added with the 4<sup>th</sup> row has a  $\lambda = 3$  subspace, adds 2 new links [19 and 20], thus preserve the mobility equal to -3. The second loop H, required to add 4 new links to the structural group because it is a  $\lambda = 5$  loop, only adds 2 new links [21 and 22]. The last loop I, which has the same properties as the previous loop, also adds

only 2 new links to the structural group. As a total the structural group lacks 4 links, which decreases the mobility by four, making the value -7, as calculated.

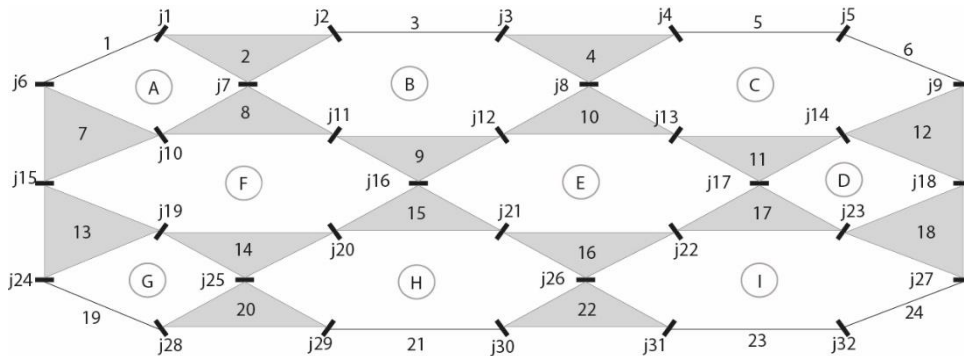


Figure 3.38. Modified Trapezoidal four rows semicircle arch  $r:2$   $n:6$   $\Omega:180^\circ$  pattern kinematic diagram.

Table 3.7 presents calculations for a trapezoidal pattern with different number of segment. As it can be observed there are no differences between even and odd numbered segment numbers as it was in the triangular pattern. Except the double row pattern all other pattern's mobility changes with each additional segment introduced to the mechanism. But during the folding process of the trapezoidal pattern tear from some of the joints, while the removal of the joints did not change the value of mobility it changed the kinematic properties of the pattern.

As a conclusion there are differences between the mobility value of even and odd numbered segmented triangular patterns. The mobility values has been compared to a structural group analysis revealing the same value of mobility. The modified trapezoid pattern's joint and link numbers (Table 3.8) are the same as the triangular pattern's values (Table 3.7), but the comparison between the kinematic diagrams of the trapezoidal and triangular patterns reveals that the subspace's numbers are different resulting in varied mobility. Lastly the joints removed from the trapezoidal patterns are the ones that tear during the model folding. The tear creases showed a similarity which suggest that the tearing did not occur randomly but, because no mobility changes have occurred it can be assumed that the cause for these tears were the thickness in the material. All tear appeared on the short creases forcing the pattern to be a 6-bar spherical loop pattern rather than a 4-bar spherical loop pattern.

Table 3.7. Single centered trapezoidal pattern mobility analysis with different number of segments and rows.

r:3 Ω:180 Semicircle h < MAX Trapezoidal pattern																	
# of segment	2 Row			3 Row			4 Row			5 Row			6 Row			increased by	
n:3	# links	6			9			12			15			18			(+3)
	# joints	7			12			17			22			27			(+5)
	# loops	Total	λ=3	λ=5	Total	λ=3	λ=5	Total	λ=3	λ=5	Total	λ=3	λ=5	Total	λ=3	λ=5	(2)
		2	2	0	4	4	0	6	6	0	8	8	0	10	10	0	
M	1			0			-1			-2			-3			(-1)	
n:4	# links	8			12			16			20			24			(+4)
	# joints	10			17			24			31			38			(+7)
	# loops	Total	λ=3	λ=5	Total	λ=3	λ=5	Total	λ=3	λ=5	Total	λ=3	λ=5	Total	λ=3	λ=5	(3)
		3	3	0	6	6	0	9	9	0	12	12	0	15	15	0	
M	1			-1			-3			-5			-7			(-2)	
n:5	# links	10			15			20			25			30			(+5)
	# joints	13			22			31			40			49			(+9)
	# loops	Total	λ=3	λ=5	Total	λ=3	λ=5	Total	λ=3	λ=5	Total	λ=3	λ=5	Total	λ=3	λ=5	(4)
		4	4	0	8	8	0	12	12	0	16	16	0	20	20	0	
M	1			-2			-5			-8			-11			(-3)	
n:6	# links	12			18			24			30			36			(+6)
	# joints	16			27			38			49			60			(+11)
	# loops	Total	λ=3	λ=5	Total	λ=3	λ=5	Total	λ=3	λ=5	Total	λ=3	λ=5	Total	λ=3	λ=5	(5)
		5	5	0	10	10	0	15	15	0	20	20	0	25	25	0	
M	1			-3			-7			-11			-15			(-4)	
n:7	# links	14			21			28			35			42			(+7)
	# joints	19			32			45			58			71			(+13)
	# loops	Total	λ=3	λ=5	Total	λ=3	λ=5	Total	λ=3	λ=5	Total	λ=3	λ=5	Total	λ=3	λ=5	(6)
		6	6	0	12	12	0	18	18	0	24	24	0	30	30	0	
M	1			-4			-9			-14			-19			(-5)	



Table 3.8. Single centered modified trapezoidal pattern mobility analysis with different number of segments and rows.

r:3 $\Omega$ :180 Semicircle $h < \text{MAX}$ Trapezoidal pattern -MODIFIED																	
# of segment	2 Row			3 Row			4 Row			5 Row			6 Row			increased by	
n:3	# links	6			9			12			15			18			(+3)
	# joints	7			11			16			20			25			(+4) to odd (+5) to even
	# loops	Total	$\lambda=3$	$\lambda=5$	Total	$\lambda=3$	$\lambda=5$	Total	$\lambda=3$	$\lambda=5$	Total	$\lambda=3$	$\lambda=5$	Total	$\lambda=3$	$\lambda=5$	(+1) to odd (+2) to even
	M	1			0			-1			-2			-3			(-1)
n:4	# links	8			12			16			20			24			(+4)
	# joints	9			15			21			27			33			(+6)
	# loops	Total	$\lambda=3$	$\lambda=5$	Total	$\lambda=3$	$\lambda=5$	Total	$\lambda=3$	$\lambda=5$	Total	$\lambda=3$	$\lambda=5$	Total	$\lambda=3$	$\lambda=5$	(+2)
	M	1			-1			-3			-5			-7			(-2)
n:5	# links	10			15			20			25			30			(+5)
	# joints	12			19			27			34			42			(+7) to odd (+8) to even
	# loops	Total	$\lambda=3$	$\lambda=5$	Total	$\lambda=3$	$\lambda=5$	Total	$\lambda=3$	$\lambda=5$	Total	$\lambda=3$	$\lambda=5$	Total	$\lambda=3$	$\lambda=5$	(+2) to odd (+3) to even
	M	1			0			-5			-8			-11			(-3)
n:6	# links	12			18			24			30			36			(+6)
	# joints	14			23			32			41			50			(+9)
	# loops	Total	$\lambda=3$	$\lambda=5$	Total	$\lambda=3$	$\lambda=5$	Total	$\lambda=3$	$\lambda=5$	Total	$\lambda=3$	$\lambda=5$	Total	$\lambda=3$	$\lambda=5$	(+3)
	M	1			-3			-7			-11			-15			(-4)
n:7	# links	14			21			28			35			42			(+7)
	# joints	17			27			38			48			59			(+10) to odd (+11) to even
	# loops	Total	$\lambda=3$	$\lambda=5$	Total	$\lambda=3$	$\lambda=5$	Total	$\lambda=3$	$\lambda=5$	Total	$\lambda=3$	$\lambda=5$	Total	$\lambda=3$	$\lambda=5$	(+3) to odd (+4) to even
	M	1			-4			-9			-14			-19			(-5)

### 3.1.4. Conclusion

For a designer it is fundamental to be able to manipulate all the parameters while designing. In this part of the study parameters for creating a single centered rigid origami foldable barrel vault has been presented. The parameters that can be defined by the designer are the radius,  $r$ , the number of segment,  $n$  which defines the approximation of the form, and the central angle  $\Omega$  which defines whether the cross-

section is a semicircle or horseshoe arch. These parameters defined, the designer can create an MV-Pattern based on the calculations presented on the geometrical properties. The designer can also control the foldable structure's movement using the calculations on both the geometrical properties and workspace analysis. There are limitations while creating the MV-Pattern; the height of the pattern  $h$  cannot surpass the calculated value, otherwise the diagonals created based on the fold angle,  $\alpha$  will crisscross, which will lead to a failed pattern. But the height of a single row  $h$  can be less than the calculated value creating a trapezoidal pattern instead of a triangular pattern. Height, span, and depth calculations are in relation with the inclination angle  $\sigma$  which facilitate the understanding of the motion of the rigid origami foldable barrel vault. The depth calculations do not differ if the number of segment  $n$  is an even or odd number, but the span and height calculations are different for each, which has been presented in the workspace analysis. Because the span and height calculations are based on the geometrical properties of the *pattern-generator* the calculation method do not change when the MV-Pattern is a triangular one or trapezoidal one. A calculation sheet has been prepared in Microsoft Excel 2013® to facilitate the calculations is presented in Appendix A. Mobility calculations present differences for a triangular pattern when the number of segments are even or odd. Trapezoidal patterns tear during the folding of the physical model which has been analyzed and results demonstrated that removing those specific joints did not change the mobility. For all three mobility calculation (tables 3.6, 3.7, and 3.8) a set of patterns and kinematic diagrams have been provided in Appendix B.

### **3.2. Double Centered Barrel Vaults**

Double centered arches are created by the intersection of two arcs' cross section. There are different types of double centered arches but in this study only the pointed equilateral, lancet, and obtuse arch types are analyzed. The difference between these arches is defined by the relation between the radii of the arcs  $r$  and the distance between centers of the arcs  $a$ .

In this section the final folded state of the double centered rigid origami barrel vault structure is analyzed first, then the geometrical properties of the partially folded

state. The section continues with a workspace analysis and finishes with mobility analyzes of the pattern created using the defined parameters.

### 3.2.1. Geometrical Properties

This section present the geometrical properties of double centered arches and the creation of a MV-Pattern using these parameters. Using the reverse engineering, first the final folded state of the pattern, followed by the partially folded state, and lastly the initial state is analyzed. Then the creation of an MV-Pattern is explained based on the presented parameters.

#### 3.2.1.1. Final Folded State

The creation of a double centered folded plate structure starts by defining three parameters: the distance between the centers of two arcs  $a$ , the radius  $r$ , and the number of segment  $n$  for a single arc. Figure 3.39 represents the parameters for all three types of double centered arches: (a) pointed equilateral arch, (b) lancet, and (c) obtuse arch. As the number of segments increases an approximation to the curved shaped of the arches is achieved, as it is for the single centered foldable barrel vaults.

Parameters required to create a double centered rigid origami barrel vault MV-Pattern are: length of *pattern-generator*  $s_t$ , folding angle  $\alpha$ , and the angle  $\lambda$ . First step to be able to create a crease pattern is to define the values of the parameters;  $a$  the distance between the center points,  $r$  the radius of arcs and  $n$  the number of segment for a single arc which in turn multiplied by 2 gives the total number of segments  $n_t$ . While defining theses parameters some properties of these arches need to be defined:

- If the required cross sectioned of the barrel vault is an equilateral arch:  $r = a$
- If the required cross sectioned of the barrel vault is an obtuse arch:  $r > a$
- If the required cross sectioned of the barrel vault is a lancet arch:  $(a/2) < r < a$ .

In case of the Lancet arch the radius  $r$  has higher and lower value limits depending on the distance between the two centers  $a$ . If the distance between the centers  $a$  is more than  $2r$  the arcs do not intersect thus no arch is created. The parameter  $b$  is the distance between  $r$  and  $a$ , it is required to calculate the distance between the edges of the pattern, and it is calculated using eq. (3.51).

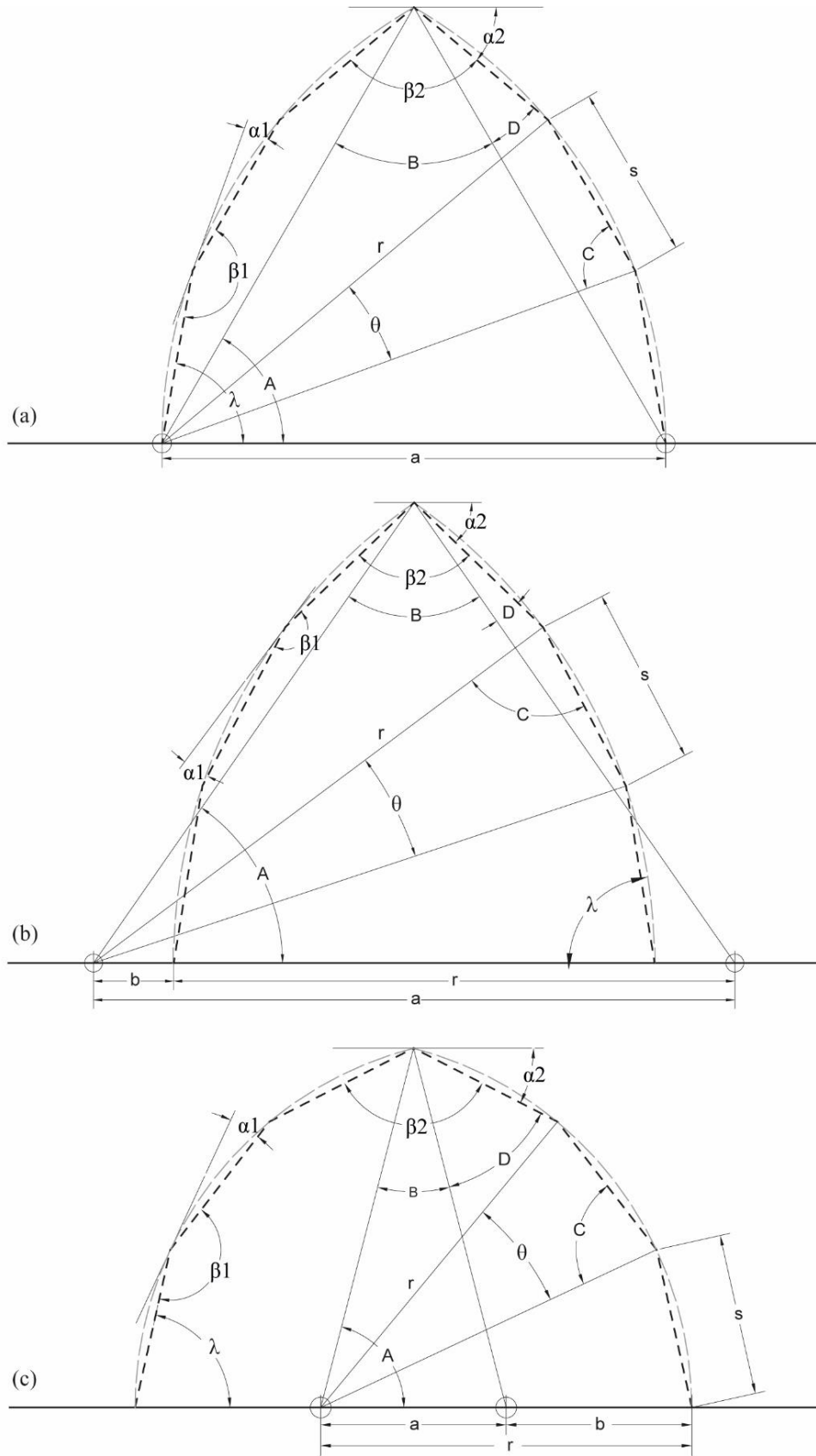


Figure 3.39. Parameters for (a) Pointed Equilateral arch, (b) Lancet arch, and (c) Obtuse arch. Bold dashed lines: *pattern-generators*.

$$b = |r - a| \quad (3.51)$$

After defining these three parameters, the first step to be able to calculate the other parameters is to calculate the angle  $\hat{A}$  using eq. (3.52).

$$\hat{A} = \cos^{-1}\left(\frac{a}{2r}\right) \quad (3.52)$$

Then the segments' angle  $\theta$  is calculated using the angle  $\hat{A}$  with eq. (3.53).

$$\theta = \frac{\hat{A}}{n} \quad (3.53)$$

The length of the segment  $s$  and the *pattern-generator's* length  $s_t$  is calculated using the same eqs. (3.2) and (3.3) as in the single centered arches calculations.

Angles  $\hat{B}$ ,  $\hat{C}$ , and  $\hat{D}$ , need to be calculated to be able to calculate the folding angles  $\alpha$  and interior angles  $\beta$  using the following equations:

$$\hat{B} = \pi - 2\hat{A} \quad (3.54)$$

$$\hat{C} = \left(\frac{\pi - \theta}{2}\right) \quad (3.55)$$

$$\hat{D} = \hat{C} - \hat{B} \quad (3.56)$$

The angle  $\hat{D}$ , in case of a lancet arch, can have a minus sign which means that the line between the center points and the apex is passing outside the *pattern-generator* line (Figure 3.40). In Figure 3.40(a) the angle  $\hat{D}$  has a positive value but in Figure 3.40(b) a negative one.

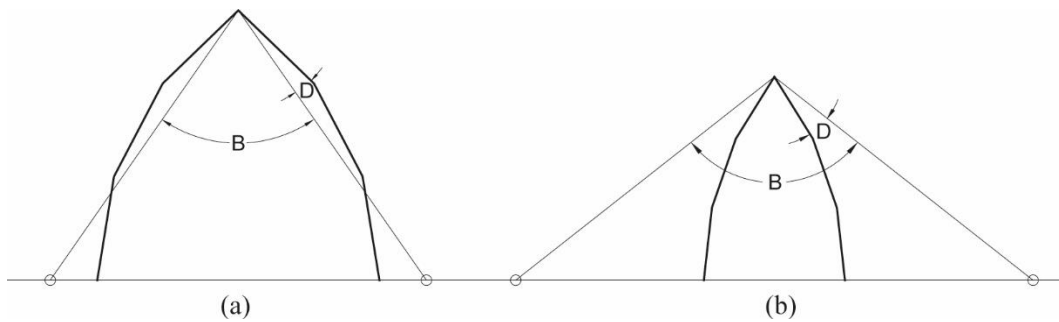


Figure 3.40. Different lancet arches.

If Figure 3.39 is analyzed in contrast to single centered arches there are two different interior angles  $\beta_1$  and  $\beta_2$ . The interior angle  $\beta_2$  is the angle of the apex, and the angle  $\beta_1$  is the other interior angle of the *pattern-generator*. The interior angles  $\beta_1$  and  $\beta_2$  are calculated using eqs. (3.57) and (3.58), respectively.

$$\beta_1 = 2\hat{C} \quad (3.57)$$

$$\beta_2 = \hat{B} + 2\hat{D} \quad (3.58)$$

Different interior angles signifies that there are two different folding angles corresponding to these angles calculated using eq. (3.59) for the folding angle  $\alpha_1$  and eq. (3.60) for the apex's folding angle  $\alpha_2$ .

$$\alpha_1 = \frac{\pi - \beta_1}{2} \quad (3.59)$$

$$\alpha_2 = \frac{\pi - \beta_2}{2} \quad (3.60)$$

The edge angle  $\lambda$  is equal to the angle  $\hat{C}$ .

$$\lambda = \hat{C} \quad (3.61)$$

And last values to be calculated are the half-row's height  $h$  and the total height of the row  $2h$ . Two different folding angles means two different half-row heights:  $h_1$  calculated with the folding angle  $\alpha_1$  (eq. (3.62)) and  $h_2$  calculated with the folding angle  $\alpha_2$  (eq. (3.63)).

$$h_1 = \tan\alpha_1 \left(\frac{s}{2}\right) \quad (3.62)$$

$$h_2 = \tan\alpha_2 \left(\frac{s}{2}\right) \quad (3.63)$$

Only one of the half-row height can be used for the crease pattern. The smallest value between  $h_1$  or  $h_2$  should be used if the bigger value is selected then the diagonal lines created by the smallest folding angle will crisscross within the height of the single row.

All the parameters required to draw a crease pattern has been demonstrated. Figure 3.41 demonstrates how parameters should be applied to draw a single row of a CP for a double centered foldable barrel vault.

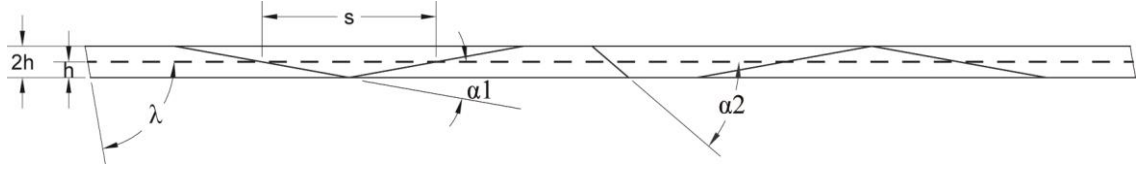


Figure 3.41. Single row crease pattern and the parameters for six segmented pointed equilateral arch.

### 3.2.1.2. Partially Folded State

The second step is the geometrical properties of the partially folded state of double centered foldable barrel vault. This section presents the relation between the parameters while the structure moves from the initial state to its final folded state. The geometrical relations between the folding angle  $\alpha$  and inclination angle  $\sigma$  with the bending angle  $\mu$  have been demonstrated on the previous section for both type of vertexes;  $v^4$  and  $v^6$  with eqs. (3.19) and (3.18). In double centered cross-section foldable barrel vault structures there are two different folding angles  $\alpha_1$  and  $\alpha_2$  which demand a modification to the previous equations.

For double centered cross-sectioned vaults the number of pattern-generator's vertexes are not equal to the number of vertexes of the pattern as it was in the single centered cross-sectioned vaults (Figure 3.41). Except from vertexes  $v_4$  and  $v_5$  all others are created using the folding angle  $\alpha_1$ . Only the vertexes  $v_2$  and  $v_7$  are degree-6 vertexes  $v^6$  and all other angles are degree-4 vertexes  $v^4$ .

The vertexes  $v_4^4$  and  $v_5^4$  are created using the folding angle  $\alpha_2$  because this type of arches are created using two arcs making an apex point on the general cross-section which is different from the regular cross-section of single centered barrel vaults.

Firstly the degree-4 vertex equations are presented by modifying eq. (3.19) with the correct folding angle parameters. The vertexes  $v_1^4$ ,  $v_3^4$ ,  $v_6^4$  and  $v_8^4$  are created using the folding angle  $\alpha_1$  thus the equation for these vertexes' bending angle  $\lambda'$  is:

$$\lambda' = \pi - 2 \tan^{-1}(\sin \sigma \cdot \tan \alpha_1) \quad (3.64)$$

The vertexes  $v_4^4$  and  $v_5^4$  are created using a different folding angle  $\alpha_2$ , thus their bending angle  $\mu_2$  is denoted differently in the following equation.

$$\mu_2 = \pi - 2 \tan^{-1}(\sin \sigma \cdot \tan \alpha_2) \quad (3.65)$$

Then the bending angle  $\mu_1$  for the vertexes  $v_2^6$  and  $v_7^6$  is:

$$\mu_1 = \pi - 4 \tan^{-1}(\sin \sigma \cdot \tan \alpha_1) \quad (3.66)$$

As it can be observed in the Figure 3.42 the apex is constituted by two vertexes  $v_4^4$  and  $v_5^4$ , this condition do not changes when the number of segment  $n$  changes because the cross-section is constituted by two arcs. When the segment number  $n$  is increased or decreased only the number of  $v^6$  changes, the geometrical properties of  $v^4$  do not changes. The apex will always be surrounded by four  $v^4$ , the closest ones, in this example (Figure 3.42)  $v_4^4$  and  $v_5^4$ , are created using the folding angle  $\alpha_2$  and the other two,  $v_3^4$  and  $v_6^4$ , are created using folding angle  $\alpha_1$ . And the first and last angles will always be  $v^4$ , so when the number of segment increases only the number of  $v^6$  will increase.

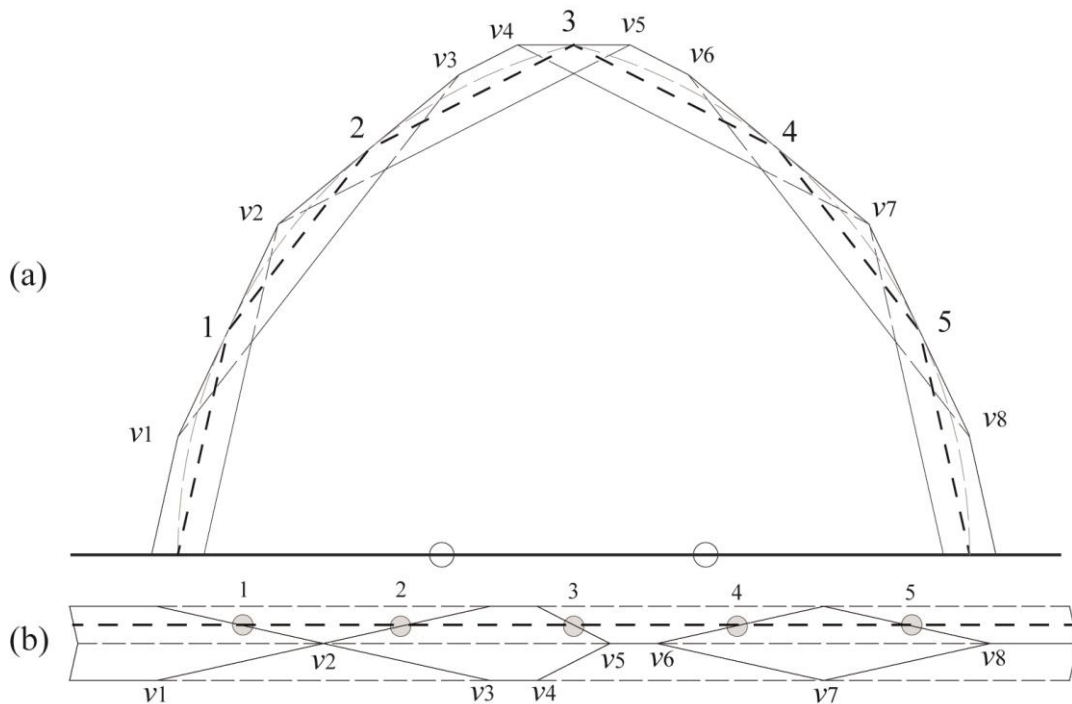


Figure 3.42. (a) Elevation and (b) MV-Pattern of a six segmented obtuse arch, created using maximum value of  $h_1$ .



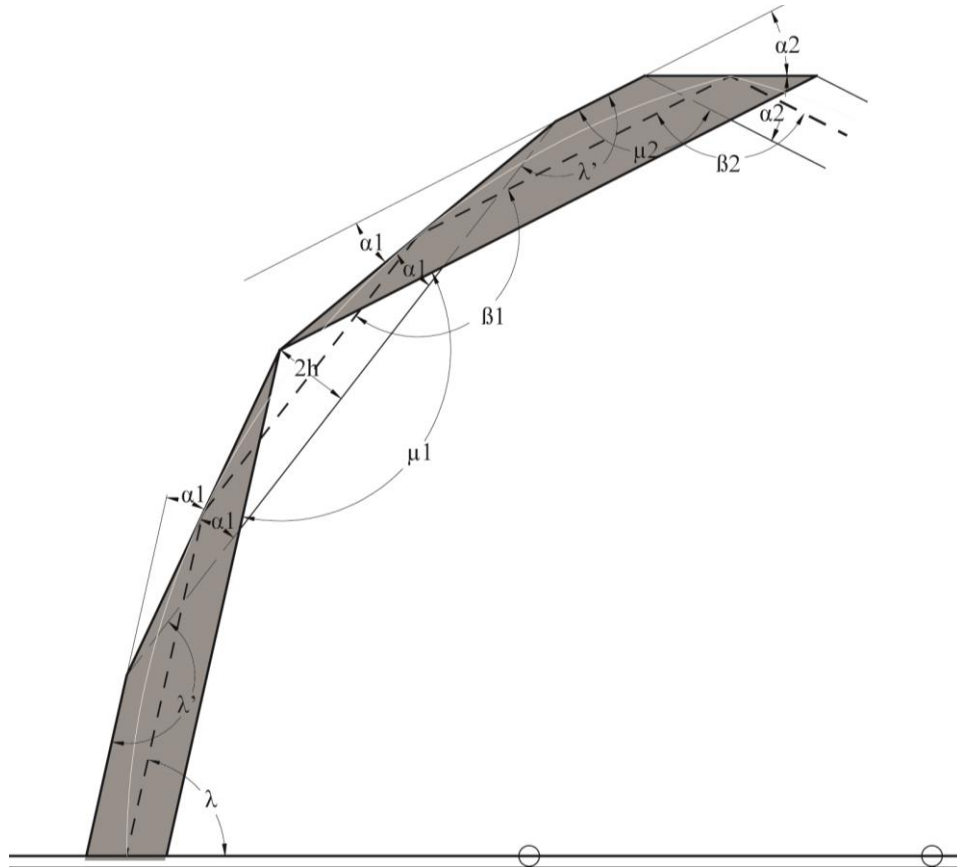


Figure 3.43. Vertexes  $v_1^4$ ,  $v_2^6$ ,  $v_3^4$  and  $v_4^4$ 's parameters.

The relation of these three different bending angles with the inclination angle  $\sigma$  and dihedral angle  $\varphi$  do not differs. The maximum and minimum values for these bending angles can be observed in Table 3.9.

Table 3.9. Maximum and minimum values of the angles  $\mu_1$ ,  $\mu_2$ ,  $\lambda'$ ,  $\varphi$ , and  $\sigma$ .

angles	Initial state (min)	Final folded state (max)
$\mu_1$ ( $v^6$ bending angle)	$\pi$	$\pi - 4\alpha_1$
$\mu_2$ ( $v^4$ bending angle)	$\pi$	$\pi - 2\alpha_2$
$\lambda'$ ( $v^4$ bending angle)	$\pi$	$\pi - 2\alpha_1$
$\varphi$ (dihedral angle)	$\pi$	0
$\sigma$ (inclination angle)	0	$\pi/2$

Figure 3.44 shows the relation between the inclination angle and all bending angles for an obtuse arch with 6 segments, a radius of 3 m, and a distance between the centers  $a$  equal to 2 m. As the inclination angle increases the bending angles decreases to reach their final folded state.

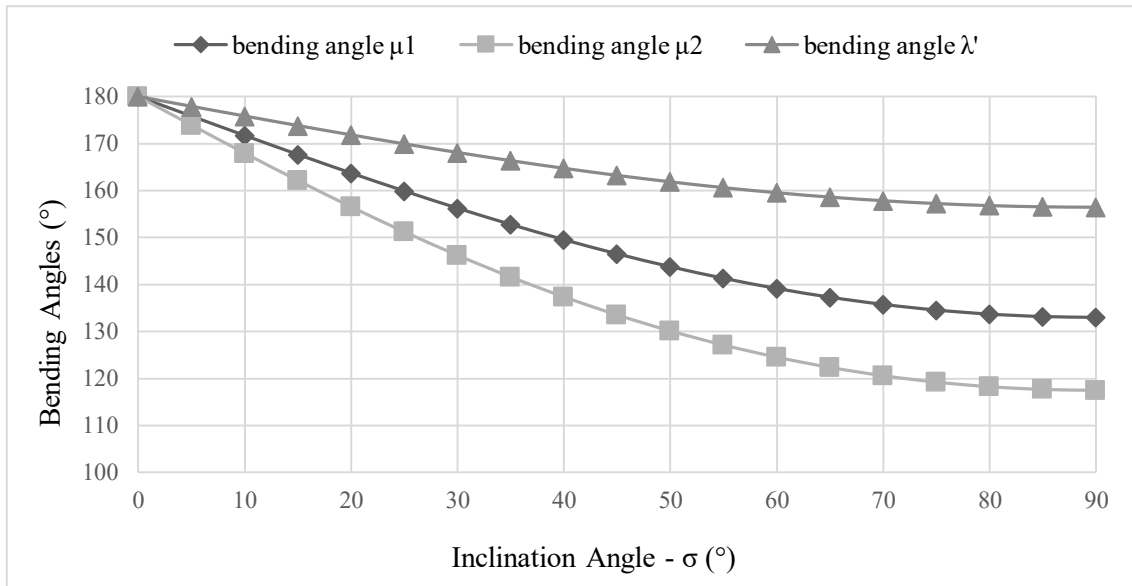


Figure 3.44. Relation between bending angles and inclination angle  $\sigma$  for a  $n_T: 6$   $r: 3$   $a: 2$  obtuse arch.

### 3.2.1.3. Initial State, MV-Pattern

In this step a single row of CP will be created using the calculated parameters presented in the previous steps. The required parameters to draw a single chain for a double centered cross-sectioned barrel vault are the angle  $\alpha_1$  and  $\alpha_2$ , the radius,  $r$  and  $a$  the distance between the two centers. Table 3.10 shows all the parameters calculated in the previous step for all three different types of double centered arches.

First the pattern-generator is drawn based on the parameter  $s_T$ , then two parallel lines A and B (Figure 3.45) are drawn to both side in a calculated equal distance  $h$ . In contrast to single centered arches, the double centered arches have two different height parameters  $h_1$  and  $h_2$  because there are two different folding angles  $\alpha_1$  and  $\alpha_2$ . As explained on the previous step, the smallest value out of  $h_1$  and  $h_2$  need to be used so that there are no crisscrossing diagonal lines. The lowest value of half-row height also means the lowest value out of folding angles  $\alpha_1$  and  $\alpha_2$  because the parameters  $h$  is dependable on the folding angle. Analyzing Table 3.10 it can be observed that the lowest half-row value is  $h_1$ . The row height  $2h$  required to create the CP is the value of  $h_1$  multiplied by 2. As it was with the single centered barrel vaults, the use of the maximum value of  $2h_1$  creates a triangular pattern and if a lesser value is used the CP becomes a trapezoidal pattern.

Table 3.10. Parameters for Obtuse, Pointed Equilateral, and Lancet arches.

	$r$ (m)	$a$ (m)	$n$	$\theta^\circ$	$s$ (m)	$s_t$ (m)	$\hat{A}^\circ$
Obtuse	3	2	3	23,51	1,222	7,33	70,52
Equilateral	3	3	3	20	1,047	6,25	60
Lancet	3	4	3	16,06	0,838	5,02	48,18
	$\hat{B}^\circ$	$\hat{C}^\circ$	$\hat{D}^\circ$	$\beta_1^\circ$	$\beta_2^\circ$	$\alpha_1^\circ$	$\alpha_2^\circ$
Obtuse	38,94	78,24	39,30	156,49	117,54	11,75	31,22
Equilateral	60	80	20	160	100	10	40
Lancet	83,62	81,96	-1,65	163,93	80,31	8,03	49,84
	$\lambda^\circ$	$b$ (m)	$h_1$ (m)	$h_2$ (m)	$2h$ (m)	$n_T$	
Obtuse	78,24	1	0,127	0,370	0,254	6	
Equilateral	80	0	0,091	0,437	0,183	6	
Lancet	81,96	1	0,059	0,496	0,118	6	

The first two diagonals [1 and 2] are placed on the intersection points of the pattern-generator using the value of the folding angle  $\alpha_1$ . Then the 3<sup>rd</sup> diagonal is placed using the folding angle  $\alpha_2$ , then the following two lines [4 and 5] are placed. All five diagonals should be on opposite directions to each other to be able to create a convex form when the CP is folded (Figure 3.45). Lastly the edge diagonals are placed using the edge angle  $\lambda$  parameter given by eq. (3.61).

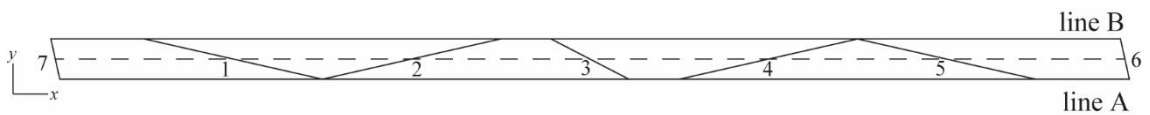


Figure 3.45. Unfolded crease pattern for the six segmented obtuse arch.

The creation of the pattern from a row is done by simple congruence transformation, reflection by line B which creates the first double row, then the double row is translated as many times as needed in  $y$ -direction (Figures 3.46 and 3.47).

The created CP need an MV-Assignment which will turn it into a MV-Pattern. The MV-Assignment is done by following Maekawa's theorem. For both Figures 3.46 and 3.47 the full lines are mountain folds and the dashed lines are valley folds.

The triangular pattern (Figure 3.46) created using the maximum value of  $2h_1$  have a variety of vertexes because of the use of different folding angles on its creation due to the geometrical shape selected as a cross-section. There are 8 vertexes: two are  $v^6$

and six are  $v^4$ . The number of  $v^4$  do not changes as the number of segment increases, only the number of  $v^6$  increases, as it was in the triangular pattern of a single circled barrel vault pattern.

Table 3.11. Number of vertexes on triangular patterns.

$n_T$	$v^4$	$v^6$	$v$ total
4	6	0	6
6	6	2	8
8	6	4	10
10	6	6	12

As it can be observed the number of segments  $n_T$  is always an even number because the division of segment  $n$  is done to only one of the arc then the number is multiplied by 2 to calculate the segment number  $n_T$  for the whole cross-section. The designer should take this property into account while deciding the segment number  $n$ .

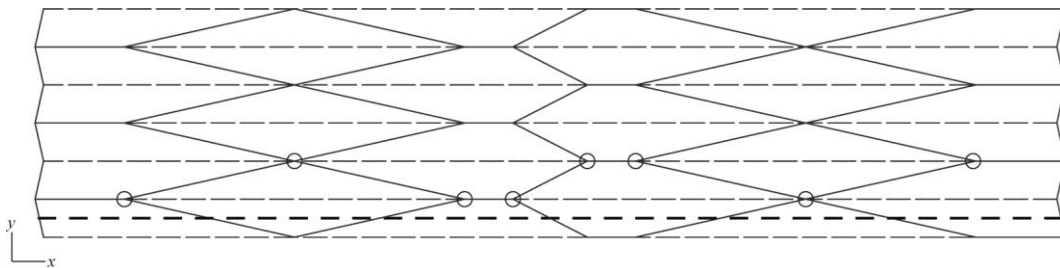


Figure 3.46. MV-Pattern created by using maximum value of  $h$  for a  $n_T$ : 6, obtuse arch. Triangular pattern.

As it was with the single centered barrel vaults, the use of the maximum value of  $2h_1$  creates a triangular pattern and if a lesser value is used the CP becomes a trapezoidal pattern. The trapezoidal pattern (Figure 3.47) has been created using a lower value than the maximum value resulting only in  $v^4$  type vertexes (Table 3.12), as it was for the single centered trapezoidal pattern.

Table 3.12. Number of vertexes on trapezoidal patterns.

$n$	$v^4$	$v^6$	$v$ total
4	6	0	6
6	8	0	8
8	10	0	10
10	12	0	12

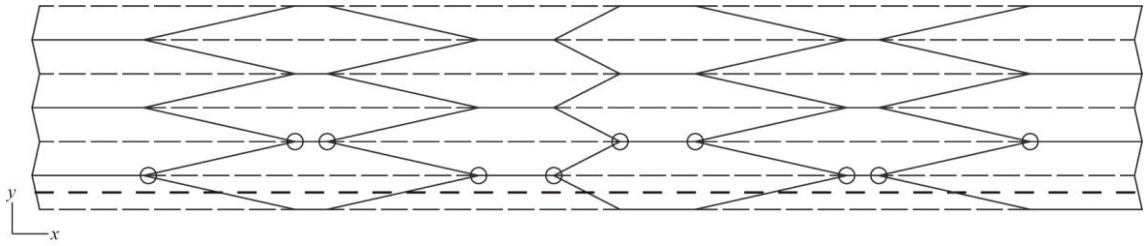


Figure 3.47. MV-Pattern created by using value of  $h$  as 0,08 m for a  $n_T$ : 6, obtuse arch. Triangular pattern.

### 3.2.1.4. Conclusion

In this section the limitations used while creating a double centered barrel vault have been discussed. As it is for the single centered barrel vault structures, some parameters need to be specified by the designer for the double centered barrel vaults. These parameters are the radius  $r$ , the distance between the two center points,  $a$ , of the arc constituting the cross-section, and the number of segments  $n$ . The number of segment  $n$  is the number of segments for only one of the arc, the value then is multiplied by two to obtain the total number of segment  $n_T$ . The properties of these parameters have been discussed alongside the rigid foldability of the patterns created using the method of creation. The rigid foldability of the created MV-Pattern has been tested on both Rigid Origami Simulator and Freeform Origami softwares created by Tachi (Tachi, 2009a; Tachi, 2009c).

The process of transforming a CP into a MV-Pattern do not change between the double centered barrel vault types: pointed equilateral, lancet and obtuse.

As it is in the single centered barrel vaults, if the structure needs to have a temporary stop point within the folding process the inclination angle  $\sigma$  can be specified which will give the height, span, and depth of the desired point. The edge angle  $\lambda$  need to be recalculated for this specific point, which is explained in the following section.

Radius and the distance between centers: Whether the cross-section is a pointed equilateral arch, a lancet arch or an obtuse arch depends on the values attributed to the parameters  $r$ , radius and  $a$ , the distance between the two centers. The relations between these two parameters are listed below.

For an equilateral arch:  $r = a$

For an obtuse arch:  $r > a$

For a lancet arch:  $(a/2) < r < a$ .

If the value attributed to  $r$  is more than  $2a$  the arcs will not intersect, thus no cross-section will be created. It has been observed that as the distance between the centers increases the folding angle  $\alpha_1$  becomes more acute, which decreases the height of a single row.

Height of a single row: The double centered vaults possess two different half-row heights,  $h_1$  and  $h_2$  because of the geometry of the cross-section creating two different folding angle  $\alpha_1$  and  $\alpha_2$ . The smallest value between the two heights need to be selected to be able to calculate the single row height  $2h$ . Calculations showed that the smallest value is always  $h_1$  because the apex interior angle  $\beta_2$  is more acute than the interior angle  $\beta_1$  resulting in a bigger folding angle  $\alpha_2$  than the folding angle  $\alpha_1$  which in return result in a higher height value  $h_2$ . To use the higher half-row value  $h_2$  will result in the crisscrossing of the diagonal lines created using the folding angle  $\alpha_1$ . Using the maximum value of  $2h_1$  as the single row's height will result in a triangular pattern, while the use of a smaller value than  $2h_1$  will result in a trapezoidal pattern.

Specific angle: The angle  $\hat{D}$  can have negative/minus sign: this is because the lancet arch's radius lines from the centers to the apex are outside the pattern itself as it can be observed in Figure 3.40.

All arch types' trapezoidal and triangular MV-Patterns' rigid foldability have been tested on Rigid Origami Simulator (Tachi, 2009c), all patterns created have folded without problems. Same patterns have been tested on the Freeform Origami software (Tachi, 2009a) in this software while all pattern flat-folded without deformation, the software suggested additional creases to the pattern created, which can be observed on Figures 3.48 and 3.49 as gray lines.

When the suggested grey lines are applied to the triangular MV-Pattern the pattern become composed of  $v^6$ , as it can be observed in the figure 3.50 while the dimensions do not change the edge form change both in form and geometry.

Both trapezoidal and triangular MV-Patterns are developable and flat-foldable if the medium surface is assumed to have no thickness. Models using thick cardboard have been created to be able to understand the changes suggested by the Freeform Origami software. Models have showed that  $v^4$  do not flat folds without tearing the material while the  $v^6$  folds flat without resistance with axis-shift method (Figures 3.51)

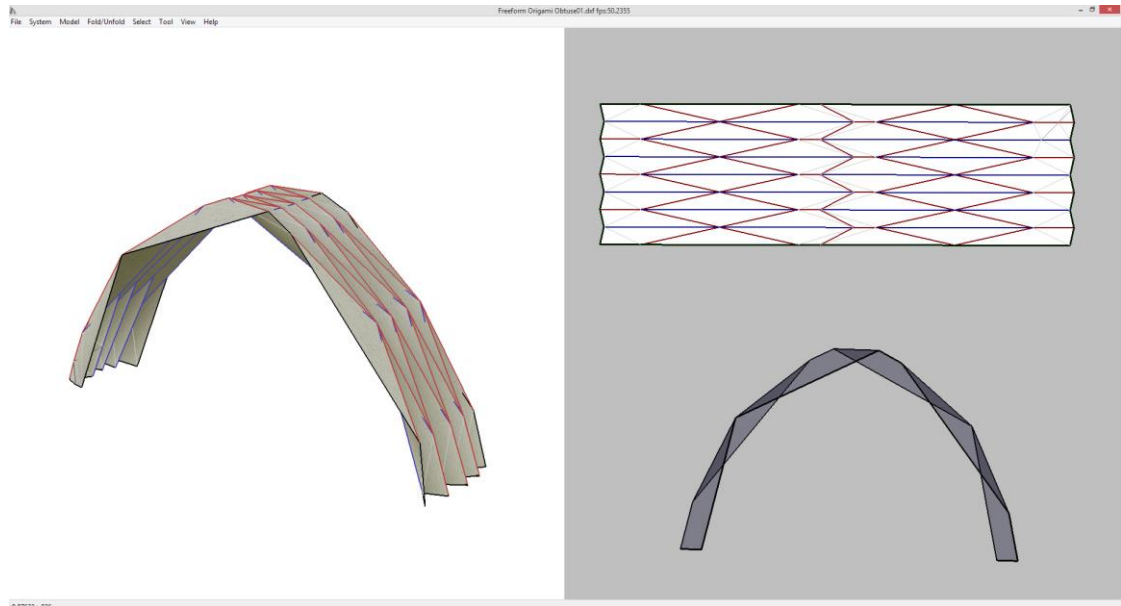


Figure 3.48. Triangular pattern rigid origami obtuse barrel vault tested on Freeform-Origami software (Tachi, 2009a).

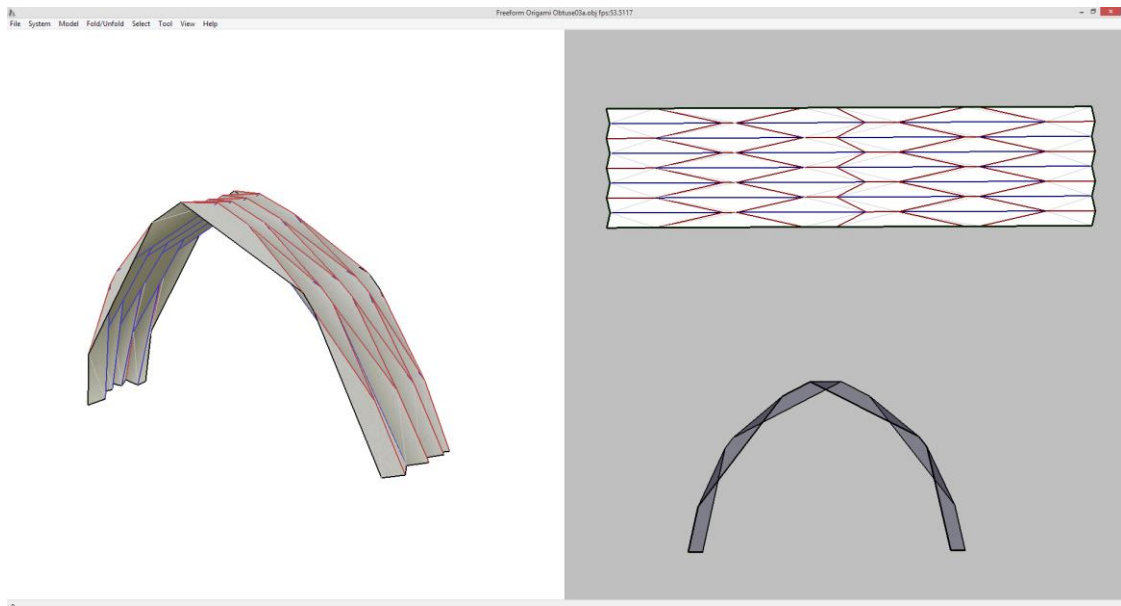


Figure 3.49. Trapezoidal pattern rigid origami obtuse barrel vault tested on Freeform-Origami software (Tachi, 2009a).

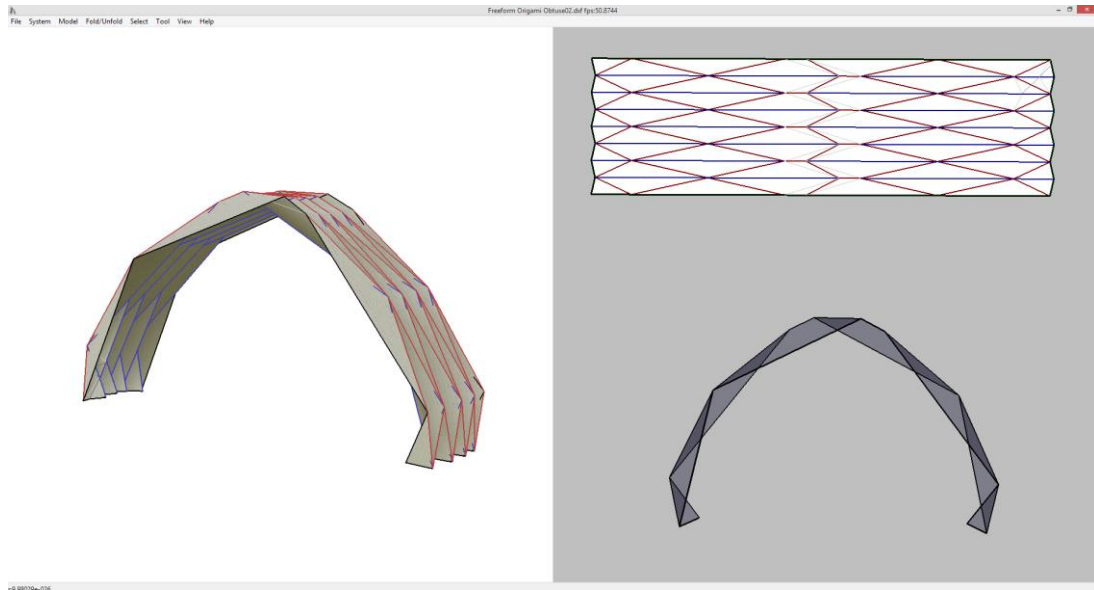


Figure 3.50. Rearranged triangular pattern rigid origami obtuse barrel vault tested on Freeform-Origami software (Tachi, 2009a).

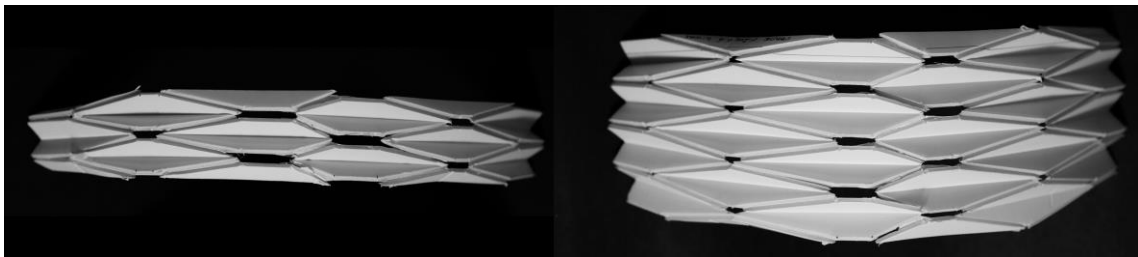


Figure 3.51. Model of trapezoidal pattern (left) and triangular pattern (right) for an obtuse barrel vault.

### 3.2.2. Workspace Analysis

The workspace analysis for double centered rigid origami barrel vault is first carried out by analyzing the geometrical properties of the depth and then by the analysis of the span, height, and volume based on the cross-section. Translational and rotational motions were observed in all types of arches while folding. While the structure takes its final folded state its depth and span decreases, but the height increases, as it is with the single centered structures.



### 3.2.2.1. Depth

The same geometrical relation exists between the properties of the double centered barrel vault and the single centered barrel vault, so eq. (3.29) for the depth calculation can be used with a small modification for these mechanism. As stated before the double centered mechanisms have two different folding angles  $\alpha_1$  and  $\alpha_2$  resulting in two different single row height  $h$ . So, as it was in the previous calculations the lowest value of single row's height should be used, which is  $h_1$ . This modification has been added to eq. (3.29) to calculate the depth of the double centered barrel vaults (eq. (3.67)).

$$TD_l = 2h_1 \cdot \cos \sigma \cdot R_n \quad (3.67)$$

The depth depend on the number of row  $R_n$  the design requires, the single row's height  $h_1$ , and the inclination angle  $\sigma$ . As the inclination angle increases the depth decreases as it can be observed in figure 3.52. Figure 3.52 has been created for a double centered lancet arch with  $r$ : 3 m,  $n$ : 3,  $a$ :4 m,  $2h_1$ : 0,118 m, and 10 rows.

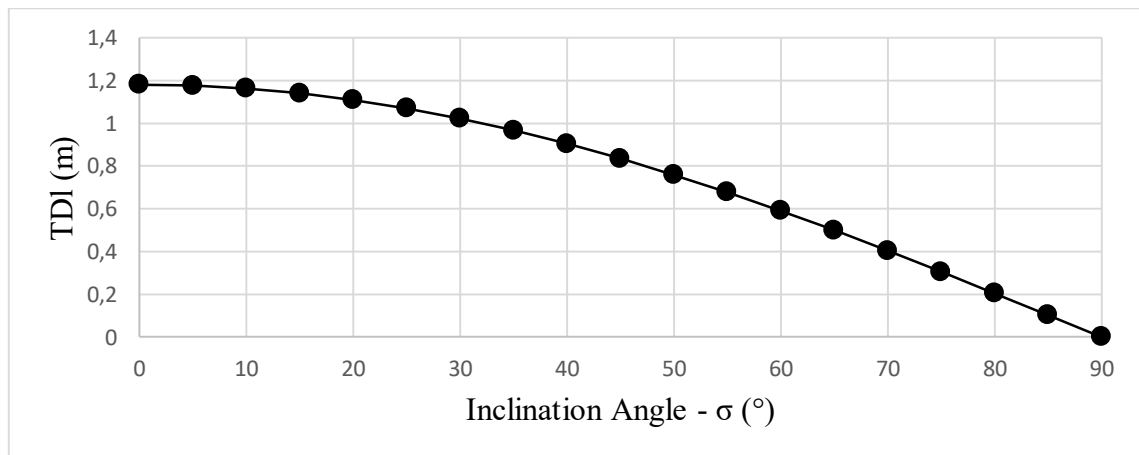


Figure 3.52. Relation between the inclination angles  $\sigma$  and the total depth,  $TD_l$  of a 10 row double centered barrel vault pattern.

### 3.2.2.2. Span and Height

The span and height are affected by the cross-section of the type of arch. The span and height calculation are created by analyzing the geometrical properties of the *pattern-generator* to understand parameters related to the deployment process. In double centered

arches, as it was in the single centered arches, the *pattern-generator*'s apex is considered fixed for the calculations. As the MV-Pattern folds from its initial state where inclination angle  $\sigma$  is equal to 0 (zero) to its final folded state where the inclination angle  $\sigma$  is equal to  $90^\circ$ , the span and height changes in relation to this angle. In Figure 3.53 all types of arches pattern-generators have been demonstrated, with inclination angle values of  $0^\circ$ ,  $10^\circ$ ,  $30^\circ$ ,  $50^\circ$ ,  $70^\circ$ ,  $90^\circ$ , and the placement of each center during the folding motion.

In Figure 3.54 parameters valid for all types of double centered arches can be observed on the drawing of the obtuse arch. The *pattern-generator* noted as **1** is the final folded state, and the *pattern-generator* noted as **2** is its position when the inclination angle is equal to  $30^\circ$ .

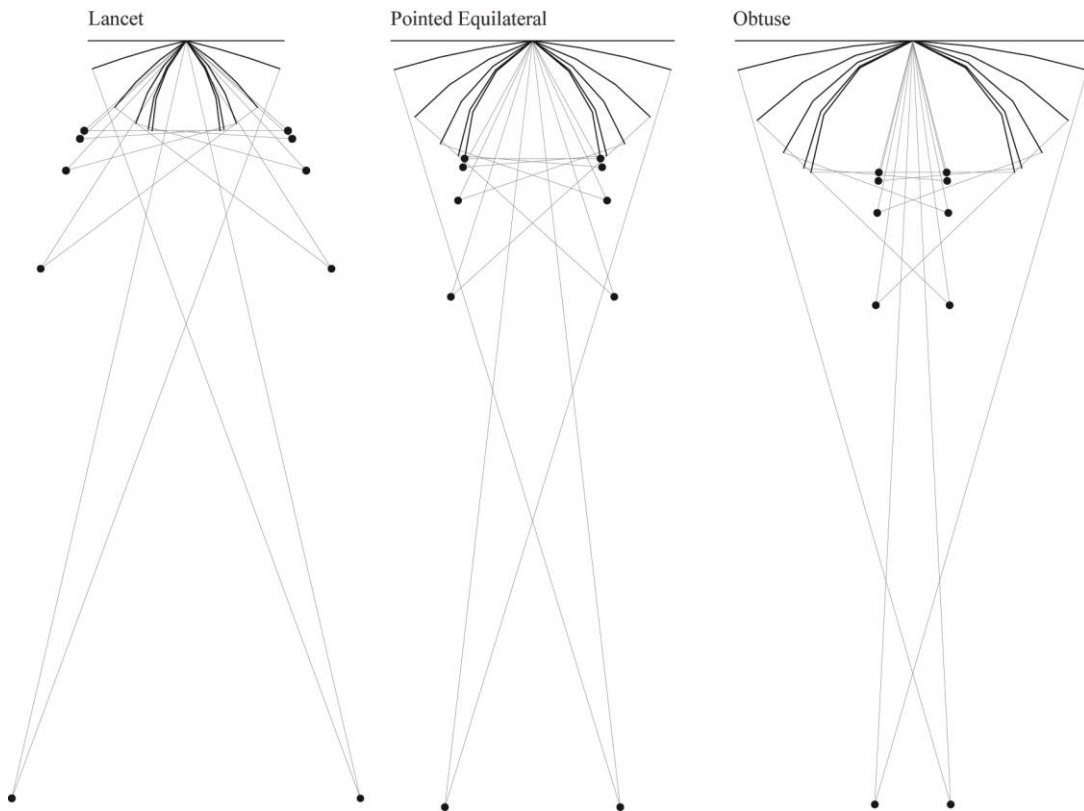


Figure 3.53. Lancet, Pointed equilateral and Obtuse arches' development with  $n:3$  and  $n:6$ .

To be able to calculate the height  $H$  and span  $S$  the segments' angles  $\theta$  and  $\delta$  values need to be in relation with the inclination angle  $\sigma$ . The relation of the angle  $\delta$  with the inclination angle  $\sigma$  has already been explained in eq. (3.17). In double centered arches, as explained in the previous section, there are two types of folding angles  $\alpha_1$  and  $\alpha_2$  which created two different projected angle  $\delta_1$  and  $\delta_2$  which are defined by the following equations respectively:

$$\delta_1 = \tan^{-1}(\sin \sigma \cdot \tan \alpha_1) \quad (3.68)$$

$$\delta_2 = \tan^{-1}(\sin \sigma \cdot \tan \alpha_2) \quad (3.69)$$

Because both the span and height calculations are done using the *pattern-generator*, the required angles to be able to calculate the segments' angle  $\theta$  are the interior angles  $\beta_{1d}$  and  $\beta_{2d}$ . The relation of the interior angles with the inclination angle  $\sigma$  is achieved by the following equations:

$$\beta_{1d} = \pi - 2\delta_1 \quad (3.70)$$

$$\beta_{2d} = \pi - 2\delta_2 \quad (3.71)$$

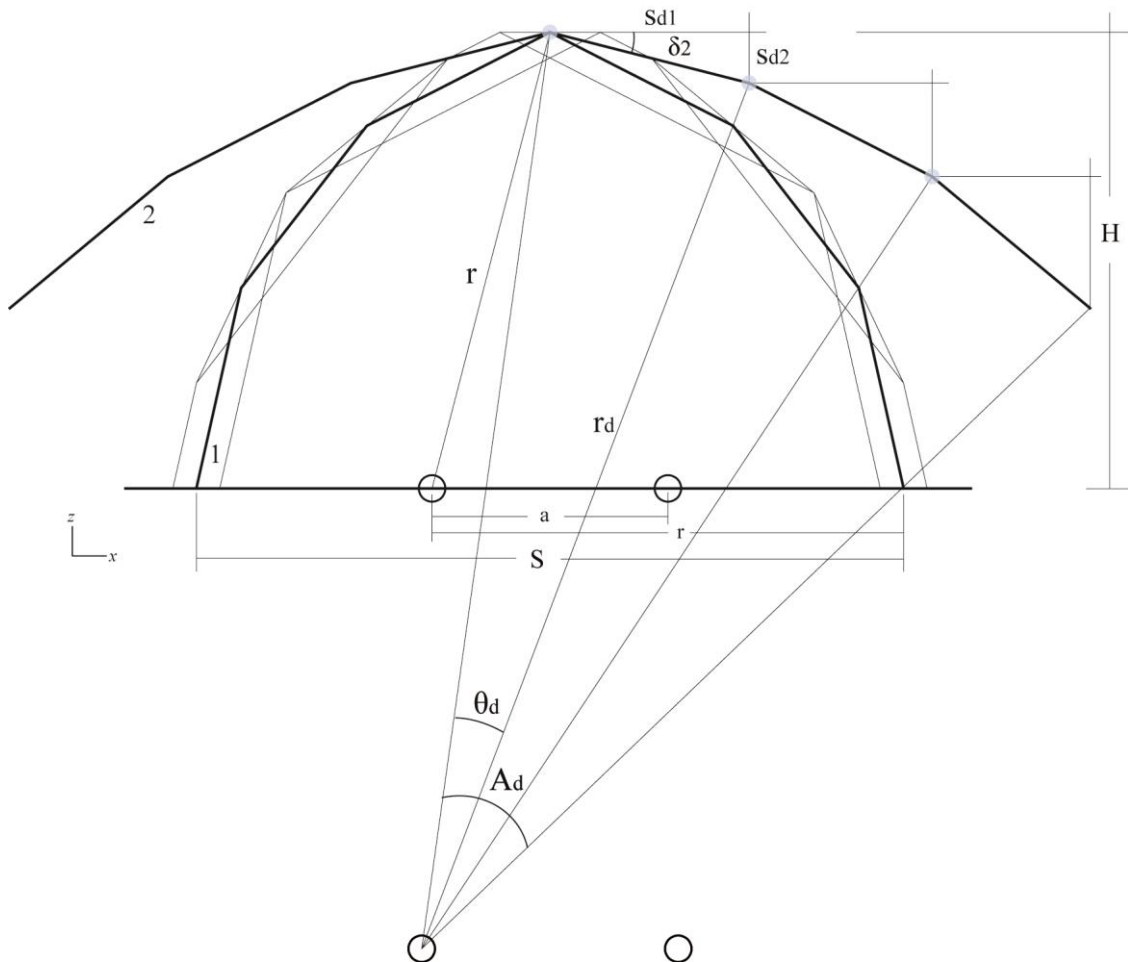


Figure 3.54: Parameters for Obtuse arch's pattern-generator with  $n:3$  and  $n_T:6$ .

The segments' angle that is changing during the deployment is subscripted as  $\theta_d$  representing the value of the angle during the folding process. The segments' angle is calculated using the following equation:

$$\theta_d = \pi - 2 \left( \frac{\beta_{1d}}{2} \right) = \pi - \beta_{1d} \quad (3.72)$$

If eq. (3.70) is substituted in eq. (3.72) the value of the segment's angle during the deployment process  $\theta_d$  can be put in relation with the projected angle  $\delta_I$  (eq. (3.73)).

$$\theta_d = \pi - (\pi - 2\delta_1) = 2\delta_1 \quad (3.73)$$

Span: The span is calculated by adding each segment's length projected to the x-axis  $s_{d1}$  to each other starting from the apex; it is calculated by eq.(3.74).

$$s_{d1} = s \cdot \cos(\delta_2 + i\theta_d) \quad (3.74)$$

The span is calculated with eq. (3.75) because the calculations are done starting from the apex to calculate the total span the sum of the projected segment's length is multiplied by 2.

$$S = 2s(\sum_{i=0}^{n-1} \cos(\delta_2 + i\theta_d)) \quad (3.75)$$

As the inclination angle  $\sigma$  decreases the span  $S$  increases as it can be observed in Figure 3.55.

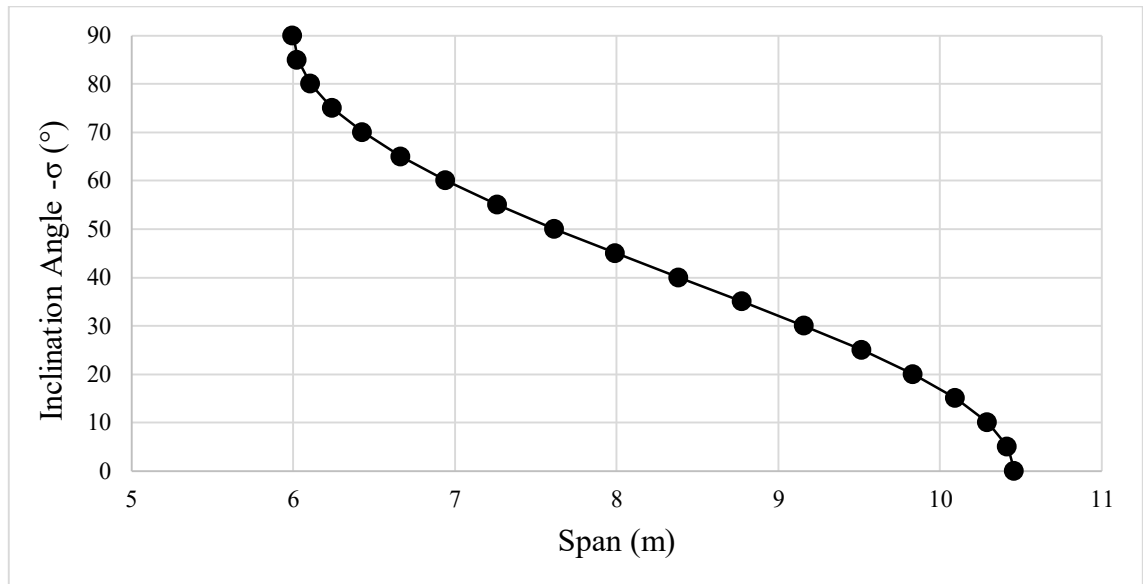


Figure 3.55. Relation between the inclination angle  $\sigma$  and the span  $S$  of an obtuse arch  $r$ : 4 m,  $a$ : 2 m, and  $n$ : 3.

Height: the height  $H$  is calculated with the same method as the span (eq. (3.77)); by adding segment's length  $s_{d2}$  projected to the z-axis (eq. (3.76)).

$$s_{d2} = s \cdot \sin(\delta_2 + i\theta_d) \quad (3.76)$$

$$H = s(\sum_{i=0}^{n-1} \sin(\delta_2 + i\theta_d)) \quad (3.77)$$

Where  $i$  is a series of number starting from 0 till  $(n-1) - n$  as the number of segments. Figure 3.56 shows that as the inclination angle  $\sigma$  increases so does the height  $H$  of the structure.

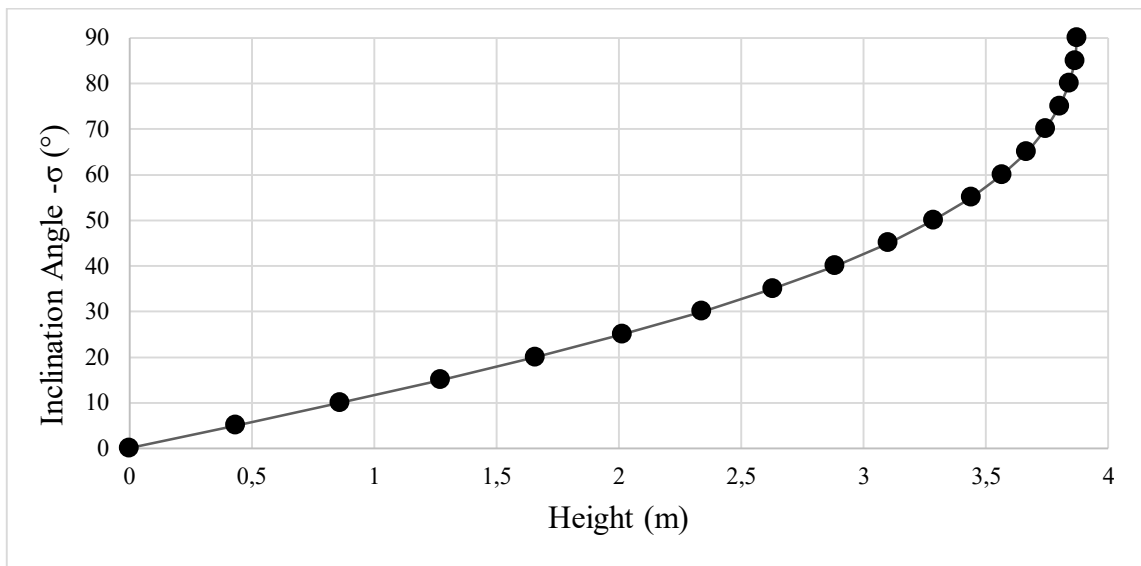


Figure 3.56. Relation between the inclination angle  $\sigma$  and the height  $H$  of an obtuse arch  $r$ : 4 m,  $a$ : 2 m, and  $n$ : 3.

### 3.2.2.3. Volume

The volume is calculated with the same method used in single centered arches; by multiplying the depth  $TD_i$  with the cross-section area  $A$ . The cross-section area is calculated by adding two segments' areas to area of the triangle created between the apex and the edges of the pattern-generator. The area are showed in Figure 3.57. The area of the triangle  $A_T$  is calculated with eq. (3.78) where the parameters height  $H$  (eq. (3.77)) and span  $S$  (eq. (3.75)) are used.

$$A_T = \frac{S \cdot H}{2} \quad (3.78)$$

The segment area is calculated using the parameters radius  $r_d$  and angle  $\widehat{A}_d$  which are the values during the deployment process. The angle  $\widehat{A}_d$  is obtained by multiplying the deployment process segment's angle  $\theta_d$  with the number of segments  $n$  (eq.(3.79)).

$$A_d = n \cdot \theta_d \quad (3.79)$$

$$r_d = \frac{s}{2 \sin\left(\frac{\theta_d}{2}\right)} \quad (3.80)$$

Eq. 3.80 calculates the radius during the development process, it is the same equation as eq. (3.40) presented in the single centered barrel vault development radius.

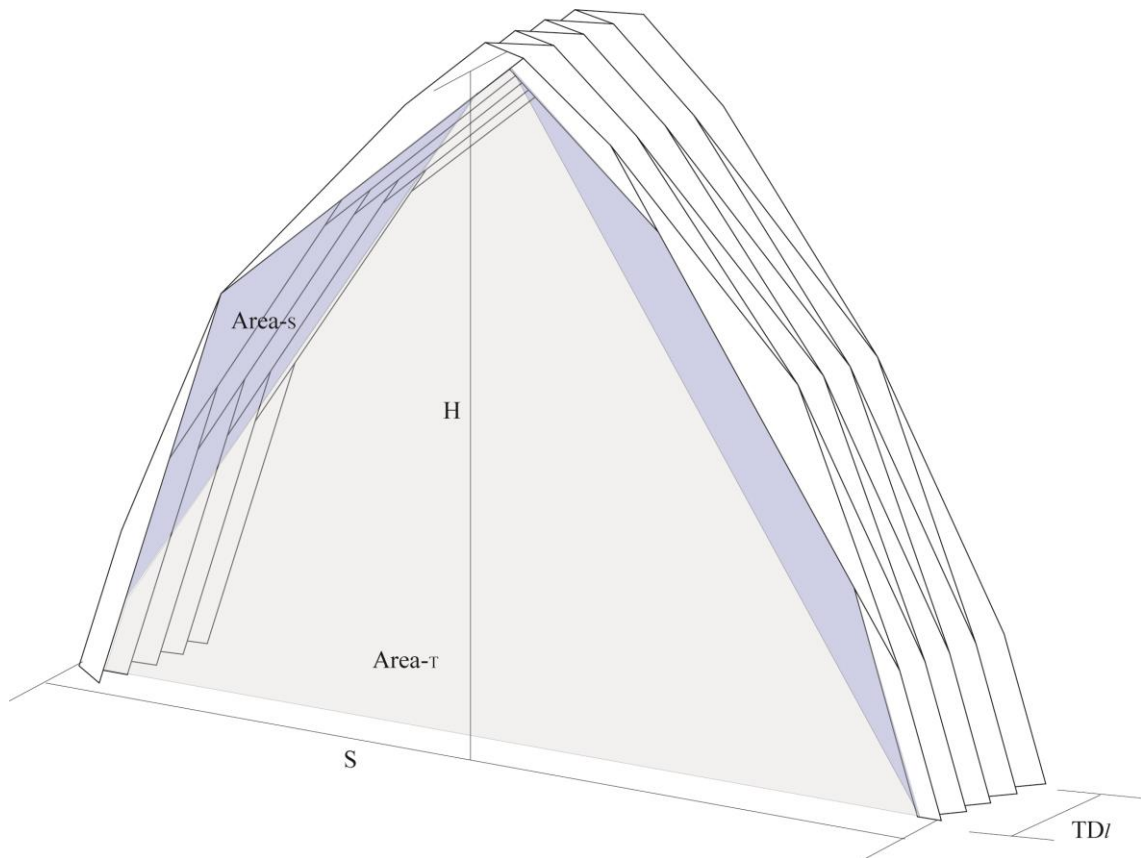


Figure 3.57. Double centered barrel vaults' volume parameters.

The segments' area  $A_s$  is calculated using the previous two parameters; eq. (3.81):

$$A_s = \frac{1}{2} r_d^2 (A_d - \sin(A_d)) \quad (3.81)$$

The cross-section area is calculated using the following equation where the triangle's area  $A_T$  is added to the sector area  $A_S$ , which is multiplied by two because there are two arcs thus two sectors.

$$A = \frac{S \cdot H}{2} + 2 \left( \frac{1}{2} r_d^2 (A_d - \sin(A_d)) \right) = \frac{(S \cdot H) + 2r_d^2(A_d - \sin(A_d))}{2} \quad (3.82)$$

The volume is calculated by multiplying the depth (eq. (3.67)) with the cross-section area (eq. (3.82)).

$$V = TD_l \cdot Area \quad (3.83)$$

A calculation sheet has been prepared in Microsoft Excel 2013® for all the parameters in both geometrical analysis and workspace analysis sections (Appendix C).

Figure 3.58 represent the volume of an obtuse arch with  $n:3$   $r:4m$  and  $a:2m$  created with the volume equation (eq. (3.83)). As it can be observed the volume has a rapid increase till it reaches its peak around the  $35^\circ$  of inclination angle, then it slowly decreases to its final folded state, as it was in the single centered arches' volume calculations.

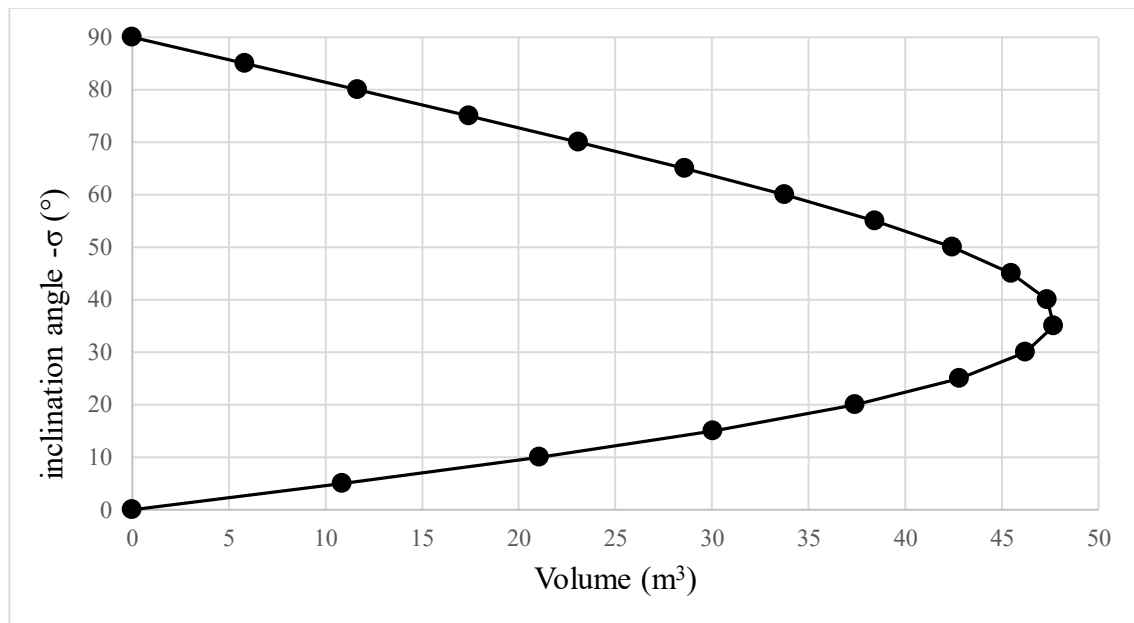


Figure 3.58. Relation between the inclination angle  $\sigma$  and the volume  $V$  of an obtuse arch  $r: 4$  m,  $a: 2$  m, and  $n: 3$ .

### 3.2.3. Mobility Analysis

This section analyses the mobility of double centered arch types using the same method used in single centered arch types. The CP of different types of arches have the same properties, so this analysis is conducted on only one type of arch's CP. The analysis starts with a double row of a six segmented obtuse arch CP, because the pattern's segment number  $n$  is defined for only one arc composing the arch, and since the defined number is multiplied by 2 to have the total number of segment  $n_T$ , it creates a CP with always an even numbered segments, thus no difference occurs to the mobility when  $n$  increases as it existed in the single centered arch's CP. Since the CP can grow in a single direction the analysis will be conducted by adding 1 row to the previous one starting from a double row. Firstly, triangular patterns and their modified versions, and then trapezoidal patterns and their modified versions will be presented.

The CP is analyzed first by calculating the number of independent loops using the Euler's equation (eq.(3.47)), then their mobility is calculated using the modified version of the Freudenstein and Alizade's mobility equation (eq.(3.49)), and finally the mobility is verified by the properties of structural groups.

#### 3.2.3.1. Triangular Patterns

In this section the mobility analysis is conducted for a triangular pattern (h: max) with 6 segments. The analysis starts with a double row CP analysis followed by an attempt on modifying the pattern by removing joints based on the tears that appeared during the folding process of the physical model. The analysis continues by adding a single row each time to understand the changes occurring in the mobility. Multiple tables are presented concerning the mobility calculations at the end of the section.

Double row: The panels of a rigid origami structures are considered as links. The number of links in this mechanism is 12, and the number of joints is 15 (Figure 3.59). The number of independent loops,  $L_{62}$  is calculated using eq. (3.47) for a double row triangular pattern there are 4 loops:  $L_{62} = 15 - 12 + 1 = 4$ . The 1<sup>st</sup> loop is a 6-bar mechanism and all the remaining three loops are 4-bar mechanism. All four loops are  $\lambda = 3$  because all joints' axis meet at a central point. The mobility calculation for the double row pattern  $M_{62}$  is made



by substituting the number of joints and loops to eq. (3.50). For 15 revolute joints and 4  $\lambda = 3$  loops, the mobility is equal to 3:  $M_{62} = 15 - (4 \cdot 3) = 3$ .

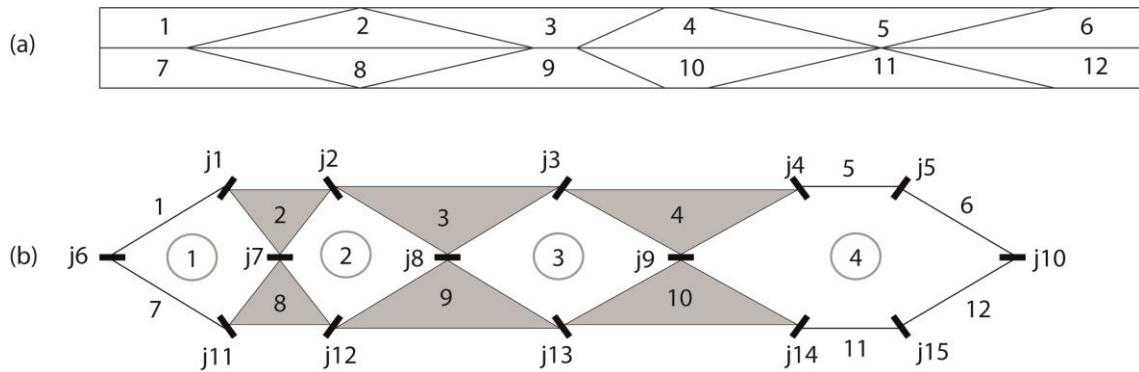


Figure 3.59. Triangular double row obtuse arch  $n:3$   $nT:6$  (a) crease pattern (b) kinematic diagram.

The result can be verified by the properties of structural groups: a loop of 4-bar spherical linkage has a mobility of 1. When a second loop is added to a  $\lambda = 3$  mechanism only 2 links are required to preserve the mobility. The 2<sup>nd</sup> and 3<sup>rd</sup> loops add 2 new links each preserving the mobility equal to 1. The 4<sup>th</sup> loops also adds 4 new links [5, 6, 11, and 12] two of these links are additional links increasing the mobility by 2 to 3.

During the folding process of the physical model some tears developed suggesting the mechanism has excessive joints. To analyse this, the joints where the tears appeared are removed and a modified kinematic diagram is created. In this case of the double row of double centered arch the joint 8 is removed from the mechanism (Figure 3.60).

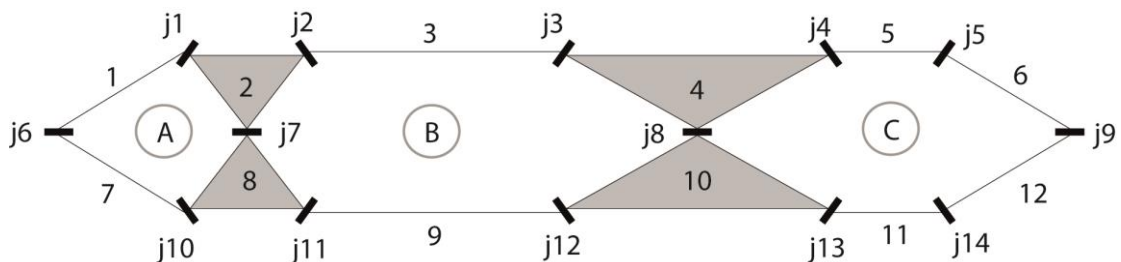


Figure 3.60. Modified triangular double row obtuse arch  $n:3$   $nT:6$  pattern's kinematic diagram.

Selvi's equation (eq. (3.48)) is used to calculate the new loop B subspace, created by the combination of loops 2 and 3; which is equal to  $\lambda = 5$ :  $\lambda = (3 + 3) + (1 - 2) = 5$  (Selvi, 2012).

By removing the joint number 8, the total number of joints within the mechanism decreases to 14. The mobility for a modified:  $M_{62M} = 14 - ((2 \cdot 3) + (1 \cdot 5)) = 3$ .

Removing this joint did not change the mobility. The structural group properties need to be reanalyzed since the mechanism became a mix of loops with different subspace number. The first loop A is a 4-bar spherical mechanism with  $\lambda = 3$  with a mobility equal to 1, the second loop B has  $\lambda = 5$ , which requires additional 4 links to preserve mobility. The second loop B adds 4 new links [4, 5, 10, and 11] to the structural group preserving the mobility. The third loop C is a  $\lambda = 3$  6-bar mechanism adding 4 new links [5, 6, and 11, 12] increasing the mobility to 3, which verifies the new calculated mobility.

3 Rows: A third row is added to the mechanism which adds 6 new link and 10 new joints. The new row adds 4 new loops (Figure 3.61), making 8 loops in total also calculated using eq. (3.47):  $L_{63} = 25 - 18 + 1 = 8$ .

The mobility of the CP decreases with the introduction of a new row:  $M_{63} = 25 - (8 \cdot 3) = 1$ . The mobility can be verified using the structural group properties by continuing to analyze the double row pattern which has a calculated mobility equal to 3. The 5<sup>th</sup> loop adds 2 new links [17 and 18] to the mechanism that requires only 2 new links to conserve the mobility, thus with this loop the mobility is preserved. The 6<sup>th</sup> and 7<sup>th</sup> loops add only 1 new link each decreasing the mobility to 1. The last loop 8<sup>th</sup> adds 2 new links preserving the mobility equal to 1.

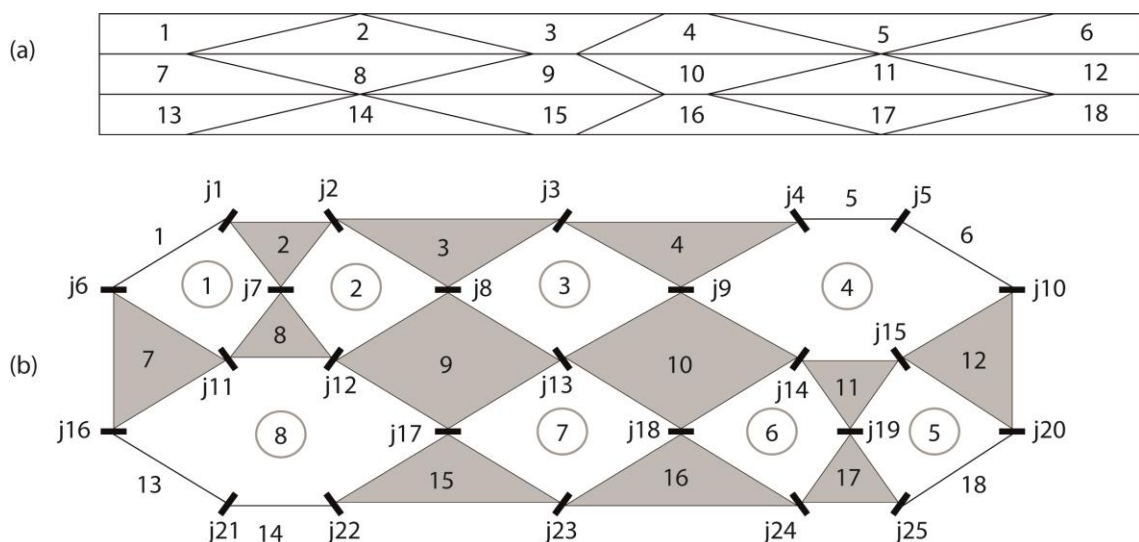


Figure 3.61. Triangular 3 row obtuse arch  $n:3$   $nT:6$  (a) crease pattern (b) kinematic diagram.

The tears that appeared during the folding process occurred at the joints 8 and 18 which have been removed to create the modified pattern (Figure 3.62). The new loops' subspace number have been calculated using the eq. (3.48), the loops B and E have  $\lambda = 5$ . The new mobility is also equal to 1:  $M_{63M} = 23 - ((4 \cdot 3) + (2 \cdot 5)) = 1$ .

As the mobility calculation for a modified 3 rows pattern shows removing the joints did not affect the value of the mobility.

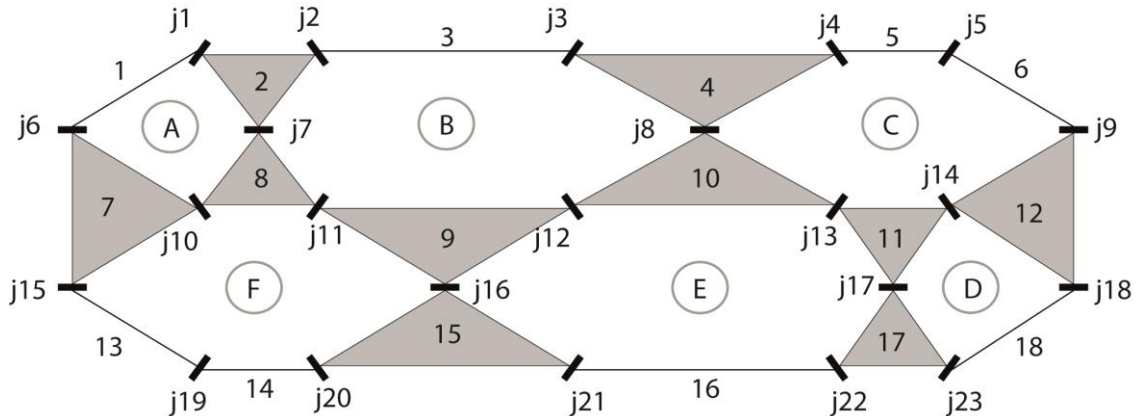


Figure 3.62. Modified triangular 3 row obtuse arch  $n:3$   $n7:6$  pattern's kinematic diagram.

When the structural group properties are analyzed the new loop D adds 2 new links [17, and 18] to the mechanism which preserve the mobility equal to 3. The loop E, composed of the 6<sup>th</sup> and 7<sup>th</sup> loop add 2 new links [14 and 15], but according to structural group properties for a  $\lambda = 5$  mechanism to be able to preserve the mobility 4 new links should be added. When the loop E introduces 2 new links the mobility decreases by 2 making the mobility equal to 1. The last loop F adds 2 new links [13 and 14] preserving the mobility equal to 1.

**4 Rows:** A fourth row is added to mechanism introducing 6 new links and 10 new joints. The 4-row pattern have a total of 24 links and 35 joints (Figure 3.63). there are 12 loops:  $L_{64} = 35 - 24 + 1 = 12$ .

Again the mobility decreases with the introduction of a new row, the new mobility is equal to -1:  $M_{64} = 35 - (12 \cdot 3) = -1$ . The mobility is once more verified by the structural properties; the new loop, 9<sup>th</sup> loop, introduces 2 new links to the mechanism [19, and 20] preserving the mobility equal to 1. The 10<sup>th</sup> and 11<sup>th</sup> loops adds each one 1 new link [22;and 23] where each one needed to add 2 new links to preserve

the mobility, so the mobility decreases to -1. The 12<sup>th</sup> loop introduces 2 new links [23 and 24] preserving the mobility equal to -1 which verifies the calculations.

Additional to the joints removed in the 3 row pattern, joint 28 is removed creating a modified pattern with 24 links and 32 joints (Figure 3.64). The new loop H created by removing joint 28 constitutes a double spherical linkage with  $\lambda = 5$ .

The new modified mechanism has 9 loops instead of 12 loops. Again, removing joints make no difference in the mobility value:  $M_{64M} = 14 - ((6 \cdot 3) + (3 \cdot 5)) = -1$ .

When the structural group is analyzed the new loop G introduced 2 new links [19 and 20] preserving the mobility equal to 1. Loop H introduces 2 new links [21 and 22] which should have introduced 4 new links to preserve the mobility because it's a double spherical linkage. The introduction of loop H decreases the mobility by 2 making the mobility value equal to -2. The last loop J adds 2 more links [23 and 24] which preserve the mobility equal to -1.

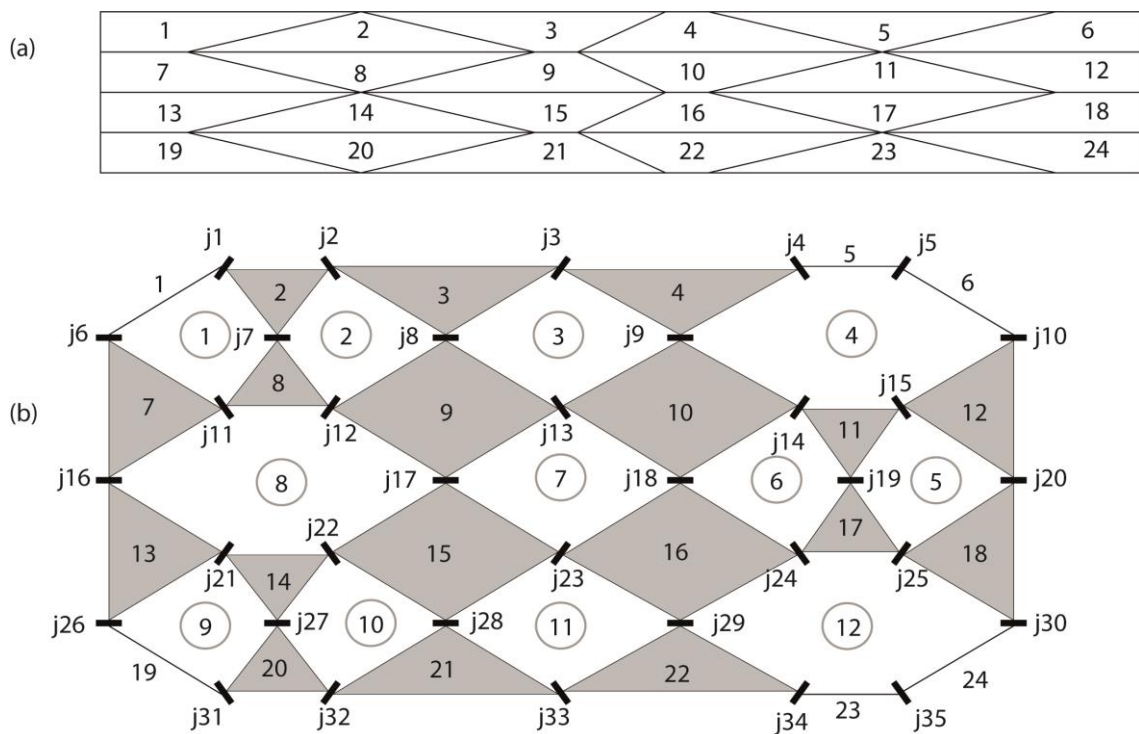


Figure 3.63. Triangular 4 row obtuse arch  $n:3$   $n_T:6$  (a) crease pattern (b) kinematic diagram.

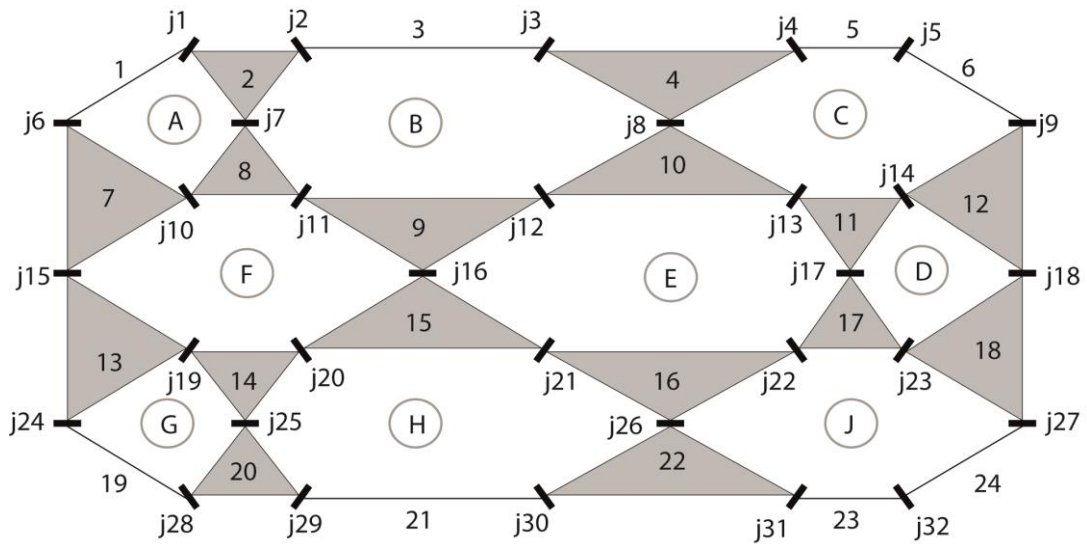


Figure 3.64. Modified triangular four rows obtuse arch  $n:3$   $n_T:6$  pattern's kinematic diagram.

Table 3.13 presents results for a triangular pattern with different number of segments. As it can be observed for any number of segments, as the number of row increases the mobility decreases, and as the number of segment increases more rows are required to achieve an overconstrained mechanism. Removing the joints that tear during the folding process did not affect the mobility value but only the number of joints and loops. Kinematic diagrams and patterns for Tables 3.13 and 3.14 can be analyzed in Appendix D.

Table 3.13. Double centered triangular pattern mobility analysis with different number of segments and rows.

r:5 a:2 Obtuse h: max Triangular Pattern																	
# of segment	2 Row			3 Row			4 Row			5 Row			6 Row			increased by	
n:2 nr:4	# links	8			12			16			20			24			(+4)
	# joints	10			17			24			31			38			(+7)
	# loops	T	$\lambda=3$	$\lambda=5$	T	$\lambda=3$	$\lambda=5$	T	$\lambda=3$	$\lambda=5$	T	$\lambda=3$	$\lambda=5$	T	$\lambda=3$	$\lambda=5$	(3)
		3	3	0	6	6	0	9	9	0	12	12	0	15	15	0	
M	1			-1			-3			-5			-7			(-2)	
n:3 nr:6	# links	12			18			24			30			36			(+6)
	# joints	15			25			35			45			55			(+10)
	# loops	T	$\lambda=3$	$\lambda=5$	T	$\lambda=3$	$\lambda=5$	T	$\lambda=3$	$\lambda=5$	T	$\lambda=3$	$\lambda=5$	T	$\lambda=3$	$\lambda=5$	(4)
		4	4	0	8	8	0	12	12	0	16	16	0	20	20	0	
M	3			1			-1			-3			-5			(-2)	
n:4 nr:8	# links	16			24			32			40			48			(+8)
	# joints	20			33			46			59			72			(+13)
	# loops	T	$\lambda=3$	$\lambda=5$	T	$\lambda=3$	$\lambda=5$	T	$\lambda=3$	$\lambda=5$	T	$\lambda=3$	$\lambda=5$	T	$\lambda=3$	$\lambda=5$	(5)
		5	5	0	10	10	0	15	15	0	20	20	0	25	25	0	
M	5			3			1			-1			-3			(-2)	
n:5 nr:10	# links	20			30			40			50			60			(+10)
	# joints	25			41			57			73			89			(+16)
	# loops	T	$\lambda=3$	$\lambda=5$	T	$\lambda=3$	$\lambda=5$	T	$\lambda=3$	$\lambda=5$	T	$\lambda=3$	$\lambda=5$	T	$\lambda=3$	$\lambda=5$	(6)
		6	6	0	12	12	0	18	18	0	24	24	0	30	30	0	
M	7			5			3			1			-1			(-2)	

Table 3.14. Double centered modified triangular pattern mobility analysis with different number of segments and rows.

r:5 a:2 Obtuse h: max Triangular Pattern - MODIFIED																	
# of segment	2 Row			3 Row			4 Row			5 Row			6 Row			increased by	
n:2 nr:4	# links	8			12			16			20			24			(+4)
	# joints	9			15			21			27			33			(+6)
	# loops	T	$\lambda=3$	$\lambda=5$	T	$\lambda=3$	$\lambda=5$	T	$\lambda=3$	$\lambda=5$	T	$\lambda=3$	$\lambda=5$	T	$\lambda=3$	$\lambda=5$	(2)
		2	1	1	4	2	2	6	3	3	8	4	4	10	5	5	
M	1			-1			-3			-5			-7			(-2)	
n:3 nr:6	# links	12			18			24			30			36			(+6)
	# joints	14			23			32			41			50			(+9)
	# loops	T	$\lambda=3$	$\lambda=5$	T	$\lambda=3$	$\lambda=5$	T	$\lambda=3$	$\lambda=5$	T	$\lambda=3$	$\lambda=5$	T	$\lambda=3$	$\lambda=5$	(3)
		3	2	1	6	4	2	9	6	3	12	8	4	15	10	5	
M	3			1			-1			-3			-5			(-2)	
n:4 nr:8	# links	16			24			32			40			48			(+8)
	# joints	19			31			43			55			67			(+12)
	# loops	T	$\lambda=3$	$\lambda=5$	T	$\lambda=3$	$\lambda=5$	T	$\lambda=3$	$\lambda=5$	T	$\lambda=3$	$\lambda=5$	T	$\lambda=3$	$\lambda=5$	(4)
		4	3	1	8	6	2	12	9	3	16	12	4	20	15	5	
M	5			3			1			-1			-3			(-2)	
n:5 nr:10	# links	20			30			40			50			60			(+10)
	# joints	24			39			54			69			84			(+15)
	# loops	T	$\lambda=3$	$\lambda=5$	T	$\lambda=3$	$\lambda=5$	T	$\lambda=3$	$\lambda=5$	T	$\lambda=3$	$\lambda=5$	T	$\lambda=3$	$\lambda=5$	(5)
		5	4	1	10	8	2	15	12	3	20	16	4	25	20	5	
M	7			5			3			1			-1			(-2)	

### 3.2.3.2. Trapezoidal Patterns

In this section the mobility analysis is conducted for a trapezoidal pattern ( $h < \max$ ) with 6 segments. If the pattern have been created with a smaller value than the maximum value of the pattern's height  $h$  the pattern created has trapezoidal panels. The steps followed in this section are the same as the previous one: first the CP is analyzed, then its modified kinematic diagram.

Double row: there are 12 links and 16 joints in a double row trapezoidal mechanism. (Figure 3.65). The number of independent loops,  $L_{62T}$  is calculated using eq. (3.48):  $L_{62T} = 16 - 12 + 1 = 5$ . All loops are 4-bar spherical loops with  $\lambda = 3$ .

The mobility is equal to 1:  $M_{62T} = 16 - (5 \cdot 3) = 1$ . When the structural group properties are analyzed, the first loop is a 4-bar linkage with a mobility equal to 1. Each loops add 2 new links to the mechanism so the mobility is preserved.

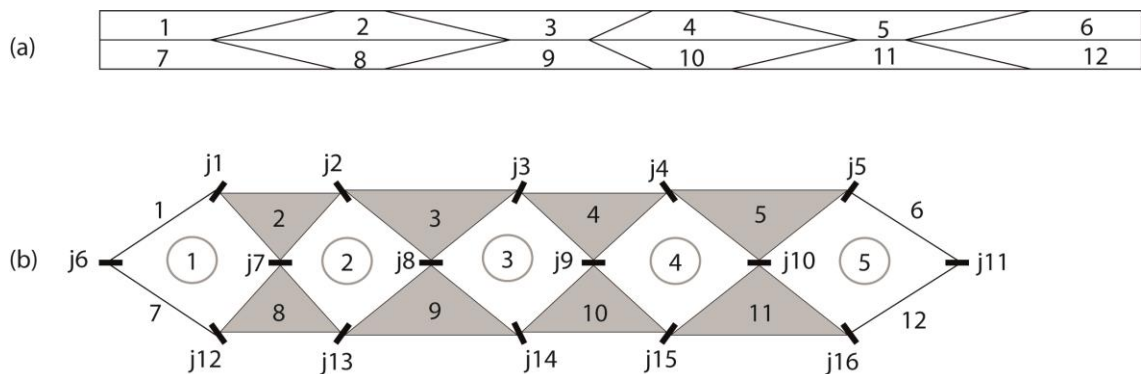


Figure 3.65. Trapezoidal double row obtuse arch  $n:3$   $nT:6$  (a) crease pattern (b) kinematic diagram.

The joints 8 and 10 are removed from the mechanism (Figure 3.66) because the tears appeared at those joints during the folding process of the physical model. The loop A is a 4-bar spherical loop with mobility equal to 1. The 2<sup>nd</sup> and 3<sup>rd</sup> loops B and C are  $\lambda = 5$  mechanisms each and add 4 new links [3, 4, 9, and 10; 5, 6, 11, and 12] which preserves the mobility equal to 1:  $M_{62TM} = 14 - ((1 \cdot 3) + (2 \cdot 5)) = 1$ .

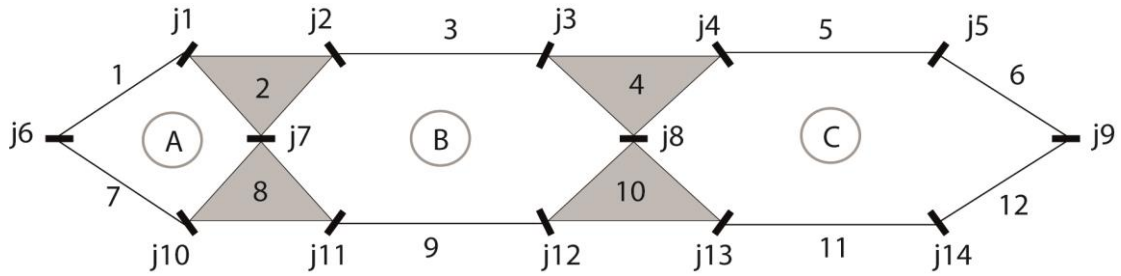


Figure 3.66. Modified trapezoidal double row obtuse arch  $n:3$   $n_T:6$  pattern's kinematic diagram.

3 Rows: A third row is added to the mechanism introducing 6 new links and 11 new joints. The new row adds 5 new loops to the mechanism (Figure 3.67): .  
 $L_{63T} = 27 - 18 + 1 = 10$ .

The double row trapezoidal pattern's mobility was 1:  $M_{63T} = 27 - (10 \cdot 3) = -3$ . The 6<sup>th</sup> loop adds 2 new links to the mechanism preserving the mobility. All the following loops 7<sup>th</sup>, 8<sup>th</sup>, 9<sup>th</sup> and 10<sup>th</sup> each add only one link. To preserve the mobility each of the loops should have introduced 2 new links, thus decreasing by 4 the value of mobility to -3 as calculated.

Some of the creases tear [joints: 8, 10, 18, and 20] during the folding process which have been removed to modify the kinematic diagram (Figure 3.68). By removing these joints the mechanism became a 6-bar spherical mechanism combined with different subspace numbers. The loops B, C, F and E are  $\lambda = 5$  mechanisms. The mobility calculation for the modified pattern:  $M_{63TM} = 23 - ((2 \cdot 3) + (4 \cdot 5)) = -3$ .

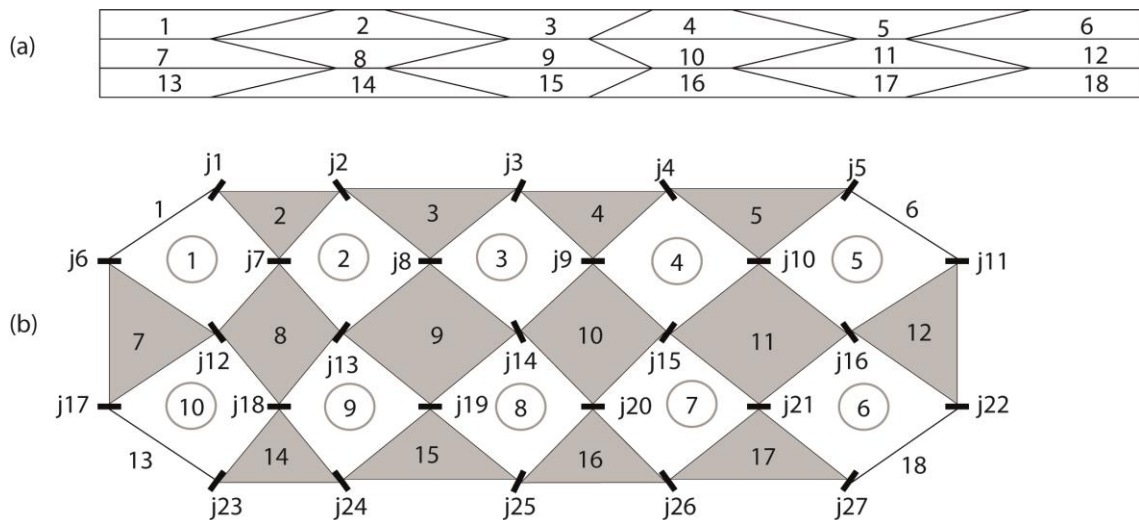


Figure 3.67. Trapezoidal 3 row obtuse arch  $n:3$   $n_T:6$  (a) crease pattern (b) kinematic diagram.



In the modified 3 rows trapezoidal pattern the new loop introduces 2 new links [17 and 18] preserving the mobility equal to 1. But the following two loops E and F are  $\lambda = 5$  mechanisms which requires that they each add 4 new links to the mechanism, but instead each adds only 2 new links [15 and 16; 13 and 14] decreasing the mobility to -3 which justify the calculations.

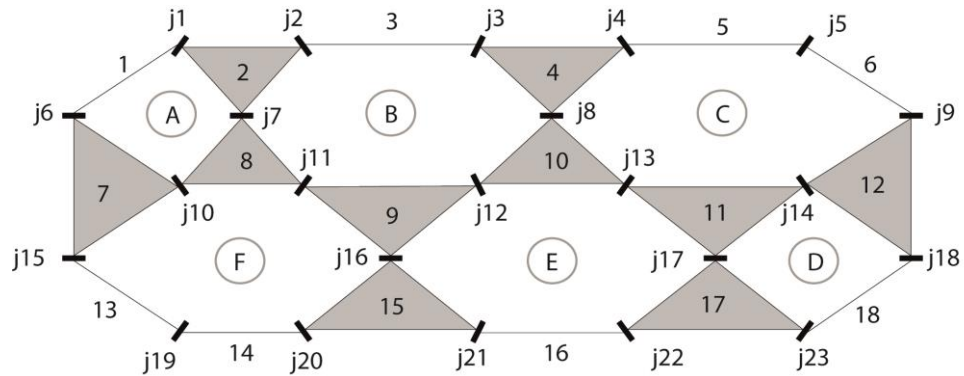


Figure 3.68. Modified trapezoidal 3 row obtuse arch  $n:3$   $n_T:6$  pattern's kinematic diagram.

4 Rows: a fourth row is added to the mechanism which increases the number of loops to 15, the number of links to 24, and the number of joints to 38 (Figure 3.69). There are 15 loops:  $L_{64T} = 38 - 24 + 1 = 15$ , and the mobility is -7:  $M_{64T} = 38 - (15 \cdot 3) = -7$ .

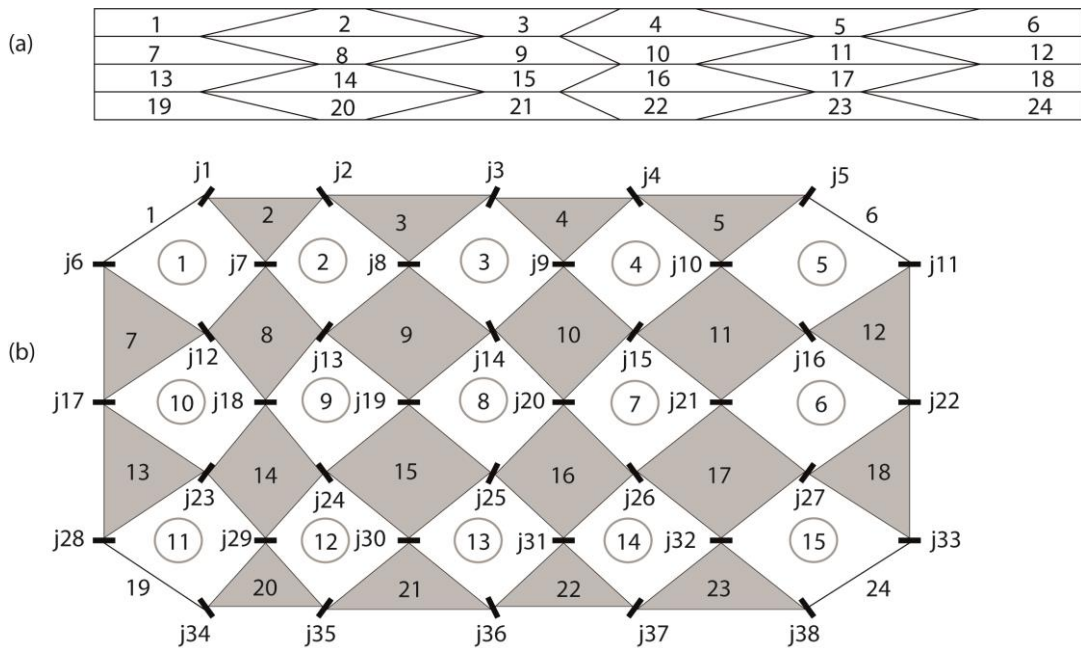


Figure 3.69. Trapezoidal 4 row obtuse arch  $n:3$   $n_T:6$  (a) crease pattern (b) kinematic diagram.

The 11<sup>th</sup> loop adds 2 new links [19 and 20] to the mechanism preserving the mobility calculated on the 3-row trapezoidal pattern equal to -3. All the following loops 12<sup>th</sup>, 13<sup>th</sup>, 14<sup>th</sup>, and 15<sup>th</sup> each adding 1 new links; although each should have added 2 new links. Because each loop adds 1 link the mobility decreases by 4 which makes it equal to -7 as calculated.

The removal of joints 8, 10, 18, 20, 30 and 32 from this pattern modified the kinematic diagram from a 15 loops mechanism to 9 loop mechanism (Figure 3.70) with the same number of links and 32 joints. The new loops H and J are  $\lambda = 5$  loops.

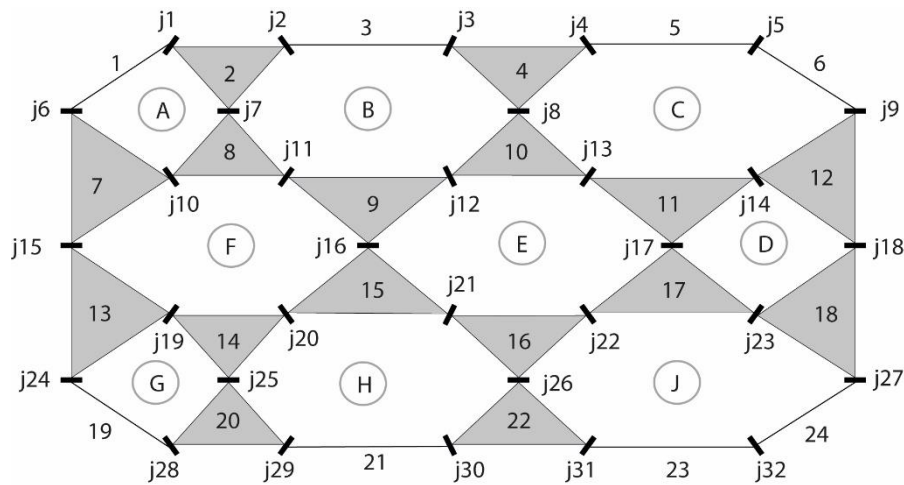


Figure 3.70. Modified trapezoidal 4 row obtuse arch  $n:3$   $n_T:6$  pattern's kinematic diagram.

The loop G adds 2 new links to the mechanism preserving the mobility calculated in 3 row pattern as -3. To preserve the mobility the loops H and J should add 4 new links each because they are  $\lambda=5$  mechanisms, but because each add only 2 new links the mobility decreases to -7, as calculated:  $M_{64TM} = 32 - ((3 \cdot 3) + (6 \cdot 5)) = -3$ .

Tables 3.15 and 3.16 present the results of the mobility calculations for both the trapezoidal pattern and the modified trapezoidal pattern. As it can be observed the mobility does not change when the pattern is modified by removing joints, but the kinematic properties of the pattern changes. Kinematic diagrams and patterns are presented in Appendix D.

Table 3.15. Double centered trapezoidal pattern mobility analysis with different number of segments and rows.

r:5 a:2 Obtuse h < MAX Trapezoidal pattern																	
# of segment	2 Row			3 Row			4 Row			5 Row			6 Row			increased by	
n:2 nr:4	# links	8			12			16			20			24			(+4)
	# joints	10			17			24			31			38			(+7)
	# loops	T	$\lambda=3$	$\lambda=5$	T	$\lambda=3$	$\lambda=5$	T	$\lambda=3$	$\lambda=5$	T	$\lambda=3$	$\lambda=5$	T	$\lambda=3$	$\lambda=5$	(3)
		3	3	0	6	6	0	9	9	0	12	12	0	15	15	0	
M	1			-1			-3			-5			-7			(-2)	
n:3 nr:6	# links	12			18			24			30			36			(+6)
	# joints	16			27			38			49			60			(+11)
	# loops	T	$\lambda=3$	$\lambda=5$	T	$\lambda=3$	$\lambda=5$	T	$\lambda=3$	$\lambda=5$	T	$\lambda=3$	$\lambda=5$	T	$\lambda=3$	$\lambda=5$	(5)
		5	5	0	10	10	0	15	15	0	20	20	0	25	25	0	
M	1			-3			-7			-11			-15			(-4)	
n:4 nr:8	# links	16			24			32			40			48			(+8)
	# joints	22			37			52			67			82			(+15)
	# loops	T	$\lambda=3$	$\lambda=5$	T	$\lambda=3$	$\lambda=5$	T	$\lambda=3$	$\lambda=5$	T	$\lambda=3$	$\lambda=5$	T	$\lambda=3$	$\lambda=5$	(7)
		7	7	0	14	14	0	21	21	0	28	28	0	35	35	0	
M	1			-5			-11			-17			-23			(-6)	
n:5 nr:10	# links	20			30			40			50			60			(+10)
	# joints	28			47			66			85			104			(+19)
	# loops	T	$\lambda=3$	$\lambda=5$	T	$\lambda=3$	$\lambda=5$	T	$\lambda=3$	$\lambda=5$	T	$\lambda=3$	$\lambda=5$	T	$\lambda=3$	$\lambda=5$	(9)
		9	9	0	18	18	0	27	27	0	36	36	0	45	45	0	
M	1			-7			-15			-23			-31			(-8)	

Table 3.16. Double centered modified triangular pattern mobility analysis with different number of segments and rows.

r:5 a:2 Obtuse h < MAX Trapezoidal pattern -MODIFIED																	
# of segment	2 Row			3 Row			4 Row			5 Row			6 Row			increased by	
n:2 nT:4	# links	8			12			16			20			24			(+4)
	# joints	9			15			21			27			33			(+6)
	# loops	T	$\lambda=3$	$\lambda=5$	T	$\lambda=3$	$\lambda=5$	T	$\lambda=3$	$\lambda=5$	T	$\lambda=3$	$\lambda=5$	T	$\lambda=3$	$\lambda=5$	(2)
		2	1	1	4	2	2	6	3	3	8	4	4	10	5	5	
M	1			-1			-3			-5			-7			(-2)	
n:3 nT:6	# links	12			18			24			30			36			(+6)
	# joints	14			23			32			41			50			(+9)
	# loops	T	$\lambda=3$	$\lambda=5$	T	$\lambda=3$	$\lambda=5$	T	$\lambda=3$	$\lambda=5$	T	$\lambda=3$	$\lambda=5$	T	$\lambda=3$	$\lambda=5$	(3)
		3	1	2	6	2	4	9	3	6	12	4	8	15	5	10	
M	1			-3			-7			-11			-15			(-4)	
n:4 nT:8	# links	16			24			32			40			48			(+8)
	# joints	19			31			43			55			67			(+12)
	# loops	T	$\lambda=3$	$\lambda=5$	T	$\lambda=3$	$\lambda=5$	T	$\lambda=3$	$\lambda=5$	T	$\lambda=3$	$\lambda=5$	T	$\lambda=3$	$\lambda=5$	(4)
		4	1	3	8	2	6	12	3	9	16	4	12	20	5	15	
M	1			-5			-11			-17			-23			(-6)	
n:5 nT:10	# links	20			30			40			50			60			(+10)
	# joints	24			39			54			69			84			(+15)
	# loops	T	$\lambda=3$	$\lambda=5$	T	$\lambda=3$	$\lambda=5$	T	$\lambda=3$	$\lambda=5$	T	$\lambda=3$	$\lambda=5$	T	$\lambda=3$	$\lambda=5$	(5)
		5	1	4	10	2	8	15	3	12	20	4	16	25	5	20	
M	1			-7			-15			-23			-31			(-8)	

As a conclusion the mobility calculations have been performed for both type of patterns and each calculation has been compared to a structural group analysis revealing the same value. When the tables of both modified triangular and modified trapezoidal patterns are analyzed, it reveals that all the properties are the same. As it was in the single centered arches, the tears occurring in the creases showed a similarity suggesting it is not random. It has also been observed that the trapezoidal patterns of both single centered and double centered arches have the same properties – mobility, number of links, joints and loops.

### 3.2.4. Conclusion

In this part of the study parameters for creating a double centered rigid origami foldable barrel vault has been presented. The parameters that can be defined by the designer are the radius,  $r$ , the number of segment,  $n$  for a single arc,  $n_T$  for the entire structure, and the distance between the centers  $a$  which defines whether the cross-section is a lancet, pointed equilateral or obtuse arch. Once these parameters defined, an MV-Pattern can be created based on the calculations presented on the geometrical properties section. If in a certain point during the folding stage the structure need to be stopped and fixed in that precise form the calculations from the partially folded state of geometrical properties and the workspace analysis calculations can be used. As it was in the single centered rigid origami barrel vault structures, the double centered structures also have a limitation regarding the height of a single row  $h$ . In double centered structures due to the form of the cross-section there are two different folding angles; one is the arc's folding angle  $\alpha_1$  and the second is the apex's folding angle  $\alpha_2$ . Two different folding angle creates two different height  $h_1$  and  $h_2$ , during the creation of the pattern the smaller of the two height should be selected. If the highest value is selected the diagonal lines will crisscross within the height of the pattern which in turn will lead to a failure in creating a foldable pattern. But the height can be less than the calculated maximum height which will create a trapezoidal pattern. In the workspace analysis calculations for the depth, span, height, and volume of the rigid origami structure has been put in relation with the inclination angle  $\sigma$  to facilitate the understanding of the properties of the structure during the folding process. Span and height calculations are based on the *pattern-generator* so that they are independent c from the height of the row which affect whether the pattern is triangular or trapezoidal

one. A calculation sheet has been prepared in Microsoft Excel 2013® to facilitate the calculations which is presented in Appendix C. In both triangular and trapezoidal patterns tears appeared in the process of folding the physical model, these creases were in relation with the removed joints. Removing those joints did not change the mobility calculations. For all four mobility calculation (Tables 3.13, 3.14, 3.15, and 3.16) a set of patterns and kinematic diagrams have been provided in Appendix D.

### **3.3. Conclusion**

In this chapter a method of designing a MV-Pattern for each type of rigid origami barrel vault using a *pattern-generator* has been presented. The two types of rigid origami barrel vaults are defined by the properties of the arch selected as the cross-section; semicircle and horseshoe arch are single centered, while lancet, pointed equilateral and obtuse are double centered arches. The pattern generation for both types starts with the definition of three parameters which in turn define all the other parameters required to design a rigid origami barrel vault. The relations between parameters have been demonstrated in the geometrical properties section. A calculation sheet prepared in Microsoft Excel 2013® for each barrel vault type has been provided to facilitate the calculations of the parameters. In the workspace analysis of each type, parameters of the deployment of the structure have been demonstrated in relation to one parameters - inclination angle - that defines the depth, span, height and volume of the structure during this process. Mobility analysis carried out for both type demonstrated that tears occurring during the folding of the physical model were related to the thickness of the material used because when these specific joints have been removed, the mobility did not changed.

## CHAPTER 4

### DEPLOYABLE PSEUDO-DOME STRUCTURE

In this chapter a novel method of creating deployable pseudo-dome structures has been presented. The structure is called pseudo-dome because the form created by folding is an approximation to a dome form. The method of using a *pattern-generator* is applied to create a quarter of a circle as a cross-section that is rotated to create a developable MV-Pattern.

In this chapter first the cross-section is analyzed to create a segmentation that allows the creation of a central pattern which can rotate to create a pseudo-dome. Then follows by a geometrical analysis starting from the final folded state and initial state simultaneously and finishing with the analysis of the partially folded state of the MV-Pattern. The geometrical analysis is followed by the workspace analysis where the relations between the folding angles and the span, height, area, and volume are presented to understand the parameters' changes during the deployment movement. Then a mobility analysis is carried out to understand the kinematics of the created MV-Pattern. Lastly a conclusion is presented.

#### 4.1. Segmentation

The geometrical form of the cross-section needs to be selected to be able to create a segmentation. A pseudo-dome can be created by rotating a crease pattern along an axis (Figure 4.1). Two methods were analyzed and because the first method, where a semicircle is used as a cross-section (Figure 4.1(a)) creates a non-developable pattern, the method chosen in this study is the second one (Figure 4.1(b)) where a quarter of a circle is rotated 360° around the z-axis creating a developable pattern. Figure 4.1 demonstrates the two methods: (a) a semicircle cross-section is rotated along the x-axis, the pattern-generator is segmented and when the crease pattern is created, as it can be observed the created pattern is a non-developable pattern, (b) a quarter of a circle is used as a cross-section which is then rotated along the z-axis, the pattern-generator is segmented and based on these segments a crease pattern is created which is a developable one.

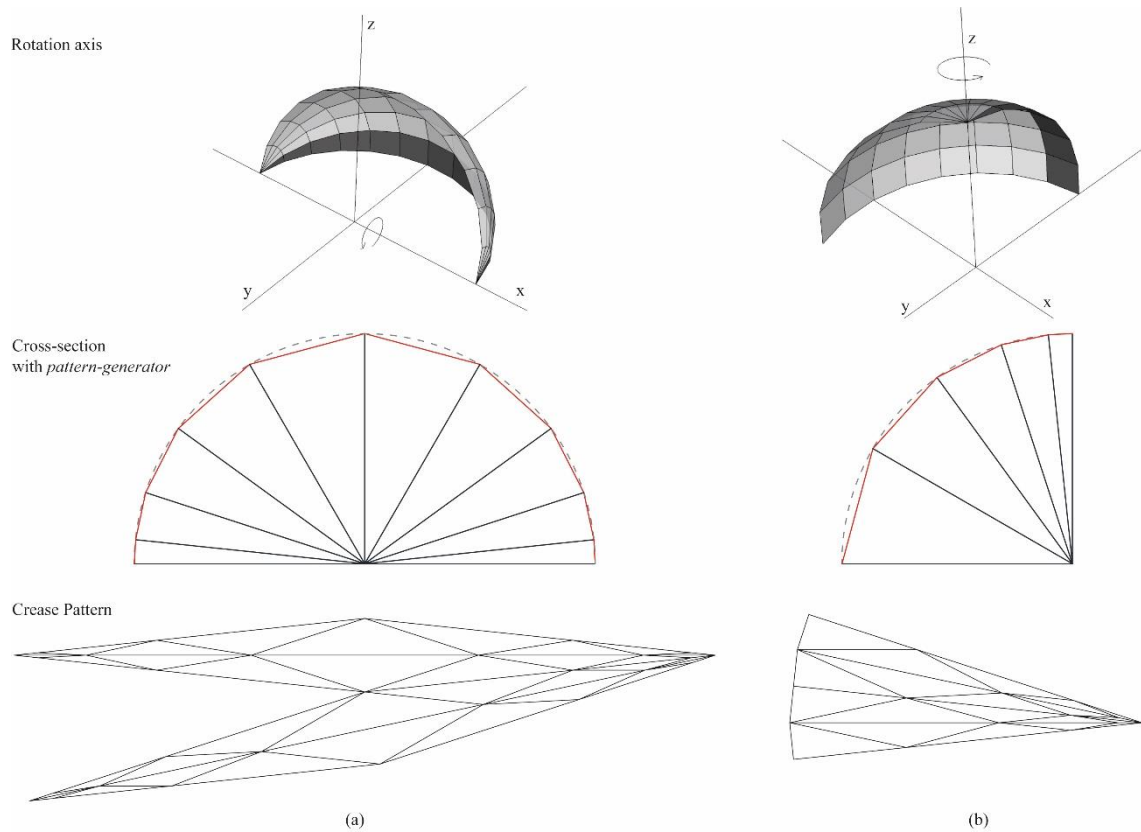


Figure 4.1. Dome creation methods (a) Polar rotation of a semicircle along the x-axis (b) Polar rotation of a quarter of a circle around z-axis.

For rigid origami deployable structures, an approximation to a dome can be achieved by increasing the number of segments (Figure 4.2) as it was in barrel vault structures. But the segmentation cannot be the same as in deployable barrel vaults where the segments were divided equally creating equilateral polygonal segments with an accordion-like translational deployment. A pattern that will have a rotational deployment needs to have a central point to prevent surfaces to intersect with each other. So, to achieve a radially deployable MV-Pattern, the segments' length needs to decrease toward the central point.

Different methods have been explored to create this specific decreasing segmentation. First hands-on model folding have been tried which presented difficulties on the generalization of the crease pattern creation. Then mathematical methods have been explored: geometric and arithmetic progressions. Arithmetic sequence proved to create an increasing segmentation that can be controlled by parameters like the first segment angle and number of segments, which provided a foldable crease pattern.

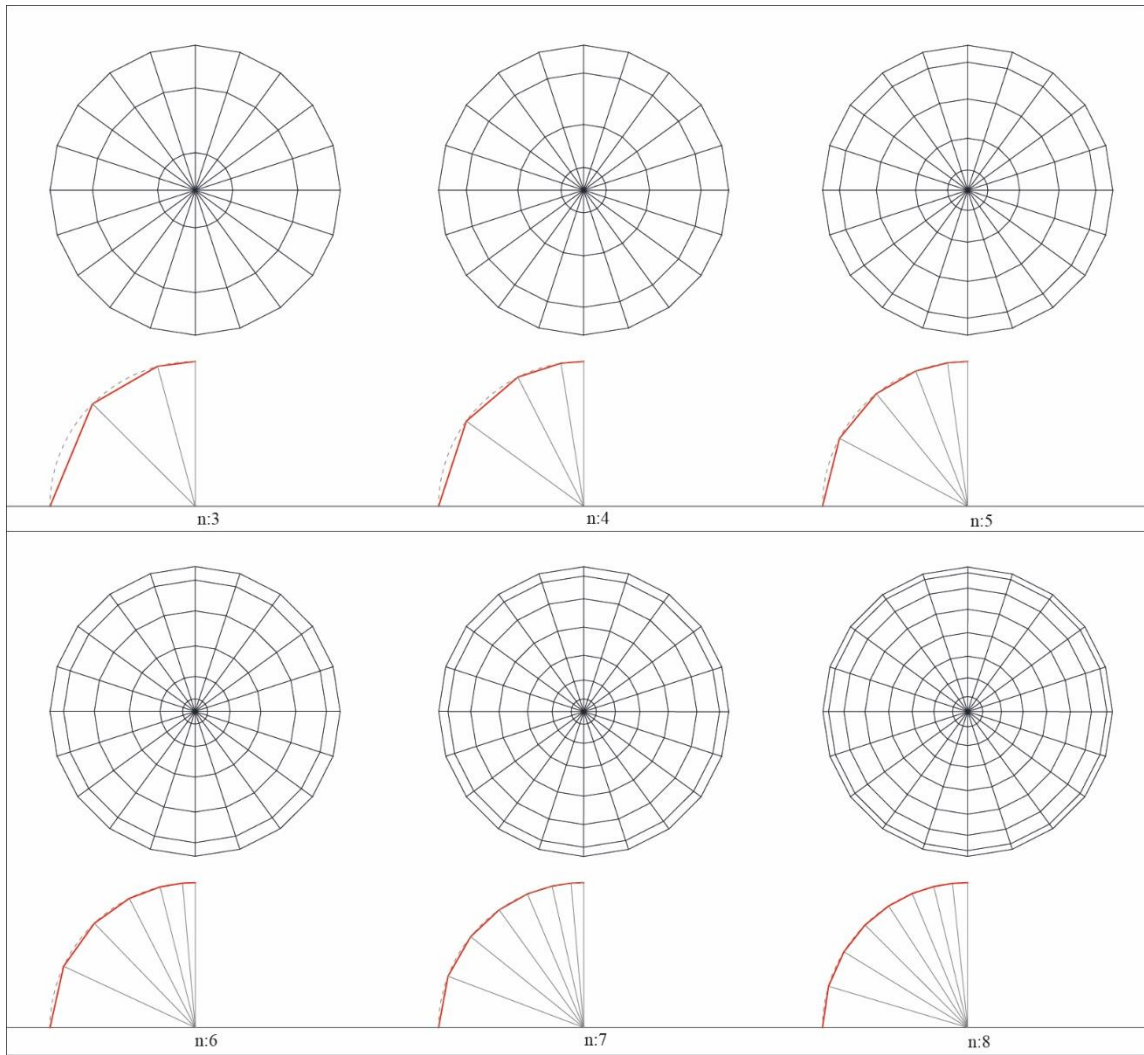


Figure 4.2. Segmentation of an arc by 3, 4, 5, 6, 7, and 8; and the top view of the segmented domes.

Parameters to define the segmentation by arithmetic sequence are the radius of the arc  $r$ , the number of segments  $n$ , and finally the first segment's angle  $\theta_1$ . By defining these parameters all the parameters required to create an MV-Pattern for a rigid origami pseudo-dome structure can be calculated. The pattern-generator created by this division is used differently than it is used in barrel vault structures where the pattern-generator was the center of a single row. In this method the pattern generator is the folding lines.

In an arithmetic sequence the sum of the sequence is calculated with the following eq. (4.1):

$$S_n = \frac{n(\theta_1 + \theta_l)}{2} \quad (4.1)$$



where  $S_n$  is the sum of the angles in the sequence,  $n$  is the number of segments,  $\theta_1$  the first term of the sequence (both defined by the designer), and  $\theta_l$  the last term of the sequence which is the last angle. The sum of the angles should be  $\pi/2$  because the arc is a  $90^\circ$  and the division needs to be within this range. The parameter that needs to be calculated from this equation is the last angle  $\theta_l$ ; the equation for the last angle becomes eq. (4.2):

$$\theta_l = \left(\frac{\pi}{2}\right) - \theta_1 = \left(\frac{\pi}{n}\right) - \theta_1 \quad (4.2)$$

When the last angle has been calculated the common difference  $CD$  can be calculated allowing the calculation of all the angles. It can be calculated by eq. (4.3), where  $n$  is the number of segments and  $\theta_l$  the first term of the sequence (the segment closer to the central point) are the parameters defined by the designer,  $\theta_1$  is the last angle of the arithmetic sequence calculated with eq. (4.2).

$$CD = \frac{\theta_l - \theta_1}{n-1} \quad (4.3)$$

For each segment, the segment's angle  $\theta_k$  can be calculated by eq. (4.4), where  $k$   $\theta_k$  is the segment's angle for segment  $k$ . The numbering of the segments is done from the top to the bottom of the cross-section (Figure 4.3). Using eq. (4.4) each segment's angle needs to be calculated separately.

$$\theta_k = \theta_1 + ((k - 1)CD) \quad (4.4)$$

All calculations have been implemented in Microsoft Excel 2013® medium (Appendix E), where a graphic interface simulates the segmentation based on the changes on parameters  $r$ ,  $n$  and  $\theta_1$ .

## 4.2. Geometrical Analysis

This section presents the parameters based on geometrical properties and their calculations for the creation of an MV-Pattern for a rigid origami pseudo-dome

structure. This section starts with the analysis of the final folded state and the initial state, MV-Pattern, and ends with the partially folded state of the structure.

Contrary to the rigid origami barrel vault structure, the geometrical analysis of the final and initial state are conducted simultaneously because of the geometry of the rigid origami pseudo-dome structure.

#### 4.2.1. Final Folded State and Initial State

In the previous section all the angles have been calculated using eq. (4.4). To be able to draw the MV-Pattern more parameters are required.

Segment length  $s_n$  for each segment's angle can be calculated using eq. (4.5), which is the same equation used to calculate the segments' length in rigid origami barrel vaults eq. (3.2). Where  $n$  is the segment number and  $\theta_n$  is the segment's angle of the calculated segment length.

$$s_n = 2r \sin\left(\frac{\theta_n}{2}\right) \quad (4.5)$$

To be able to calculate angles between the segments, the interior angle  $\beta$  has to be calculated based on the angles  $\hat{A}$ . The angles  $\hat{A}_n$  are different for each segment and are in relation with the segment's angle  $\theta_n$ . The relation between these parameters are presented in eq. (4.6).

$$\hat{A}_n = \frac{\pi - \theta_n}{2} \quad (4.6)$$

As observed in Figure 4.3 the number of interior angles  $\beta$  is equal to  $n - 1$ . For example for the cross-section illustrated in Figure 4.3 where there are four segments, four segment angles, and three interior angles. The calculation of the interior angles  $\beta_i$  is done by eq. (4.7).

$$\beta_i = \hat{A}_{i+1} + \hat{A}_i \quad (4.7)$$

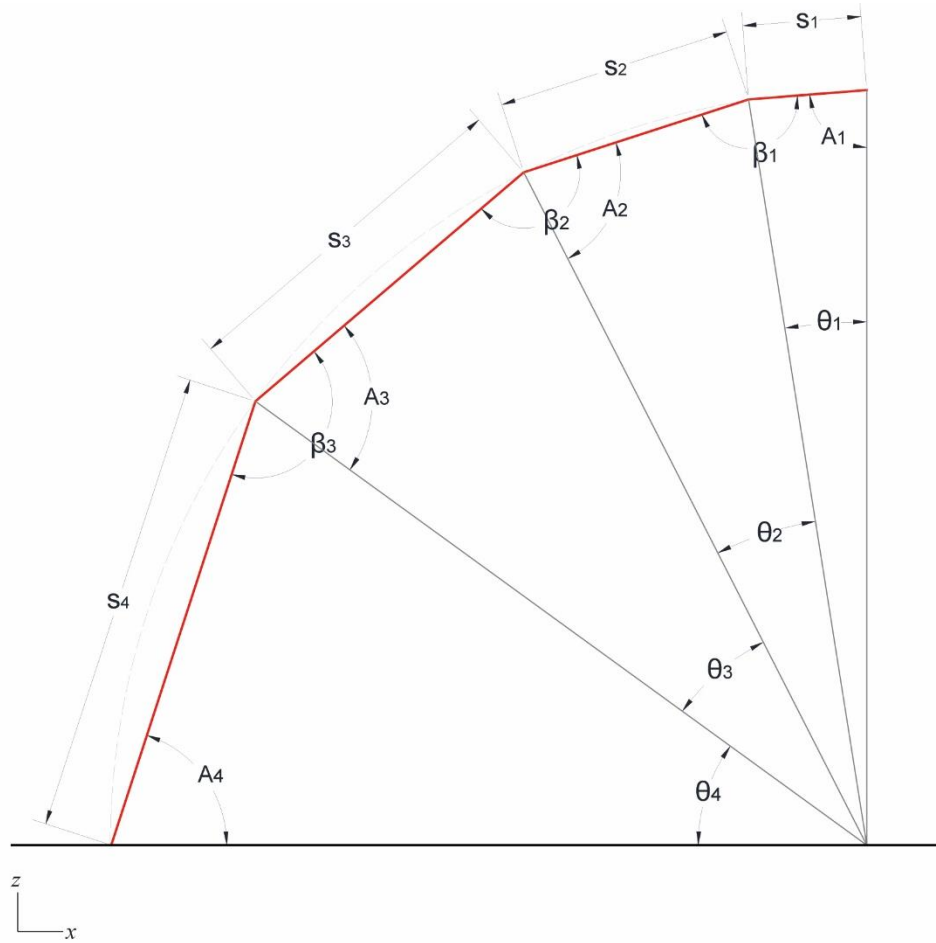


Figure 4.3. Parameters of the cross-section of a pseudo-dome  $r: 5\text{m}$ ,  $n: 4$ ,  $\theta_1: 9^\circ$ .

There are two different denotations: a parameter with  $n$ , is numbered based on the number of segments as the segment's angle  $\theta_n$ , segment length  $s_n$ , and angles  $A_n$ , and parameter with  $i$ , is numbered based on the number of interior angles  $\beta_i$ , meaning  $[n - 1]$ , like the folding angles  $\alpha_{i1}$ ,  $\alpha_{i2}$  and their projected angles  $\delta_{i1}$ ,  $\delta_{i2}$ , interior angle's segment length  $a_i$ , and the bending angles  $\mu_i$ . When a parameter that has been defined by an  $n$  but instead it is denoted with  $i$ , the parameter should be calculated based on the value of  $i$ .

The interior angle's segment length  $a_i$  cannot be calculated by the crease pattern, the calculations are done using the segment angles  $\theta_i$  (Figure 4.4(b)), except for the last segment's length  $a_l$  which can only be calculated after the calculation of all the folding angles  $\alpha$ . The interior angle's segment length is calculated by eq. (4.8), where  $i$  is the number of the segment needing to be calculated.

$$a_i = 2r \cos\left(\frac{\pi - (\theta_i + \theta_{i+1})}{2}\right) \quad (4.8)$$

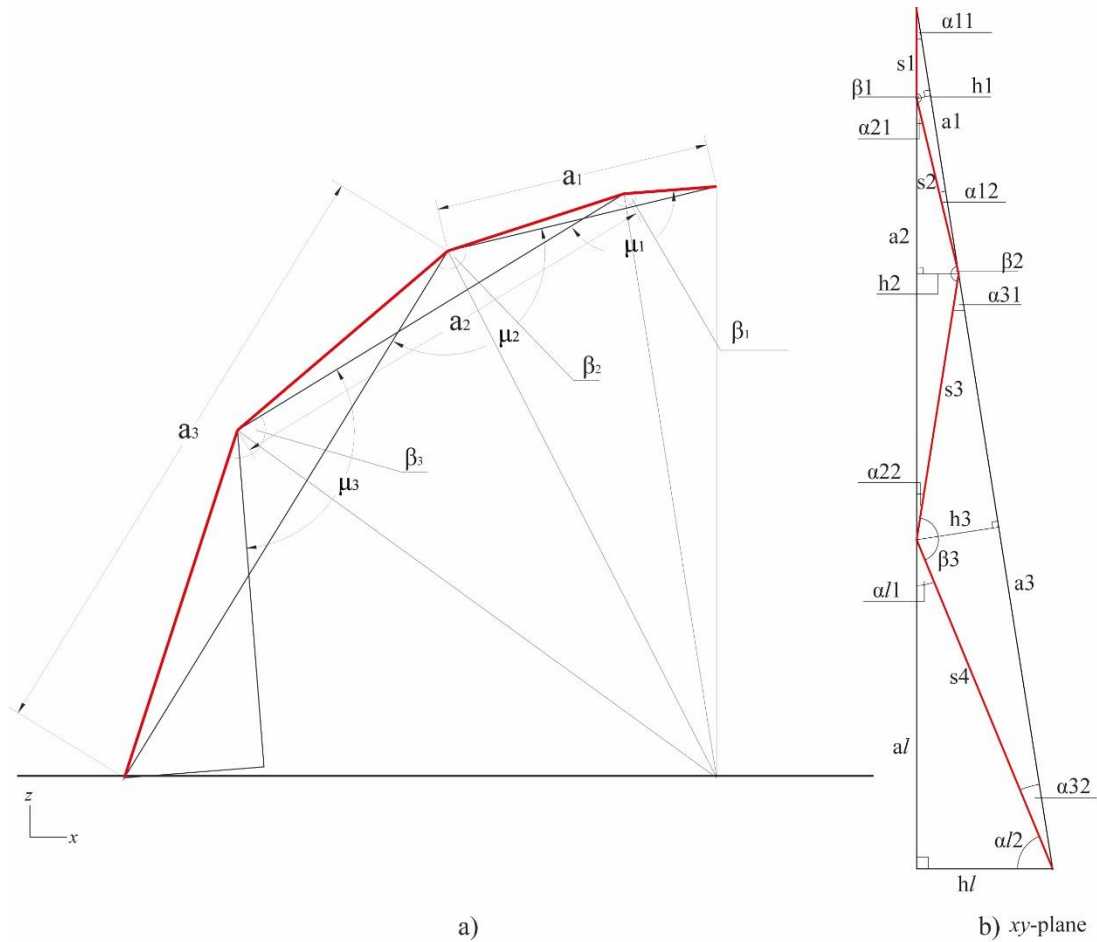


Figure 4.4. Parameters of (a) the final folded state and (b) the crease pattern, for a dome with  $r: 5\text{m}$ ,  $n: 4$ ,  $\theta_1: 9^\circ$ .

The folding angles  $\alpha$  have to be calculated in order to comprehend the geometry of the initial folded state. The folding angles are different for each triangle creating the pattern; the denotation of the folding angles has been done according to their position in respect to the central point of the pattern, and their complementary angle which are the interior angles  $\beta$ . For example the triangle with the interior angle  $\beta_3$  from Figure 4.4(b); its opposite segment's length has been denoted  $a_3$ , the angle closer to the central point, the first angle  $\alpha_{31}$ ; the first subscript refers to the interior angle's number, and the second subscript defines that it is the first folding of the triangle closest to the central point. The second folding angle has been denoted with the same logic  $\alpha_{32}$ , defining the second folding angle of the third interior angle.

None of the triangles is neither an isosceles nor a right triangle, they are obtuse scalene triangles, thus to be able to calculate the folding angles the law of sines (eq. (4.9)) has been used, where  $i$  defines the number of the interior angle.

$$\frac{\sin \beta_i}{a_i} = \frac{\sin \alpha_{i1}}{s_{(i+1)}} = \frac{\sin \alpha_{i2}}{s_i} \quad (4.9)$$

If eq. (4.9) is applied to the third triangle with the interior angle  $\beta_3$  the equation would be:

$$\frac{\sin \beta_3}{a_3} = \frac{\sin \alpha_{31}}{s_4} = \frac{\sin \alpha_{32}}{s_3} \quad (4.9)$$

which gives eq. (4.10) for the first folding angle  $\alpha_{i1}$ , and eq. (4.11) for the second folding angle  $\alpha_{i2}$ . Where  $s_i$  is the segment length for the required interior angle's number calculated using eq. (4.5).

$$\alpha_{i1} = \sin^{-1} \left( \frac{\sin \beta_i \cdot s_{(i+1)}}{a_i} \right) \quad (4.10)$$

$$\alpha_{i2} = \sin^{-1} \left( \frac{\sin \beta_i \cdot s_i}{a_i} \right) \quad (4.11)$$

The height of each triangle  $h_i$  has been calculated using eq. (4.12), which is subscribed according to the interior angle  $\beta$ , and where  $i$  stands for the required interior angle's number (Figure 4.4(b)).

$$h_i = \sin \alpha_{i1} \cdot s_i \quad (4.12)$$

The last parameters to calculate are the folding angles  $\alpha_{i1}$  and  $\alpha_{i2}$ , the segments' length  $a_i$  and  $h_i$  which defines the maximum height of the single row. The folding angles  $\alpha_{i1}$  and  $\alpha_{i2}$  are calculated by eqs. (4.13) and (4.14) respectively, where  $i$  is the number of the last interior angle.

$$\alpha_{i1} = \pi - (\beta_i + \alpha_{(i-1)2}) \quad (4.13)$$

$$\alpha_{i2} = \frac{\pi}{2} - \alpha_{i1} \quad (4.14)$$

Using the calculated last folding angles the segment length of  $h_i$  and  $a_i$  can be calculated by eqs. (4.15) and (4.16) respectively, again where  $i$  is the number of the last interior angle.

$$h_l = s_{(i+1)} \sin \alpha_{l1} \quad (4.15)$$

$$a_l = s_{(i+1)} \sin \alpha_{l2} \quad (4.16)$$

A single row of the crease pattern is created by placing the segments according to their respective interior angles by reversing their directions, as illustrated in Figure 4.4, and then the vertexes are joined. And so the row is mirrored with respect to one of the edge and the central point. The pattern created using these parameters has a MV-Assignment based on Maekawa's theorem (Figure 4.5). Parameters required to draw the MV-Pattern in Figure 4.5 have been presented in Table 4.1.

Table 4.1. Parameters for a  $r$ : 5m  $n$ : 5 and  $\theta_l$ :  $6^\circ$  rigid origami dome pattern.

$r$ (m)	$n$	$\theta 1$ (°)	$\theta l$ (°)	$CD$		
5	5	6	30	6		
segments angle $\theta_i$ (°)		$\theta 1$	$\theta 2$	$\theta 3$	$\theta 4$	$\theta 5$
		6,00	12,00	18,00	24,00	30,00
segment length $s_i$ (m)		$s 1$	$s 2$	$s 3$	$s 4$	$s 5$
		0,5234	1,0453	1,5643	2,0791	2,5882
angle $A_i$ (°)		$A 1$	$A 2$	$A 3$	$A 4$	$A 5$
		87	84,00	81,00	78,00	75,00
interior angle $\beta_i$ (°)		$\beta 1$	$\beta 2$	$\beta 3$	$\beta 4$	
		171,00	165,00	159,00	153,00	
side length $a_i$ (m)		$a 1$	$a 2$	$a 3$	$a 4$	$a l$
		1,5643	2,5882	3,5837	4,5399	2,4615
folding angles $\alpha_{i1}$ $\alpha_{i2}$ (°)		$\alpha_{11}$	$\alpha_{21}$	$\alpha_{31}$	$\alpha_{41}$	$\alpha_{l1}$
		6,00	9,00	12,00	15,00	18,00
		$\alpha_{12}$	$\alpha_{22}$	$\alpha_{32}$	$\alpha_{42}$	$\alpha_{l2}$
		3,00	6,00	9,00	12,00	72,00
height $h_i$ (m)		$h 1$	$h 2$	$h 3$	$h 4$	$h l$
		0,0547	0,1635	0,3252	0,5381	0,7998

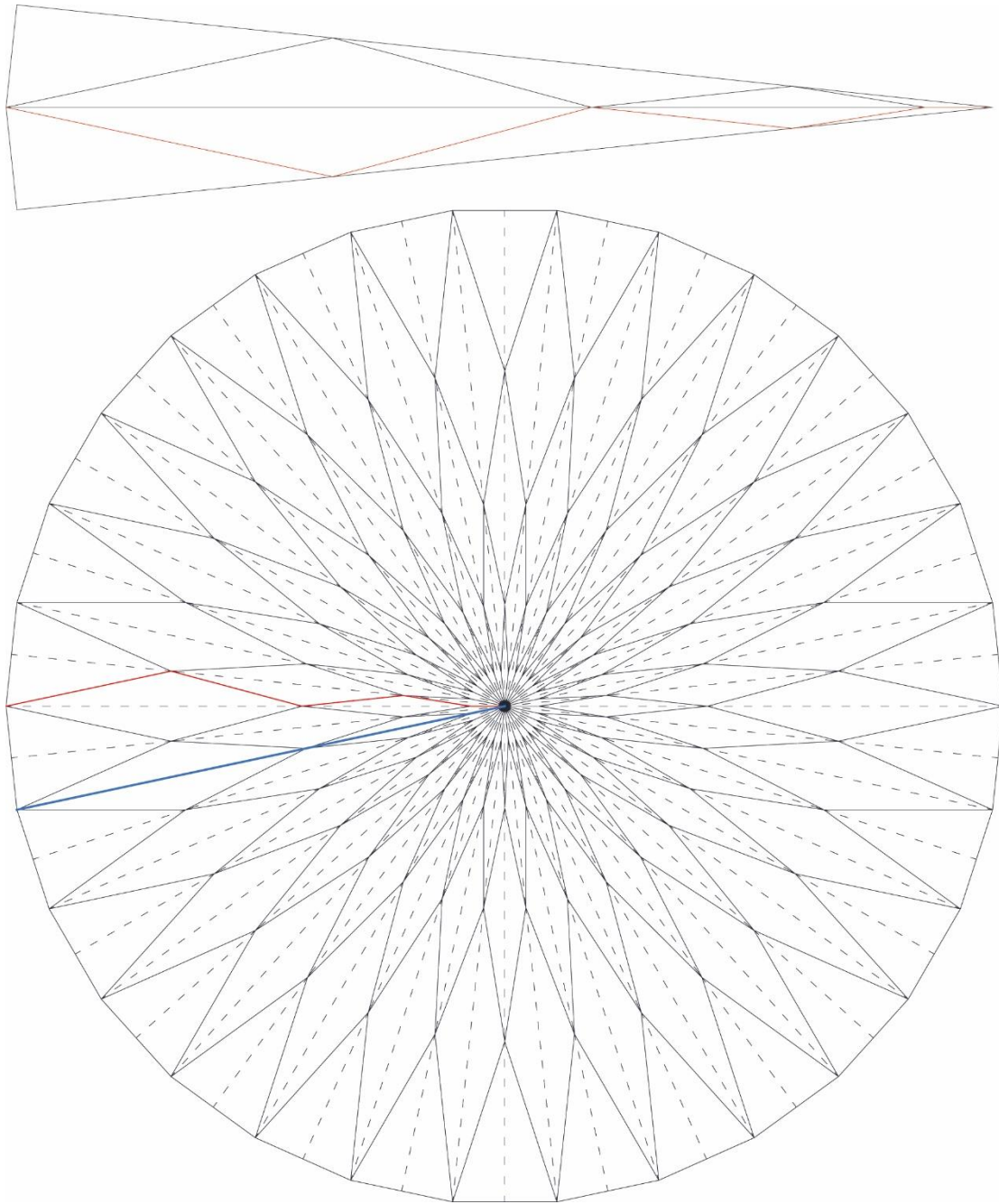


Figure 4.5. MV-Pattern for a dome with  $r: 5m$ ,  $n: 5$ ,  $\theta_I: 6^\circ$ .

#### 4.2.2. Partially Folded State

In this section the geometrical properties of the partially folded state will be analyzed. In contrary to single centered rigid origami barrel vaults, rigid origami pseudo-dome structures have multiple bending angles, because of the general geometry of the pattern.

The denotation of the bending angles  $\mu_i$  are in relation to the vertex's numbering, which is also in relation to the interior angle's number  $\beta_i$  (Figure 4.6). The vertexes are numbered starting from the central point of the pattern  $V_\theta$ , up to the decided number of segment  $V_i$ . Rigid origami barrel vault structures' patterns are regular polygons thus the relation of the bending angle  $\mu$  with the folding angle  $\alpha$ , in degree-6 vertexes are the same (eq. (3.12)). As it has been presented in the previous section, the folding angles  $\alpha_{i1}$  and  $\alpha_{i2}$  are different for each vertex. Thus, for a pseudo-dome pattern with degree-6 vertexes eq. (3.12) have been modified as eq. (4.17), where  $i$  is the number of the interior angle. Figure 4.6 shows the denotations for all angles and vertexes. The projected angles  $\delta$  of the folding angles and their respected folding angles  $\alpha$  have the same denotation. It is assumed that both the inclination angles  $\sigma$ , and dihedral angles  $\varphi$ , are the same for each fold.

$$\mu_i^6 = \pi - 2(\delta_{(i-1)2} + \delta_{(i+1)1}) \quad (4.17)$$

The calculations for the projected angle  $\delta_{(i-1)2}$  is done using the length of the crease lines between the vertexes, thus the lines are denoted based on their vertexes' number in the end points.

$$\delta_{(i-1)2} = \tan^{-1} \left( \frac{V_{(i-1)d}V_{(i-1)c}}{V_{ia}V_{(i-1)c}} \right) \quad (4.18)$$

The lines  $V_{(i-1)d}V_{(i-1)c}$  and  $V_{ia}V_{(i-1)c}$  are calculated as follows:

$$V_{(i-1)d}V_{(i-1)c} = \sin\sigma \cdot h_{(i-1)} \quad (4.19)$$

$$V_{ia}V_{(i-1)c} = \frac{h_{(i-1)}}{\tan\alpha_{(i-1)2}} \quad (4.20)$$

Substituting eqs. (4.19) and (4.20) in eq.(4.18) the equation for the projected angle becomes as follows:

$$\delta_{(i-1)2} = \tan^{-1}(\sin\sigma \cdot \tan\alpha_{(i-1)2}) \quad (4.21)$$



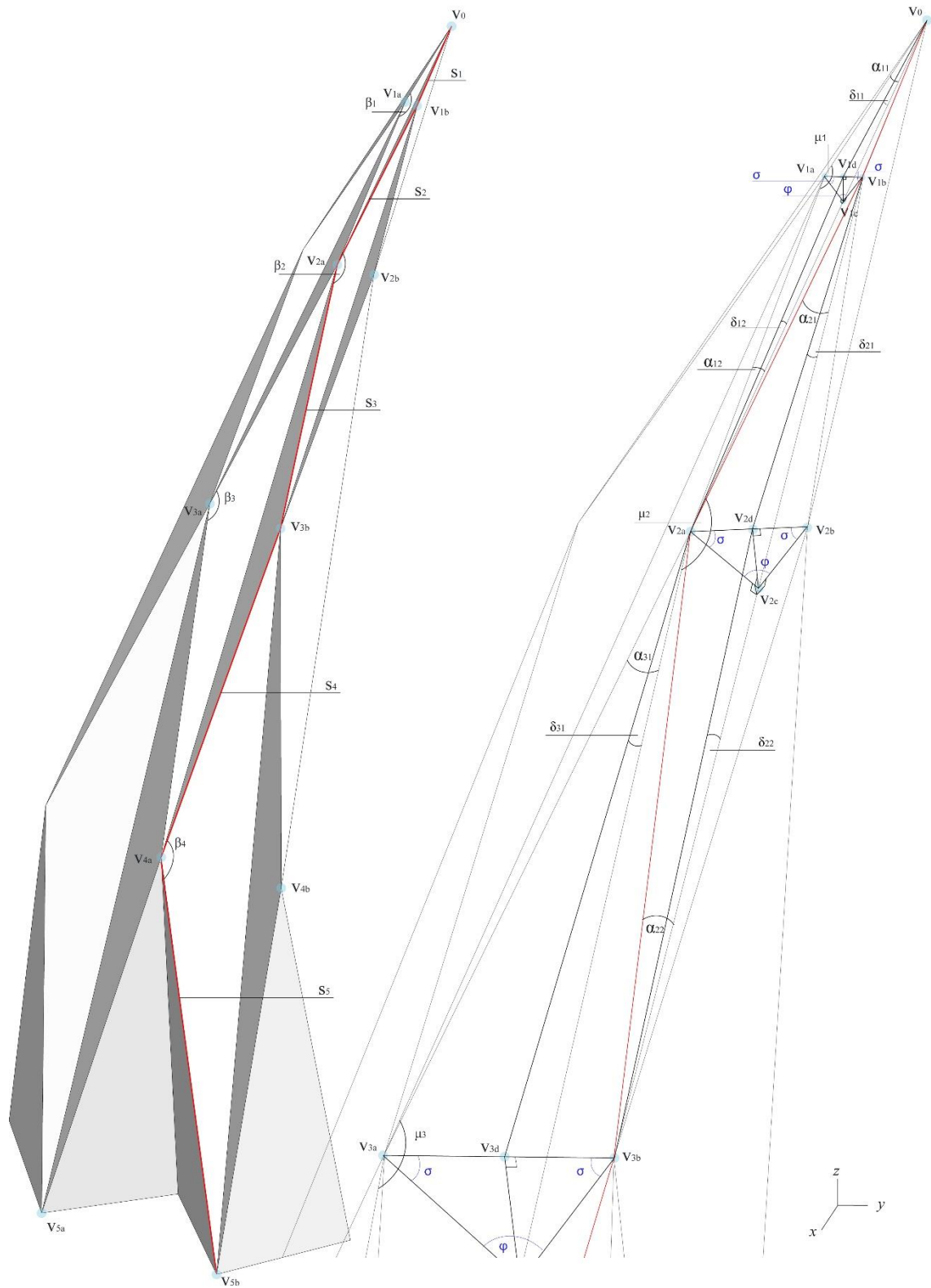


Figure 4.6. Parameters of a partially folded state of a dome with  $r: 5\text{m}$ ,  $n: 5$ ,  $\theta_1: 6^\circ$ .

The calculations for the projected angle  $\delta_{(i+1)1}$  are as follows:

$$\delta_{(i+1)1} = \tan^{-1} \left( \frac{V_{(i+1)d}V_{(i+1)c}}{V_{ia}V_{(i+1)c}} \right) \quad (4.22)$$

The lines  $V_{(i+1)d}V_{(i+1)c}$  and  $V_{ia}V_{(i+1)c}$  are calculated as follows:

$$V_{(i+1)d}V_{(i+1)c} = \sin\sigma \cdot h_{(i+1)} \quad (4.23)$$

$$V_{ia}V_{(i+1)c} = \frac{h_{(i+1)}}{\tan\alpha_{(i+1)1}} \quad (4.24)$$

Substituting eqs. (4.23) and 84.24) in eq. (4.22) the projected angles becomes:

$$\delta_{(i+1)1} = \tan^{-1}(\sin\sigma \cdot \tan\alpha_{(i+1)1}) \quad (4.25)$$

Substituting eqs. (4.21) and (4.25) in eq.(4.17) the relation between the bending angle  $\mu$  and the inclination angle  $\sigma$  becomes:

$$\mu_i^6 = \pi - 2(\tan^{-1}(\sin\sigma \cdot \tan\alpha_{(i-1)2}) + \tan^{-1}(\sin\sigma \cdot \tan\alpha_{(i+1)1})) \quad (4.26)$$

As it can be observed in Figure 4.6 the first vertexes following the central point are degree-4 vertexes. The relation between the bending angle  $\mu$  and the projected angles  $\delta$  of the folding angles for degree-4 vertexes is:

$$\mu_i^4 = \pi - 2(\delta_{(i+1)1}) \quad (4.27)$$

Same relation has been applied to calculate the first bending angle creating eq. (4.28):

$$\mu_i^4 = \pi - 2(\tan^{-1}(\sin\sigma \cdot \tan\alpha_{(i+1)1})) \quad (4.28)$$

The dihedral angle  $\varphi$  is calculated by eq. (4.29):

$$\varphi = \pi - 2\sigma \quad (4.29)$$

The association of the angles in degree-6 vertexes in their initial and final folded state can be described as:

$$\mu_{imin}^6 = \pi - 2 \left( \left( \tan^{-1}(\sin \sigma \cdot \tan \alpha_{(i-1)2}) \right) + \left( \tan^{-1}(\sin \sigma \cdot \tan \alpha_{(i+1)1}) \right) \right) = \pi \quad (4.30)$$

$$\begin{aligned} \mu_{imax}^6 &= \pi - 2 \left( \left( \tan^{-1}(\sin \sigma \cdot \tan \alpha_{(i-1)2}) \right) + \left( \tan^{-1}(\sin \sigma \cdot \tan \alpha_{(i+1)1}) \right) \right) \\ &= \pi - 2(\alpha_{(i-1)2} + \alpha_{(i+1)1}) \end{aligned} \quad (4.31)$$

The association of the angles in 4-edge vertexes are:

$$\mu_{imin}^4 = \pi - 2(\tan^{-1}(\sin \sigma \cdot \tan \alpha_{(i+1)1})) = \pi \quad (4.32)$$

$$\mu_{imax}^4 = \pi - 2(\tan^{-1}(\sin \sigma \cdot \tan \alpha_{(i+1)1})) = \pi - 2(\alpha_{(i+1)1}) \quad (4.33)$$

Table 4.2. Maximum and minimum values of the angles  $\mu$ ,  $\phi$ , and  $\sigma$  for a pseudo-dome pattern.

angles	Initial state (min)	Final folded state (max)
$\mu^6$ (bending angle)	$\pi$	$\pi - 2(\alpha_{(i-1)2} + \alpha_{(i+1)1})$
$\mu^4$ (bending angle)	$\pi$	$\pi - 2(\alpha_{(i+1)1})$
$\phi$ (dihedral angle)	$\pi$	0
$\sigma$ (inclination angle)	0	$\pi/2$

The designer may choose to select the dihedral angle, calculate the inclination angle using eq. (4.29), and then place the result to eq. (4.26); or he/she may choose to select the inclination angle and substitute it in eq. (4.26) to calculate each bending angle.

The relation of the bending angles of a dome presented in the previous section (Figures 4.5 and 4.6) with defined parameters  $r:5$   $n:5$   $\theta_I:6$  has been presented in Figure 4.7. The first bending angle  $\mu_I$  is a degree-4 vertex and the other ones are degree-6 vertexes.

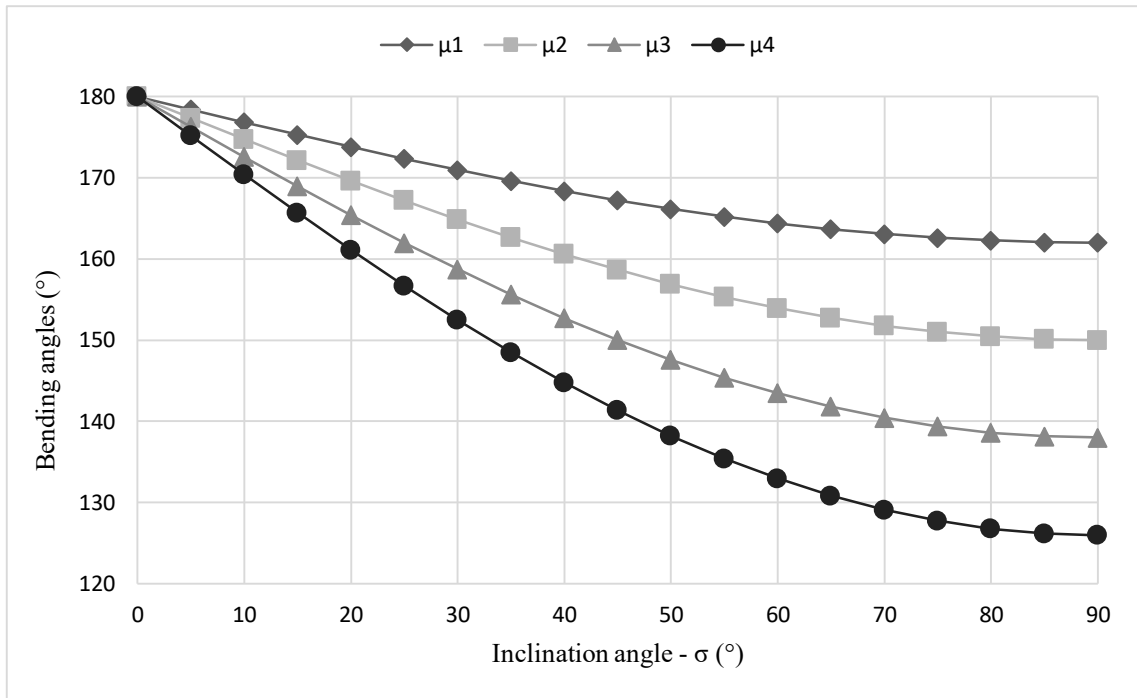


Figure 4.7. Relation between the bending angles and inclination angle for a dome  $r$ : 5m,  $n$ : 5,  $\theta_1$ :  $6^\circ$ .

### 4.2.3. Conclusion

In this section limitations have been discussed. For creating a pseudo-dome pattern the designer has to select some parameters: the radius  $r$ , the segment number  $n$ , and the degree of the first angle  $\theta_1$  to calculate the arithmetic series. These parameters allow the calculations of all the geometrical properties of the pattern. In this section a created pattern has also been tested in the RigidOrigami software created by Tachi (Tachi, 2009c).

Segmentation: for the pattern to be an approximation of a dome, the segmentation has to be created by an arithmetic sequence, so to have segments' length that increases from the top (center of the pattern) to the bottom of the structure, the following rule has to be satisfied. The last segment's angle has to be bigger than the first segment's angle:

$$\theta_n > \theta_1$$

Central Angle: the central point denoted as  $V_\theta$  in Figure 4.8, is the tip of the central angle. This angle needs to be a division of  $2\pi$ , to be able to create a full rigid origami dome structure.

There are some combinations of  $r$ ,  $n$  and  $\theta_I$  that do not produce a pattern or need a complementary triangle to produce a pattern. These combinations can be determined by the following rules:

- If  $\alpha_{21} + \beta_1 = 180^\circ$  the central angle is the folding angle  $\alpha_{11}$
- If  $\alpha_{21} + \beta_1 > 180^\circ$  the pattern's last triangles overlap thus no pattern can be created.
- If  $\alpha_{21} + \beta_1 < 180^\circ$  a complementary triangle is needed to determine the central angle (Figure 4.8).

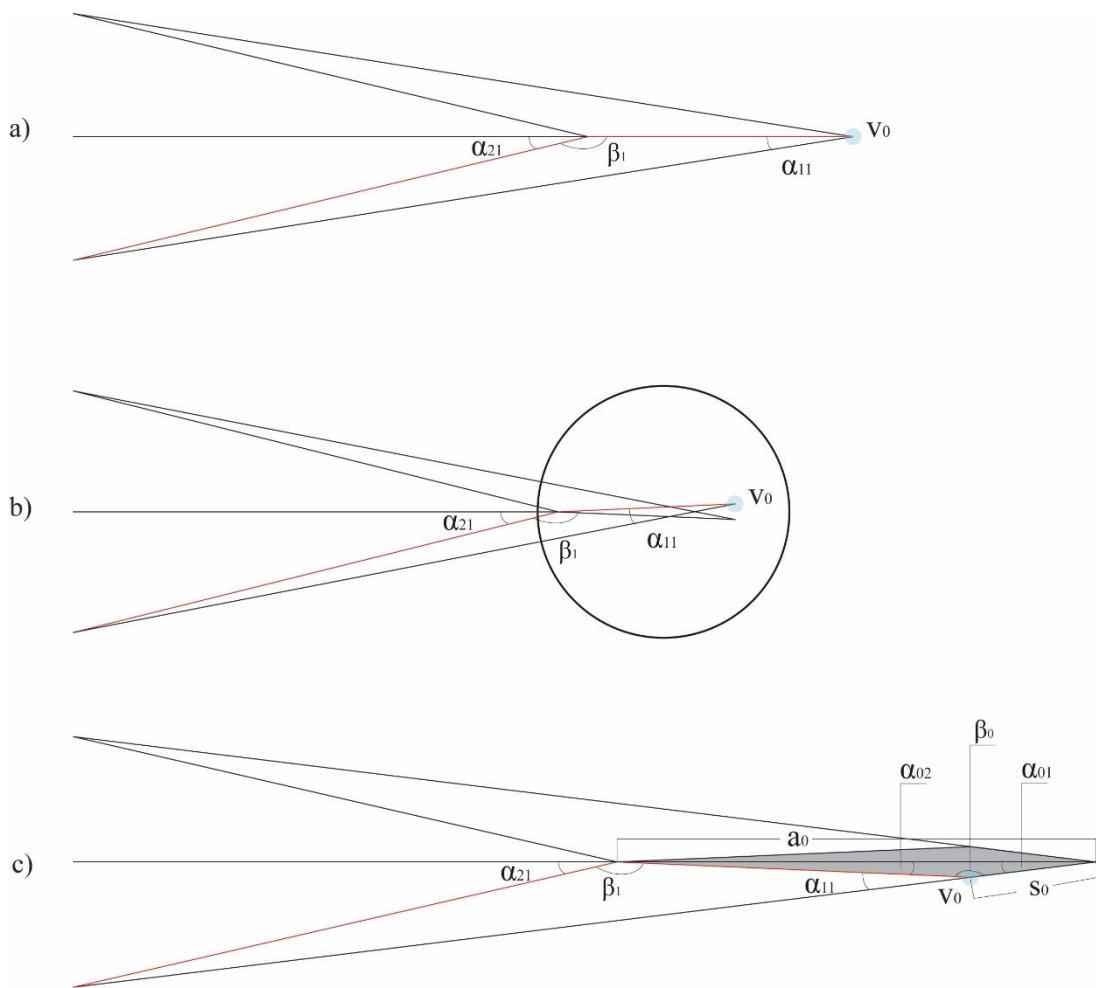


Figure 4.8. (a)  $r: 5m$ ,  $n: 4$ ,  $\theta_I: 9^\circ$  Pattern (b)  $r: 5m$ ,  $n: 4$ ,  $\theta_I: 6^\circ$  Overlapping Pattern (c)  $r: 5m$ ,  $n: 4$ ,  $\theta_I: 12^\circ$  Complementary Pattern.

In the third situation, where a complementary angle is needed, new parameters are included to the calculations denoted with the number zero, as it can be observed in Figure 4.8. The calculations are done as follows:

$$\beta_0 = \pi - \alpha_{11} \quad (4.34)$$

$$\alpha_{02} = \pi - (\beta_1 + \alpha_{21}) \quad (4.35)$$

$$\alpha_{01} = \pi - (\beta_0 + \alpha_{02}) \quad (4.36)$$

The side lengths  $s_0$  and  $a_0$  are calculated using the law of sines which gives eqs. (4.37) and (4.38), respectively:

$$s_0 = \frac{\sin \alpha_{02} \cdot s_1}{\sin \alpha_{01}} \quad (4.37)$$

$$a_0 = \frac{\sin \beta_0 \cdot s_1}{\sin \alpha_{01}} \quad (4.38)$$

The last parameter added is the bending angle  $\mu_0$  which can be calculated by eq. (4.28) because the  $V_0$  becomes a degree-4 vertex. It should not be forgotten that when this addition has been done to the pattern, the vertex  $V_1$  becomes a 6-edge vertex thus calculated by eq. (4.26).

Relation between number of segments  $n$  and the first segment angle  $\theta_1$ : The evaluation sheet created in Microsoft Excel 2013® shows the relation between the folding angle  $\alpha_{21}$  and the interior angle  $\beta_1$ , it also shows that there is a relation between the number of segments  $n$  the cross-section is divided and the first segment angle  $\theta_1$ ; both parameters being decided by the designer.

An analysis of these parameters is conducted to determine the geometrical relations. The arithmetic sequence can be described as follows:

$$\begin{aligned} 90^\circ &= \theta + \theta + CD + \theta + 2CD + \dots + n\theta + (n-1)CD \\ 90^\circ &= n\theta + \frac{n(n-1)}{2}CD \end{aligned} \quad (4.39)$$

where  $CD$  is the common difference,  $n$  is the number of segment and  $\theta$  is the first angle.

It has been defined that a pattern can be created if  $\alpha_{21} + \beta_1 = 180^\circ$ , this equation also means that  $\sin \alpha_{21} = \sin \beta_1$ : when this equality is substituted to the sine law presented in eq. (4.9) for the interior angle  $\beta_2$  the equation becomes:

$$\frac{\sin \beta_2}{a_2} = \frac{\sin \alpha_{21}}{s_3} \rightarrow \frac{\sin \beta_2}{a_2} = \frac{\sin \beta_1}{s_3} \quad (4.40)$$

All the parameters can be described in terms of the segment angle  $\theta$  and common difference  $CD$  in the following equations:

$$\beta_1 = A_1 + A_2 = \frac{\pi-\theta}{2} + \frac{\pi-(\theta+CD)}{2} = \pi - \theta - \frac{CD}{2} = \sin\left(\theta + \frac{CD}{2}\right) \quad (4.41)$$

$$\begin{aligned} \beta_2 &= A_2 + A_3 = \frac{\pi-(\theta+CD)}{2} + \frac{\pi-(\theta+2CD)}{2} \\ &= \pi - \theta - \frac{3CD}{2} = \sin\left(\theta + \frac{3CD}{2}\right) \end{aligned} \quad (4.42)$$

$$a_2 = 2r \cos\left(\frac{\pi-2\theta-3CD}{2}\right) = 2r \sin\left(\theta + \frac{3CD}{2}\right) \quad (4.43)$$

$$s_3 = 2r \sin\left(\frac{\theta}{2} + CD\right) \quad (4.44)$$

Eq. (4.45) is obtained when all these equalities (eqs. (4.41), (4.42), (4.43), and (4.44)) are substituted in eq. (4.40):

$$\begin{aligned} \sin\left(\theta + \frac{3CD}{2}\right) \cdot 2r \sin\left(\frac{\theta}{2} + CD\right) &= \sin\left(\theta + \frac{CD}{2}\right) \cdot 2r \sin\left(\theta + \frac{3CD}{2}\right) \\ \frac{\theta}{2} + CD &= \theta + \frac{CD}{2} \\ \theta &= CD \end{aligned} \quad (4.45)$$

A new condition is created where if the first segment angle  $\theta$  is equal to the common difference  $CD$  a pattern can be created without a complementary triangle. Also, when this equality is substituted in eq. (4.39) the relation between the number of segments  $n$  and the first segment angle  $\theta$  can be found (eq. (4.46)).

$$90^\circ = n\theta + \frac{n(n-1)}{2}\theta \rightarrow \theta = \frac{180^\circ}{n(n+1)} \quad (4.46)$$

This relation between the segment number  $n$  and the first segment's angle  $\theta_1$  prove that a close correlation exists between these parameters to design a pattern. So to be able to design a pattern without having to create a complementary triangle, the first angle's value should be calculated using eq. (4.46). In this case the only parameters the designer need to decide are the radius  $r$ , and the number of segments  $n$ . The initial calculation sheet has been modified to accommodate this correlation between the first segment's angle and segment number (Appendix E).

But in cases where the designer has a need to design a pattern with a complementary angle then, based on eq. (4.45) the rules for the central angle can be rewritten as:

- If  $\theta = CD$  a pattern can be created with the central angles  $\alpha_{11}$
- If  $\theta > CD$  because of the overlap no pattern can be created
- If  $\theta < CD$  a complementary triangle is needed to create the pattern.

In case a complementary angle is required to design a pattern the calculation sheet presented in Appendix F should be used for the new parameters.

A pattern with five segments (Figure 4.9) has been tested in RigidOrigami software created by Tachi (Tachi, 2009c), to see if the created pattern is a rigid folding pattern. The simulation demonstrated that during the folding process the central point sinks which is an unwanted motion (Figure 4.9). The degree-4 vertexes near the central point causes this unwanted motion as the cardboard model also showed by tearing from the mountain folds during the folding process (Figure 4.10, circles). Thus these mountain folds were transformed to cut lines separating the folds (Figure 4.11), and the new pattern has been tested again in the RigidOrigami Software (Tachi, 2009c) (Figure 4.12). By introducing cut lines the unwanted motion have been avoided. Another solution may be to remove the triangles that creates the degree-4 vertexes and create an oculus at the center.

To be able to achieve the initial creation of a dome (a 360 degree rotation along the z-axis) the pattern has been cut along one of the radial lines showed as a dark line in Figure 4.11.



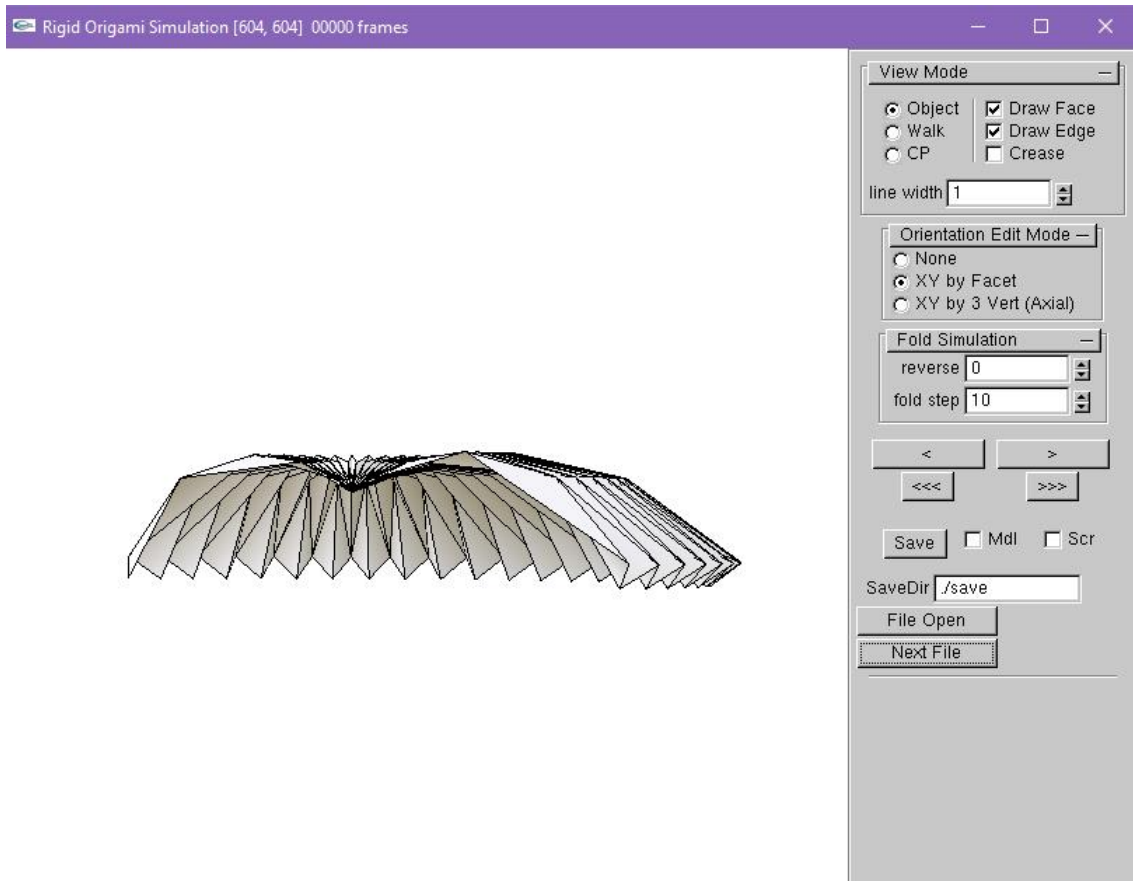


Figure 4.9.  $r$ : 5m,  $n$ : 5,  $\theta_1$ :  $6^\circ$  Pattern's simulation in RigidOrigami software (Tachi, 2009c).

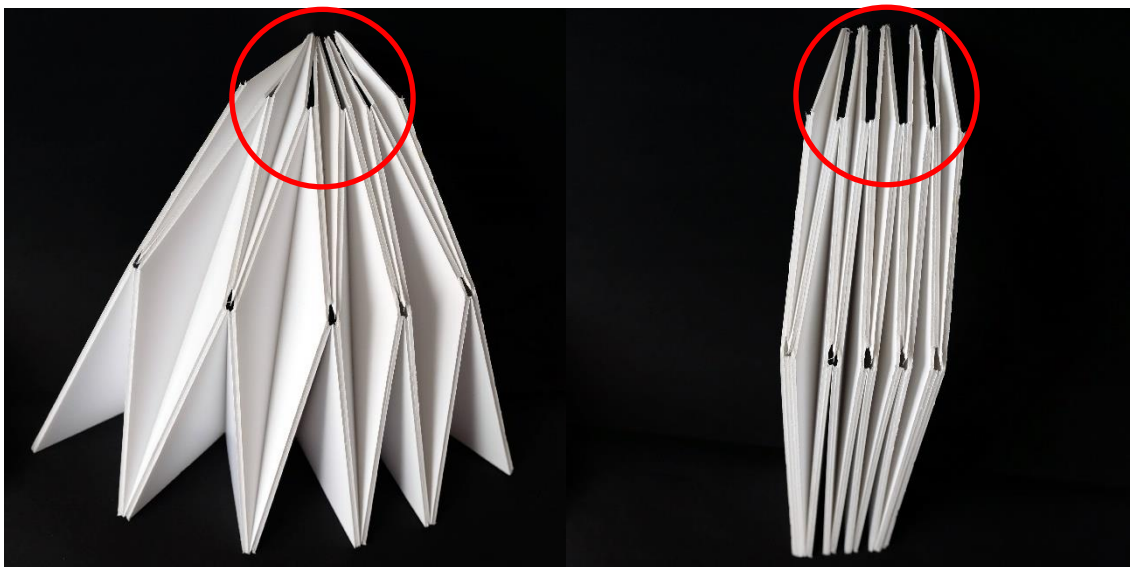


Figure 4.10. Model of  $n$ : 4 pseudo-dome created with shift-axis method.

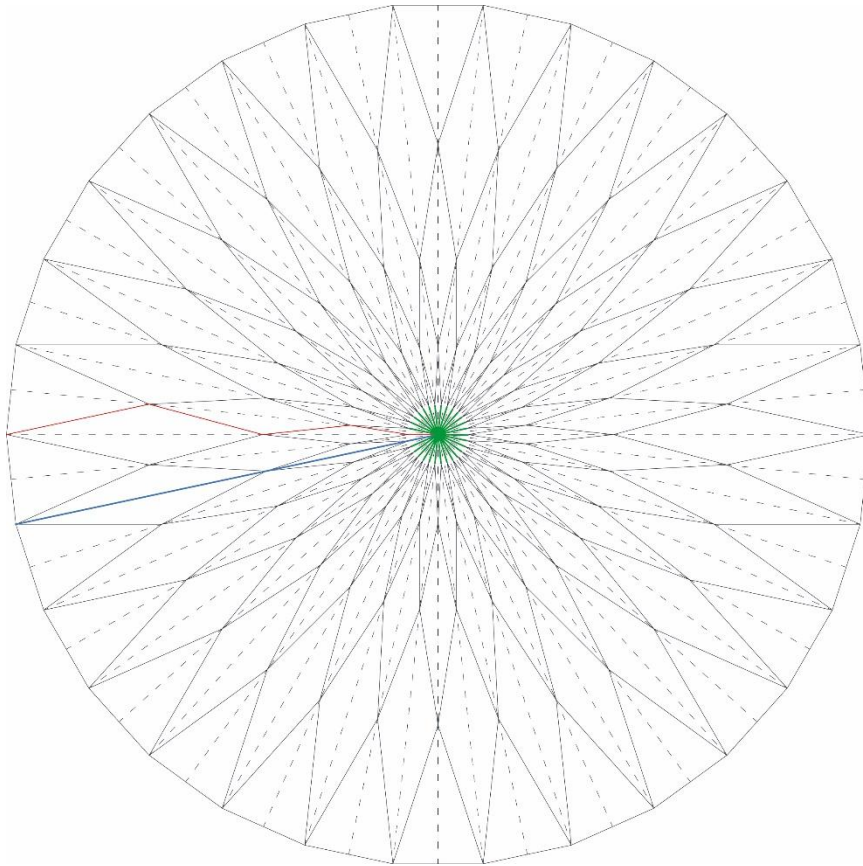


Figure 4.11.  $r: 5m$ ,  $n: 5$ ,  $\theta_I: 6^\circ$  Pattern. Red line: generator-line, Blue line: cut line, Green lines: cut lines.

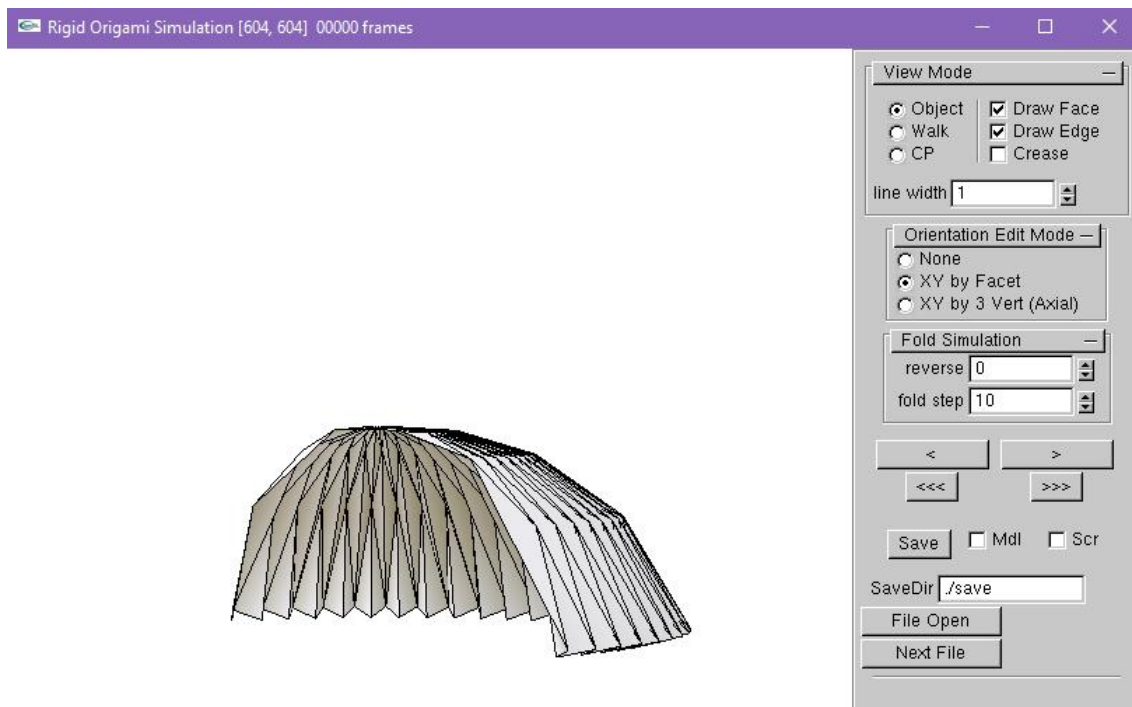


Figure 4.12.  $r: 5m$ ,  $n: 5$ ,  $\theta_I: 6^\circ$  Pattern with cut lines' simulation in RigidOrigami software (Tachi, 2009c).

### 4.3. Workspace Analysis

In this section the parameters will be analyzed during their deployment process. The first parameters required to do a workspace analysis are presented by a geometrical analysis. Then using these parameters the analyses of span, height, coverage area and volume is conducted.

The changes occurring during the folding process of the following parameters help understand the movement of the pattern (Figure 4.13). The parameters required are the radius  $r_d$ , the segments' angles  $\theta_{id}$ , the complementary angle  $A'i$  and the angle  $\rho_i$  which is the projected angle of the folding angles.

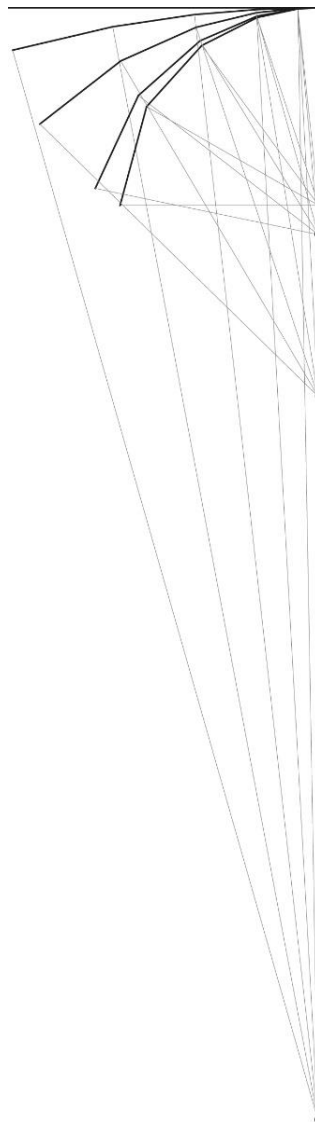


Figure 4.13. Pattern-generator's motion during folding process of a pseudo-dome cross-section.

When the final folded state of the pattern is analyzed (Figure 4.14) an interesting relation between the angles  $A_i$  and the segment's angle  $\theta_i$  along with the folding angles  $\alpha_i$  can be observed (eq. (4.47)). The triangle created by the two segment's angles  $\theta_i$  and  $\theta_{(i+1)}$  with the interior angle's segment length  $a_i$  gives the following equation:

$$A_i - \alpha_{i1} + A_{i+1} - \alpha_{i2} + \theta_i + \theta_{i+1} = 180^\circ \quad (4.47)$$

The angles  $A_i$  in eq. (4.47) can be substituted using eq. (4.6) which gives an equality between the folding angles and the segment's angles (eq. (4.48)).

$$90 - \frac{\theta_i}{2} - \alpha_{i1} + 90 - \frac{\theta_{i+1}}{2} - \alpha_{i2} + \theta_i + \theta_{i+1} = 180^\circ$$

$$\frac{\theta_i + \theta_{i+1}}{2} = \alpha_{i1} + \alpha_{i2} \quad (4.48)$$

This equality can also be described where these parameters are substituted by their deployment states (eq. (4.49)).

$$\frac{\theta_{id} + \theta_{(i+1)d}}{2} = \delta_{i1} + \delta_{i2} \quad (4.49)$$

The relation presented in eq. (4.49) helps to define the changes occurring during the folding process to the radius  $r_d$  (eq. (4.50)). It should be stated that, because of the geometry of the cross-section and the segmentation method, there are multiple equalities that can be reached to calculate the radius  $r_d$  during the development process:

$$r_d = \frac{a_i}{2 \sin\left(\frac{\theta_{id} + \theta_{(i+1)d}}{2}\right)} = \frac{a_i}{2 \sin(\delta_{i1} + \delta_{i2})} \quad (4.50)$$

The radius relation with the segment angles can also be described as:

$$r_d = \frac{s_i}{2 \sin\left(\frac{\theta_{id}}{2}\right)} \quad (4.51)$$

When both eqs. (4.50) and (4.51) are equated, the segment angles can be calculated independently using eq. (4.52).

$$\frac{a_i}{2 \sin(\delta_{i1} + \delta_{i2})} = \frac{s_i}{2 \sin\left(\frac{\theta_{id}}{2}\right)}$$

$$\theta_{id} = 2 \sin^{-1} \left( \frac{s_i \cdot \sin(\delta_{i1} + \delta_{i2})}{a_i} \right) \quad (4.52)$$

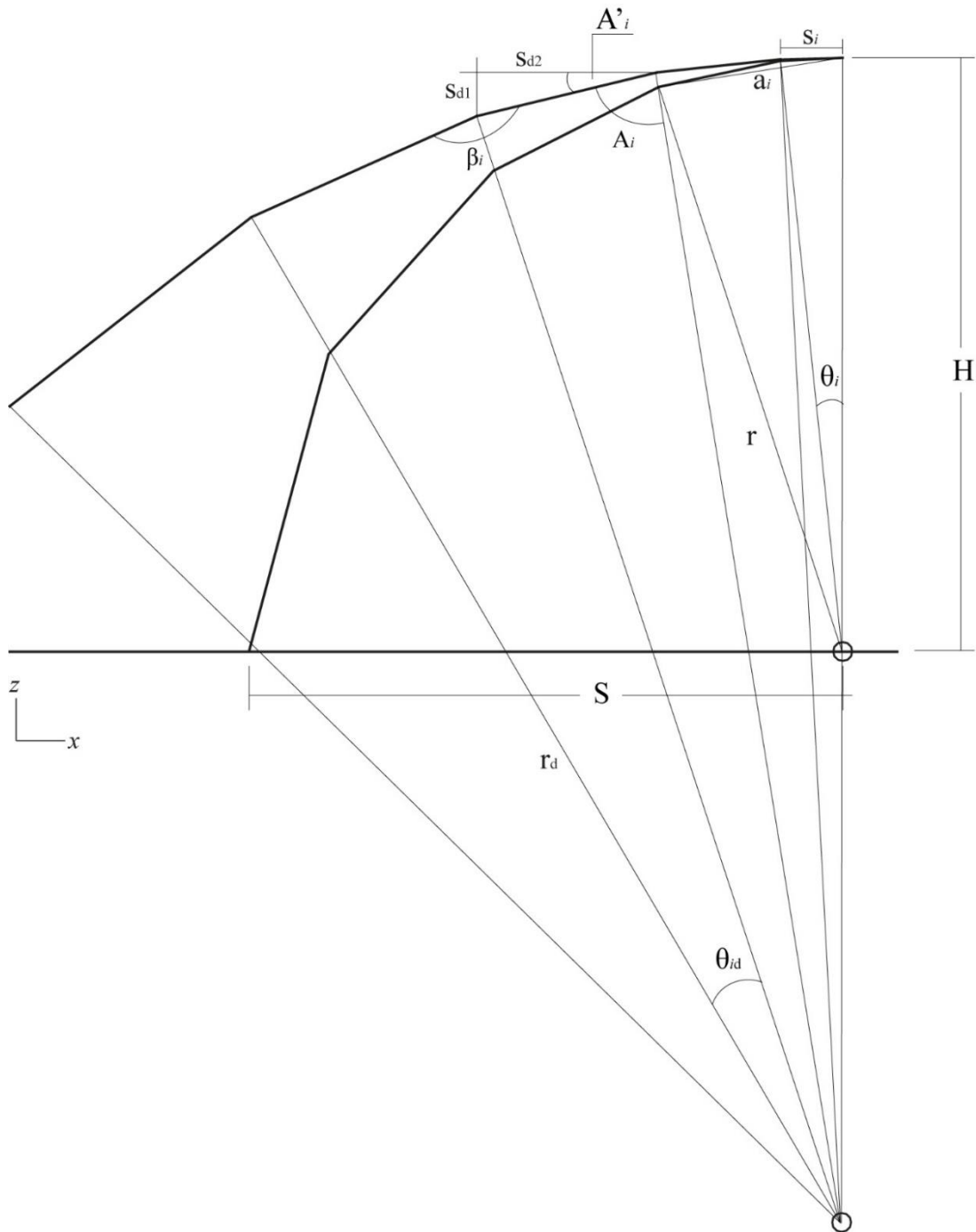


Figure 4.14. Parameters for pseudo-dome pattern-generator with  $r$ : 5m,  $n$ : 5,  $\theta_I$ :  $6^\circ$

Only the last segments' angle  $\theta_{id}$  is calculated differently using the following equation:

$$\theta_{id} = 2 \sin^{-1} \left( \frac{s_{(i+1)} \cdot \sin(\delta_{i1} + \delta_{i2})}{a_i} \right) \quad (4.43)$$

The reason for this difference lies in the following equality (eq. (4.54)) which is reached by equating the radius equation.

$$\frac{a_i}{2 \sin(\delta_{i1} + \delta_{i2})} = \frac{s_{(i+1)}}{2 \sin\left(\frac{\theta_i}{2}\right)} \quad (4.54)$$

The next parameter is the complementary angle  $A'_i$  which is required to calculate the span and height of the mechanism during its folding process. When the geometry of the angles  $A_i$  with their complementary angles  $A'_i$  is analyzed a relation between the complementary angles and the segment angles  $\theta_i$  can be reached.

$$A'_i = \frac{\theta_{id}}{2} + \sum_{k=1}^{i-1} \theta_{(i-k)d} \quad (4.55)$$

Each complementary angle is calculated separately because of the geometrical properties of the pattern. The growth of the complementary angles can be defined by the addition of all the previous segment's angles added to their respective half segment's angles.

The last parameter required to be able to calculate the span, height and coverage area is the angle  $\rho_i$ . This angle is the projected angle of the folding angles  $\alpha$  on the  $xy$ -plane, unlike the projected angle  $\delta$  of the folding angle which is on the  $xz$ -plane (Figure 4.15).

First a general method to calculate the angle  $\rho$  is presented. Then, because the pattern-generator does not lay on a plane when deployed, a method to calculate the projected segment length  $s'_i$  is presented based on the angle  $\rho$ .

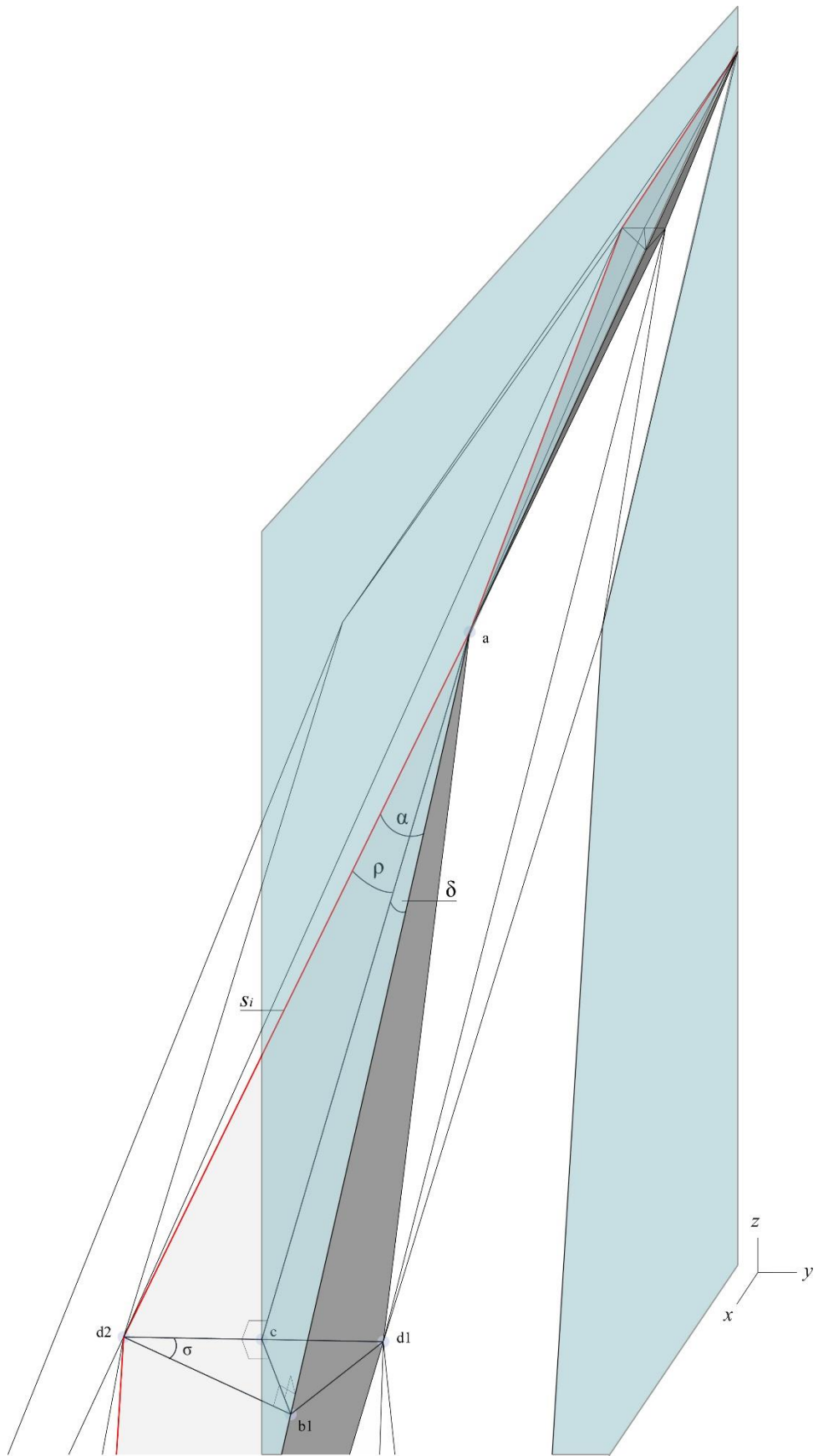


Figure 4.15. Parameters for a pseudo-dome.

Eqs. (4.56), (4.57) and (4.58) present the relation between the folding angle  $\alpha$ , the projected angle  $\rho$  and the inclination angle  $\sigma$ , which can be observed in Figure 4.15.

$$ad_1 = \frac{d_1 b_1}{\sin \alpha} \quad (4.56)$$

$$cd_1 = d_1 b_1 \cdot \cos \sigma \quad (4.57)$$

$$\sin \rho = \frac{cd_1}{ad_1} \quad (4.58)$$

When eqs. (4.56) and (4.57) are substituted in eq. (4.58) the sine of the angle  $\rho$  can be calculated using eq. (4.59). Eq. (4.59) is simplified in eq. (4.60) which gives a general calculation method for the projected angles  $\rho_i$ .

$$\sin \rho = \frac{d_1 b_1 \cdot \cos \sigma}{\frac{d_1 b_1}{\sin \alpha}} = \cos \sigma \cdot \sin \alpha \quad (4.59)$$

$$\rho = \sin^{-1}(\cos \sigma \cdot \sin \alpha) \quad (4.60)$$

The limits of this angle are defined by the inclination angle  $\sigma$ ;

- Final folded state  $\sigma = \pi/2$  then  $\rho = 0$
- Initial state  $\sigma = 0$  then  $\rho = \alpha_{11}$

As it has been demonstrated, all folding angles are different for a pattern denoted based on the interior angle's number and their location to the central point. For the eq. (4.60) to be specified based on the folding angles the equation can be presented as eq. (4.61) for folding angles  $\alpha_{i1}$  and eq. (4.62) for folding angles  $\alpha_{i2}$ .

$$\rho_{i1} = \sin^{-1}(\cos \sigma \cdot \sin \alpha_{i1}) \quad (4.61)$$

$$\rho_{i2} = \sin^{-1}(\cos \sigma \cdot \sin \alpha_{i2}) \quad (4.62)$$

The folding angle  $\alpha$  creating the central point of the pattern is used to calculate the central angle  $\rho_T$ . In case it is a pattern where the condition  $\theta_1 = \mathbf{CD}$  is achieved the folding angle  $\alpha_{11}$  is used. But if the pattern has been created as a complementary pattern where  $\theta_1 > \mathbf{CD}$  then the calculations for the central angle are done with the folding angle  $\alpha_{01}$ .



As it can be observed in Figure 4.15, the pattern-generator does not lay on a plane, thus calculations for height and span cannot be performed accurately unless the segment lengths are projected on a plane. The  $xz$ -plane, that the segment lengths  $s_i$  have been projected, passes through the interior angle length  $a_1$  and  $a_3$  as it can be observed in Figure 4.15. The  $xz$ -plane, which is assumed as the plane of calculations, passes through the odd numbered interior segment length  $a_i$ . The folding angles required for the calculation of the projected segment length are defined by the number of the interior angle length numbers.

The projected segment length is denoted as  $s'_i$  and it coincides to line  $ac$  on Figure 4.15. The projected folding angle  $\rho_{i1}$  and  $\rho_{i2}$  are used to calculate  $s'_{i1}$  for odd numbered segment lengths  $s_i$  (eq. (4.63)) and  $s'_{i2}$  for even numbered segment lengths (eq. (4.64)) respectively. The relation between these angles can be seen in Figure 4.14.

$$s'_{i1} = \cos \rho_{i1} \cdot s_i \quad (4.63)$$

$$s'_{i2} = \cos \rho_{i2} \cdot s_i \quad (4.64)$$

If the number of segments is odd, the last segment of the sequence is calculated using the last folding angle's projected angle  $\rho_{i1}$  (eq. (4.65)).

$$s'_n = \cos \rho_{i1} \cdot s_n \quad (4.65)$$

The following section presents the calculations of the height, span and coverage area using the parameters presented in this section.

### 4.3.1. Height, Span and Coverage Area

The calculations for the height, span, and coverage area of the pseudo-dome structure are carried out based on the geometrical properties of the pattern-generator (Figure 4.16). To calculate the height and span each segment length is projected to  $z$ -axis ( $s_{d1i}$ ) and  $x$ -axis ( $s_{d2i}$ ), respectively (Figure 4.14).

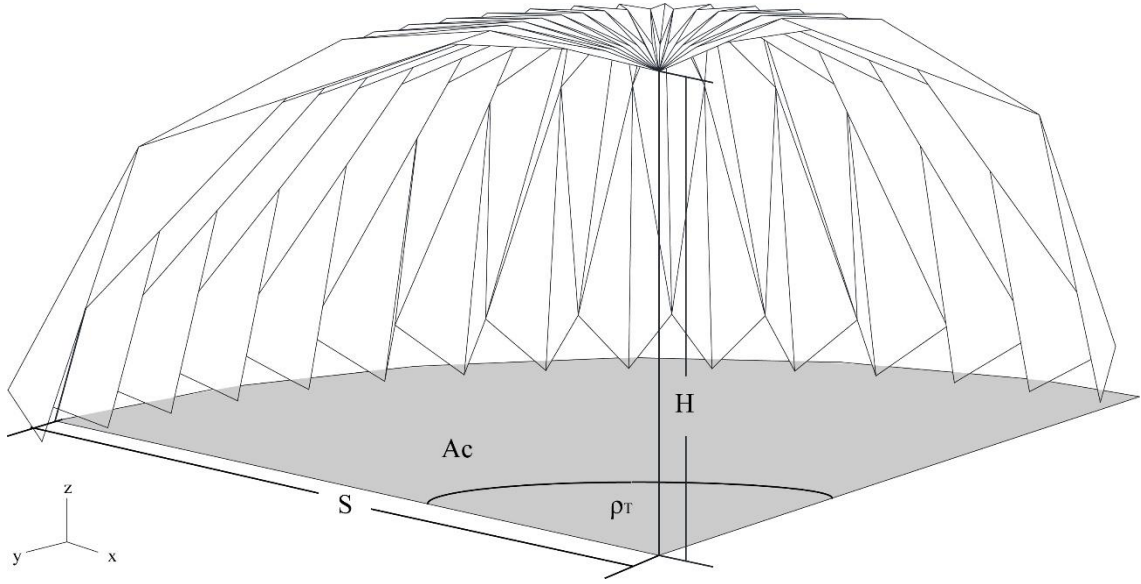


Figure 4.16. Height, Span and Coverage Area illustration for a  $n: 5$  and  $\sigma: 40^\circ$  pseudo-dome

Height: the height is calculated by adding all the projected lengths  $s_{dli}$  for each segment. A single segment is calculated as follows:

$$s_{dli} = s'_i \cdot \sin A'_i \quad (4.66)$$

The parameter  $A'_i$  needs to be calculated separately for each segment using eq. (4.55). The parameter  $s'_i$  is the general denotation for the projected segment length which is calculated separately as explained in the previous section.

The height of the pseudo-dome is calculated by adding all  $s_{dli}$  using the following equation (eq. (4.67)):

$$H = \sum_{i=1}^n s'_i \cdot \sum_{i=1}^n \sin A'_i \quad (4.67)$$

As it can be observed in Figure 4.17, as the inclination increases the height increases reaching its full height in the final flat-folded state.

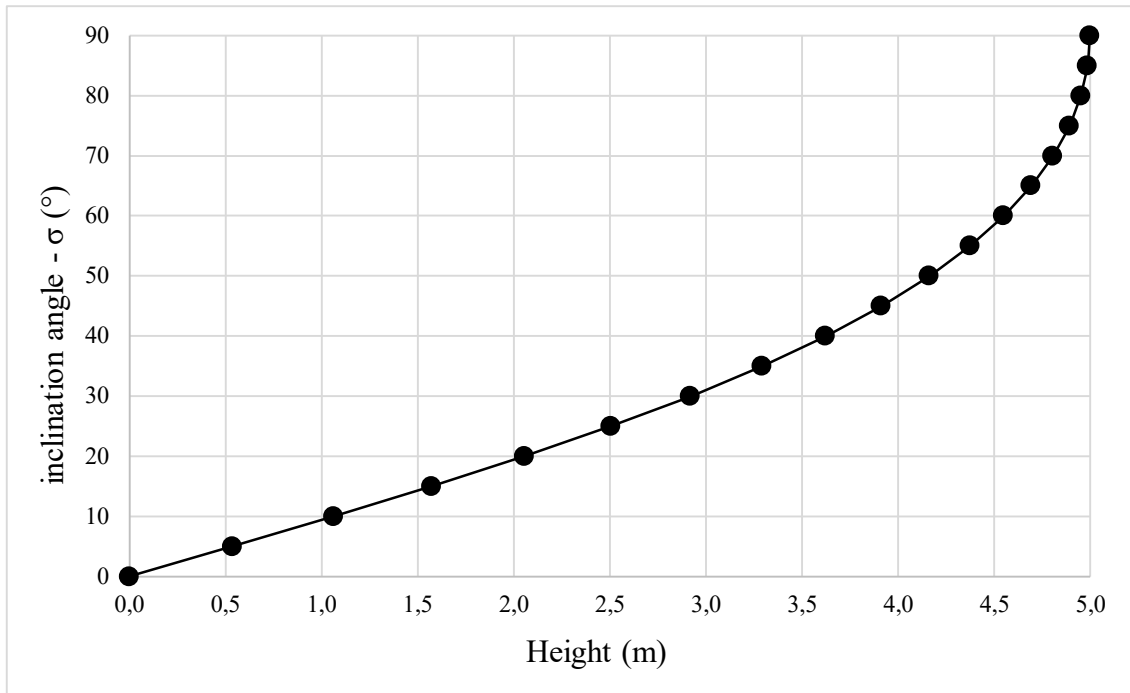


Figure 4.17. The relation between the inclination angle  $\sigma$  and the height  $H$  during the folding process of a pseudo-dome  $r$ : 5m,  $n$ : 4, and  $\theta_I$ :  $9^\circ$ .

Span: the span is calculated by adding projected lengths  $s_{di2}$  calculated for each segment. A single segment is calculated using the following equation:

$$s_{d2i} = s'_i \cdot \cos A'_i \quad (4.68)$$

As it was for the height calculation each  $A'_i$  and  $s'_i$  need to be calculated for each segment. The span of the pseudo-dome is calculated by adding all  $s_{d2i}$  using the eq. (4.69).

$$S = \sum_{i=1}^n s'_i \cdot \sum_{i=1}^n \cos A'_i \quad (4.69)$$

As it can be observed in Figure 4.18 as the inclination increases the height decreases reaching its minimum span in the final flat-folded state. The span is maximum in its initial state.

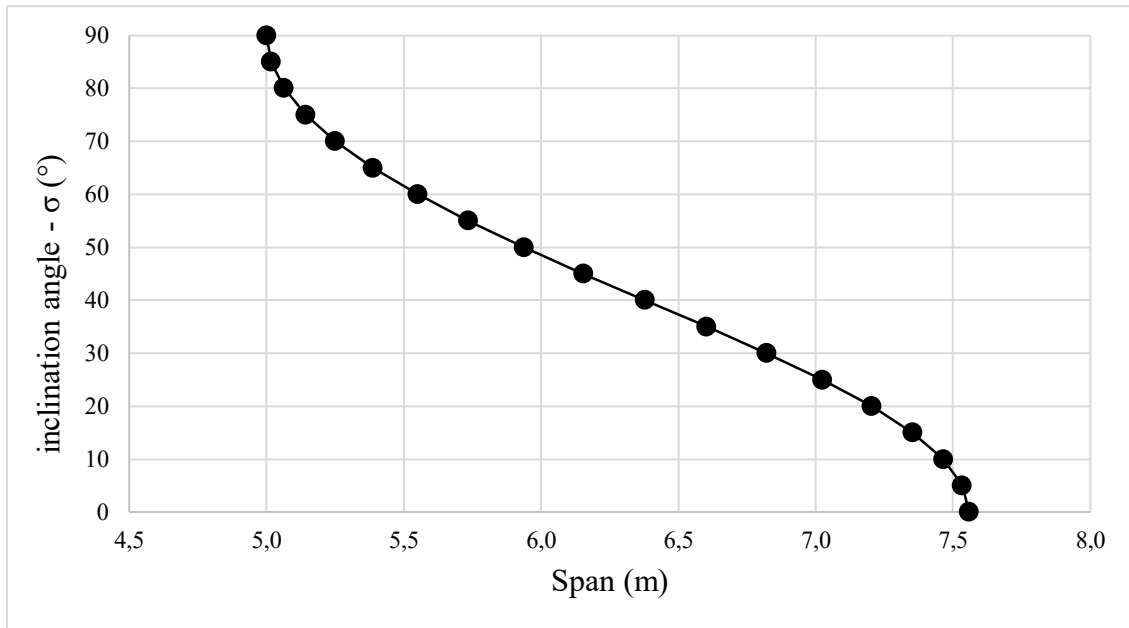


Figure 4.18. The relation between the inclination angle  $\sigma$  and the span  $S$  during the folding process of a pseudo-dome  $r$ : 5m,  $n$ : 4, and  $\theta_I$ :  $9^\circ$ .

Coverage Area: to be able to calculate the coverage area  $A_c$  the central angle  $\rho_T$  needs to be calculated based on the number of rows in the pattern. The calculations of the central angle is carried out by first defining the central angle of a single row based on the condition between the first segment's angle  $\theta_I$  and the common difference  $CD$ , then this angle is multiplied by the total number of rows  $R_T$ .

There are conditions to be able to calculate the total number of rows because the crease pattern is a central pattern and thus the number of row cannot be selected randomly. Table 4.3 presents these conditions, where depending on the relation between the first angle and common difference the central folding angle is selected, then this angle divide  $360^\circ$  which is the condition for developability, to calculate the total number of rows.

The quotient of the division presented in Table 4.3 is the number of rows  $R_T$ . There are cases where the divisor is not a multiplier of  $360^\circ$  or  $2\pi$ , in these cases the pattern is considered a non-developable one, because there will be a gap in the central angle. As explained on the geometrical analysis section's conclusion, even though the created pattern's central angle  $\rho_T$  is equal to  $2\pi$  the pattern needs to be cut so that it reaches a flat-folded final folded state that is a quarter of a circle.

Table 4.3. Conditions for selecting and calculating the total number of rows  $R_T$ .

condition	Folding angle $\alpha_{i1}$	Projected angle $\rho_{i1}$	$R_T$	condition
$\theta_1 = CD$	$\alpha_{11}$	$\rho_{11}$	$360^\circ / \alpha_{11}$	The quotient of the division need to be a natural number
$\theta_1 > CD$	$\alpha_{01}$	$\rho_{01}$	$360^\circ / \alpha_{01}$	

The central angle  $\rho_T$  is calculated using eq. (4.70) where the projected angle  $\rho_{i1}$  is selected based on whether the pattern is a pattern or a complimentary pattern.

$$\rho_T = \rho_{i1} \cdot R_T \quad (4.70)$$

Since all the parameters to calculate the coverage area  $A_c$  have been presented, it can be calculated using eq. (4.71) where  $S$  is the span calculated using eq. (4.69).

$$A_c = \frac{1}{2} \rho_T S^2 \quad (4.71)$$

As it can be observed in figure 4.19 as the inclination increases the coverage area decreases reaching its minimum area in the final flat-folded state.

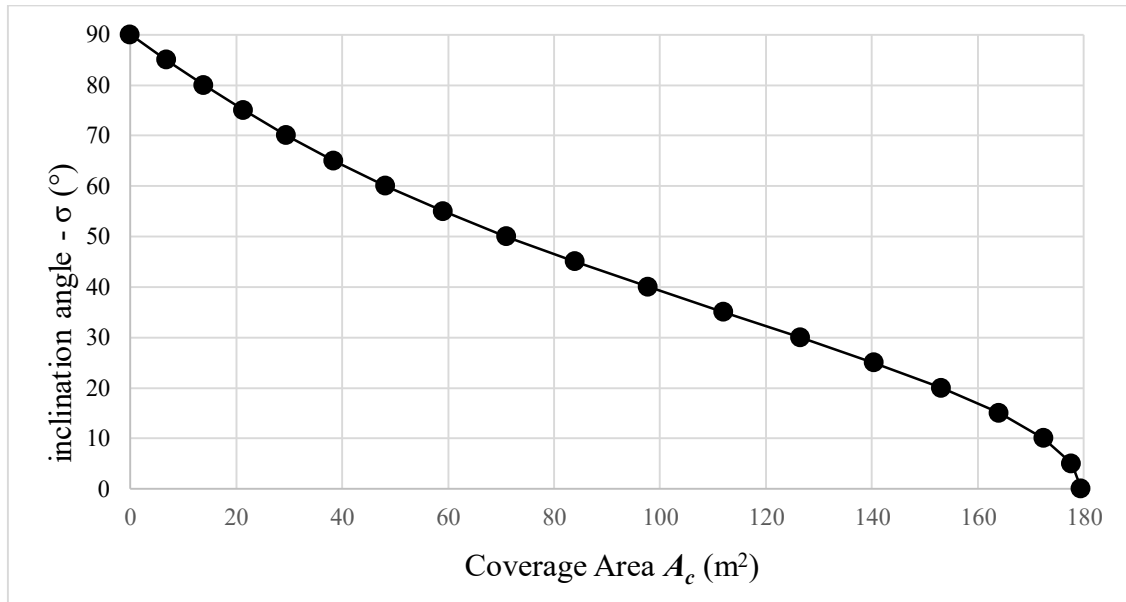


Figure 4.19. The relation between the inclination angle  $\sigma$  and the coverage area  $A_c$  during the folding process of a pseudo-dome  $r$ : 5m,  $n$ : 4, and  $\theta_1$ :  $9^\circ$ .

### 4.3.2. Volume

The volume is calculated using the *Pappus's Centroid Theorem* where the volume of a revolved solid is calculated by the product of the cross-section area  $A$  and the distance  $d_c$  the geometric centroid of the cross-section area travels (Weisstein) (eq. (4.72)).

$$V = A \cdot d_c \quad (4.72)$$

The cross-section area  $A$  of the pseudo-dome changes during the folding process reaching the quarter of a circle only on its final folded state. Until the final folded state the cross-section area is considered as a semi-parabola as it can be observed in Figure 4.20.

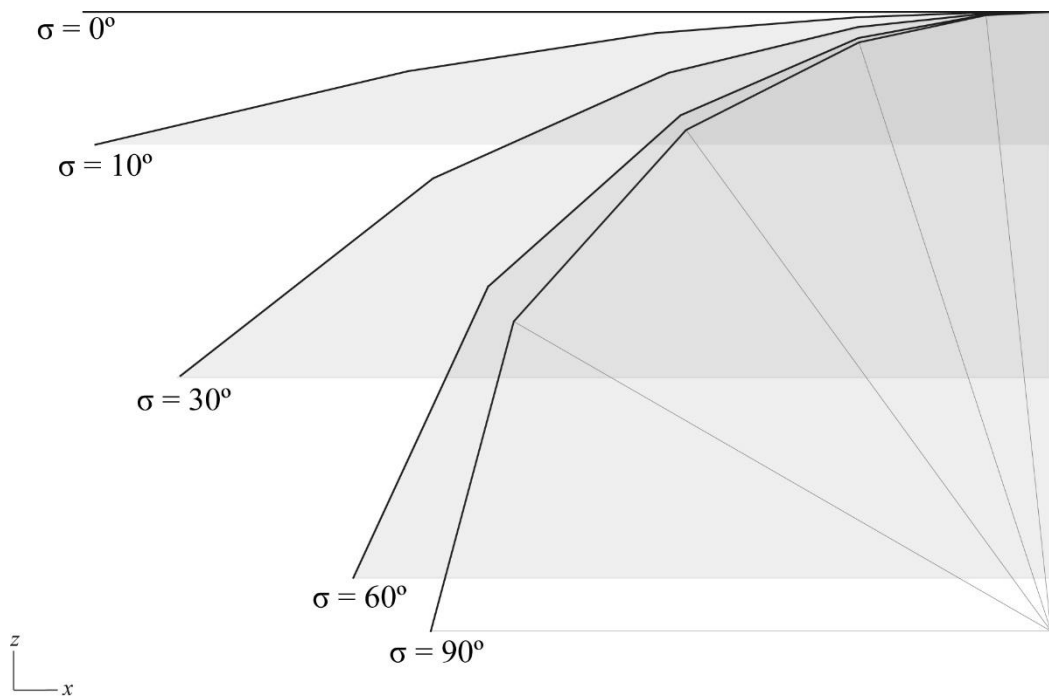


Figure 4.20. Pattern-generator's motion during folding process of a pseudo-dome cross-section. Inclination angle values  $90^\circ$ ,  $60^\circ$ ,  $30^\circ$ ,  $10^\circ$  and  $0^\circ$  from the initial state to final folded state.

The area of a semi parabola is calculated using eq. (4.73), where  $S$  is the span (eq. (4.69)) and  $H$  is the height (eq. (4.67)) of the pseudo-dome structure.

$$A = \frac{2SH}{3} \quad (4.73)$$

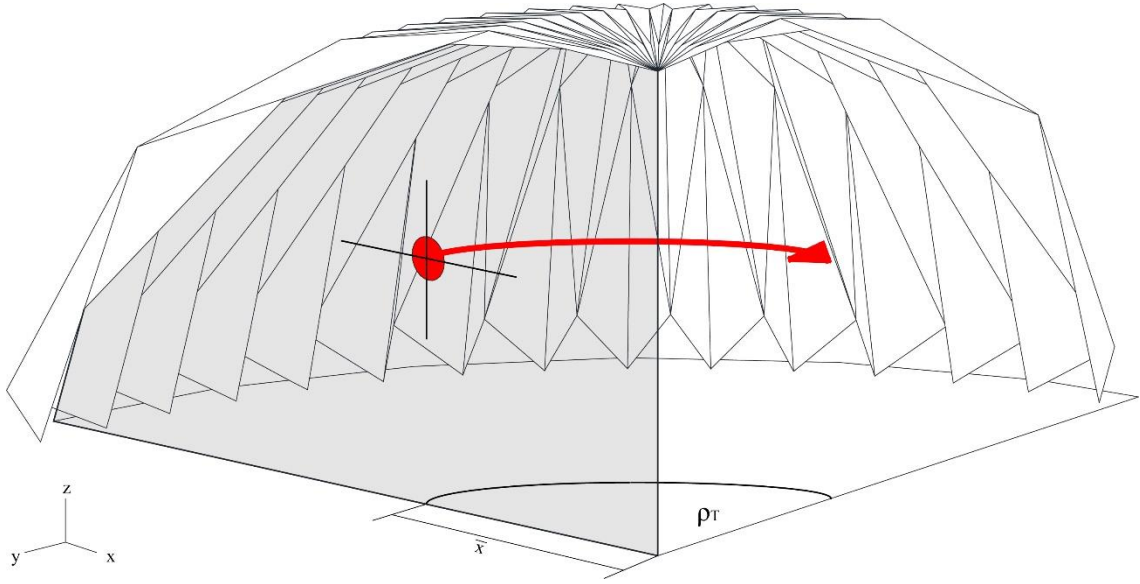


Figure 4.21. Parameters for the volume calculations of a pseudo-dome.

The parameters  $d_c$  is the distance the geometric centroid of a cross-section area travels and for a revolved solid this distance is equal to  $2\pi r$ , because the area is revolving around the z-axis (Figure 4.21). But in this case, because the revolution depends on the inclination angle  $\sigma$  and the central angle  $\rho_T$ , the calculation of  $d_c$  is done using the arc length equation. The radius  $r$  of the revolution in Pappus's theorem is equal to  $\bar{x}$  distance of the centroid and because of the geometry the radius depends on the span  $S$  of the pseudo-dome. The  $\bar{x}$  distance of the centroid is calculated in eq. (4.74) for the semi parabola geometries. And based on these parameters the equation to calculate the volume of a pseudo-dome rigid foldable structure is eq. (4.75), where eq. (4.73) and eq. (4.74) have been substituted in eq. (4.72).

$$d_c = \frac{3S}{8} \cdot \rho_T \quad (4.74)$$

$$V = \frac{2SH}{3} \cdot \frac{3S}{8} \cdot \rho_T = \frac{S^2 H \rho_T}{4} \quad (4.75)$$

For all the calculations in this section the central angle's  $\rho_T$  should be in radian.

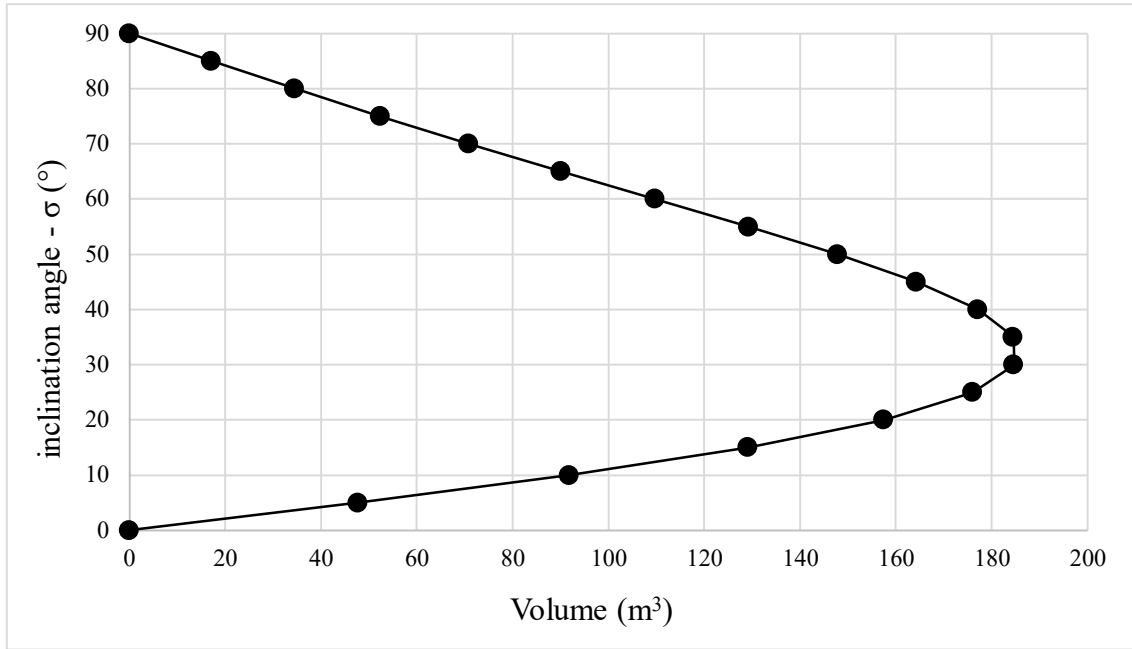


Figure 4.22. The relation between the inclination angle  $\sigma$  and the volume  $V$  during the folding process of a pseudo-dome  $r: 5\text{m}$ ,  $n: 4$ , and  $\theta_I: 9^\circ$ .

Figure 4.22 represents the volume of a pseudo-dome structure with  $n: 4$ ,  $r: 5\text{ m}$  and an first segment angle  $\theta_I: 9^\circ$  created with the volume equation (eq. (4.75)). As it can be observed, the volume has a rapid increase till it reaches its peak around the  $30^\circ$  of inclination angle then it slowly decreases to its final folded state, as it was in both barrel vaults' volume calculations.

#### 4.4. Mobility Analysis

This section analyses the mobility of patterns created to form a pseudo-dome with the same method used in the mobility analysis of rigid origami barrel vaults. First the number of loops will be calculated (eq. (4.76)), then the mobility will be calculated using Freudenstein and Alizade's mobility equation (eq. (4.77)). The complementary patterns' mobility analysis has not been presented. The analysis will be conducted with different number of segments. After calculating the pattern's mobility, the modified version where cut lines are introduced to the pattern will be calculated. All calculations will be verified with the structural group properties.

$$L = j - l + 1 \quad (4.76)$$



$$M_{nr} = \sum_{i=1}^j fi - \sum_{k=1}^L \lambda_k + q - j_p = \sum_{i=1}^j fi - \sum_{k=1}^L \lambda_k \quad (4.77)$$

where  $M$  is the mobility,  $nr$  is the number of segment and rows in a pattern,  $fi$  is the DOF for  $i^{th}$ -kinematic pair,  $\lambda_k$  is the degree of space or subspace of  $k^{th}$  loop,  $q$  is the number of excessive links and  $j_p$  is the number of passive joints. But because the analysis revealed that pseudo-dome origami mechanisms have no excessive links or passive joints the equation have been defined as such (eq. (4.77)).

#### 4.4.1. Double Row Patterns

In this section double row patterns with 3, 4 and 5 segments and a modified pattern (created by removing the joints located on the cut lines that has been presented in the conclusion of the geometrical analysis section of this chapter) will be analyzed.

3-segment pattern: Double row for three segments and first segment angle  $\theta_1$ :  $15^\circ$  has 6 links and 6 joints creating a single loop  $\lambda = 3$  (Figure 4.23). The calculation of the number of loop,  $L = 6 - 6 + 1 = 1$ , coincides with the kinematic diagram.

The mobility is equal to 3 when calculated with eq. (4.77):  $M_{32} = 6 - (1 \cdot 3) = 3$ .

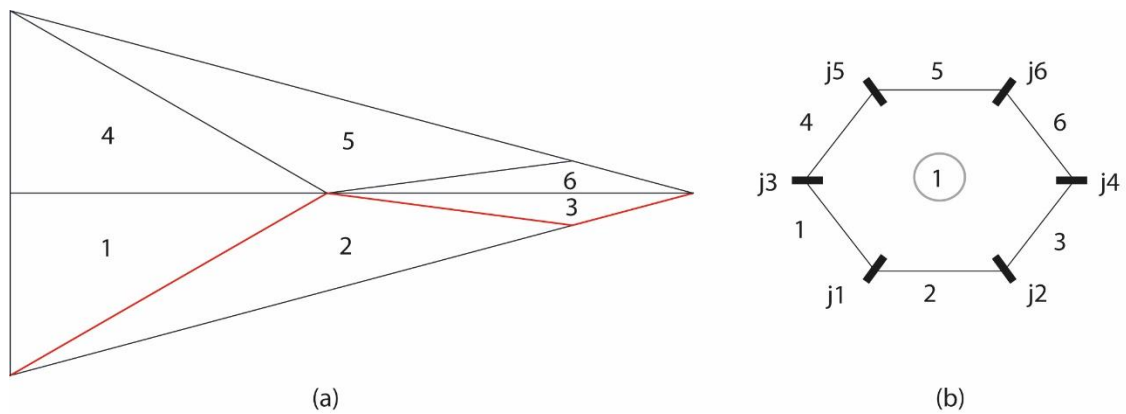


Figure 4.23.  $r$ : 5m,  $n$ : 3,  $\theta_1$ :  $15^\circ$  double row (a) crease pattern and (b) kinematic diagram.

4-segment pattern: Double row pattern with four segments and first segment angle  $\theta_1$ :  $9^\circ$  has 8 links and 9 joints creating two  $\lambda = 3$  loops (Figure 4.24). The loop calculations coincide with the kinematic diagram.

The mobility is equal to 3:  $M_{42} = 9 - (2 \cdot 3) = 3$ . When structural group properties are analyzed the mobility is the same value as the calculated one. The 1<sup>st</sup> loop is a spherical 6-bar loop which has a mobility of 3, to preserve this mobility 2 links need to be added to the system because it is a  $\lambda = 3$  mechanism. The links [4 and 8] are added preserving the mobility equal to 3 (Figure 4.24).

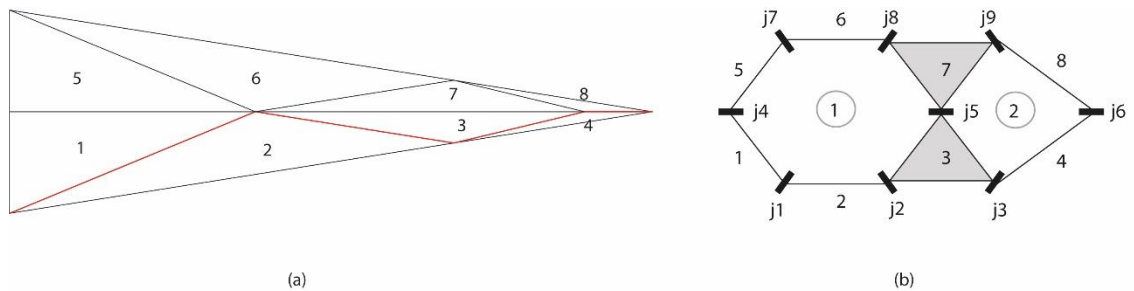


Figure 4.24.  $r$ : 5m,  $n$ : 4,  $\theta_1$ :  $9^\circ$  double row (a) crease pattern and (b) kinematic diagram.

5-segment pattern: Double row for a five segments and first angle  $\theta_1$ :  $6^\circ$  has 10 links and 11 joints creating two  $\lambda = 3$  loops (Figure 4.25). Again, the loop calculations coincide with the kinematic diagram.

The mobility is equal to 5 when calculated with eq. (4.77):  $M_{52} = 11 - (2 \cdot 3) = 5$ ; when the structural group properties are analyzed the mobility calculations are correct. The 1<sup>st</sup> loop is a 6-bar mechanism with mobility equals to 3 and it needs only 2 new links to preserve the mobility, but the 2<sup>nd</sup> loop adds 4 new links [4, 5, 9, and 10] which increases the mobility, as calculated, to 5.

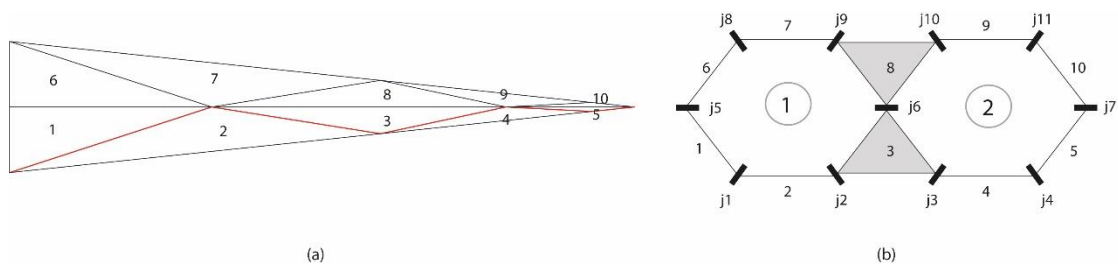


Figure 4.25.  $r$ : 5m,  $n$ : 5,  $\theta_1$ :  $6^\circ$  double row (a) crease pattern and (b) kinematic diagram.

### 4.4.2. 3-Row Patterns

In this section as it was in double row patterns, 3-row patterns with 3, 4 and 5 segments and their modified patterns will be analyzed.

3-segment pattern: A new row has been added to the double row to be able to analyze the mobility. A new row in three segmented pattern adds 3 new links and 4 new joints giving a total of 9 links and 10 joints (Figure 4.26). The new pattern has 2 loops which can also be calculated by eq. (4.76).

The mobility is equal to 4 when calculated with eq. (4.77):  $M_{33} = 10 - (2 \cdot 3) = 4$ . When the structural group properties are analyzed the mobility becomes also equal to 4. The 2<sup>nd</sup> loop, a 4-bar loop, is added to a 6-bar loop with mobility 3, and as stated before to preserve the mobility, the new loop should bring 2 new links [8 and 9] as it is the case. But there is 1 more link [7] which increases the mobility to 4.

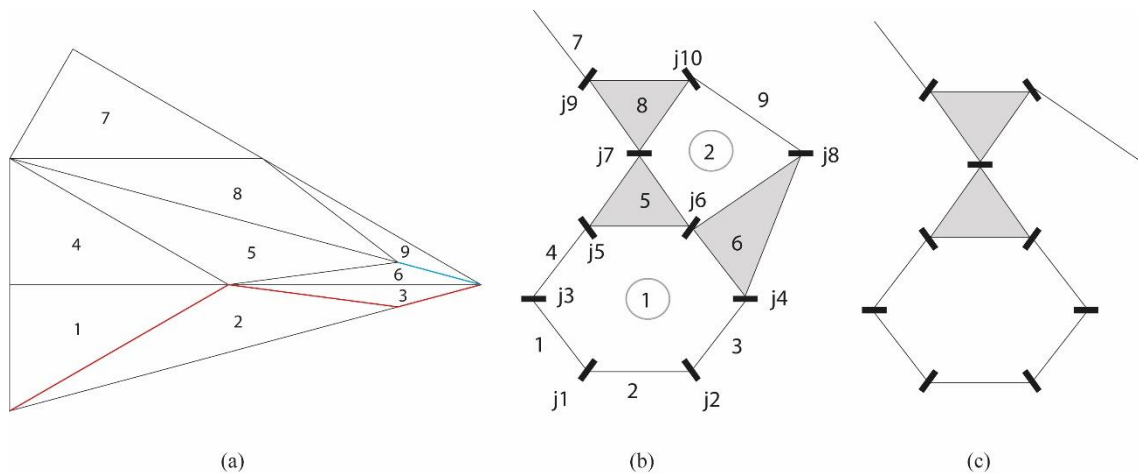


Figure 4.26.  $r: 5m$ ,  $n: 3$ ,  $\theta_l: 15^\circ$  three rows (a) crease pattern, (b) kinematic diagram, and the (c) modified kinematic diagram.

When the cutline is introduced, the joint number 8 is removed from the system, so the total number of links stays 9 but the number of joints decreases to 9. Removing this joint decreases the number of loops and increases the mobility:  $M_{33M} = 9 - (1 \cdot 3) = 6$ .

The mobility is equal to 6 when the structural group properties are analyzed where a 6-bar loop with mobility 3, is attached with 3 additional links, which justifies the mobility calculation of the modified pattern.

4-segment pattern: The three rowed four segmented pattern adds 4 new links and 5 new joints and a new  $\lambda = 3$  loop is added to the mechanism. The loop calculations confirm the number of loops using the eq. (4.76).

The mobility is calculated as 5 using the eq. (4.77):  $M_{43} = 14 - (3 \cdot 3) = 5$ . The 3<sup>rd</sup> loop adds 3 new links [10, 11 and 12]; the necessary number of links to preserve the mobility is equal to 2, thus the mobility increases by one becoming equal to 4. The link 9 is an additional link which adds 1 to the mobility. The mobility for this four segmented three row pattern is equal to 5 according to the structural group properties which is equal to the calculated mobility.

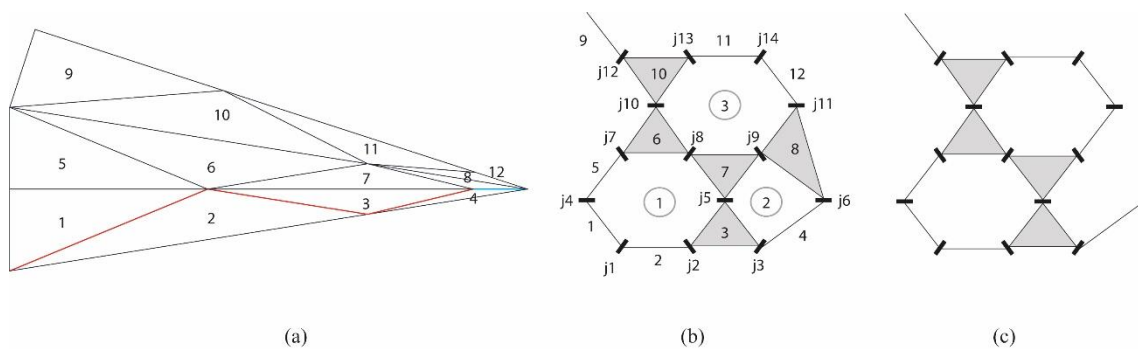


Figure 4.27.  $r: 5m, n: 4, \theta_I: 9^\circ$  three rows (a) crease pattern, (b) kinematic diagram, and the (c) modified kinematic diagram.

When the cut line is introduced to this mechanism, joint 6 is removed leaving the mechanism with a total of 13 joints and 12 links. Removing this joint breaks the loop number 2, changing the mechanism into a 2 looped mechanism. The calculated mobility is equal to 7:  $M_{43M} = 13 - (2 \cdot 3) = 7$ .

The mobility is also equal to 7 when the structural group properties are analyzed. The 6-bar loop has an addition of 4 links increasing the mobility to 5 and when the additional links [4 and 9] are added the mobility again increases by 2 to a total of 7, which justifies the calculations.

5-segment pattern: For the 3-row 5-segment pattern, 5 new links and 7 new joints are introduced making the total of 15 links and 18 joints. 2 new loops are added to the mechanism which is confirmed by the calculations.

The calculated mobility is equal to 6:  $M_{53} = 18 - (4 \cdot 3) = 6$ . When the structural group properties are analyzed the mechanism's mobility is also equal to 6. The 3<sup>rd</sup> loop

is a 4-bar loop which adds 2 new links [14 and 15] preserving the mobility equal to 5, the 4<sup>th</sup> loop is a 6-bar loop which adds 2 new links [12 and 13] preserving the mobility equal to 5. The additional link [11] increases the mobility by 1 to 6 as calculated.

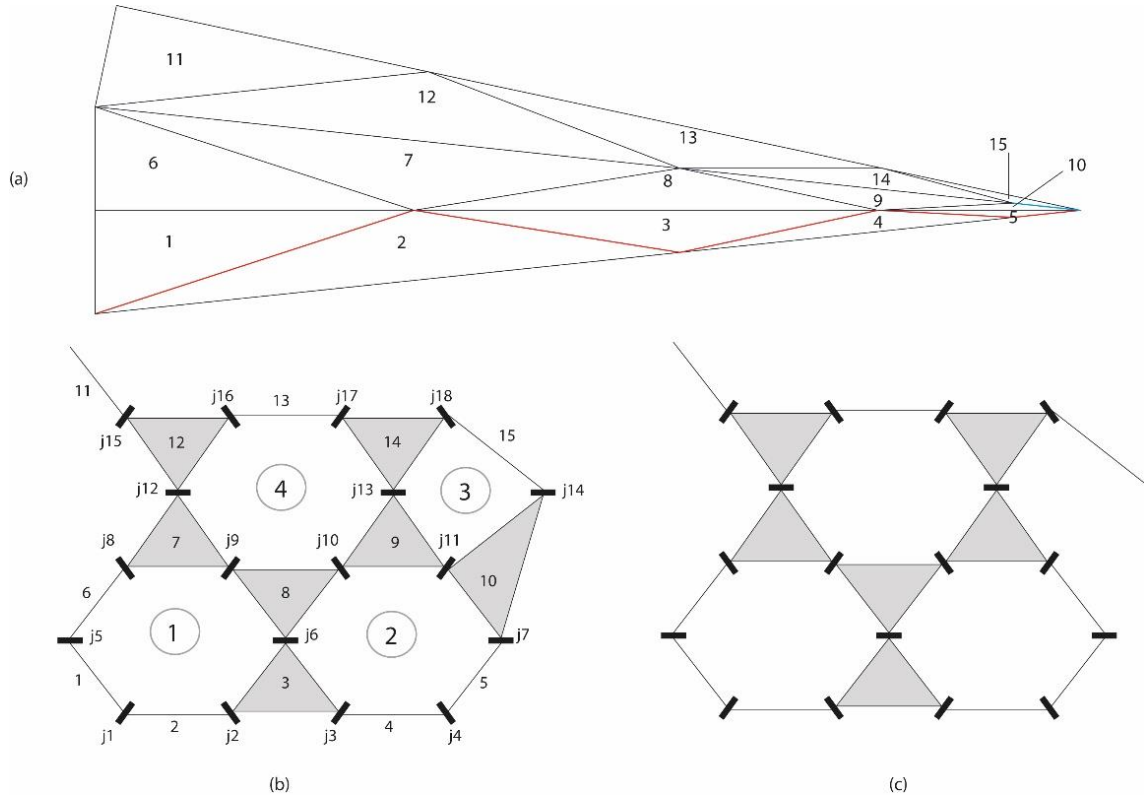


Figure 4.28.  $r: 5m, n: 5, \theta_I: 6^\circ$  three rows (a) crease pattern, (b) kinematic diagram, and the (c) modified kinematic diagram.

When the cutline is introduced, the connection between the links 10 and 15 is lost by removing the joint number 14 (Figure 4.28). The total number of joints decreases to 17 but the number of links stays the same. Removing the joint also decreased the number of loops to 3. Both the mobility calculated with eq. (4.77) and that of the structural group properties is equal to 8:  $M_{53M} = 17 - (3 \cdot 3) = 8$ .

Based on the structural group properties, the 3<sup>rd</sup> loop adds 3 new links increasing the mobility from 5 to 6. The 2 additional links [11 and 15] increase the mobility to 8, verifying the calculation.

### 4.4.3. 4-Row Patterns

In this section 4-row patterns with 3, 4 and 5 segments and their modified patterns will be analyzed.

3-segment pattern: A new row is added with 3 new links and 4 new joints making a total of 12 links and 14 joints. The new row also adds a 3<sup>rd</sup> loop (Figure 4.29).

The mobility is equal to 5:  $M_{34} = 14 - (3 \cdot 3) = 5$ . When the structural group properties are analyzed the mobility is also equal to 5. 3 new links [10, 11, and 12] are introduced to the mechanism increasing its mobility to 5.

In this pattern no new cutline is introduced, but the cutline introduced in 3-row and 3-segment pattern is applied. The mobility is equal to 7. In the structural group properties the 6-bar mechanism with mobility 3 is attached to another 6-bar mechanism again with mobility 3 through the joint number 7, making this pattern a mechanism with mobility 7:  $M_{34M} = 13 - (2 \cdot 3) = 7$ .

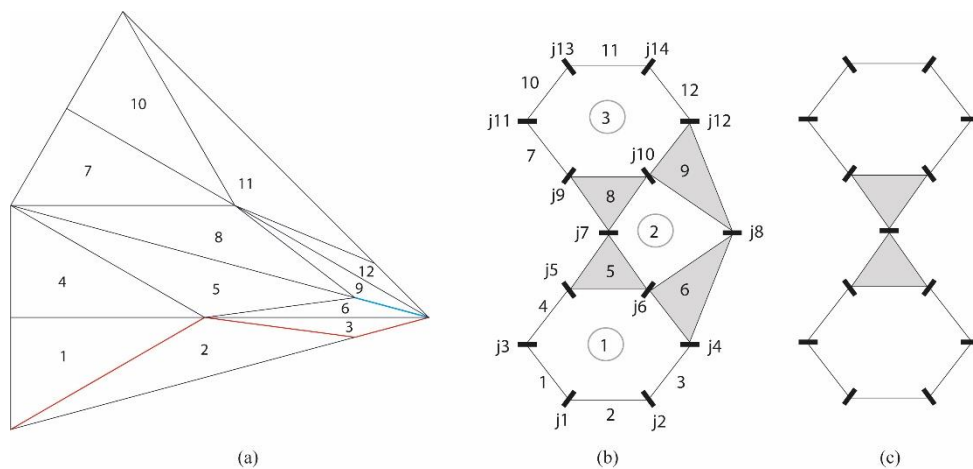


Figure 4.29.  $r$ : 5m,  $n$ : 3,  $\theta_I$ : 15° four rows (a) crease pattern, (b) kinematic diagram, and the (c) modified kinematic diagram.

4-segment pattern: The 4-row and 4-segment pattern adds 4 new links and 6 new joints and 2 new  $\lambda = 3$  loops to the mechanism. The loops calculations confirm the number of loops using eq. (4.76):  $L = 20 - 16 + 1 = 5$ .

The mobility is equal to 5:  $M_{44} = 20 - (5 \cdot 3) = 5$ . When the structural group properties are analyzed the 1<sup>st</sup> loop is a 6-bar loop with a mobility equal to 3. The 2<sup>nd</sup> loops adds 2 new links [4 and 8] preserving the mobility. The 3<sup>rd</sup> loop adds 3 new links

increasing the mobility by 1. The 4<sup>th</sup> loop adds 4 new links including the additional joint [9] increasing the mobility by 2, making it equal to 6. The 5<sup>th</sup> loop adds only one link [16] decreasing the mobility by one. The 4-segment and 4-row pattern's mobility is equal to 5 based on its structural group properties.

When the new outline is introduced to this mechanism joints 6 and 17 are removed (Figure 4.30) the mechanism is left with a total of 18 joints and 16 links. The removed joints belong to the new row; the modifications done on the 4-segment and 3-row pattern are the same. The new mechanism has 3 loops and the calculated mobility is equal to 9:  $M_{44M} = 18 - (3 \cdot 3) = 9$ .

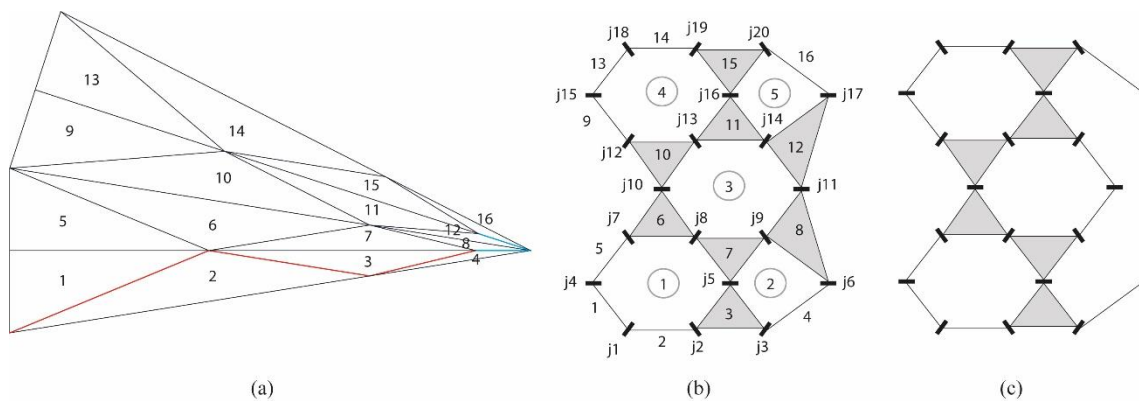


Figure 4.30.  $r$ : 5m,  $n$ : 4,  $\theta_l$ :  $9^\circ$  four rows (a) crease pattern, (b) kinematic diagram, and the (c) modified kinematic diagram.

The 1<sup>st</sup> loop is a 6-bar loop with a mobility of 3; the 2<sup>nd</sup> loops adds 4 new links [8, 10, 11, and 12] increasing the mobility by 2. The 3<sup>rd</sup> loops also adds 4 new links [9, 13, 14, and 15] again increasing the mobility by 2, the total mobility till this step is equal to 7. Finally the two additional links [4 and 16] increases the mobility by 2 making it equal to 9 as calculated.

5-segment pattern: the 4<sup>th</sup> row introduces 5 new links and 7 new joints making the total of links equal to 20 and joints to 25. 2 new loops are added to the mechanism which is confirmed by the calculations (Figure 4.31):  $L = 25 - 20 + 1 = 6$ .

The calculated mobility is equal to 7:  $M_{54} = 25 - (6 \cdot 3) = 7$ . When the structural group properties are analyzed, the same result is achieved. The 1<sup>st</sup> loop is a 6-bar loop with mobility 3. The 2<sup>nd</sup> loop adds 4 new links [4, 5, 9, and 10] increasing the mobility by 2. The 3<sup>rd</sup> loops adds 2 new links [14 and 15] preserving the mobility equal to 5. The

4<sup>th</sup> loop adds 2 new links [12 and 13] again preserving the mobility. The 5<sup>th</sup> loop adds 4 new links [11, 16, 17, and 18] increasing the mobility to 7. The 6<sup>th</sup> loops adds 2 new links [19 and 20] preserving the mobility.

No new outline is added, the one created in the previous row is preserved. The total number of joints is equal to 24 and the number of links is 20. The calculated mobility is equal to 9:  $M_{54M} = 24 - (5 \cdot 3) = 9$ .

The same result is achieved when the structural group analysis is conducted. The 1<sup>st</sup> loop has a mobility equal to 3. The 2<sup>nd</sup> loop adds 4 new links increasing the mobility to 5. The 3<sup>rd</sup> loop adds 3 new links which increases the mobility by 1. The 4<sup>th</sup> loop adds 4 new links increasing the mobility to 8 and the last loop (5<sup>th</sup> loop) adds 3 new links increasing the mobility to 9.

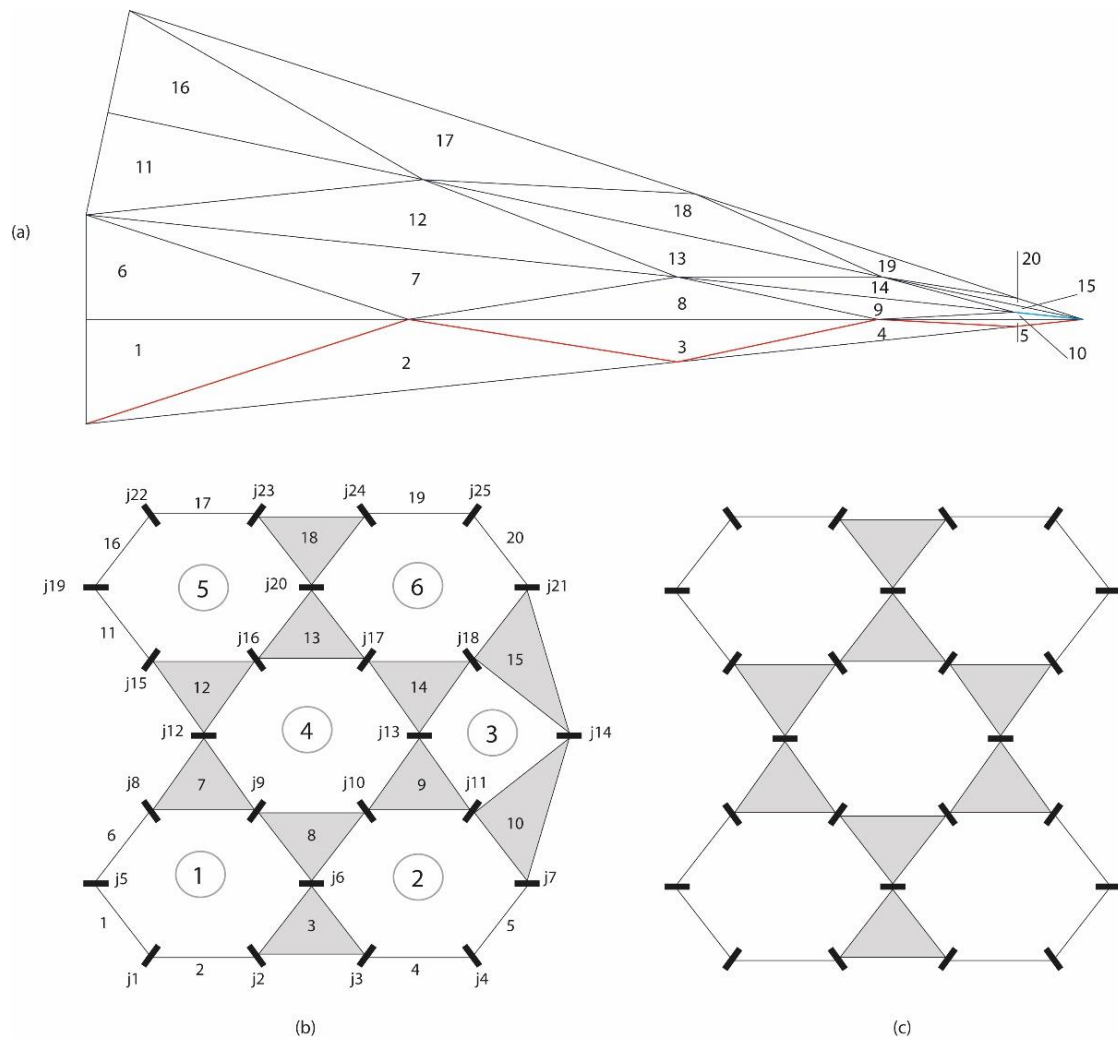


Figure 4.31.  $r: 5m, n: 5, \theta_I: 6^\circ$  four rows (a) crease pattern, (b) kinematic diagram, and the (c) modified kinematic diagram.



#### 4.4.4. 5-Row Patterns

In this section 5-row patterns with 3, 4 and 5 segments and their modified pattern are analyzed.

3-segment pattern: A new row is added with 3 new links and 4 new joints making a total of 15 links and 18 joints. The new row also adds a 4<sup>th</sup> loop (Figure 4.32).

The mobility calculations are equal to 6:  $M_{35} = 18 - (4 \cdot 3) = 6$ . When the structural group properties are analyzed the mobility is also equal to 6. The 3<sup>rd</sup> loop adds 4 new links [7, 10, 11, and 12] increasing the mobility to 5. The 4<sup>th</sup> loop adds 2 new links [14 and 15] which preserve the mobility. Finally the additional link [13] increases the mobility to 6, as calculated.

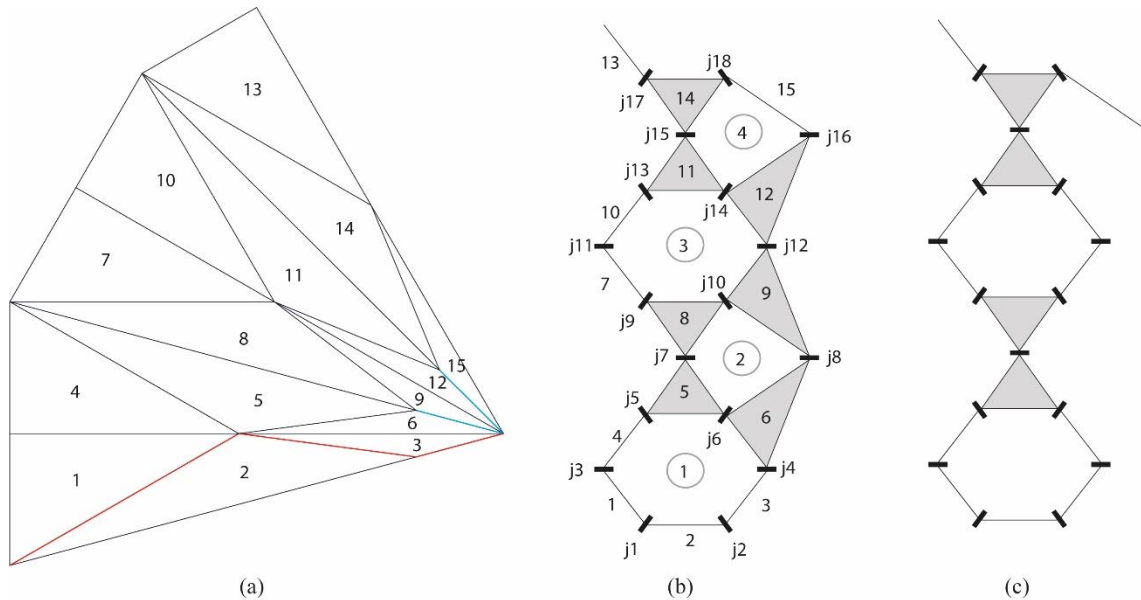


Figure 4.32.  $r: 5m, n: 3, \theta_l: 15^\circ$  five rows (a) crease pattern, (b) kinematic diagram, and the (c) modified kinematic diagram.

A new cutline is added, joints 8 and 16 are removed from the pattern decreasing the number of joints to 16. The calculated mobility of the modified pattern is equal to 10:  $M_{44M} = 16 - (2 \cdot 3) = 10$ . When the structural properties were analyzed in the previous part, the mobility of the modified 4-row and 3-segment pattern was equal to 7, with this modification 3 additional links are added to the mechanism increasing the mobility to 10.

4-segment pattern: The fifth row adds 4 new links and 5 new joints and one new  $\lambda = 3$  loop is added to the mechanism.

The mobility is equal to 7:  $M_{45} = 25 - (6 \cdot 3) = 7$ . When the structural group properties are analyzed the 1<sup>st</sup> loop is a 6-bar loop with a mobility equal to 3. The 2<sup>nd</sup> loops adds 2 new links [4 and 8] preserving the mobility. The 3<sup>rd</sup> loop adds 3 new links [10, 11, and 12] increasing the mobility by 1. The 4<sup>th</sup> loop adds 4 new links [9, 13, 14, and 15] increasing the mobility by 2, making it equal to 6. The 5<sup>th</sup> loop adds only one link [16] decreasing the mobility to 5. The 6<sup>th</sup> loop adds 3 new links [18, 19, and 20] increasing the mobility to 6 and finally the mobility increases to 7 again by the addition of link 17 same as the calculation:

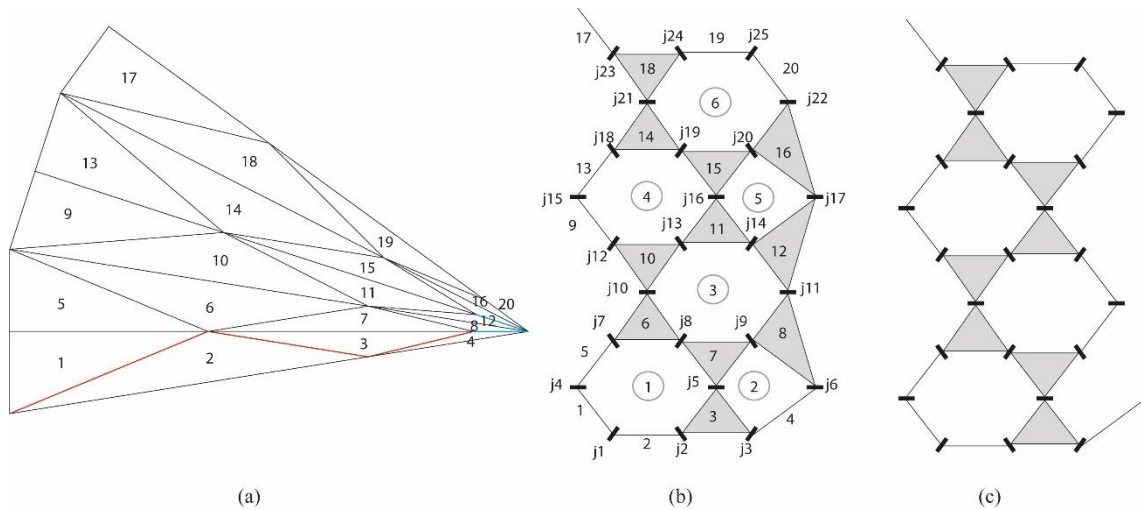


Figure 4.33.  $r: 5m$ ,  $n: 4$ ,  $\theta_I: 9^\circ$  five rows (a) crease pattern, (b) kinematic diagram, and the (c) modified kinematic diagram.

No new cutline is introduced, but the previously removed joints are removed again in this 5-row pattern. The joints removed were joints 6 and 17. The modified pattern has 20 links and 23 joints (Figure 4.33). The calculated mobility for the modified pattern is equal to 11:  $M_{45M} = 23 - (4 \cdot 3) = 11$ .

When the structural group properties are analyzed, the 1<sup>st</sup> loop has a mobility equal to 3, because it is a 6-bar loop. The 2<sup>nd</sup> loop adds 4 new links [8, 10, 11, and 12] increasing the mobility to 5. The 3<sup>rd</sup> loop adds again 4 new links [9, 13, 14, and 15] increasing the mobility to 7. The last loop (4<sup>th</sup> loop) adds also 4 new links [16, 18, 19, and 20] increasing the mobility to 9. And finally the 2 additional links [4 and 17] are added increasing the mobility to 11 same as the calculated value.

5-segment pattern: The 5<sup>th</sup> row increases the number of links to 25 and the number of joints to 32 (Figure 4.34).

The calculated mobility is equal to 8:  $M_{55} = 32 - (8 \cdot 3) = 8$ . When the structural group properties are analyzed the same result is achieved. The 1<sup>st</sup> loop is a 6-bar loop with mobility 3. The 2<sup>nd</sup> loop adds 4 new links [4, 5, 9, and 10] increasing the mobility by 2. The 3<sup>rd</sup> loop adds 2 new links [14 and 15] preserving the mobility equal to 5. The 4<sup>th</sup> loop adds 2 new links [12 and 13] again preserving the mobility. The 5<sup>th</sup> loop adds 4 new links [11, 16, 17, and 18] increasing the mobility to 7. The 6<sup>th</sup> loop adds 2 new links [19 and 20] preserving the mobility. The 7<sup>th</sup> loop adds 2 new links [24 and 25] preserving the mobility. The 8<sup>th</sup> loop also adds 2 new links [22 and 23] preserving the mobility. Finally the additional link [21] is added increasing the mobility to 8.

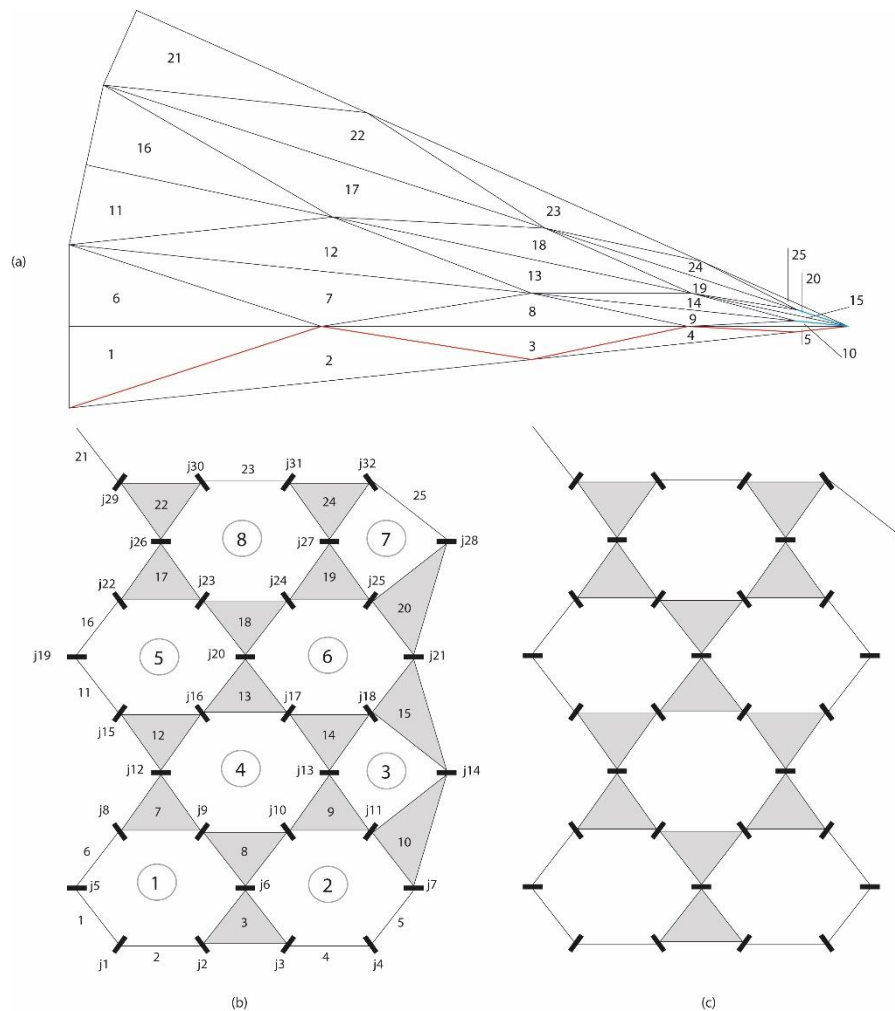


Figure 4.34.  $r: 5m, n: 5, \theta_I: 6^\circ$  five rows (a) crease pattern, (b) kinematic diagram, and the (c) modified kinematic diagram.

A new outline is added, joints 14 and 28 are removed to create the modified pattern which decreases number of joints to 25 and the number of links 25 is preserved. The calculated mobility of the modified pattern is equal to 12:  $M_{55M} = 30 - (6 \cdot 3) = 12$ .

The same result is achieved when the structural group analysis is conducted. The 1<sup>st</sup> loop has a mobility equal to 3. The 2<sup>nd</sup> loop adds 4 new links increasing the mobility to 5. The 3<sup>rd</sup> loop adds 3 new links which increases the mobility by 1 to 6. The 4<sup>th</sup> loop adds 4 new links increasing the mobility to 8. The 5<sup>th</sup> loop adds 3 new links increasing the mobility to 9. The last loop (6<sup>th</sup> loop) adds 3 new links increasing the mobility to 10. And finally, when the 2 additional links are added, the mobility becomes 12, same as the calculations.

Tables 4.4 and 4.5 present the mobility calculations for patterns with different number of segments and rows.

Table 4.4. Pseudo-dome pattern mobility analysis with different number of segments and rows.

Pseudo-Dome Pattern																	
# of segment	2 Row			3 Row			4 Row			5 Row			6 Row			increased by	
n:3	# links	6			9			12			15			18			(+3)
	# joints	6			10			14			18			22			(+4)
	# loops	T	$\lambda=3$	$\lambda=5$	T	$\lambda=3$	$\lambda=5$	T	$\lambda=3$	$\lambda=5$	T	$\lambda=3$	$\lambda=5$	T	$\lambda=3$	$\lambda=5$	(1)
		1	1	0	2	2	0	3	3	0	4	4	0	5	5	0	
M	3			4			5			6			7			(+1)	
n:4	# links	8			12			16			20			24			(+4)
	# joints	9			14			20			25			31			(+5) to odd (+6) to even
	# loops	T	$\lambda=3$	$\lambda=5$	T	$\lambda=3$	$\lambda=5$	T	$\lambda=3$	$\lambda=5$	T	$\lambda=3$	$\lambda=5$	T	$\lambda=3$	$\lambda=5$	(1) to odd (2) to even
		2	2	0	3	3	0	5	5	0	6	6	0	8	8	0	
M	3			5			5			7			7				
n:5	# links	10			15			20			25			30			(+5)
	# joints	11			18			25			32			39			(+7)
	# loops	T	$\lambda=3$	$\lambda=5$	T	$\lambda=3$	$\lambda=5$	T	$\lambda=3$	$\lambda=5$	T	$\lambda=3$	$\lambda=5$	T	$\lambda=3$	$\lambda=5$	(2)
		2	2	0	4	4	0	6	6	0	8	8	0	10	10	0	
M	5			6			7			8			9			(+1)	
n:6	# links	12			18			24			30			36			(+6)
	# joints	14			22			31			39			48			(+8) to odd (+9) to even
	# loops	T	$\lambda=3$	$\lambda=5$	T	$\lambda=3$	$\lambda=5$	T	$\lambda=3$	$\lambda=5$	T	$\lambda=3$	$\lambda=5$	T	$\lambda=3$	$\lambda=5$	(2) to odd (3) to even
		3	3	0	5	5	0	8	8	0	10	10	0	13	13	0	
M	5			7			7			9			9				

Table 4.5. Pseudo-dome modified pattern mobility analysis with different number of segments and rows.

Pseudo-Dome Modified Pattern																	
# of segment	2 Row			3 Row			4 Row			5 Row			6 Row			increased by	
n:3	# links	6			9			12			15			18			(+3)
	# joints	6			9			13			16			20			(+3) to odd (+4) to even
	# loops	T	$\lambda=3$	$\lambda=5$	T	$\lambda=3$	$\lambda=5$	T	$\lambda=3$	$\lambda=5$	T	$\lambda=3$	$\lambda=5$	T	$\lambda=3$	$\lambda=5$	(1)
		1	1	0	1	1	0	2	2	0	2	2	0	3	3	0	
M	3			6			7			10			11			(+3) to odd (+1) to even	
n:4	# links	8			12			16			20			24			(+4)
	# joints	9			13			18			23			28			(+5) to odd (+6) to even
	# loops	T	$\lambda=3$	$\lambda=5$	T	$\lambda=3$	$\lambda=5$	T	$\lambda=3$	$\lambda=5$	T	$\lambda=3$	$\lambda=5$	T	$\lambda=3$	$\lambda=5$	(1)
		2	2	0	2	2	0	3	3	0	4	4	0	5	5	0	
M	3			7			9			11			13			(+2)	
n:5	# links	10			15			20			25			30			(+5)
	# joints	11			17			24			30			37			(+6) to odd (+7) to even
	# loops	T	$\lambda=3$	$\lambda=5$	T	$\lambda=3$	$\lambda=5$	T	$\lambda=3$	$\lambda=5$	T	$\lambda=3$	$\lambda=5$	T	$\lambda=3$	$\lambda=5$	(1) to odd (2) to even
		2	2	0	3	3	0	5	5	0	6	6	0	8	8	0	
M	5			8			9			12			13			(+3) to odd (+1) to even	
n:6	# links	12			18			24			30			36			(+6)
	# joints	14			21			29			37			45			(+8) to odd (+9) to even
	# loops	T	$\lambda=3$	$\lambda=5$	T	$\lambda=3$	$\lambda=5$	T	$\lambda=3$	$\lambda=5$	T	$\lambda=3$	$\lambda=5$	T	$\lambda=3$	$\lambda=5$	(2)
		3	3	0	4	4	0	6	6	0	8	8	0	10	10	0	
M	5			9			11			13			15			(+2)	

When Table 4.4 is analyzed, even numbered segments presents a different growth than odd numbered segments when their number of joints and number of loops for each additional row is analyzed. Odd segment numbered patterns' mobility increases by 1 with each additional row. Even segment numbered patterns' mobility increases with each double row as it can be observed.

When Table 4.5 is analyzed, it can be observed that in even segment numbered patterns, when the joint related to the tearing crease is removed, have a linear growth of mobility value when compared to the original pattern mobility.

As a conclusion both original and modified patterns for a pseudo-dome mechanism has been analyzed and each calculation have been compared to a structural group analysis revealing the same values. It has been observed that each new row increased the mobility of the mechanism. Removing the joints, creating degree-4 vertexes near the central point of the pattern, also proved to increase the mobility of the mechanism. These particular crease joints can be modified to avoid tearing and also to limit the increase of the mobility of the overall pattern.

## 4.5. Conclusion

In this chapter a method of designing a MV-Pattern for a pseudo-dome structure using a pattern-generator has been presented. The design starts by defining three parameters the radius  $r$ , the number of segments  $n$  and the first segment angle  $\theta_1$ . These parameters generate all the required parameters to design a pattern. The relations between parameters have been demonstrated in the geometrical analysis. A calculation sheet prepared in Microsoft Excel 2013® has been provided to facilitate the calculations of the parameters (Appendix E). In the workspace analysis, changes of the span, height, coverage area and volume during the deployment process were analyzed and put in relation with the inclination angle  $\sigma$ . In the last section mobility analysis were conducted to understand the mechanism.

# CHAPTER 5

## CASE STUDIES

In this chapter possible architectural applications of the presented rigid origami structures will be explored with two case studies. The objective is to present the proposed design method with these case studies. The first case study is the creation of a deployable double centered barrel vault that will provide cover to an archeological site when needed. The second case study is the creation of a semi-pseudo-dome deployable structure that will provide cover to a concert stage.

Both case studies will present the step by step design method. First step is the decisions of the main parameters based on the requirements of the sites and the calculations of the parameters required to draw a pattern. Second step is the creation of the MV-Pattern based on the calculated parameters. Third step is the calculations of depth, span, height, and volume for the created and placed pattern. The last step is the conclusion of the designed pattern.

### 5.1. Case Study 1

The first case study is the creation of a canopy for an archeological dig site located in İzmir which should be deployable in need. The created structure need to cover a small dig site located in the Smyrna archeological dig site in İzmir, Turkey. The site dimensions are 8,5 m by 12 m and the site has a 3 m depth. A deployable structure is needed to create a cover over this site that can be folded/unfolded when needed. The structure will provide protection, to the antiquities being dig and to archeologist, from extreme weather conditions. The structure will be on site, so the deployability of it and its dimensions during the deployment states are necessary parameters for the designer.

A step by step approach of the design of a barrel vault deployable structure will be presented, where choices of the main parameters will be explained. Then parameters will be calculated and the pattern will be created.

### 5.1.1. Step 1 – Parameters Calculations

The first step is to decide the cross-section of the deployable rigid origami structure. Double centered barrel vault has been selected because the double centered arches are more complex to design than the single centered ones. As presented in chapter 3 there are three types of double centered arches: Pointed equilateral, Lancet and Obtuse. Each presents different span and height properties, in this case because the site has a considerable depth, a high height is not required, and so the obtuse arch cross-section becomes more adequate for this site.

Obtuse cross-section arch has more span than height where the radius  $r$  is greater than the distance between its two centers  $a$ . There are three main parameters that need to be decided radius  $r$ , distance between two centers  $a$ , and the number of segments for one arc  $n$ . The parameters  $r$  and  $a$  are in relation with the site's span, equal to 8,5 m, but the parameter  $n$  is more a question of aesthetic.

The span of an obtuse cross-section barrel vault, when in its final folded state, is calculated:

$$S = 2r - a \quad (5.1)$$

Even though this equation has not been presented it can be deduced by the geometrical properties presented on chapter 3.

So based on eq. (5.1) to have a span  $S$  of 9 m when the structure is on its final folded state the parameters are:  $r$ : 6 m and  $a$ : 3 m. The last parameter to decide is the number of segment  $n$  which will be equal to 4 –  $n$ : 4 and  $n_i$ : 8. Based on these parameters all the parameters can be calculated to draw a crease pattern.

Angle  $\hat{A}$  is calculated using eq. (3.52):

$$\hat{A} = \cos^{-1} \left( \frac{a}{2r} \right) = \cos^{-1} \left( \frac{3}{2 \cdot 6} \right) = 75,522^\circ \quad (5.2)$$

Based on this angle the segment's angle  $\theta$  is calculated using eq. (3.53):

$$\theta = \frac{\hat{A}}{n} = \frac{75,522}{4} = 18,88^\circ \quad (5.3)$$



The length of the segment  $s$  (eq. (5.4)) and the pattern generator's length  $s_t$  (eq. 5.5)) are calculated using eqs. (3.2) and (3.3):

$$s = 2r \sin\left(\frac{\theta}{2}\right) = 2 \cdot 6 \cdot \sin\left(\frac{18,88}{2}\right) = 1,968 \text{ m} \quad (5.4)$$

$$s_t = n_t \cdot s = 8 \cdot 1,968 = 15,745 \text{ m} \quad (5.5)$$

Then the angles  $\hat{B}$ ,  $\hat{C}$ , and  $\hat{D}$  are calculated using eqs. (3.54), (3.55), and (3.56):

$$\hat{B} = \pi - 2\hat{A} = 180 - (2 \cdot 75,522) = 28,955^\circ \quad (5.6)$$

$$\hat{C} = \left(\frac{\pi - \theta}{2}\right) = \left(\frac{180 - 18,88}{2}\right) = 80,559^\circ \quad (5.7)$$

$$\hat{D} = \hat{C} - \hat{B} = 80,56 - 28,955 = 51,604^\circ \quad (5.8)$$

Based on these angles the interior angles  $\beta_1$  and  $\beta_2$  are calculated, where  $\beta_2$  is the apex's interior angle. Also based on these angles the edge angle  $\lambda$  is calculated.

$$\beta_1 = 2\hat{C} = 2 \cdot 80,559 = 161,119^\circ \quad (5.9)$$

$$\beta_2 = \hat{B} + 2\hat{D} = 28,955 + (2 \cdot 51,604) = 132,164^\circ \quad (5.10)$$

$$\lambda = \hat{C} = 80,559^\circ \quad (5.11)$$

The folding angle  $\alpha_1$  and the apex's folding angle  $\alpha_2$  are calculated with the following equations:

$$\alpha_1 = \frac{\pi - \beta_1}{2} = \frac{180 - 161,119}{2} = 9,44^\circ \quad (5.12)$$

$$\alpha_2 = \frac{\pi - \beta_2}{2} = \frac{180 - 132,164}{2} = 23,91^\circ \quad (5.13)$$

Finally the half-row's heights  $h_1$  calculated with the folding angle  $\alpha_1$  and  $h_2$  calculated with the folding angle  $\alpha_2$  can be calculated leading to the total height of the row  $2h$ .

$$h_1 = \tan\alpha_1 \left(\frac{s}{2}\right) = \tan(9,44) \cdot \left(\frac{1,968}{2}\right) = 0,1636 \text{ m} = 16,36 \text{ cm} \quad (5.14)$$

$$h_2 = \tan\alpha_2 \left(\frac{s}{2}\right) = \tan(23,91) \cdot \left(\frac{1,968}{2}\right) = 0,4364 \text{ m} = 43,64 \text{ cm} \quad (5.15)$$

$$2h = 2 \cdot h_1 = 2 \cdot 0,1636 = 0,3272m = 32,72 \text{ cm} \quad (5.16)$$

The importance of calculating the row's height with the smallest value of the half-row's height calculated is important, because if the higher value is used in this case  $h_2$  then the diagonals would have crisscrossed within the height of the row.

All these parameter calculations have been presented to understand the steps and the geometrical relations between the parameters. To facilitate the calculations a calculation sheet has been prepared in Microsoft Excel 2013® which is presented in Appendix C.

Table 5.1 presents all the parameters calculated in this step of the design of a double centered cross-sectioned arch barrel vault. Not all these parameters are used to create a crease pattern, but as it can be observed from the calculation process, all are in relation with each other.

Table 5.1. Design Parameters for Obtuse arch cross-sectioned rigid origami barrel vault.

	$r$ (m)	$a$ (m)	$n$	$\theta^\circ$	$s$ (m)	$s_t$ (m)	$\hat{A}^\circ$
Obtuse	6	3	4	18,880	1,96824	15,74592	75,52249
	$\hat{B}^\circ$	$\hat{C}^\circ$	$\hat{D}^\circ$	$\beta_1^\circ$	$\beta_2^\circ$	$\alpha_1^\circ$	$\alpha_2^\circ$
Obtuse	28,955	80,559	51,604	161,1194	132,164	9,440311	23,91782
	$\lambda^\circ$	$b$ (m)	$h_1$ (m)	$h_2$ (m)	$2h$ (m)	$n_T$	
Obtuse	80,55969	3	0,163631	0,436468	0,327263	8	

### 5.1.2. Step 2 – MV-Pattern Creation

In this section a step by step explanation is provided for the creation of a crease pattern. Parameters required to draw a crease pattern are the length of segment  $s$ , the pattern generator length  $s_t$ , the folding angle  $\alpha_1$ , the apex's folding angle  $\alpha_2$ , the edge angle  $\lambda$  and the height of a half-row  $h_1$ . The location of these parameters is represented in Figure 5.1 which is a representation of these parameters and not the pattern designed in this case study.

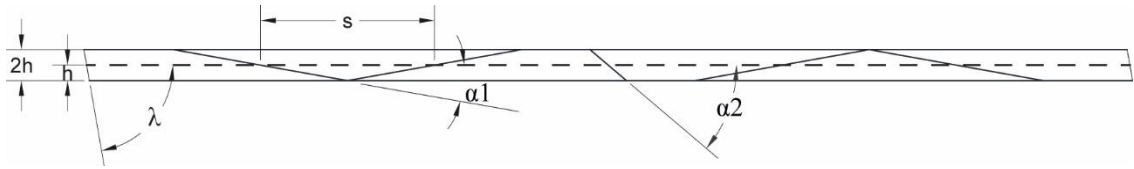


Figure 5.1. Design Parameters for double centered barrel vaults.

Firstly the *pattern-generator* is drawn using the value of  $s_t$  (pattern-generator length). It is important to mark segments intersection points (Figure 5.2.(1) dots). Then parallel lines are placed on both side of the *pattern-generator* using the smallest value of half-row height, in this case  $h_1$  (Figure 5.2.(2)). Since the row height  $2h$  has been draw the diagonals need to be drawn based on the folding angles. It is recommended to place the diagonal starting from one of the ends, so that the direction of the folding lines are correct. Using the folding angle  $\alpha_1$  the first diagonal is placed (Figure 5.2.(3)) then by changing the direction of the diagonals, the rest of them are placed (Figure 5.2.(4)) till the apex intersection. As explained the double centered arch is created using two arcs creating an apex which have a different interior angle thus a different folding angle  $\alpha_2$  than the rest of the pattern. The apex's diagonal is placed using the value of the folding angle  $\alpha_2$ , again on the opposite direction of the last placed diagonals (Figure 5.2.(5)). The rest of the diagonals are placed on opposing directions (Figure 5.2.(6)). Last parameter is the edge angle  $\lambda$  placed on the same direction as the last diagonals (Figure 5.2.(7)). The final folded state value of this parameter has been used for this particular design.

Figure 5.2 presents the steps of drawing a single row of a crease pattern. Starting from the third step two different rows are drawn to show the difference between rows if the rotation of the first diagonal is different.

The creation of the second row is done by a simple congruence transformation: reflection (Figure 5.3(1)). As it can be observed the mirror image of the first row is actually the row created with a diagonal with a different direction in Figure 5.2 (7). The whole of the pattern is created by translating the double rows in a single direction (Figure 5.3(2)).

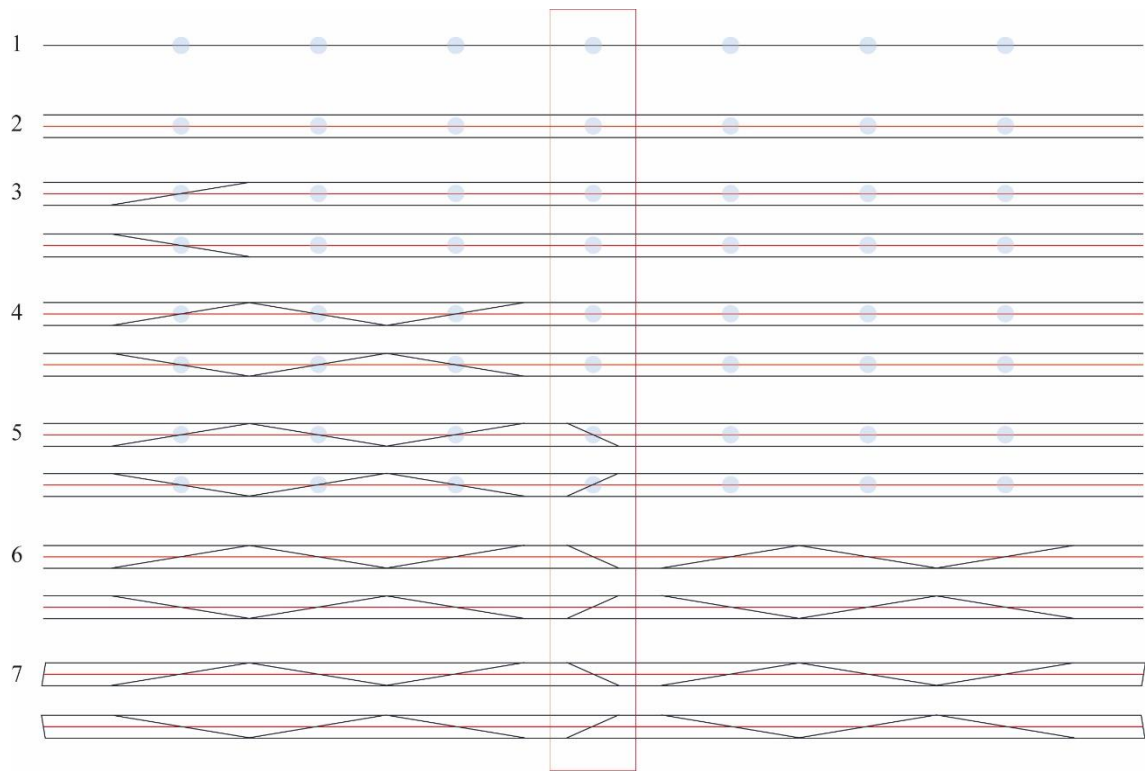


Figure 5.2. Pattern's drawing steps

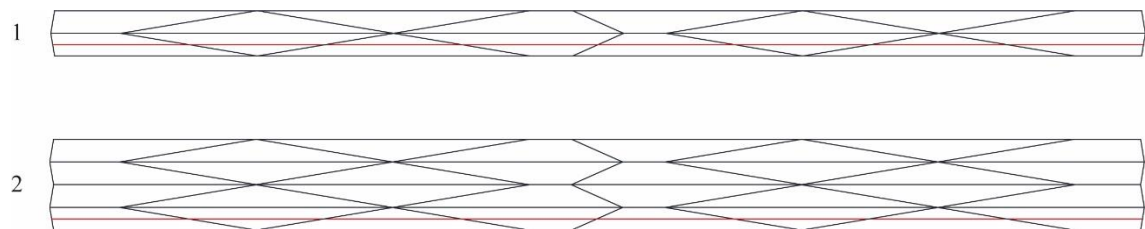


Figure 5.3. Increasing single row.

The pattern created in figure 5.3 is a 4 row crease pattern, where the red line represent the pattern-generator. Before deciding on the number of rows the CP need to be transformed to a MV-Pattern. The assignment of the mountain and valley folds is done based on Maekawa theorem where the difference of mountain folds and valley folds need to be equal to 2 (eq. (2.1)). Based on that theorem the MV-Pattern is created (Figure 5.4). No difference occurs if the MV-Assignment is inversed, because mountain and valley folds are considered dual to each other. Figure 5.4 presents two different MV-Pattern created with different MV-Assignment and their final folded state, so that the duality of mountain and valley folds can be understood. For both MV-Patterns in Figure 5.4 the dashed lines are valley folds and solid lines are mountain folds.

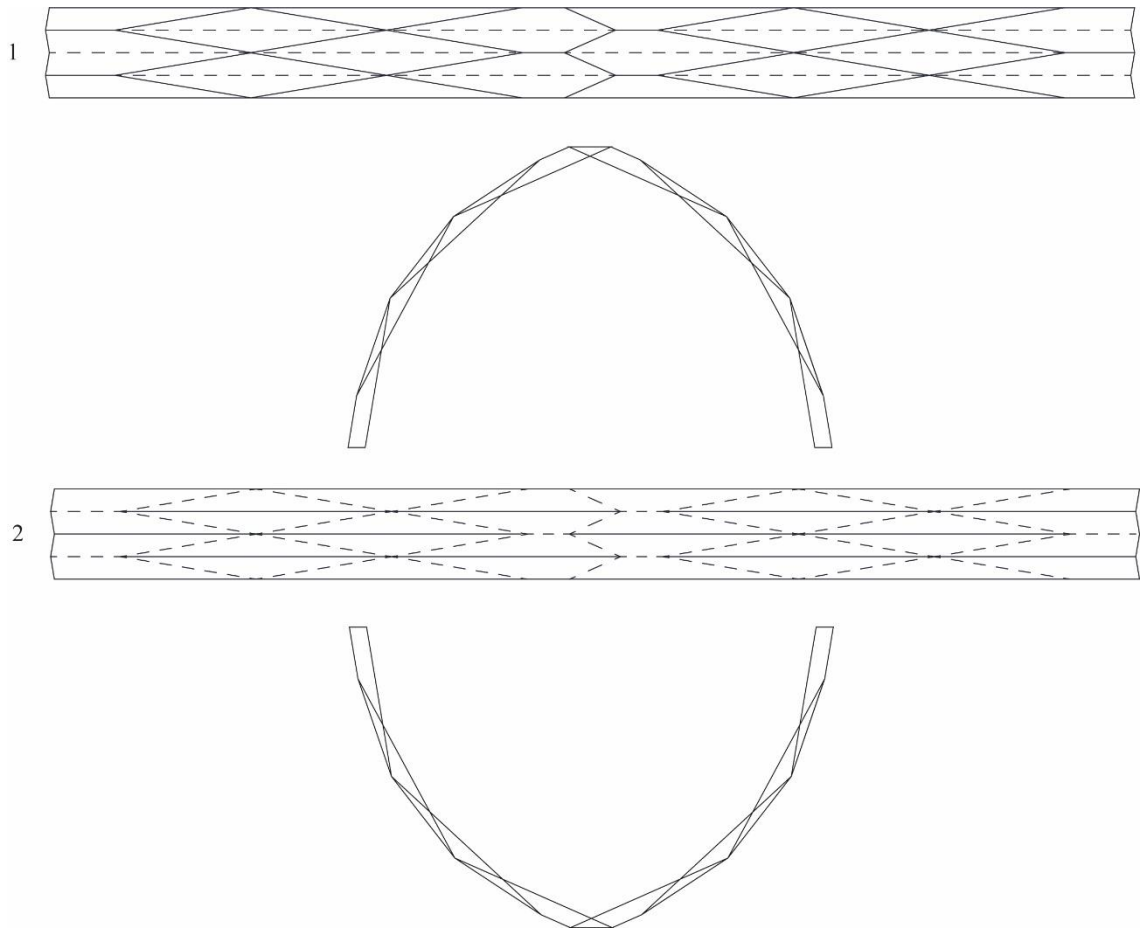


Figure 5.4. MV-Patterns and their final folded states.

### 5.1.3. Step 3 – Dimensions of the Created Pattern

In this step the dimensions (depth, span, height and volume) of the designed pattern will be discussed. The designed pattern is a flat-foldable and developable pattern which means that, for the deployable structure to be able to create a volume, the inclination angle's  $\sigma$  value should be between  $\pi/2$  and 0, where 0 is the initial state and  $\pi/2$  is the final folded state. Based on the dimension of the site that need to be covered the dimensions the number of rows  $R_n$  has been decided to be 50 rows. As the parameters  $r$ ,  $a$ , and  $n$ ; number of rows  $R_n$  is also a parameter decided by the designer.

The structure is assembled on the ground in its initial state, then erected to its place. Instead of fixing the joints as it was the case in oricrete (Chudoba, van der Woerd, Schmerl, & Hegger, 2014), the structure is folded to its final folded state which is flat and placed to its location so that when needed the structure is deployed to cover the area.

A limit should be imposed to the maximum value of the inclination angle  $\sigma$ , so that the structure do not open totally to its flat-folded initial state. To be able to impose the limits of the deployment all changes occurring to the dimensions, in relation to the inclination angle  $\sigma$  need to be analyzed. Site dimensions are a criteria to decide these limits. Also the dimension (depth, span, height and volume) calculations are done assuming the surface of the deployable structure has no thickness.

The span of the structure is calculated using eq. (3.75) with different inclination angle values to understand the deployment process. Figure 5.5 is the representation of the changes occurring to the designed structure during the deployment process. The mean value for this particular deployable structure is 12,37331 m which coincide to an inclination angle of 42,5°, to simplify the calculations the value for the inclination angle has been selected as 40°. As the inclination angle reach 90° the final flat-folded state, the span decreases.

The site dimension that coincides to the span is 8,5 m, the radius  $r$  and distance between the centers  $a$  have been decided considering this dimension, which represent the final folded state's dimensions because the design process starts by this state. If the minimum limit for the inclination angle is set as 40°, the span will not surpass 12,65 m as it can be observed in Figure 5.5.

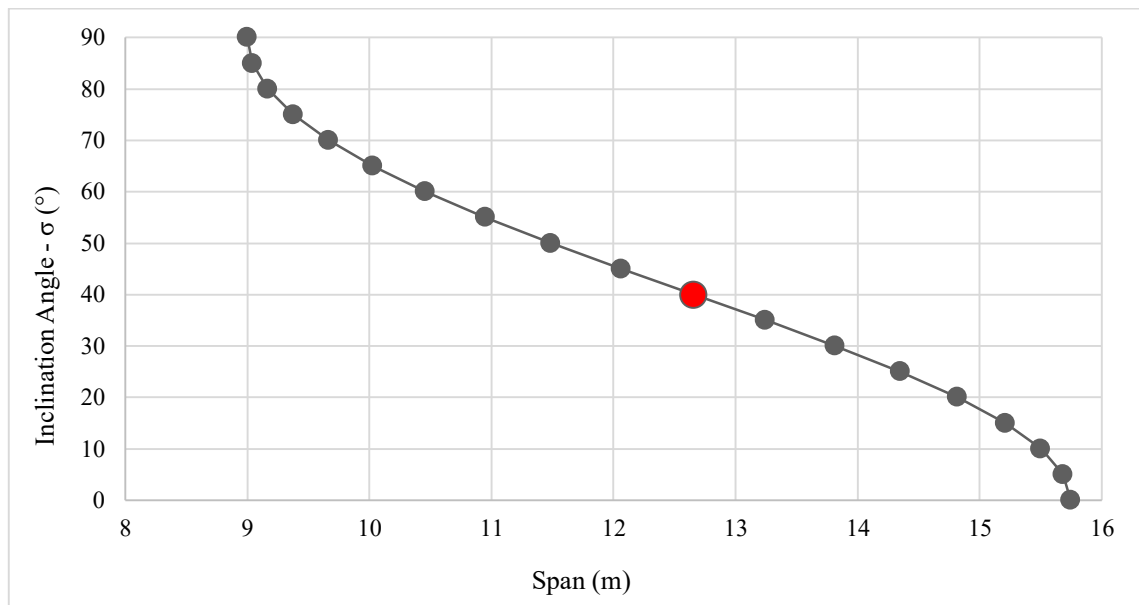


Figure 5.5. Span changes for an obtuse barrel vault with  $n:4$ ,  $r:6m$ , and  $a:3m$ .

The height of the structure has been calculated using eq. (3.77) with different values of inclination angles as it is in the span calculations. When the decided minimum value of the inclination ( $40^\circ$ ) is analyzed in Figure 5.6, it can be observed that after this angle there is a rapid height increase till its final folded state. The value of height is 4,3 m for this inclination angle.

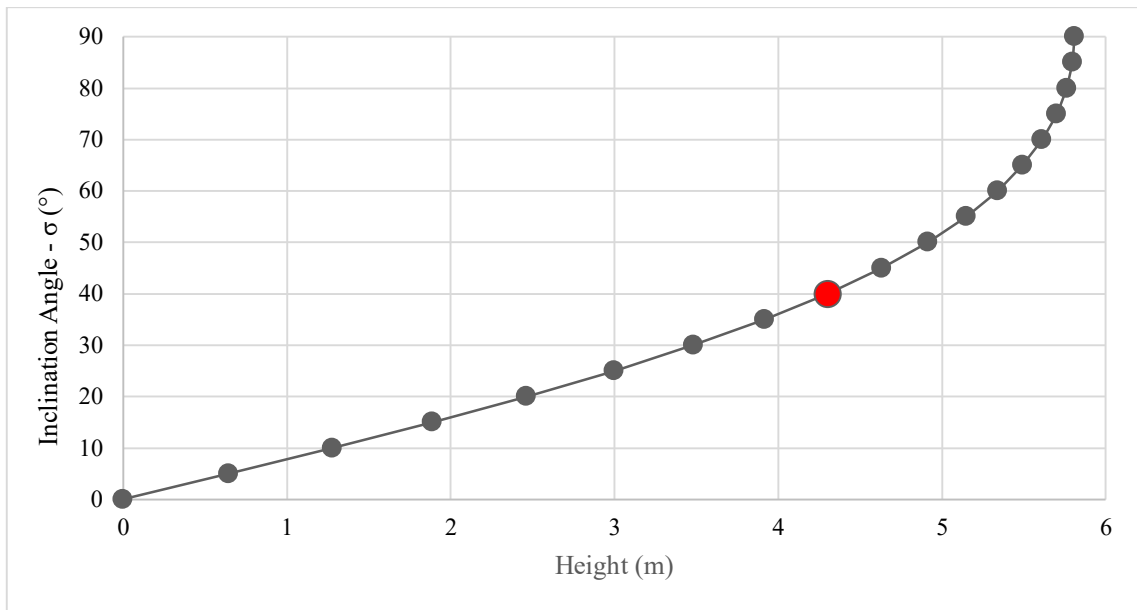


Figure 5.6. Height changes for an obtuse barrel vault with  $n:4$ ,  $r:6\text{m}$ , and  $a:3\text{m}$ .

The relation between the depth and the inclination angle is analyzed by calculating the depth with different values of inclination angle using eq. (3.67) (Figure 5.7). The changes occurring to the depth during the deployment process will help imposing limits for the structure. The limit has already being imposed as  $40^\circ$  for the inclination angle which coincide to a value of 12,53 m, which is very close to the span value with the same inclination angle.

The total area of the site can be covered when the inclination angle is set as  $40^\circ$ , which is the minimum value that the inclination angle can have after the erection of the deployable structure. To able to achieve this, some constrains can be included to the joints or the structure can be limited by secondary small structures so that once erected the value of the inclination angle do not drop under  $40^\circ$ .

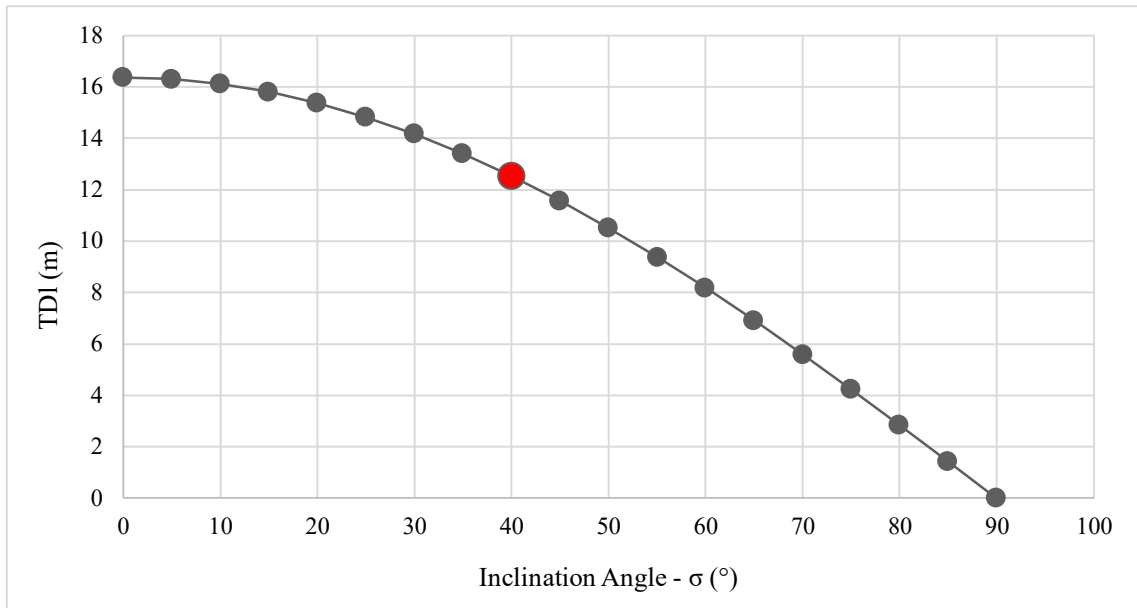


Figure 5.7. Depth changes for an obtuse barrel vault with  $n:4$ ,  $r:6\text{m}$ , and  $a:3\text{m}$ .

Even though the inclination angle has been set, the volume should be calculated for different inclination values to be able to observe the changes. Figure 5.8 presents the changes occurring to the designed structure, calculated using eq. (3.83) with different inclination angle values. As it can be observed, the angle value selected for the maximum space coverage of the structure is close to the maximum value of the volume which is equal to  $387\text{ m}^3$ .

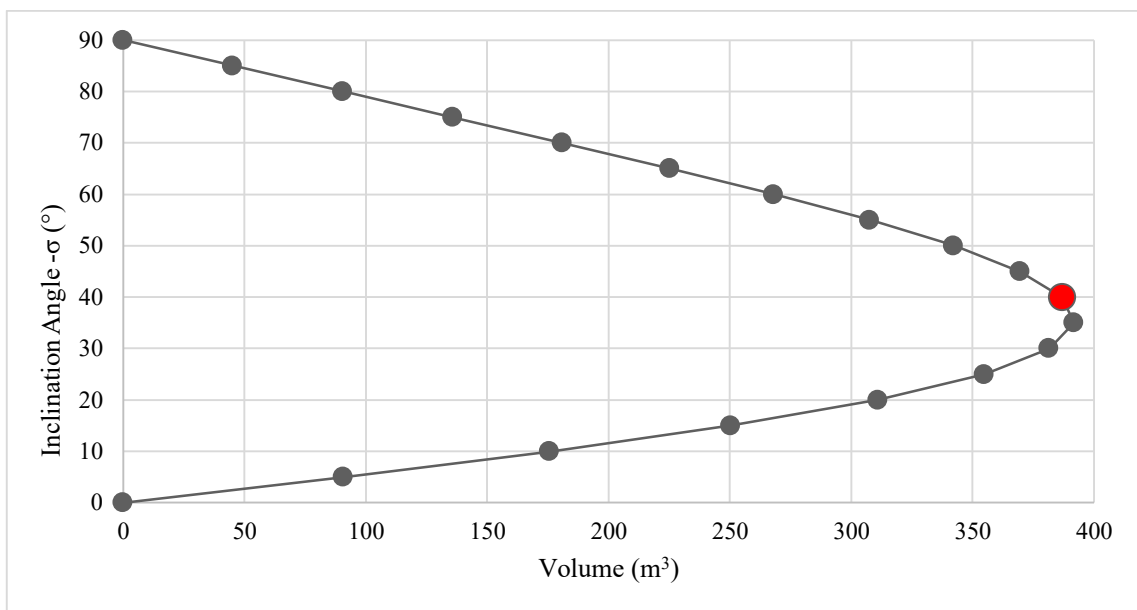


Figure 5.8. Volume changes for an obtuse barrel vault with  $n:4$ ,  $r:6\text{m}$ , and  $a:3\text{m}$ .



Figure 5.9 presents the deployable structure with the defined inclination angle equal to  $40^\circ$  which is the minimum value it can reach after the erection of the structure. Figure 5.10 presents the deployment process for different inclination angles equal to  $40^\circ$ ,  $55^\circ$ , and  $70^\circ$  going from lighter to darker folded state respectively. As it can be observed as the inclination increases the height increases but the volume, depth, and span decreases.

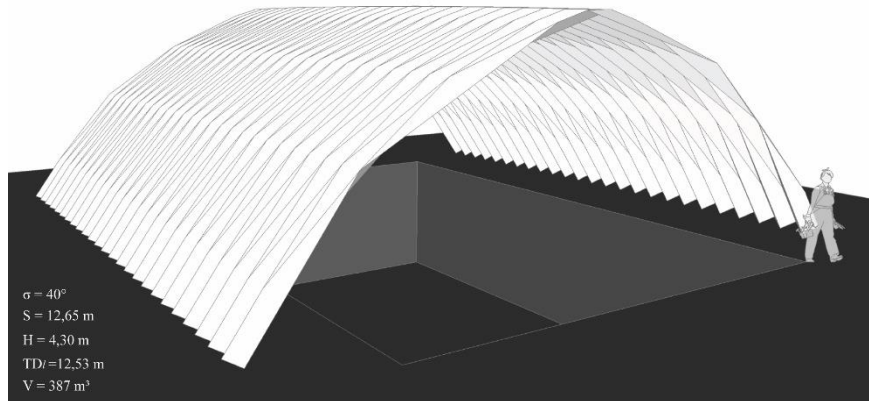


Figure 5.9. Deployable Obtuse Barrel Vault structure with  $n:4$ ,  $r:6\text{m}$ ,  $a:3\text{m}$  and  $\sigma:40^\circ$ .

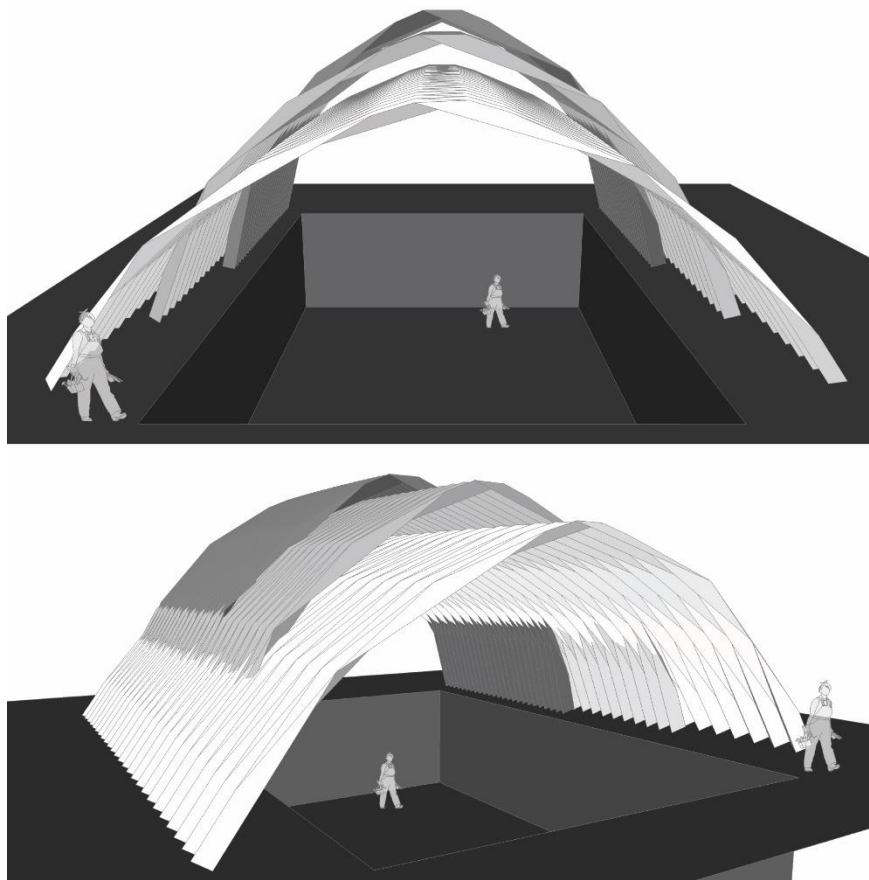


Figure 5.10. Deployable Obtuse Barrel Vault structure with  $n:4$ ,  $r:6\text{m}$ ,  $a:3\text{m}$  and  $\sigma:40^\circ$ ,  $\sigma:55^\circ$ , and  $\sigma:70^\circ$ .

#### 5.1.4. Conclusion

The steps of creating a deployable flat-foldable obtuse barrel vault structure has been presented. The choice of the type of barrel vault has been decided based on the requirement of the site, which demands more span than height. The properties of the barrel vault types are analyzed: pointed equilateral cross-sectioned barrel vault have an equal height and span, the lancet cross-sectioned one have more height than span, and finally the obtuse cross-sectioned one have more span than height. So the choice of cross-section type for this particular site have been decided as an obtuse arch.

In step 1 all equations, needed in the creation of the pattern, have been demonstrated to emphasize the relation between the parameters. In step 2 a successive pattern creation have been demonstrated using the calculated parameters in the first step. The last step demonstrated the calculations of the dimensions of the structure with different inclination angle values to be able to decide a maximum opening limit once the structure is in its partially folded state. This limit has been created because to fold the structure from its initial state, each time there is a need to cover the area, demands too much effort/ too much mechanical effort.

When the mobility is calculated using the Freudenstein and Alizade's equation the mobility is equal to -91, which is an over-constrained mechanism. This designed deployable barrel vault mechanism has 400 links, 644 joints and 245  $\lambda=3$  loops.

Structural loads are not being calculated but for the structure to be more stable it is recommended to use lighter materials or materials with less thickness towards the apex. Also considering the structural behavior of the barrel vaults a secondary structure should be placed to compensate the outward forces at the lower parts of the structure created by the geometry of the barrel vault. The outward forces in this type of structure would be even more severe because the structure is a deployable one and not a static one where the forces are stable and fixed.

The designed pattern is a triangular pattern. If there was a need to design a trapezoidal pattern decreasing the height  $h_1$  would have been sufficient. There are no differences in the design steps between two crease patterns.

## 5.2. Case Study 2

The second case study is the creation of a temporary canopy for a concert. The created structure need to cover a small concert stage. The stage dimensions are 5 m by 10 m. The structure will provide protection against extreme weather conditions and provide good acoustics for the performers, due to these needs a semi-pseudo-dome has been decided to be created. The structure need to be transportable and deployable with a fixed maximum opening angle to be able to be used as a stage cover.

A step by step approach of the design of the structure will be presented. Where choices of the main parameters will be explained. Then parameters will be calculated and the pattern will be created.

### 5.2.1. Step 1 – Parameters Calculations

The design of a semi-pseudo- dome starts with deciding the parameters: radius  $r$ , and the number of segments  $n$ . Eq. (4.39) allow the calculation of the first segment's angle  $\theta_1$  based on the number of segments. Thus the first segment's angle is no longer a decided parameter.

The stage is a 5 m by 10 m so the radius  $r$  is decided as 5 m knowing that the radius value defined is the final folded state of the pattern. The number of segments  $n$  is both an aesthetic choice and a functional choice. For this particular stage the number of segment  $n$  has been decided as 6 to provide enough space under the structure.

These two parameters allows the designer to create a deployable semi-dome structure. The first parameter to calculate is the first segment's number:

$$\theta_1 = \frac{180^\circ}{n(n+1)} = \frac{180}{6 \cdot (6+1)} = 4,2857^\circ \quad (5.17)$$

Because the segmentation of a pseudo-dome deployable structure is created using an arithmetic sequence the last segment's angle  $\theta_l$  and the common difference  $CD$  need to be calculated to be able to calculate the rest of the segment's angles. As proven with eq. (4.38) for a pattern to be created without a complementary triangle the common difference need to be equal to the first segment's angle. Each segment's angle can be

calculated using the following equation (eq. (4.4)). Where  $n$  is the number of segment's angle needed.

$$\theta_2 = \theta_1 + ((n - 1)CD) = 4,2857 + ((2 - 1)4,2857) = 8,5714^\circ \quad (5.18)$$

$$\theta_3 = 4,2857 + ((3 - 1)4,2857) = 12,8571^\circ \quad (5.19)$$

$$\theta_4 = 4,2857 + ((4 - 1)4,2857) = 17,1429^\circ \quad (5.20)$$

$$\theta_5 = 4,2857 + ((5 - 1)4,2857) = 21,4286^\circ \quad (5.21)$$

$$\theta_l = \theta_6 = 4,2857 + ((6 - 1)4,2857) = 25,7143^\circ \quad (5.22)$$

Segment length  $s_n$  for each segment's angle is calculated using eq. (4.5):

$$s_1 = 2r \sin\left(\frac{\theta_1}{2}\right) = 2 \cdot 6 \cdot \sin\left(\frac{4,2857}{2}\right) = 0,374 \text{ m} \quad (5.23)$$

$$s_2 = 2 \cdot 6 \cdot \sin\left(\frac{8,5714}{2}\right) = 0,747 \text{ m} \quad (5.24)$$

$$s_3 = 2 \cdot 6 \cdot \sin\left(\frac{12,8571}{2}\right) = 1,120 \text{ m} \quad (5.25)$$

$$s_4 = 2 \cdot 6 \cdot \sin\left(\frac{17,1429}{2}\right) = 1,490 \text{ m} \quad (5.26)$$

$$s_5 = 2 \cdot 6 \cdot \sin\left(\frac{21,4286}{2}\right) = 1,859 \text{ m} \quad (5.27)$$

$$s_6 = 2 \cdot 6 \cdot \sin\left(\frac{25,7143}{2}\right) = 2,225 \text{ m} \quad (5.28)$$

The angles  $\hat{A}_n$  are calculated for each segment using the eq. (4.6).

$$\hat{A}_1 = \frac{180 - \theta_1}{2} = \frac{180 - 4,2857}{2} = 87,8571^\circ \quad (5.29)$$

$$\hat{A}_2 = \frac{180 - 8,5714}{2} = 85,7143^\circ \quad (5.30)$$

$$\hat{A}_3 = \frac{180 - 12,8571}{2} = 83,5714^\circ \quad (5.31)$$

$$\hat{A}_4 = \frac{180 - 17,1429}{2} = 81,4286^\circ \quad (5.32)$$

$$\hat{A}_5 = \frac{180 - 21,4286}{2} = 79,2857^\circ \quad (5.33)$$

$$\hat{A}_6 = \frac{180 - 25,7143}{2} = 77,1429^\circ \quad (5.34)$$

With these angles the interior angles can be calculated using eq. (4.7). The annotation on interior angles is different because there are  $n-1$  number of parameters.

$$\beta_i = \beta_1 = \hat{A}_{i+1} + \hat{A}_i = \hat{A}_2 + \hat{A}_1 = 87,8571 + 85,7143 = 173,57^\circ \quad (5.35)$$

$$\beta_2 = \hat{A}_3 + \hat{A}_2 = 83,5714 + 87,8571 = 169,29^\circ \quad (5.36)$$

$$\beta_3 = \hat{A}_4 + \hat{A}_3 = 81,4286 + 83,5714 = 165^\circ \quad (5.37)$$

$$\beta_4 = \hat{A}_5 + \hat{A}_4 = 79,2857 + 81,4286 = 160,71^\circ \quad (5.38)$$

$$\beta_5 = \hat{A}_6 + \hat{A}_5 = 77,1429 + 79,2857 = 156,43^\circ \quad (5.39)$$

Since the interior angles have been calculated their segment length  $a_i$  can be calculated using the following equation (eq. (4.8)).

$$\begin{aligned} a_i = a_1 &= 2r \cos\left(\frac{\pi - (\theta_i + \theta_{i+1})}{2}\right) = 2r \cos\left(\frac{\pi - (\theta_1 + \theta_2)}{2}\right) \\ &= 2 \cdot 6 \cdot \cos\left(\frac{180 - (4,2857 + 8,5714)}{2}\right) = 1,120 \text{ m} \end{aligned} \quad (5.40)$$

$$a_2 = 2 \cdot 6 \cdot \cos\left(\frac{180 - (8,5714 + 12,8571)}{2}\right) = 1,859 \text{ m} \quad (5.41)$$

$$a_3 = 2 \cdot 6 \cdot \cos\left(\frac{180 - (12,8571 + 17,1429)}{2}\right) = 2,588 \text{ m} \quad (5.42)$$

$$a_4 = 2 \cdot 6 \cdot \cos\left(\frac{180 - (17,1429 + 21,4286)}{2}\right) = 3,303 \text{ m} \quad (5.43)$$

$$a_5 = 2 \cdot 6 \cdot \cos\left(\frac{180 - (21,4286 + 25,7143)}{2}\right) = 3,999 \text{ m} \quad (5.44)$$

The last segment length  $a_6$  is calculated as follow:

$$a_i = a_6 = s_{(i+1)} \sin \alpha_{i2} = s_6 \sin \alpha_{62} = 2,149 \text{ m} \quad (5.45)$$

Using these calculated parameters are enough to design the pattern, but to be absolutely certain of the design the folding angles also need to be calculated. In this design each folding angle is different and in relation to the interior angles  $\beta_i$ , interior angles' segment length  $a_i$ , and the segment length  $s_n$ . The folding angles' annotation is based on the interior angles number and their position in respect to the center point of the pattern.

For the first triangle with the interior angle  $\beta_1$  both folding angles are calculated as follow:

$$\alpha_{11} = \sin^{-1} \left( \frac{\sin(\beta_1) \cdot s_2}{a_1} \right) = \sin^{-1} \left( \frac{\sin(173,57) \cdot 0,747}{1,120} \right) = 4,29^\circ \quad (5.46)$$

$$\alpha_{12} = \sin^{-1} \left( \frac{\sin(\beta_1) \cdot s_1}{a_1} \right) = \sin^{-1} \left( \frac{\sin(173,57) \cdot 0,374}{1,120} \right) = 2,14^\circ \quad (5.47)$$

All the folding angles are calculated with the same equations:

$$\alpha_{21} = \sin^{-1} \left( \frac{\sin(\beta_2) \cdot s_3}{a_2} \right) = \sin^{-1} \left( \frac{\sin(169,29) \cdot 1,120}{1,859} \right) = 6,43^\circ \quad (5.48)$$

$$\alpha_{22} = \sin^{-1} \left( \frac{\sin(\beta_2) \cdot s_2}{a_2} \right) = \sin^{-1} \left( \frac{\sin(169,29) \cdot 0,747}{1,859} \right) = 4,29^\circ \quad (5.49)$$

$$\alpha_{31} = \sin^{-1} \left( \frac{\sin(165) \cdot 1,490}{2,588} \right) = 8,57^\circ \quad (5.50)$$

$$\alpha_{32} = \sin^{-1} \left( \frac{\sin(165) \cdot 1,120}{2,588} \right) = 6,43^\circ \quad (5.51)$$

$$\alpha_{41} = \sin^{-1} \left( \frac{\sin(160,71) \cdot 1,859}{3,303} \right) = 10,71^\circ \quad (5.52)$$

$$\alpha_{42} = \sin^{-1} \left( \frac{\sin(160,71) \cdot 1,490}{3,303} \right) = 8,57^\circ \quad (5.53)$$

$$\alpha_{51} = \sin^{-1} \left( \frac{\sin(156,43) \cdot 2,225}{3,999} \right) = 12,86^\circ \quad (5.54)$$

$$\alpha_{52} = \sin^{-1} \left( \frac{\sin(156,43) \cdot 1,859}{3,999} \right) = 10,71^\circ \quad (5.55)$$

The last folding angles are calculated independent from interior angles:

$$\alpha_{l1} = \alpha_{61} = 180 - (\beta_i + \alpha_{(i-1)2}) = 180 - (\beta_5 + \alpha_{42}) = 15^\circ \quad (5.56)$$

$$\alpha_{l2} = \alpha_{62} = \frac{180}{2} - \alpha_{61} = 75^\circ \quad (5.57)$$

As it can be observed all parameters are in correlation with each other geometrically. All the calculations have been presented to make the denotation clear and to point out the relations between the angles creating the pattern. Table 5.2 presents all the parameters calculated in this step. To facilitate the calculations a calculation sheet has been prepared in Microsoft Excel 2013® which is presented in Appendix E.

Table 5.2. Design Parameters for semi-pseudo-dome deployable structure.

Semi-pseudo- dome	$r$ (m)	$n$	$\theta_1$ (°)	$\theta_1$ (°)	$CD$	
	5	6	4,2857	25,7143	4,2857	
Segment's angle $\theta_n$ (°)	$\theta_1$	$\theta_2$	$\theta_3$	$\theta_4$	$\theta_5$	$\theta_6$
	4,2857	8,5714	12,8571	17,1429	21,4286	25,7143
Segment length $s_n$ (m9)	$s_1$	$s_2$	$s_3$	$s_4$	$s_5$	$s_6$
	0,374	0,747	1,120	1,490	1,859	2,225
Angle $A_n$ (°)	$A_1$	$A_2$	$A_3$	$A_4$	$A_5$	$A_6$
	87,8571	85,7143	83,5714	81,4286	79,2857	77,1429
Angle $\beta_i$ (°)	$\beta_1$	$\beta_2$	$\beta_3$	$\beta_4$	$\beta_5$	
	173,57	169,29	165,00	160,71	156,43	
Side length $a_i$ (m)	$a_1$	$a_2$	$a_3$	$a_4$	$a_5$	$a_6$
	1,120	1,859	2,588	3,303	3,999	2,149
Folding angle $\alpha_{i1}$ & $\alpha_{i2}$ (°)	$\alpha_{11}$	$\alpha_{21}$	$\alpha_{31}$	$\alpha_{41}$	$\alpha_{51}$	$\alpha_{61}$
	4,29	6,43	8,57	10,71	12,86	15,00
	$\alpha_{12}$	$\alpha_{22}$	$\alpha_{32}$	$\alpha_{42}$	$\alpha_{52}$	$\alpha_{62}$
	2,14	4,29	6,43	8,57	10,71	15,00

### 5.2.2. Step 2 – MV-Pattern Creation

In this section a step by step explanation is provided for the creation of a crease pattern. Parameters required to draw a crease pattern are the length of segments  $s_n$ , the interior angles  $\beta_i$ , and the interior angles' segment lengths  $a_i$ . The folding angles  $\alpha_{i1}$  and  $\alpha_{i2}$  are required to control the drawing parameters. The location of these parameters is represented in figure 5.11.

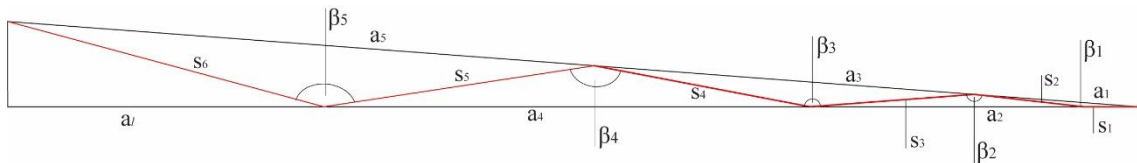


Figure 5.11. Design Parameters for semi-pseudo-dome.

In contrast to the barrel vault deployable structures the *pattern-generator* is not a straight line, but an angular line defined by both the segment length  $s_n$  and interior angles  $\beta_i$ . The first step in drawing the pattern is to place the first segment length  $s_1$  horizontally, then the second segment length  $s_2$  is placed with an angle of  $\beta_1$ , this process is repeated for all the calculated segments' length.

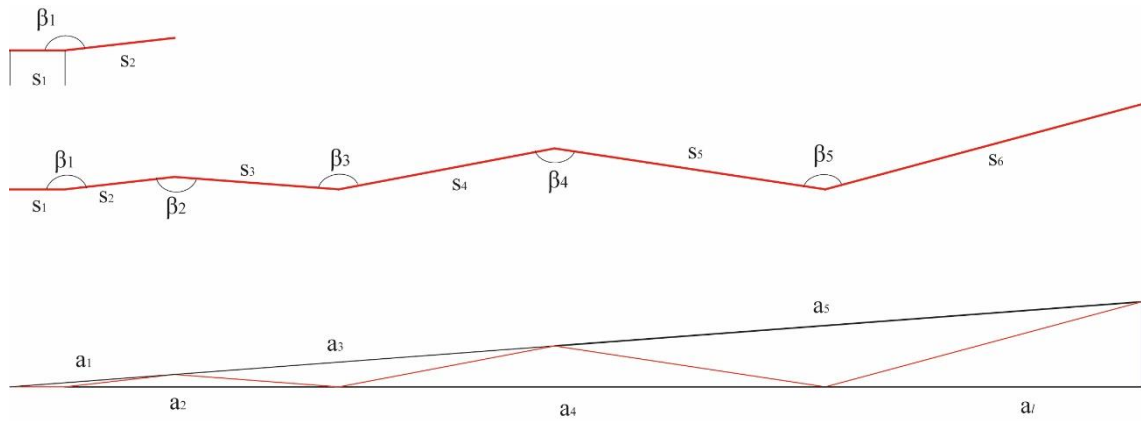


Figure 5.12. Pattern's drawing steps.

Then the calculated interior angle segments  $a_i$  are placed. The important point is that the central angle need to be equal to the calculated value of  $\alpha_{11}$ . Some patterns depending on their number of segment, have parameters that are decimal numbers with too much number after the decimal point. It is recommended to select a segment number that create smaller decimal numbers to be able to draw a more accurate pattern.

Since the first row has been drawn using the calculated parameters, it can be multiplied by simple congruence transformation: reflection (Figure 5.13(1)). Then the double row is rotated and translated via the center point of the pattern (Figure 5.13(2)).

After four rows has been created an MV-Assignment is done to create an MV-Pattern. Figure 5.13 (3) shows the MV-Pattern created by the crease pattern using the Maekawa theorem. As explained previously the mountain and valley folds are dual to each other thus even if the MV-Assignment is inversed there is no difference in the patterns deployment motion. In Figure 5.13(3) the dashed lines are valley folds and lines are mountain folds assigned based on the Maekawa theorem.



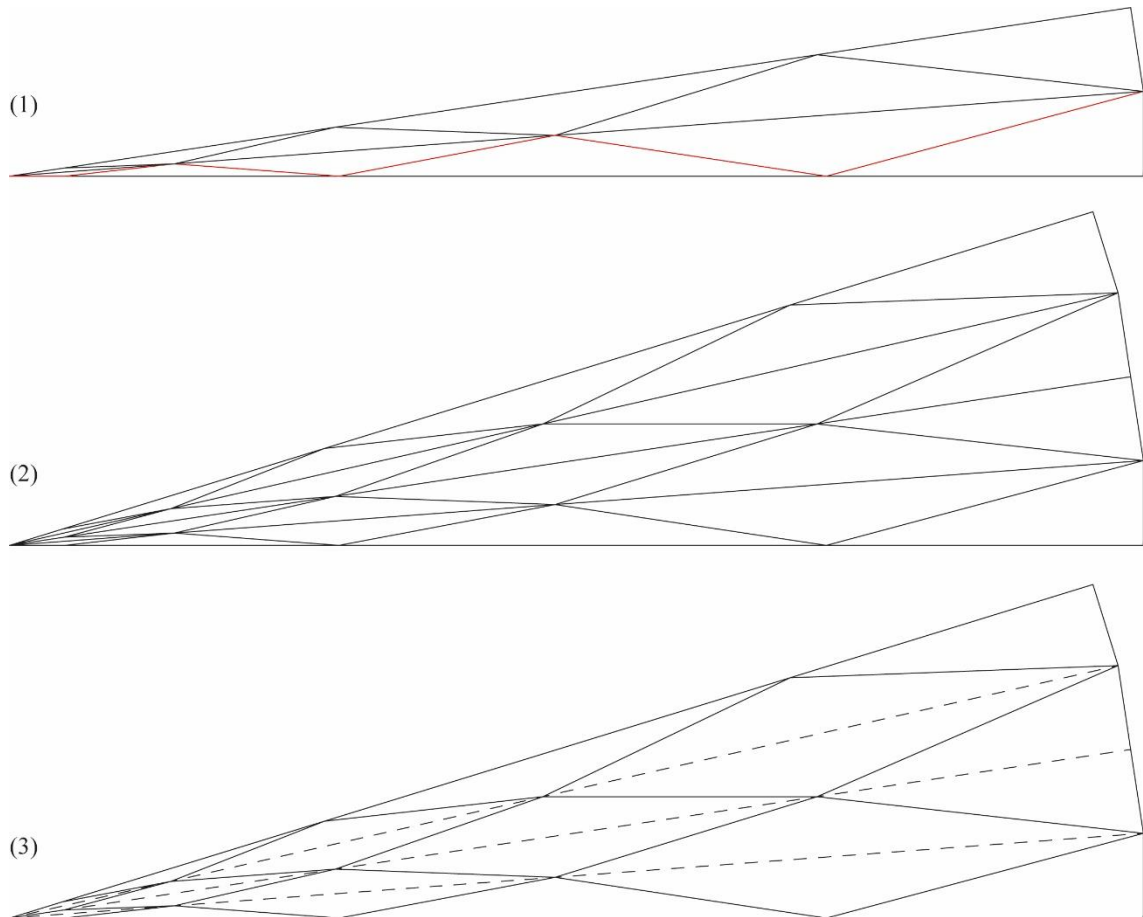


Figure 5.13. Pattern's row multiplication and MV-Pattern.

### 5.2.3. Step 3 – Dimensions of the Created Pattern

In this step the dimensions (span, height, coverage area, and volume) of the designed pattern will be discussed. The designed pattern is flat-foldable pattern, but the developability depends on the number of row. The multiplication of the number of row  $R_T$  and the folding angle  $\alpha_{11}$  should be equal to  $2\pi$  or  $360^\circ$ , only then the pattern is developable, but in this case study because the folding angle value is not a divisor of  $360^\circ$  the pattern will have a gap which will make the pattern a non-developable one (Figure 5.14).

The number of maximum row is calculated:

$$R_T = \frac{360}{\alpha_{11}} = \frac{360}{4,286} = 83,9944 \quad (5.58)$$

As it can be observed in this calculation the total number of rows  $R_T$  is not a natural number, so this particular designed pattern is a non-developable pattern. According to this calculation the maximum number of row for this pattern is 83. For this case study the number of row has been decided as 82 (Figure 5.14).

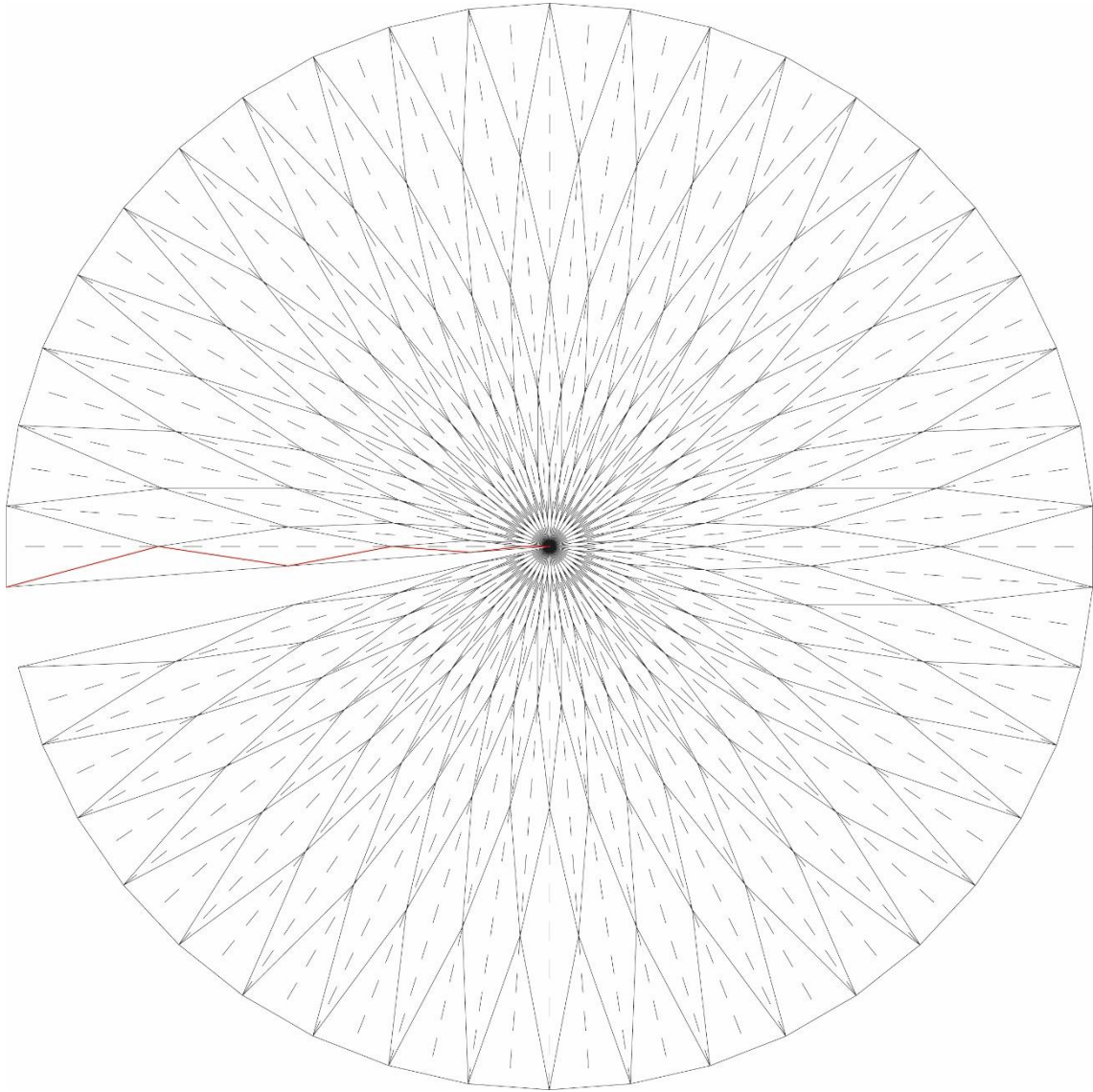


Figure 5.14. Semi-pseudo-dome pattern with  $r$ : 5m,  $n$ : 6, and  $R_T$ : 82.

In this case the structure have a temporary use, so it needs to be transportable and deployable. And also there is a need to specify a maximum opening angle for the central angle  $\rho_T$  that will create the stage cover. The maximum opening angle for a stage can be  $180^\circ$  which creates a semi-pseudo-dome. The dimension (height, span, coverage area, and volume) calculations are done assuming the surface of the deployable structure has no thickness.

When the relation between the central angle  $\rho_T$  and the inclination angle  $\sigma$  is analyzed, it can be observed that the closest value of the central angle to  $180^\circ$  is when the inclination angle is  $60^\circ$  (Figure 5.15). Thus the maximum value of the inclination angle  $\sigma$ , when the structure is deployed from final folded state to initial folded state, is  $60^\circ$ .

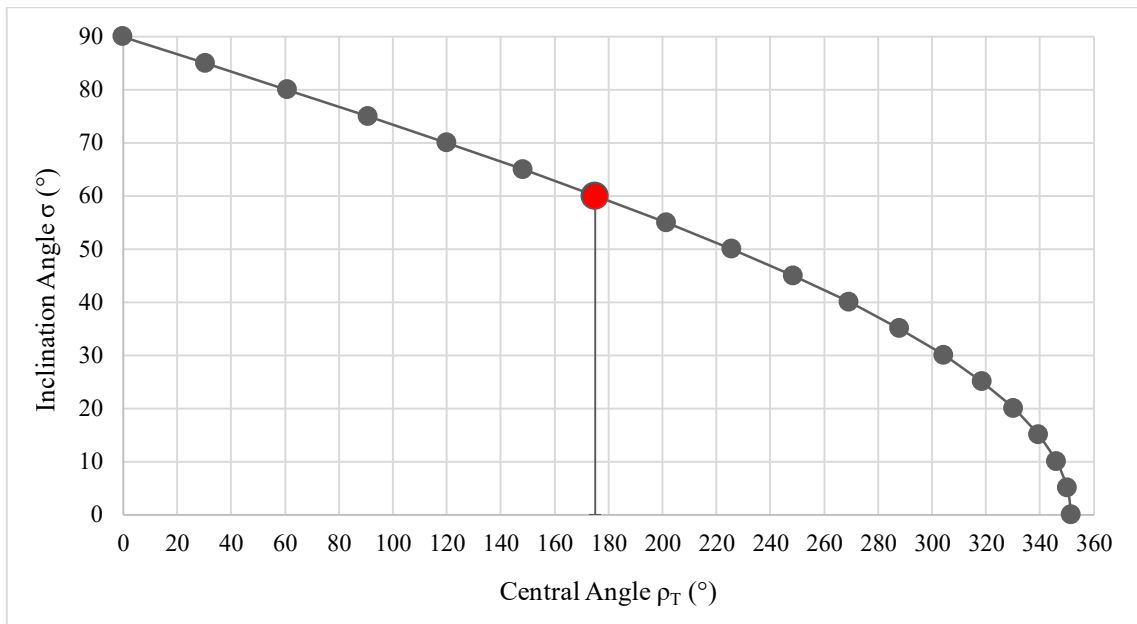


Figure 5.15. Inclination angle  $\sigma$  and Central angle  $\rho_T$  relation for a semi-pseudo-dome with  $r$ : 5m,  $n$ : 6, and  $R_T$ : 82.

The height  $H$  is calculated using the eq. (4.57) with different inclination angle values (Figure 5.16). The value of the height that coincide to a  $60^\circ$  inclination angle is 4,56 m, which provides a sufficient height for the stage. For all the following dimension calculations the  $60^\circ$  value of the inclination angle  $\sigma$  have been highlighted as a red dot.

The eq. (4.59) is used to calculate the span  $S$  of the structure. Again the changes occurring to the span in relation with the inclination angle have been demonstrated (Figure 5.17). The value of span is equal to 5.60 m for a  $60^\circ$  inclination angle.

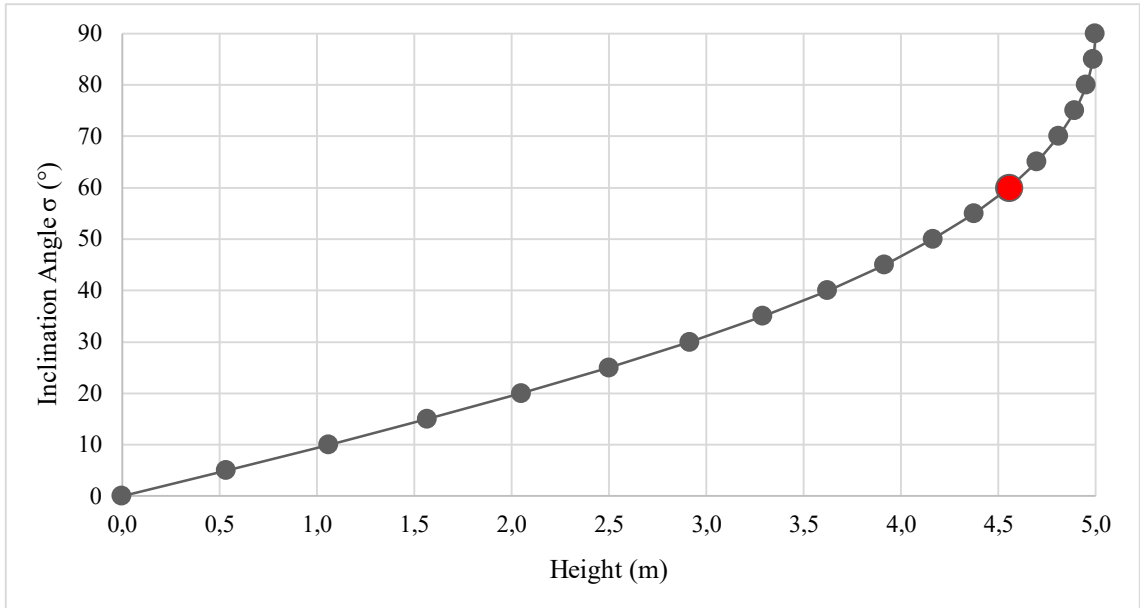


Figure 5.16. Height changes for a semi-pseudo-dome with  $r$ : 5m,  $n$ : 6, and  $R_T$ : 82.

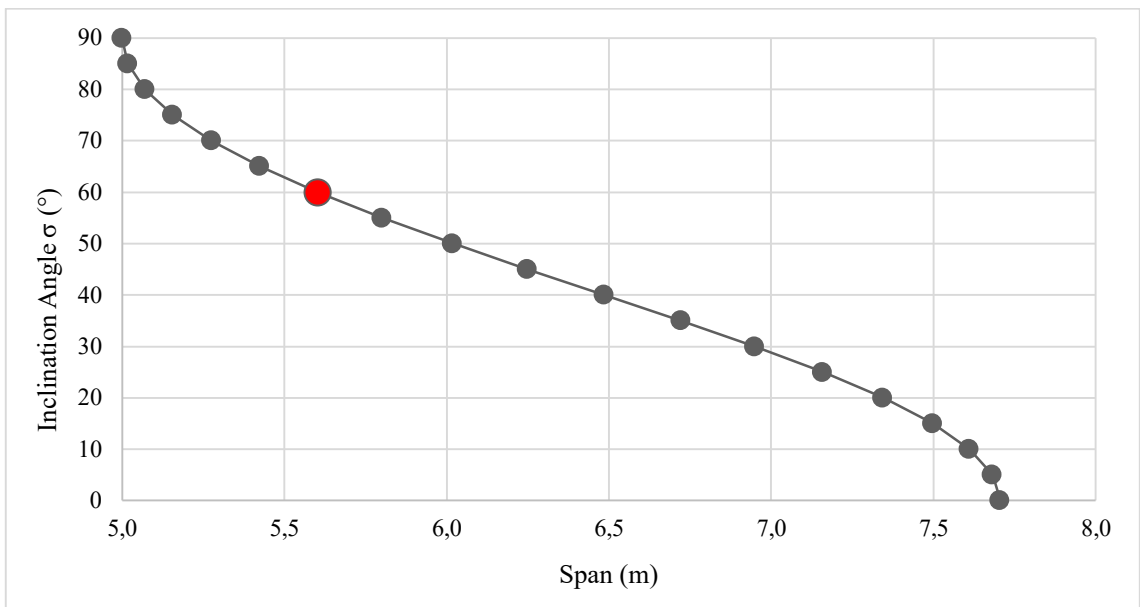


Figure 5.17. Span changes for a semi-pseudo-dome with  $r$ : 5m,  $n$ : 6, and  $R_T$ : 82.

The structure is assembled, then folded to its final flat-folded state so that it can be transported. When the stage is set the structure is placed vertically to the ground then deployed till the inclination angle reaches  $60^\circ$ .

The area that this deployable semi-pseudo-dome cover, is calculated using eq. (4.61). When calculated based on the structures maximum opening ( $\sigma=60^\circ$ ) the structure covers  $48,07\text{m}^2$ , as it can be observed in Figure 5.18.

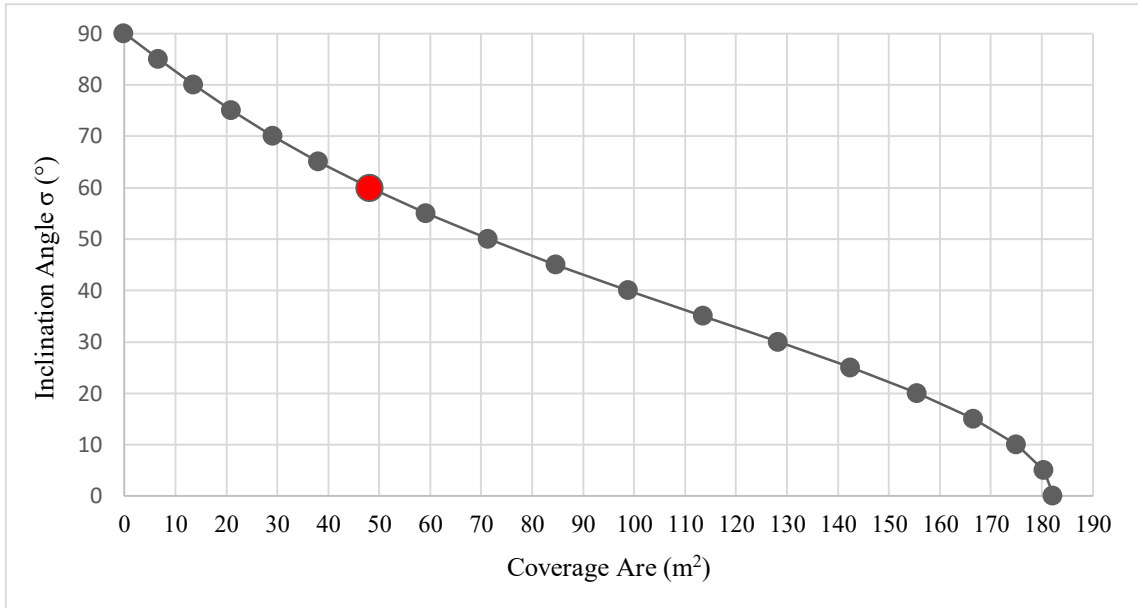


Figure 5.18. Coverage area changes for a semi-pseudo-dome with  $r$ : 5m,  $n$ : 6, and  $R_T$ : 82.

The final dimension to calculate is the volume  $V$  for the desired maximum opening. The volume is calculated using eq. (4.65) (Figure 5.19), and the volume corresponding to an inclination angle value of  $60^\circ$ , is  $109,51 \text{ m}^3$ .

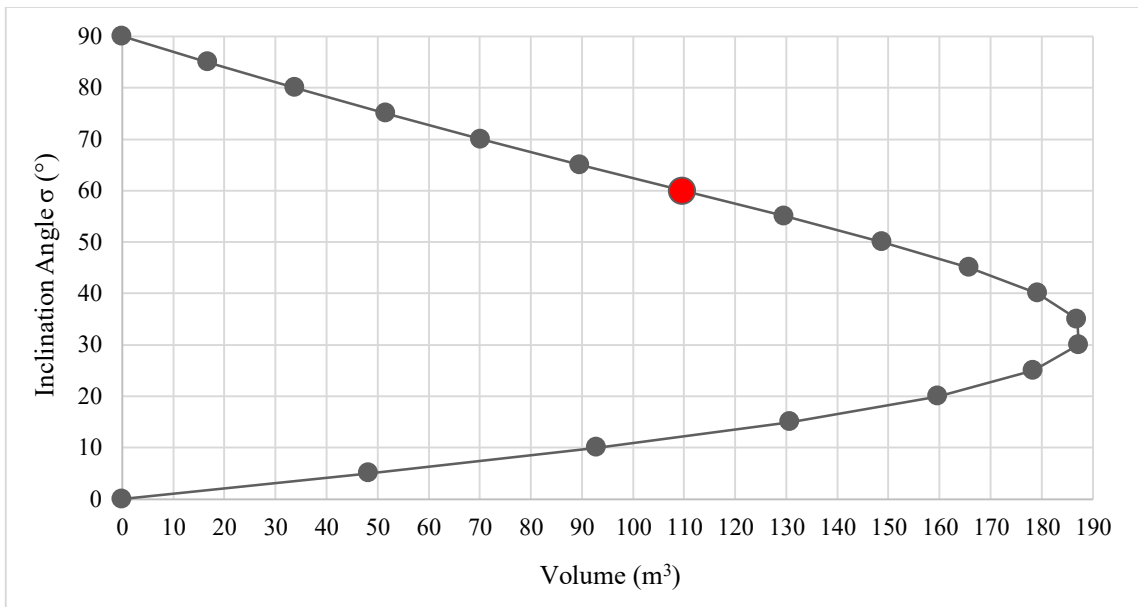


Figure 5.19. Volume changes for a semi-pseudo-dome with  $r$ : 5m,  $n$ : 6, and  $R_T$ : 82.

Figure 5.20 represent the deployable semi-pseudo-dome structure with the defined inclination angle equal to  $60^\circ$ .

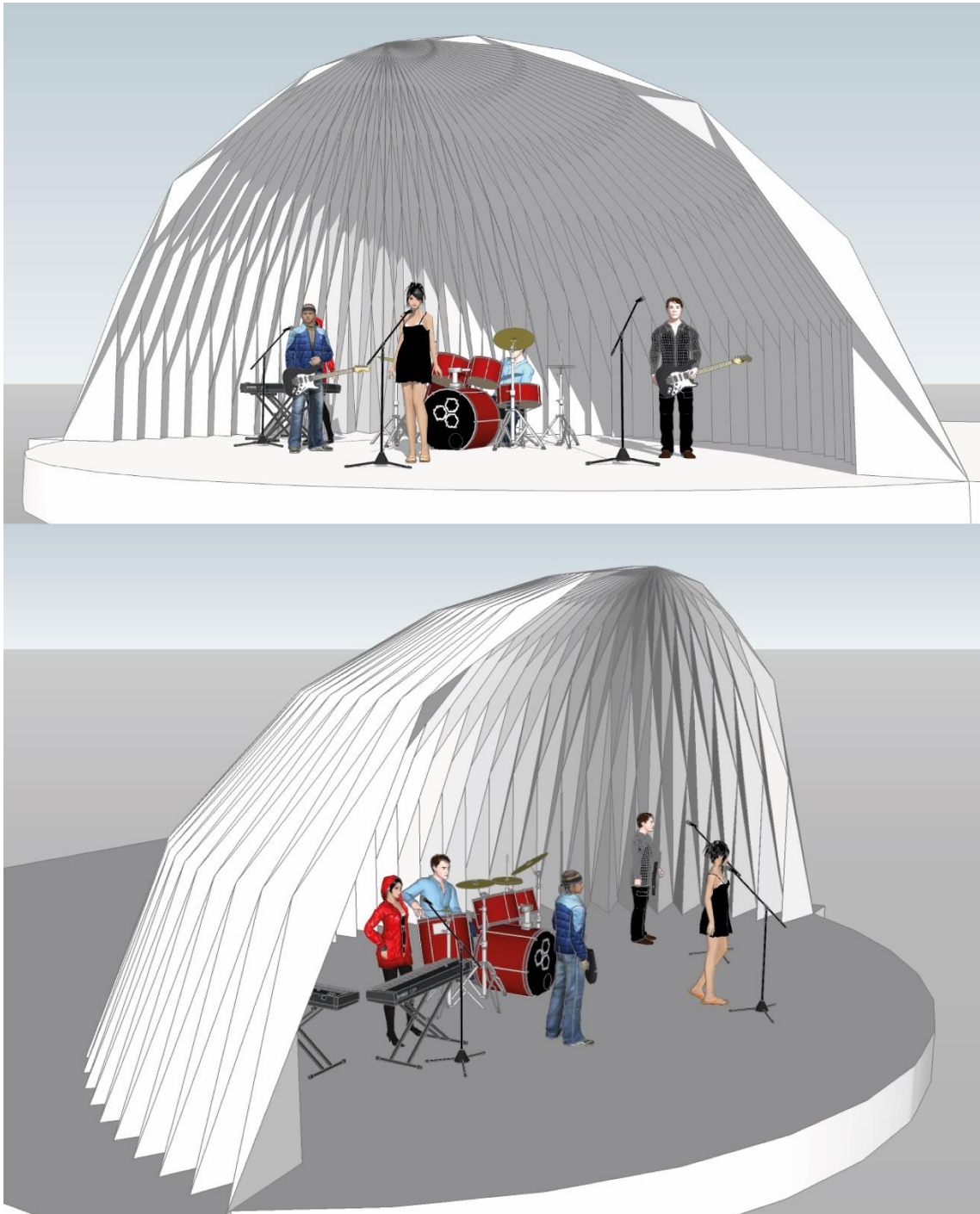


Figure 5.20. Deployable Semi-pseudo-dome structure with  $r$ : 5m,  $n$ : 6,  $R_T$ : 82, and  $\sigma$ : 60°.

#### 5.2.4. Conclusion

In case study 2 the steps of creating a semi-pseudo-dome deployable structure has been presented. The choice of the structure type have been decided based on the requirements of the function.

The first step demonstrated all the calculations necessary to create the pattern. The second step described the creation of the crease pattern and its transformation into a MV-Pattern. The third step demonstrated the calculations of the dimensions of the structure and how the inclination angle values affect the choice and the form of the structure. A limit to the inclination angle have been created based on the function. The structure is assumed to be transported in its final folded state, then deployed till the inclination angle  $\sigma$  reaches the value of  $60^\circ$ , so that the central angle  $\rho_T$  is equal to or close to  $180^\circ$ .

The designed pattern has 492 links, 694 joints, and 203 loops, when the mobility is calculated using the Freudenstein and Alizade's equation it is equal to 85.

Structural loads are not being calculated but for the structure to be more stable it is recommended to use lighter materials or materials with less thickness towards the center point of the semi-pseudo-dome.

## CHAPTER 6

### CONCLUSION

The aim of this dissertation was to develop a design method to be able to create flat-foldable deployable structures using origami patterns. In order to achieve this first, a general research to understand origami as an art and a science have been conducted, where a new classification have been created to classify the types of patterns created in this dissertation. Within this new classification both barrel vault and pseudo-dome deployable structures' patterns are classified as origami corrugation type origami. Both barrel vault and pseudo-dome patterns are created by a single sheet and they are kinetic where the movement has a linear deployment for barrel vaults and rotational deployment for pseudo-dome patterns. Their crease patterns' properties are different; barrel vaults are tessellated grid patterns and pseudo-dome are geometric patterns due to their central radial patterns.

A review of previous studies on the applications of origami patterns to folded plate structures provided a method of creating flat-foldable deployable rigid origami structures using a generator line, referred as *pattern-generator* in this dissertation. This method has been advanced by applying it to create flat-foldable deployable barrel vault structures with different arches used as cross-sections. Five different arches have been selected to be used as cross-sections: semicircle, horseshoe, pointed equilateral, lancet, and obtuse arches. These arches have been grouped under two different types based on their geometrical properties: single centered barrel vaults created with semicircle and horseshoe arches, and double centered barrel vaults created with pointed equilateral, lancet, and obtuse arches.

The geometrical properties of both types of deployable barrel vault structures have been analyzed, to understand the parameters and their relation, and to create a simple design method. First the single centered barrel vaults have been analyzed revealing a close relations between parameters. To be able to design a pattern the main parameters have been defined as the radius, the number of segments and the central angle. The central angle parameter defines whether the type of arch for the cross-section will be a semicircle or a horseshoe. Simple parameters have been selected as the design



parameters allowing a designer to create a pattern that can be transformed to a deployable structure. The design parameters could have been the structural properties like span and height of the structure. But these parameters proved to be difficult to use because the created structures are spread on the floor in their initial state and flat folded on their final folded state which created different span and height values during the whole folding process. This is why the radius, number of segments and central angle parameters have been selected as the design parameters instead of the structural properties. Once the design parameters are inputted, parameters to create the pattern can be computed using Microsoft Excel 2013® medium. Within this medium the design parameters can be changed by the designer using a spin button that changes simultaneously the values of the parameters according to the inputs. The pattern is created using the calculated folding angle and half-row height. The folding angle allows the calculation of the maximum value of the half-row height for a triangular pattern. If the calculated maximum value is exceeded the lines created using the folding angle crisscrosses and the pattern cannot be created. If less than the maximum value of the half-row height is used a trapezoidal pattern can be created. Both created pattern are CP (crease pattern) which then are transformed to MV-Patterns using Maekawa's theorem. Both types of patterns have different architectural values in both form and aesthetics.

The structural properties like span, height, depth and volume are important in an architectural application for that they have been put in relation with the inclination angle. The inclination angle allows the calculation of all structural properties at each step of the folding process starting from the initial state and ending at the final folded state. The analysis of the values showed that the structure reaches its maximum value quickly and then decreases slowly, as it has been shown. Even though the demonstrated calculations for the structural properties belong to triangular patterns they are also valid for trapezoidal patterns because they are calculated using the same pattern-generator. The created structures are deployable but with the use of the inclination angle a static folded plate structure can be created. For this purpose the inclination angle can be considered fixed once the required structural properties values are reached and then parameters like dimensions, angles etc. can be calculated to create the folded plate structure.

The mobility analysis have been conducted to understand the mechanism of the created patterns. All mobility calculations have been verified using the structural group properties. Physical models with both paper and thick materials have been created to observe the folding process of the single centered rigid origami barrel vault structures.

The model with thick material have been created using the axis-shift method of creating joints for a rigid origami. Paper and thick material models created using the triangular pattern folded without a problem, but model created with thick material using trapezoidal pattern revealed tearing in some joints that did not occur in the paper models. These joints were degree-4 vertexes where when flat folded one side's thickness was more than the other side's which forced the joint to tear, so two different trapezoidal patterns' mobility calculations have been conducted. Starting with the paper folded trapezoidal pattern and then the thick material trapezoidal pattern, where the tearing joints have been removed from the mobility calculation. Removing the joints did not changed the mobility but changed the types of linkage of the mechanism. Removed joints changed the loops from 6-bar spherical linkages to 6-bar double spherical linkages.

The second type of deployable barrel vault structures is the double centered one, where the cross-section is an arch created by two segments of arc. The geometrical analysis of double centered barrel vaults showed both similarities and differences with single centered barrel vaults. As it was with single centered barrel vaults two of the design parameters are radius and number of segments, the third one is not a central angle but the distance between the two centers which defines the type of the cross-section's arch. This parameters are in close relation with the defined radius because if the radius is equal to the distance between the two centers it creates an equilateral arch, if the radius is greater than the distance it creates an obtuse arch and finally if the radius is smaller than the distance it creates a lancet arch as the cross-section. All parameters can be computed using the provided Microsoft Excel 2013® medium to create the pattern for this type of barrel vault. The double centered cross-section creates an apex point with a folding angle different than the one calculated on a single arc. Two different folding angles create two different half-row heights. To be able to create a foldable CP the smallest value of the two half-row height should be used so that no crisscrossing occurs within the height of the row. Similar to the single centered barrel vaults using less than the calculated maximum value of the half-row height will create a trapezoidal pattern. In the same way as the single centered barrel vaults using the Maekawa's theorem, the CP of the double centered barrel vault is transformed to a MV-Pattern.

The structural properties of the double centered barrel vaults have also been put in relation to the inclination for the same reason as the single centered barrel vaults. The

use of a fixed inclination angle value will provide the necessary properties to create a folded plate double centered structure. Again as it was in single centered barrel vaults the structural properties (span, height, depth, and volume) are calculated using the pattern-generator.

The mobility calculations for double centered barrel vaults have been conducted using the same calculation and verification methods. Paper and thick material models also have been created. Both triangular and trapezoidal patterns' models created using thick material showed tears when flat folded. The triangular pattern showed tears because of the two different folding angles, the degree-4 vertexes around the apex where the joints teared when the pattern was flat folded. Similarly to the single centered barrel vaults when the tears were removed the loops became double spherical 6-bar linkages and the mobility did not changed.

The design method created for both types of barrel vault foldable plate structures uses three design parameters to compute all other parameters using Microsoft Excel 2013® medium including those used to create a CP. This method allow the designer to design either a deployable structure or a folded plate structure. By also using the geometrical properties of both type of barrel vaults, a designer can create a linearly deployed flat foldable freeform rigid origami structures composed of multiple arcs.

Another aim of this research was to propose a novel method of designing pseudo-dome flat-foldable rigid origami structures. In order to achieve this aim, the principle of the *pattern-generator* method that has been proposed in barrel vault rigid origami structures, has been transformed to create a new method of designing pseudo-dome rigid origami structures. The cross-section for the structure has been defined as a quarter of a circle because the created pattern was developable. First a segmentation method had to be found so that the length of the segments could decrease toward the center. Arithmetic sequence has been selected as the segmentation method because it presented simple mathematical method which connected the geometrical properties of the cross-section to the design parameters. This segmentation method allowed the design of a rigid origami pseudo-dome structure which is flat-foldable and deploy using a polar rotation. The geometrical analysis first started with three design parameters radius, number of segments and first angle which is used as the first term of the sequence. With these three design parameters there was three possible outcomes for a pattern creation: no-pattern, pattern, or pattern with complementary angle. To simplify the design process further geometrical analysis have been conducted revealing that the

number of segments defines the first term of the sequence which removed the use of the first angle as the design parameter. The same analysis revealed that if the first term is equal to the common difference of the sequence a pattern is created without the need for a complementary angle. So only two design parameters are required to design a pseudo-dome deployable structure. As it was with all types of rigid origami barrel vault structures all other parameters required to draw the CP are computed using Microsoft Excel 2013® medium. The pattern-generator in this method is not a line passing from the middle of a row as it is in the barrel vault structures but the segments themselves. The segments lengths are calculated from the flat folded state of the pattern using the segment angles. The CP is created using each segments' length and their interior angles, then transformed to a MV-Pattern using the Maekawa's theorem as it is in the barrel vault rigid origami structures. This method only creates triangular patterns, because to create a trapezoidal pattern the height of row should be decreased which will change the calculated central angle and increase the number of segments which will create additional interior angles creating an undesired cross-section. Further studies on the cross-section of the pseudo-dome structure may lead to the creation of a trapezoidal pattern.

The structural properties (span, height, coverage area, and volume) have been put in relation with the inclination angle as it was with the barrel vault rigid origami structures. Similarly in this method the inclination angle can be fixed to a specific value to calculate the necessary parameters to create a folded plate structure.

Physical models have been created from both paper and thick material to see if tears appeared like in the barrel vaults and also to understand the mobility of the mechanism. No tears appeared on the paper model but the some appeared on the model created with thick material. Similarly to barrel vaults the tears appeared on degree-4 vertexes around the central point. Mobility analysis revealed that with each additional row the mobility increased and when the mobility was calculated with the tearing joints removed it increased even more. These particular tearing joints can be modified to avoid further increase in mobility.

This novel design method propose the creation of a pseudo-dome deployable structure using an origami pattern by defining only two parameters. The parameters to create a CP are computed using Microsoft Excel 2013® medium. This method can be used to create more complex geometrical forms that deploy radially or it can be merged

with the barrel vault design method to create forms that deploy both radially and linearly.

This research contributes to the fields of kinetic structures by creating a new method of designing a radially deployed spatial rigid origami structure. In view of the changes occurring in the functional and spatial needs in architecture, this dissertation provides a different type of adaptive/kinetic structures.

The created design methods are preliminary studies and in view of future studies a more profound and detailed analysis is needed. The study on the rigid origami structures was conducted assuming zero-thickness, a more detailed research with different thickness options can further advance the methods presented in this dissertation. A structural analysis conducted with different thickness and different materials will increase the possibility of a large scale architectural realizations of these structures. A mobility analysis has been conducted but no detailed studies have been done on the joints which are a major part of the designed structure. A study can also be conducted on effects of how the mechanism might be affected if some plates are removed. Thus structural design and analysis of the joints and the mechanism should be conducted for further studies, which would enhance the feasibility of these structures.

For further studies the author of this dissertation plans to visualize the design method process on an open source CAD medium, which will eliminate the drawing process of the designed structure and allow an instantaneous visual outcome of the modifications.

## BIBLIOGRAPHY

- Abdul-Sater, K. (2013). Two-Configuration Synthesis of Origami-Guided Planar, Spherical and Spatial Revolute-Revolute Chains. *Journal of Mechanisms and Robotics*, 10 pages.
- Abdul-Sater, K., Lueth, T., & Irlinger, F. (2014). Kinematic Design of Miura-Ori-Based Folding. In J. Lenarčič, & O. Khatib, *Advances in Robot Kinematics* (pp. 233-241). Switzerland: Springer International Publishing. doi:10.1007/978-3-319-06698-1\_25
- Abranera (2012, May 10). *Noshi* [Online image]. Retrieved March, 2015 from <http://nipponario.abranera.com/?p=1042#sthash.AOd9jkeq.8J3q9TsY.dpbs>
- Alizade, R., Kiper, G., Bağdadioğlu, B., & Dede, M. (2014, November). Function Synthesis of Bennett 6R Mechanisms Using Chebyshev Approximation. *Mechanism and Machine Theory*, Vol. 81, 62-78. doi:10.1016/j.mechmachtheory.2014.06.010
- Alizade, R., Kiper, G., Dede, M., & Uzunoğlu, E. (2014). Derivation of Input/Output Relationships for the Bennett 6R Linkages Based on the Method of Decomposition. In V. Petuya, C. Pinto, & E.-C. Lovasz (Ed.), *New Advances in Mechanisms, Transmissions and Applications: Proceedings of the Second Conference MeTrApp 2013. Vol. 17*, pp. 225-231. Springer. doi:10.1007/978-94-007-7485-8\_28
- Alperin, R., & Lang, R. (2009). One-, Two-, and Multi-Fold Origami Axioms. In R. Lang (Ed.), *Origami4: Fourth International Meeting of Origami Science, Mathematics, and Education* (pp. 371-393). Wellesley, MA: A K Peters.
- Anonymous. (2012). *Origami & Math*. Retrieved May 09, 2015, from <http://www.paperfolding.com/math/>
- Baerlecken, D., Swarts, M., Gentry, R., & Wonoto, N. (2012). Bio-Origami: Form finding and evaluation of origami structures. In *digital Physicality: Proceedings of the 30th eCAADe. 1*, s. 497-504. Prague: Czech Technical University in Prague, Faculty of Architecture.
- Bateman, A. (n.d.). *Tess: origami tessellation software*. Retrieved 03 19, 2015, from <http://www.papermosaics.co.uk/software.html>
- Bennett, G. (1905). The Parallel Motion of Sarrus and some Allied Mechanisms. *Philosophy Magazine*, 6th series(9), 803-810.
- Bern, M., & Hayes, B. (1996). The Complexity of Flat Origami. *Proceedings of the Seventh Annual ACM-SIAM Symposium on Discrete Algorithms* (pp. 175-183). Atlanta: SIAM.

- Bowen, L., Grames, C., Magleby, S., & Lang, R. (2013, November). A Classification of Action Origami as Systems of Spherical Mechanisms. *Journal of Mechanical Design, Vol. 135*, 111008 (7 pages). doi:10.1115/1.4025379
- Buri, H. (2010). *Origami - Folded Plate Structures* (PhD Thesis). Ecole Polytechnique Federale de Lausanne, Switzerland.
- Buri, H., & Weinand, Y. (2008). Origami - Folded Plate Structures, Architecture. 10th World Conference on Timber Engineering. Miyazaki, Japan. Retrieved February 5, 2015, from Infoscience - EPFL: <https://infoscience.epfl.ch/record/118687>
- Cai, J. (2016c, June). Kinematic Analysis of Foldable Plate Structures With Rolling Joints. *Journal of Mechanisms and Robotics, Vol. 8*, 034502 (6 pages). doi:10.1115/1.4032269
- Cai, J., Deng, X., Xu, Y., & Feng, J. (2015, October). Geometry and Motion Analysis of Origami-Based Deployable Shelter Structures. *Journal of Structural Engineering, Vol. 141*(10). doi:10.1061/(ASCE)ST.1943-541X.0001238
- Cai, J., Deng, X., Xu, Y., & Feng, J. (2016b, April). Motion Analysis of a Foldable Berrel Vault Based on Regular and Irregular Yoshimura Origami. *Journal of Mechanisms and Robotics, Vol. 8*, 021017 (9 pages). doi:10.1115/1.4031658
- Cai, J., Zhang, Y., Xu, Y., Zhou, Y., & Feng, J. (2016a, March). The Foldability of Cylindrical Foldable Structures Based on Rigid Origami. *Journal of Mechanical Design, Vol. 138*, 031401 (8 pages). doi:10.1115/1.4032194
- Chen, Y., & Feng, J. (2012). Folding of a Type of Deployable Origami Structure. *International Journal of Structural Stability and Dynamics, Vol. 12*(No. 6), 1250054 (17 pages).
- Cheung, K., Tachi, T., Calisch, S., & Miura, K. (2014). Origami Interleaved Tube Cellular Materials. *Smart Materials and Structures, Vol. 23*, 094012 (10 pages). doi:10.1088/0964-1726/23/9/094012
- Chorna, O. (2012, 11 30). *Origami as a modern art phenomenon: systematization attempt*. Retrieved 4 4, 2015, from <https://oksanachorna.wordpress.com/2012/11/30/origami-as-a-modern-art-phenomenon-systematization-attempt/>
- Chudoba, R., van der Woerd, J., & Hegger, J. (2014). Oricreate: Modelling Framework for Design and Manufacturing of Folded Plate Structures. In K. Miura, T. Kawasaki, T. Tachi, R. Uehara, R. Lang, & P. Wang-Iverson (Ed.), *Origami6: Proceedings of the Sixth International Meeting on Origami Science, Mathematics, and Education* (pp. 523-536). USA: AMS.
- Chudoba, R., van der Woerd, J., Schmerl, M., & Hegger, J. (2014, June). ORICRETE: Modeling support for design and manufacturing of folded concrete structures. *Advances in Engineering Software, Vol. 72*, 119-127. doi:10.1016/j.advengsoft.2013.05.004

- Cromvik, C., & Eriksson, K. (2009). Airbag Folding Based on Origami Mathematics. In R. Lang (Ed.), *Origami4: Fourth International Meeting of Origami Science, Mathematics, and Education* (pp. 129-139). Wellesley, MA: A K Paters.
- Curletto, G., & Gambarotta, L. (2015). Rigid foldable origami structures: integrated parametric design and structural analysis. *Proceedings of the International Association for Shell and Spatial Structures (IASS): Future Visions*. Amsterdam.
- Davis, E., Demaine, E., Demaine, M., & Ramseyer, J. (2013, November). Reconstructing David Huffman's Origami Tessellations. *Journal of Mechanical Design, Vol. 135*, 111010 (7 pages). doi:10.1115/1.4025428
- De Ruysser, T. (2014). Wearable Metal Origami. In K. Miura, T. Kawasaki, T. Tachi, R. Uehara, R. Lang, & P. Wang-Iverson (Ed.), *Origami6: Proceedings of the Sixth International Meeting on Origami Science, Mathematics, and Education* (pp. 613-624). USA: AMS.
- De Temmerman, N. (2007a, June). Design and Analysis of Deployable Bar Structures for Mobile Architectural Applications (PhD Thesis). Vrije Universiteit, Brussel, Belgium.
- De Temmerman, N., Mollaert, M., Van Mele, T., & De Laet, L. (2007b, September). Design and Analysis of a Foldable Mobile Shelter System. *International Journal of Space Structures*, 22(3), pp. 161-168.
- Demaine, E. D., & O'Rourke, J. (2007). *Geometric Folding Algorithms: Linkage, Origami, Polyhedra*. New York: Cambridge University Press.
- Dinh, G. (n.d.). *Dreamer* [Online Image]. Retrieved January, 2015 from <http://www.express.co.uk/pictures/pics/2122/Origami-work-The-pinnacles-of-paper-folding/41992>
- Dureisseix, D. (2012, March). An Overview of Mechanisms and Patterns with Origami. *International Journal of Space Structures*, 27(1), pp. 1-14.
- Edmondson, B., Lang, R., Morgan, M., Magleby, S., & Howell, L. (2014). Thick Rigidly Foldable Structures Realized by an Offset Panel Technique. In K. Miura, T. Kawasaki, T. Tachi, R. Uehara, R. Lang, & P. Wang-Iverson (Ed.), *Origami6: Proceedings of the Sixth International Meeting on Origami Science, Mathematics, and Education* (pp. 149-161). USA: AMS.
- Evans, T., Lang, R., Magleby, S., & Howell, L. (2014). Rigidly Foldable Origami Twists. In K. Miura, T. Kawasaki, T. Tachi, R. Uehara, R. Lang, & P. Wang-Iverson (Ed.), *Origami6: Proceedings of the Sixth International Meeting on Origami Science, Mathematics, and Education* (pp. 119-130). USA: AMS.
- Falk, A., Von Buelow, P., & Khodadadi, A. (2015). Form Exploration of Timber-based Folded Plate Domes. *Proceedings of the International Association for Shell and Spatial Structures (IASS):Future Visions*. Amsterdam.



- Fei, L., & Sujan, D. (2013). Origami Theory and its Applications: A Literature Review. *World Academy of Science, Engineering and Technology, International Science Index 98, International Journal of Social, Education, Economics and Management Engineering*, 7(1), s. 113-117.
- Flexidome (n.d.). Research Project, Queen's University, Belfast.
- Flexidome. (2012). Origami dome [Online image] Retrieved April, 2015 from <https://flexidome.wordpress.com/2012/04/18/applications-for-origami-dome-skin/>
- Foster, C., & Krishnakumar, S. (1986/87). A Class of Transportable Demountable Structures. *Space Structures*, 129-137.
- Gardiner, M. (2009). A Brief History of Oribotics. In R. Lang (Ed.), *Origami4: Fourth International Meeting of Origami Science, Mathematics, and Education* (pp. 51-60). Wellesy, MA: A K Peters.
- Gattas, J. (2014). *Rigid Origami Toolbox*. Retrieved 03 20, 2015, from <http://joegattas.com/rigid-origami-toolbox/>
- Gattas, J., & You, Z. (2013). Rigid-foldable Piecewise Geometries. *Proceedings of the First Conference Transformables*, (pp. 319-324). Seville.
- Gattas, J., & You, Z. (2014). Structural Engineering Applications of Morphing Sandwich Structures. In K. Miura, T. Kawasaki, T. Tachi, R. Uehara, R. Lang, & P. Wang-Iverson (Ed.), *Origami6: Proceedings of the Sixth International Meeting on Origami Science, Mathematics, and Education* (pp. 421-430). USA: AMS.
- Gattas, J., & You, Z. (2015). Geometric Assembly of Rigid-Foldable Morphing Sandwich Structures. *Engineering Structures*, Vol. 94, 149-159. doi:10.1016/j.engstruct.2015.03.019
- Gattas, J., Wu, W., & You, Z. (2013a, November). Miura-Base Rigid Origami: Parametrizations of First-Level Derivative and Piecewise Geometries. *Journal of Mechanical Design*, Vol. 135, 111011 (11 pages). doi:10.1115/1.4025380
- Gioia, F., Dureisseix, D., Motro, R., & Maurin, B. (2012, March). Design and Analysis of a Foldable/Unfoldable Corrugated Architectural Curved Envelop. *Journal of Mechanical Design*, Vol. 134, 031003 (11 pages). doi:10.1115/1.4005601
- Gjerde, E. (2009). *Orgami Tessellations: Awe-inspiring Geometric Designs*. Massachusetts: A K Peters.
- Gogu, G. (2005). Chebychev-Grübler-Kutzbach's Criterion for Mobility Calculation of Multi-Loop Mechanisms Revisited via Theory of Linear Transformations. *European Journal of Mechanics A/Solids*, Vol. 24, 427-441.
- Gould, V. (Director). (2008). *Between the Folds* [Motion Picture].

- Gönenç Sorguç, A., Hagiwara, I., & Arslan Selçuk, S. (2009). Origamics in Architecture: a Medium of Inquiry for Design in Architecture. *METU JFA*, 26(2), pp. 23-247.
- Gray, S., Zeichner, N., Yim, M., & Kumar, V. (2011). A Simulator for Origami-Inspired Self-Reconfigurable Robots. In P. Wang-Iverson, R. Lang, & M. Yim (Ed.), *Origami5: Fifth International Meeting of Origami Science, Mathematics, and Education* (pp. 323-333). Boca Raton, FL: A K Peters / CRC Press.
- Greenberg, H., Gong, M., Magleby, S., & Howell, L. (2011). Identifying Links Between Origami and Compliant Mechanisms. *Mechanical Sciences*, Vol. 2, 217-225. doi:10.5194/ms-2-217-2011
- Gruber, P., Häuplik, S., Imhof, B., Özdemir, K., Waclavicek, R., & Perino, M. (2007). Deployable structures for a human lunar base. *Acta Astronautica*, Vol. 61, 484-495. doi:10.1016/j.actaastro.2007.01.055
- Guarnieri, F. (2010). *Christmas Tree* [Online image]. Retrieved January, 2015 from <http://www.grupoetor.org/outstanding-origami-fir-tree/origami-maniacs-origami-christmas-tree-fir-tree-by-francesco-origami-fir-tree-instructions-origami-fir-tree-diagram/>
- Hatori, K. (2011). History of Origami in the East and West before Interfusion. In P. Wang-Iverson, R. Lang, & M. Yim (Ed.), *Origami5: the Fifth International Meeting of Origami Science, Mathematics, and Education* (pp. 3-11). Boca Raton: A K Peters/CRC Press.
- Highsmith, C. (2007). *Air Force Academy Chapel, Colorado Springs, CO* [Online image]. ID: highsm.04090. Retrieved April, 2015 from [https://en.wikipedia.org/wiki/United\\_States\\_Air\\_Force\\_Academy\\_Cadet\\_Chapel](https://en.wikipedia.org/wiki/United_States_Air_Force_Academy_Cadet_Chapel)
- Hoffmann, S., Barej, M., Günther, B., Trautz, M., Corves, B., & Feldhusen, J. (2014). Demands on an Adapted Design Process for Foldable Structures. In K. Miura, T. Kawasaki, T. Tachi, R. Uehara, R. Lang, & P. Wang-Iverson (Ed.), *Origami6: Proceedings of the Sixth International Meeting on Origami Science, Mathematics, and Education* (pp. 489-499). USA: AMS.
- Hull, T. (2002). The Combinatorics of Flat Folds: A Survey. *Origami3: Third International Meeting of Origami Science, Mathematics, and Education* (pp. 29-38). Natick: A K Peters.
- Hull, T. (2003). Counting Mountain-Valley Assignments for Flat Folds. *Ars Combinatoria*, Vol. 67, 175-188.
- Hull, T. (2014). Coloring Connections with Counting Mountain-Valley Assignments. In K. Miura, T. Kawasaki, T. Tachi, R. Uehara, R. Lang, & P. Wang-Iverson (Ed.), *Origami6: Proceedings of the Sixth International Meetings on Origami Science, Mathematics, and Education* (pp. 3-10). USA: AMS.

- IFTToMM, (n.d.). Retrieved from IFTToMM online dictionary: <http://www.iftomm-terminology.antonkb.nl/2057/01.html#1.3.12>
- Ishida, S., Morimura, H., & Hagiwara, I. (2014). Sound-Insulating Performance of Origami-Based Sandwich Trusscore Panels. In K. Miura, T. Kawasaki, T. Tachi, R. Uehara, R. Lang, & P. Wang-Iverson (Ed.), *Origami6: Proceedings of the Sixth International Meeting on Origami Science, Mathematics, and Education* (pp. 431-438). USA: AMS.
- Jackson, P. (2011). *Folding Techniques for Designers: From Sheet to Form*. London: Laurence King Publishing.
- Keller, M. (2008). *Temporary chapel for Deaconesses of St-Loup* [Online image]. Retrieved April, 2015 from <http://www.archdaily.com/9201/temporary-chapel-for-the-deaconesses-of-st-loup-localarchitecture>
- Kenneway, E. (1987). *Complete Origami*. London: Ebury Press.
- Klett, Y., & Drechsler, K. (2011). Designing Technical Tessellations. In P. Wang-Iverson, R. Lang, & M. Yim (Ed.), *Origami5: Fifth International Meeting of Origami Science, Mathematics, and Education* (pp. 304-322). Boca Raton, FL: A K Peters/CRC Press.
- Kobayashi, H., Kresling, B., & Vincent, S. (1998, January). The geometry of unfolding tree leaves. *Proceedings: Biological Sciences, Vol. 265*(1391), 147-154. doi:10.1098/rspb.1998.0276
- Kuribayashi, K., Tsuchiya, K., You, Z., Tomus, D., Umemoto, M., Ito, T., & Sasaki, M. (2006). Self-deployable origami stent grafts as a biomedical application. *Materials Science and Engineering A, Vol. 419*, 131-137. doi:10.1016/j.msea.2005.12.016
- Lang, R. (2003). *Origami Design Secrets: Mathematical Methods for an Ancient Art*. Natick: A K Peters Ltd.
- Lang, R. (2003b). *Origami and Geometric Constructions*. Retrieved 10 2014, from <http://www.langorigami.com/science/math/hja/hja.php>
- Lang, R. (2004). *Crease Patterns for Folders*. Retrieved 04 18, 2015, from Robert J. Lang Origami: [http://www.langorigami.com/art/creasepatterns/creasepatterns\\_folders.php](http://www.langorigami.com/art/creasepatterns/creasepatterns_folders.php)
- Lang, R. (2004). *TreeMaker*. Retrieved 03 20, 2015, from <http://www.langorigami.com/science/computational/treemaker/treemaker.php>
- Lang, R. (2008, February). *The math and Magic of Origami*. Retrieved May 2015, from [http://www.ted.com/talks/robert\\_lang\\_folds\\_way\\_new\\_origami?language=en](http://www.ted.com/talks/robert_lang_folds_way_new_origami?language=en)

- Laylin, T. (2014). *Al Bahr Tower Façade Detail* [Online image]. Retrieved April, 2015 from <http://inhabitat.com/exclusive-photos-worlds-largest-computerized-facade-cools-aedas-al-bahr-towers/>
- Lebée, A. (2015). From Folds to Structures, a Review. *International Journal of Space Structures* , Vol. 30(2), 55-74. doi:10.1260/0266-3511.30.2.55
- Lee, D., & Leounis, B. (2011). Digital Origami: Modelling planar folding structures. *ACADIA Regional: Parametricism (SPC)* (pp. 25-29). Clemson: ACADIA.
- Lee, T.-U., & Gattas, J. (2016, June). Geometric Design and Construction of Structurally Stabilized Accordion Shelters. *Journal of Mechanisms and Robotics*, 031009 (8 pages). doi:10.1115/1.4032441
- Li, S., & Dai, J. S. (2012, August). Structure Synthesis of Single-Driven Metamorphic Mechanisms Based on the Augmented Assur Groups. *Journal of Mechanisms and Robotics*, Vol. 4, 031001 (8 pages). doi:10.1115/1.4006741
- Li, S., Wang, H., & Dai, J. (2015, November). Assur-Group Interred Structural Synthesis for Planar Mechanisms. *Journal of Mechanisms and Robotics*, Vol. 7, 041001 (9 pages). doi:10.1115/1.4029116
- Limburg, K. B. (2012). *St. Paulus* [Online image]. Retrieved April, 2015 from <https://de.wikipedia.org/wiki/Weckhoven>
- Lister, D. (1998, September 7). *A Miscellaneous Collection on the History of Origami*. Retrieved February 2, 2015, from <http://www.britishorigami.info/academic/lister/history.php>
- Lister, D. (2005a, June). *An Ancient Egyptian Map*. Retrieved February 02, 2015, from <http://www.britishorigami.info/academic/lister/egypt.php>
- Lister, D. (2005b, March 20). *History of Origami: outline suggestions for a basic, essential history*. Retrieved February 02, 2015, from <http://www.britishorigami.info/academic/lister/basichistory.php>
- Lister, D. (2005c, March 5). *The Exhibition of Paper Folding by Akira Yoshizawa in Amsterdam 1955 and its place in the origins of modern origami*. Retrieved February 02, 2015, from [http://www.britishorigami.info/academic/lister/yoshizawa\\_exhib1955.php](http://www.britishorigami.info/academic/lister/yoshizawa_exhib1955.php)
- Lister, D. (n.d.). *The history of paperfolding : a German perspective*. Retrieved February 02, 2015, from <http://www.britishorigami.info/academic/lister/german.php>
- Liu, S., Chen, Y., & Lu, G. (2013). The Rigid Origami Patterns for Flat Surface. *ASME 2013 International Design Engineering Technical Conferences and Computers and Information in Engineering Conference*. Vol. 6B, p. V06BT07A039 (7 pages). Oregon, USA: ASME. doi:10.1115/DETC2013-12947

- Liu, S., Lv, W., Chen, Y., & Lu, G. (2016, June). Deployable Prismatic Structures With Rigid Origami Patterns. *Journal of Mechanisms and Robotics, Vol. 8*, 031002 (11 pages). doi:10.1115/1.4031953
- Maleczek, R. (2014). Deployable Linear Folded Stripe Structures. In K. Miura, T. Kawasaki, T. Tachi, R. Uehara, R. Lang, & P. Wang-Iverson (Ed.), *Origami6: Proceedings of the Sixth International Meeting on Origami Science, Mathematics, and Education* (pp. 447-457). USA: AMS.
- Mitani, J. (2011). A Method for Designing Crease Patterns for Flat-Foldable Origami with Numerical Optimization. *Journal for Geometry and Graphics, Vol. 15*(No. 2), 195-201.
- Mitani, J. (n.d.). *Origami Applications by Jun Mitani*. Retrieved April 02, 2015, from [http://mitani.cs.tsukuba.ac.jp/origami\\_application/](http://mitani.cs.tsukuba.ac.jp/origami_application/)
- Mitchell, D. (n.d.). *A Family Tree of Origami*. Retrieved November 24, 2014, from Origami Heaven: <http://www.origamiheaven.com/familytree.htm>
- Miura, K., & Tachi, T. (2010). Synthesis of Rigid-Foldable Cylindrical Polyhedra. *Symmetry: Art and Science 8th congress and exhibition of ISIS*. Gmuend.
- Miura, K. (2009). The Science of Miura-Ori: A Review. In R. Lang (Ed.), *Origami4: Fourth International Meeting of Origami Science, Mathematics, and Education* (pp. 87-99). Wellesley, MA: A K Peters.
- Nikolic, D., Stulic, R., & Sidjanin, P. (2012). On the Flexibility of Deployable Dome Structures and their Application in Architecture. *1st International Conference on Architecture & Urban Design* (pp. 1053-1062). Albania: EPOKAUniversity.
- Nishiyama, Y. (2012). Miura Folding: Applying Origami to Space Exploration. *International Journal of Pure and Applied Mathematics, Vol. 79*(No. 2), 269-279.
- Nojima, T. (2002). Modelling of Folding Patterns in Flat Membranes and Cylinders y Origami. *JSME International Journal*, 364-370.
- Origami Resource Center (n.d.). *Mecho and Ocho* [Online image]. Retrieved March, 2015 from <http://www.origami-resource-center.com/mecho-and-ocho.html>
- Osorio, F., Paio, A., & Oliveira, S. (2014). KOS - Kinetic Origami Surface. *Rethinking Comprehensive Design: Speculative Counterculture Proceedings of the 19th International Conference of the Association of Computer-Aided Architectural Design Research in Asia CAADRIA* (pp. 1-10). Hong Kong: The Association for Computer-Aided Architectural Design Research in Asia (CAADRIA).
- Ott, P. (2007). *Die vielen Gesichter der Fassade, Showroom von Kiefer Technic* [Online image]. Retrieved April, 2015 from <http://www.gat.st/en/news/energieeffizienz-mit-understatement>

- Peraza-Hernandez, E., Hartl, D., Malak Jr, R., & Lagoudas, D. (2014). Oriami-inspired Active Structures: A Synthesis and Review. *Smart Materials and Structures*, Vol. 23, 094001 (28 pages). doi:10.1088/0964-1726/23/9/094001
- Schenk, M. (2012). *Origami in Engineering and Architecture: An art spanning Mathematics, Engineering and Architecture*. Retrieved 01 15, 2015, from [http://www.markschenk.com/research/teaching/archeng2012/handouts\\_ArchEng2012\\_Origami.pdf](http://www.markschenk.com/research/teaching/archeng2012/handouts_ArchEng2012_Origami.pdf)
- Schenk, M., & Guest, S. (2011). Origami Folding: A Structural Engineering Approach. *Origami5: Fifth International Meeting of Origami Science, Mathematics and Education* (pp. 291-303). Boca Raton: CRC Pres.
- Schneider, J. (2004, 12 10). *Flat-Foldability of Origami Crease Patterns*. Retrieved 03 02, 2015, from <http://www.sccs.swarthmore.edu/users/05/jschnei3/origamiwithfigures.pdf>
- Schramme, K., Boegle, A., & Ortolano Gonzalez, J. M. (2015). The Challenge of Rigid-Foldable Structures. *Proceedings of the International Association for Shell and Spatial Structures (IASS)*. Amsterdam.
- Schulze, B., Guest, S., & Fowler, P. (2014). When is a Symmetric Body-Hinge Structure Isostatic. *International Journal of Solids and Structures*, Vol. 51, 2157-2166. doi:10.1016/j.ijsolstr.2014.02.018
- Sekularac, N., Ivanovic Sekularac, J., & Ciric Tovarovic, J. (2012). Folded Structures in Modern Architecture. *Architecture and Civil Engineering*, 10(1), 1-16.
- Selvi, Ö. (2012, January). Structural and Kinematic Synthesis of Overconstrained Mechanisms. İzmir.
- Sembazuru Orikata [Online image]. (1797). Retrieved March, 2015 from <http://web.archive.org/web/20080501175749/origami.gr.jp/Model/Sembazuru/index-e.html>
- Sierra, F. (2006). *Hexagonal Dome* [Online image]. Retrieved April, 2015 from <https://www.flickr.com/photos/el Elvis/311453631/>
- Simon, L., Arnstein, B., & Gurkewitz, R. (1999). *Modular Origami Polyhedra*. New York: Dover Publications.
- Smith, J. (2005, January). *Notes on the History of Origami: Paper & Paper Folding*. Retrieved February 02, 2015, from <http://homepage.ntlworld.com/peterjohn.rootham-smith/history.htm>
- Stavric, M., & Wiltsche, A. (2013). Investigations on Quadrilateral Patterns for Rigid Folding Structure. In R. Stouffs, P. Janseen, S. Roudavski, & B. Tuncer (Ed.), *Proceedings of the 18th International Conference on Computer-Aided Architectural Design Research in Asia (CAADRIA)* (pp. 893-902). Hong Kong: CAADRIA.

- Tachi, T. (2009a). *FreeformOrigami*. Retrived March 15, 2015, from [http://www.tsg.ne.jp/TT/software/index.html#rigid\\_origami](http://www.tsg.ne.jp/TT/software/index.html#rigid_origami)
- Tachi, T. (2009b). Generalization of Rigid Foldable Quadrilateral Mesh Origami. In A. Domingo, & C. Lazaro (Ed.), *Proceedings of the International Association for Shell and Spatial Structures (IASS)* (pp. 2287-2294). Valencia: Editorial Universitat Politècnica de València.
- Tachi, T. (2009c). *Rigid Origami Simulator*. Retrieved March 15, 2015, from <http://www.tsg.ne.jp/TT/software/>
- Tachi, T. (2009d). Simulation of Rigid Origami. In R. Lang (Ed.), *Origami4: Fourth International Meeting of Origami Science, Mathematics, and Education* (pp. 175-187). Wellesley, MA: A K Peters.
- Tachi, T. (2009e). One-DOF Cylindrical Deployable Structures with Rigid Quadrilateral Panels. In A. Domingo, & C. Lazaro (Ed.), *Proceedings of the International Association for Shell and Spatial Structures (IASS)* (pp. 2295-2305). Valencia: Editorial Universitat Politècnica de València.
- Tachi, T. (2010a). Freeform Rigid-Foldable Structure using Bidirectionally Flat-Foldable Planar Quadrilateral Mesh. *Advances in Architectural Geometry*, 87-102.
- Tachi, T. (2010b). Geometric Considerations for Design of Rigid Origami Structures. *Proceedings of the International Association for Shell and Spatial Structures (IASS): Spatial Structures - Temporary and Permanent*. Shanghai.
- Tachi, T. (2011). Rigid-Foldable Thick Origami. In P. Wang-Iverson, R. Lang, & M. Yim (Ed.), *Origami5: Fifth International Meeting of Origami Science, Mathematics, and Education* (pp. 253-264). Boca Raton, FL: A K Peters/CRC Press.
- Tachi, T. (2013, November). Designing Freeform Origami Tesselations by Generalizing Resch's Patterns. *Journal of Mechanical Design*, Vol. 135, 111006 (10 pages). doi:10.1115/1.4025389
- Thrall, A., & Quaglia, C. (2014). Accordion shelters: A Historical Review of Origami-like Deployable Shelters developed by the US Military. *Engineering Structures*, 686-692.
- Tonon, O. (1991). Geometry of Spatial Folded Forms. *International Journal of Space Structures*, Vol. 6(No. 3), 227-240.
- Trautz, M., & Künstler, A. (2009). Deployable folded plate structures - folding patterns based on 4-fold-mechanism using stiff plates. *Proceedings of IASS Symposium*, (pp. 2306-2317). Valencia.

- Wang, K., & Chen, Y. (2011). Folding a Patterned Cylinder by Rigid Origami. In P. Wang-Iverson, R. Lang, & M. Yim (Ed.), *Origami5: Fifth International Meeting of Origami Science, Mathematics, and Education* (pp. 265-276). Boca Raton, FL: A K Paters/CRC Press.
- Watanabe, N., & Kawaguchi, K.-i. (2009). The Method for Judging Rigid Foldability. In R. Lang (Ed.), *Origami4: Fourth International Meeting of Origami Science, Mathematics, and Education* (pp. 165-174). Wellesly, MA: A K Peters.
- Wei, G., & Dai, J. (2014, May). Origami-Inspired Integrated Planar-Spherical Overconstrained Mechanisms. *Journal of Mechanical Design, Vol. 136*, 051003 (13 pages). doi:10.1115/1.4025821
- Weisstein, E. (n.d.). *Pappus's Centroid Theorem*. Retrieved from From MathWorld--A Wolfram Web Resource: <http://mathworld.wolfram.com/PappussCentroidTheorem.html>
- Zeng, Q., & Fang, Y. (2012). Structural Synthesis and Analysis of Serial-Parallel Hybrid Mechanisms with Spatial Multi-Loop Kinematic Chains. *Mechanism and Machine Theory, Vol. 49*, 198-215. doi:10.1016/j.mechmachtheory.2011.10.008
- Zhang, K., Fang, Y., Fang, H., & Dai, J. (2010, August). Geometry and Constraint Analysis of the Three-Spherical Kinematic Chain Based Parallel Mechanism. *Journal of Mechanisms and Robotics, Vol. 2*, 031014 (7 pages). doi:10.1115/1.4001783



# APPENDIX A

## SINGLE CENTERED RIGID ORIGAMI BARREL VAULT CALCULATION SHEET

Following image is a screen shots from the excel sheet prepared to calculate all the parameters to create a MV-Pattern by modifying three parameters: radius  $r$ , segment number  $n$ , and central angle  $\Omega$ . The file have been provided within a DVD with the dissertation.

File name: "BarrelVault-SingleCentered.xlsx"

	A	B	C	D	E	F	G	H	I	J	K	L	M	N	O
1						Formül Çubuğu									
2	Type of Arch		Horseshoe												
3	$r$	$n$	$\Omega$	s (meter)	$\theta$	A	B	C	$\beta$	$\alpha$	$\lambda$	h	2h	$s\tau$	
4	4	6	200	2,29443	33,33333	73,3333	160	10	146,667	16,6667	80,106	0,34345	0,68691	13,7666	
5	▲	▲	▲												
6	▼	▼	▼												
7															
8															
9	Deployed configuration								Row #		Depth / Span / Height / Volume				
10	$\sigma$	$\mu$	$\lambda'$	$\delta$	$\beta d$	$\theta d$	$rd$	$\Omega d$	Rn	TDI	S	H	V		
11	75	115,485	147,742	16,12877	147,7425	32,2575	4,12968	193,545	10	1,77784	8,20173	4,61669	54,7608		
12	▲								▲						
13	▼								▼						
14	$\sigma = 90$	the final folded state													
15	$\sigma = 0$	the initial state													
16															

## APPENDIX B

### SINGLE CENTERED RIGID ORIGAMI BARREL VAULT PATTERN AND KINEMATIC DIAGRAMS

Following tables are a series of patterns and kinematic diagrams of a single centered rigid origami barrel vault. Patterns and kinematic diagrams are representatives of the following data tables:

- Table 3.5: Single centered triangular pattern mobility analysis with different number of segments and rows.
- Table 3.10: Single centered trapezoidal pattern mobility analysis with different number of segments and rows.
- Table 3.11: Single centered modified trapezoidal pattern mobility analysis with different number of segments and rows.

Both triangular patterns and trapezoidal patterns with different numbers of segments and different numbers of rows are presented in the following tables. For each cell a CP with a red line, as the pattern-generator, and a black dot to represent the joint that have been removed if a modification has been done to the mechanism. Again for each cell under the CP a kinematic diagram of the original pattern and if modified the modified kinematic diagram is drawn with an \* next to it.

Single Centered Patterns and Kinematic Diagrams

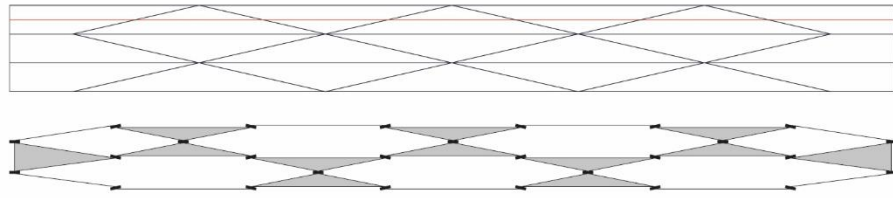
Triangular Pattern 2 Rows

n:7	
n:6	
n:5	
n:4	
n:3	

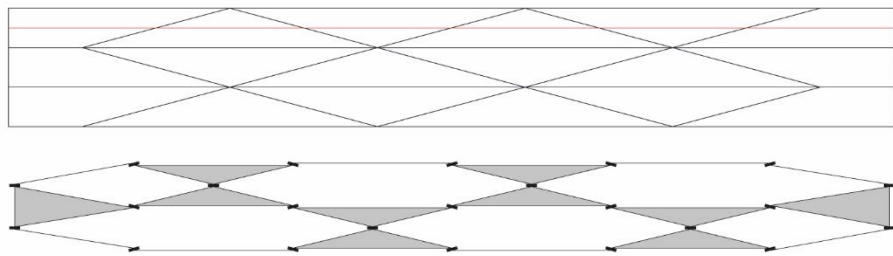
Single Centered Patterns and Kinematic Diagrams

Triangular pattern 3 Rows

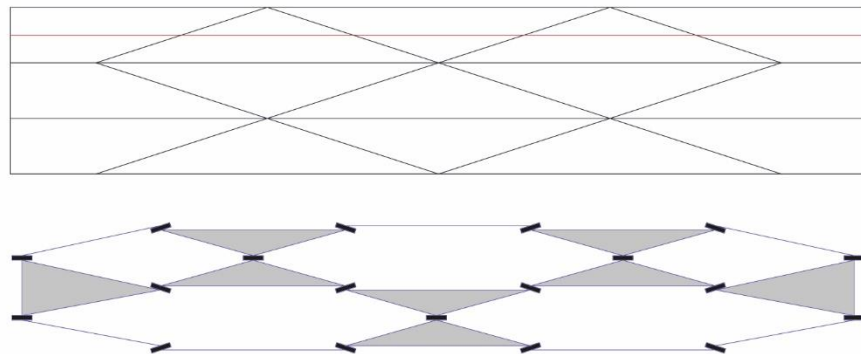
n:7



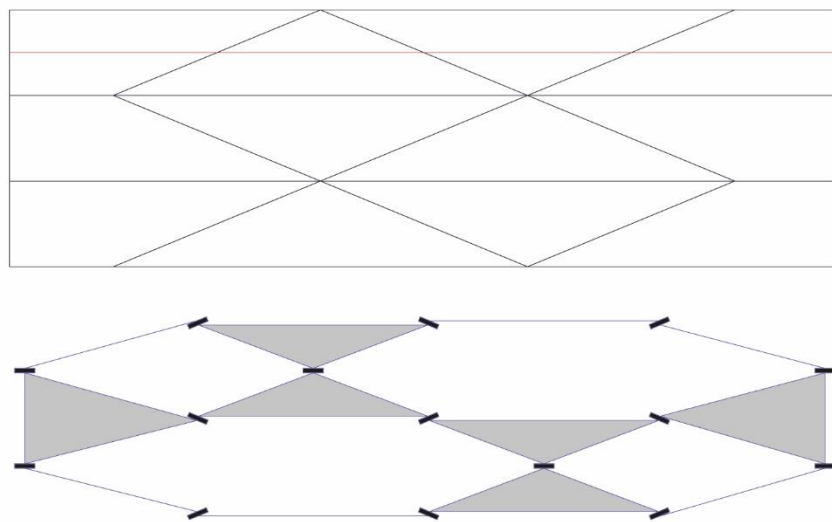
n:6



n:5

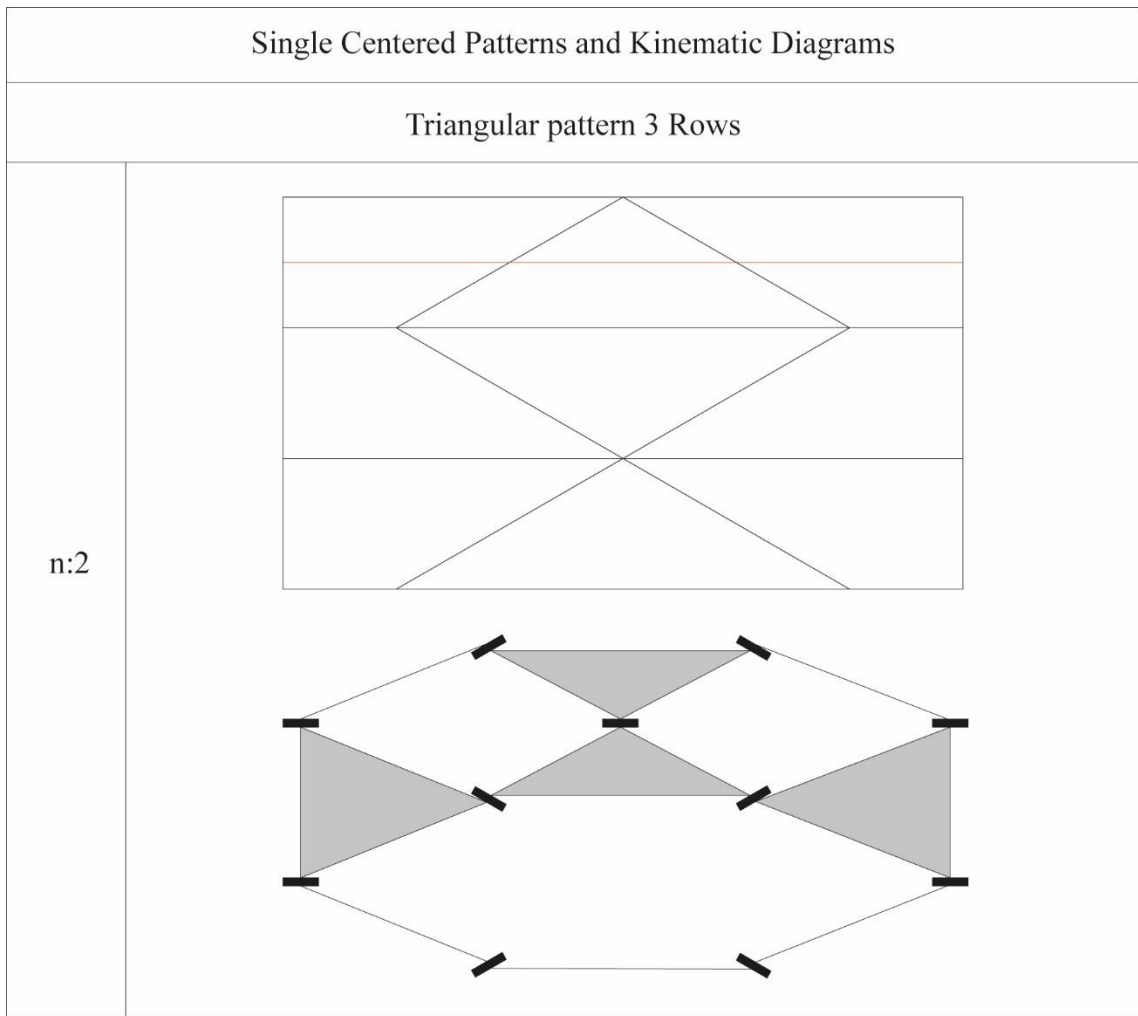


n:4



(cont. on the next page)

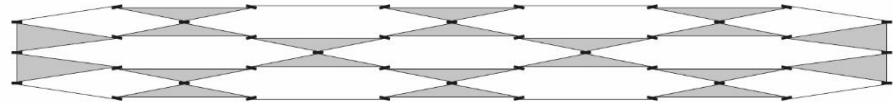
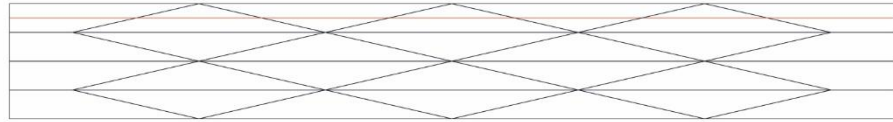
(cont.)



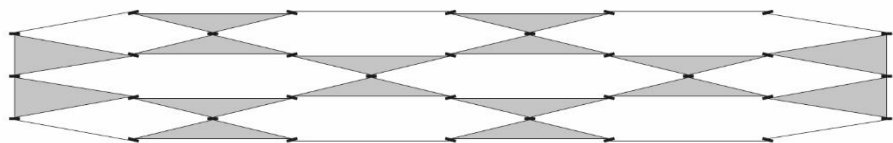
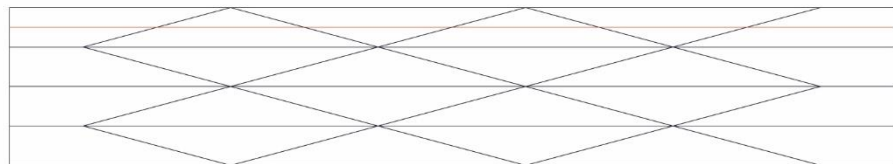
Single Centered Patterns and Kinematic Diagrams

Triangular pattern 4 Rows

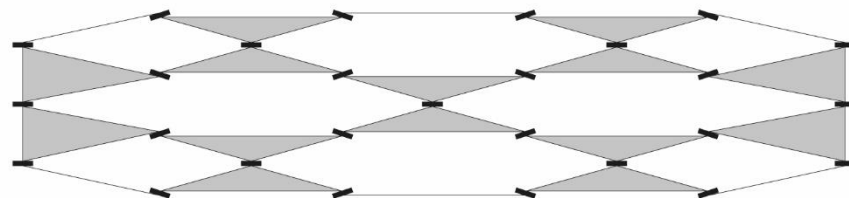
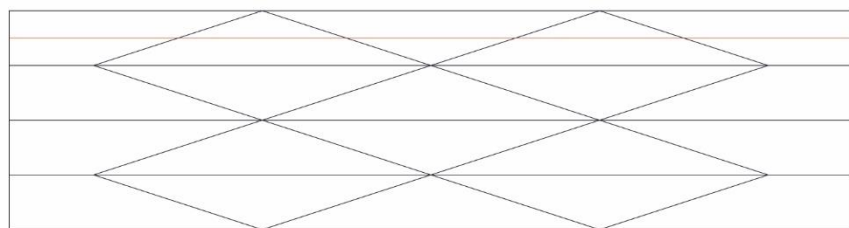
n:7



n:6

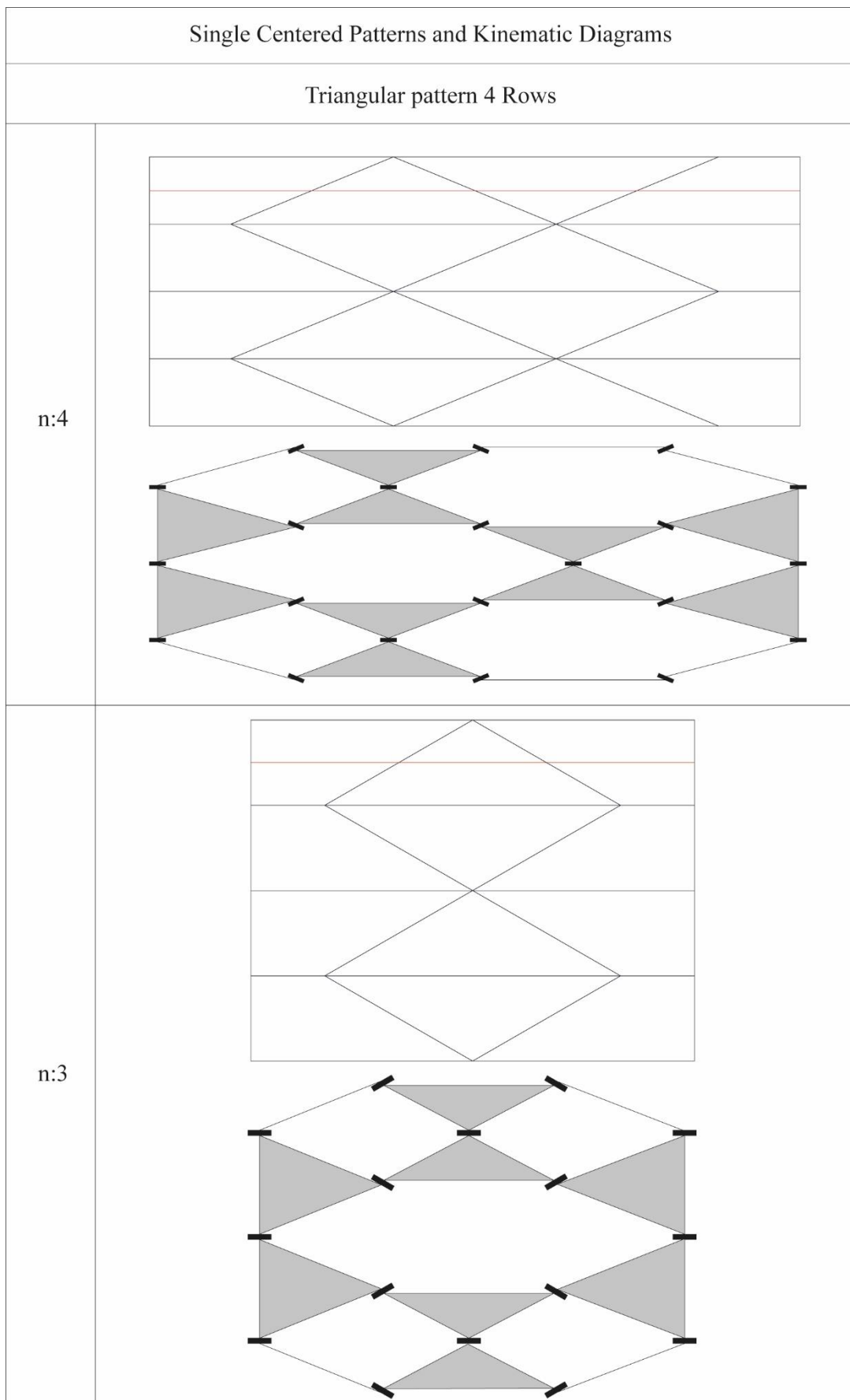


n:5



(cont. on the next page)

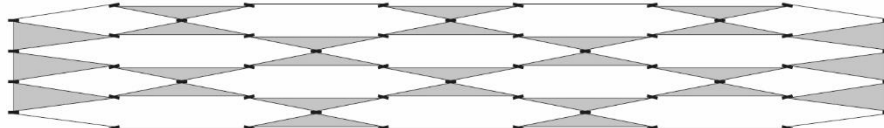
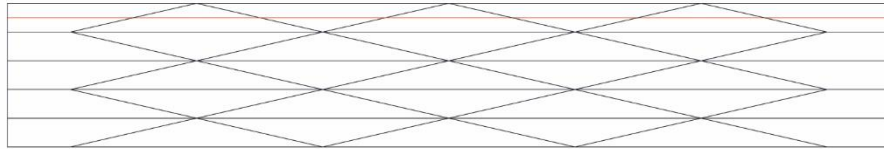
(cont.)



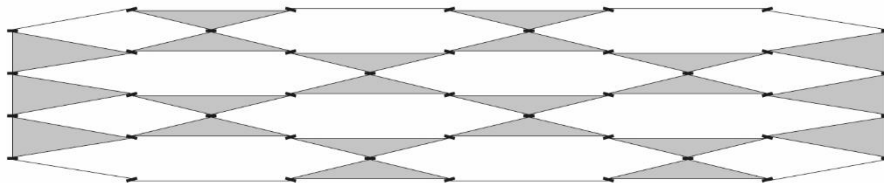
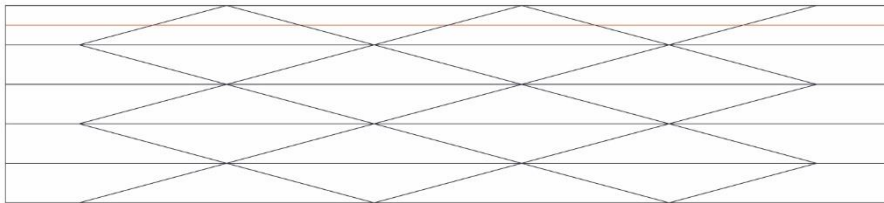
Single Centered Patterns and Kinematic Diagrams

Triangular pattern 5 Rows

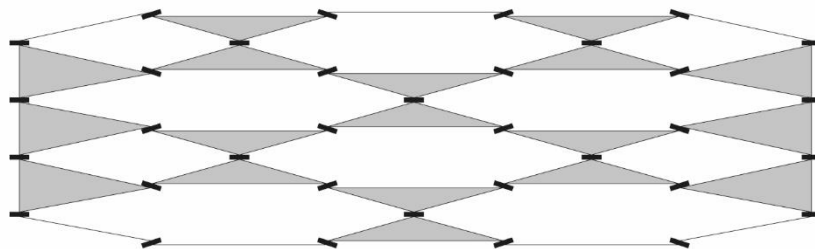
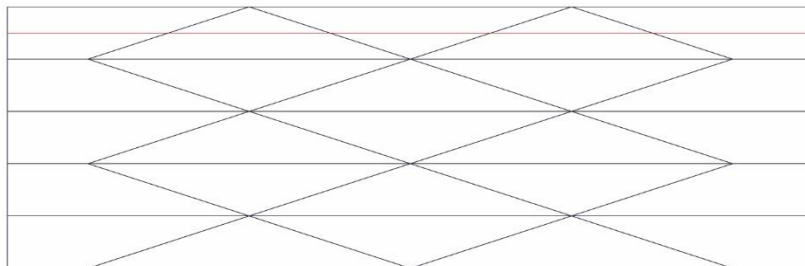
n:7



n:6



n:5



(cont. on the next page)

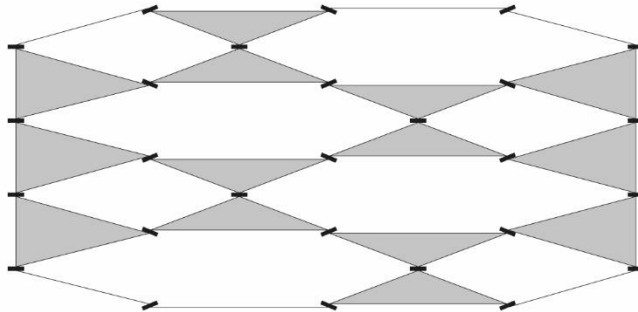
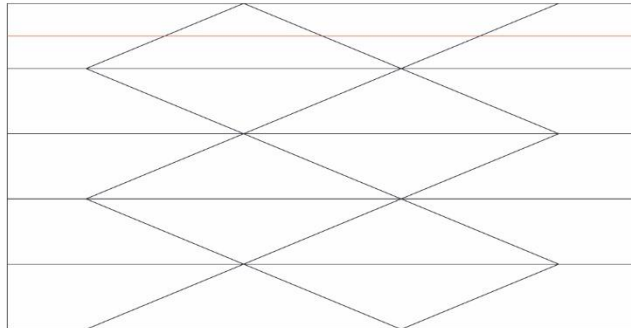


(cont.)

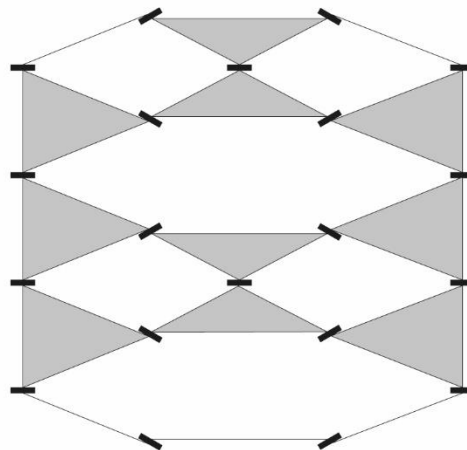
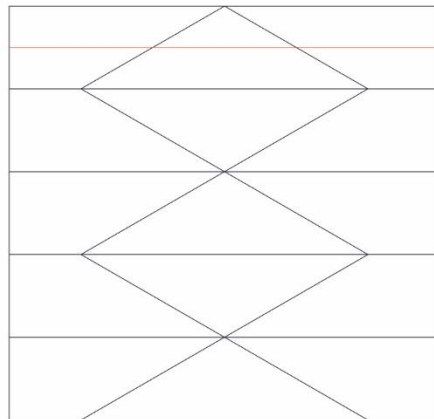
Single Centered Patterns and Kinematic Diagrams

Triangular pattern 5 Rows

n:4



n:3



Single Centered Patterns and Kinematic Diagrams	
Trapezoidal pattern 2 Rows	
	<ul style="list-style-type: none"> <li>● removed joints</li> <li>* modified kinematic diagram</li> </ul>
n:7	
n:6	
n:5	
n:4	
n:3	

### Single Centered Patterns and Kinematic Diagrams

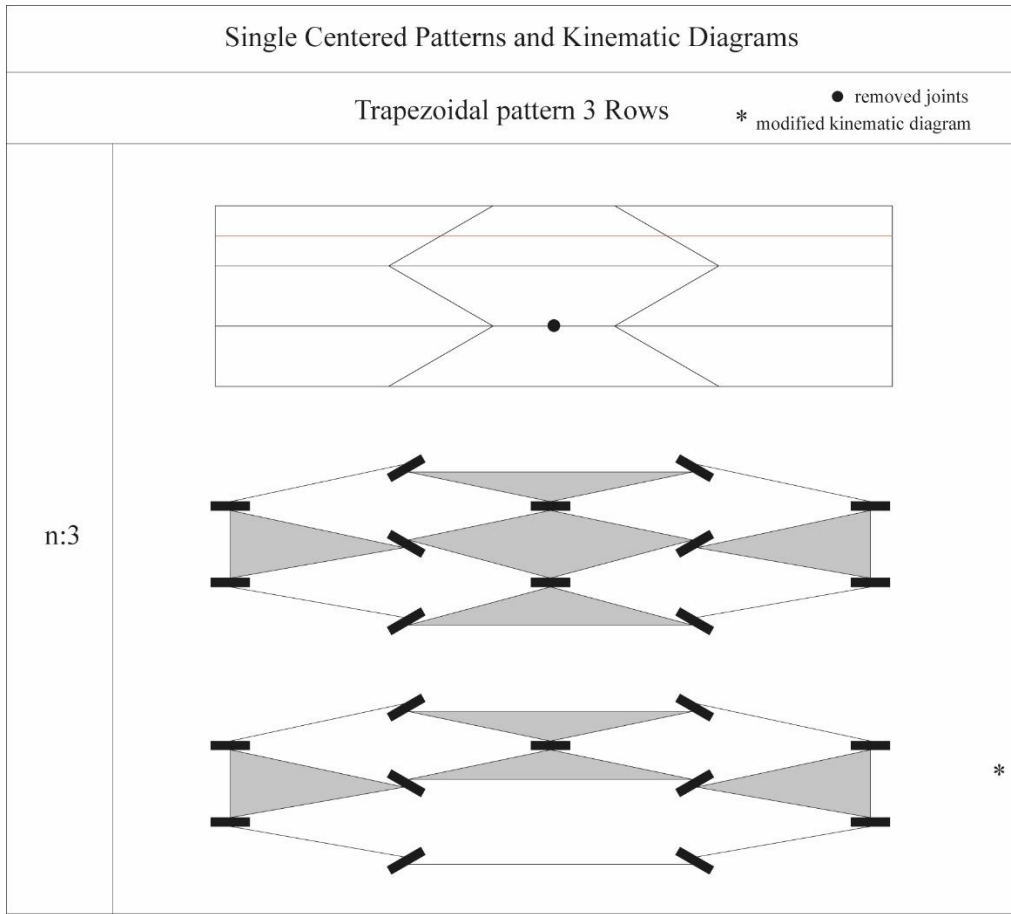
Trapezoidal pattern 3 Rows

● removed joints  
\* modified kinematic diagram

n:7	
n:6	
n:5	
n:4	

(cont. on the next page)

(cont.)

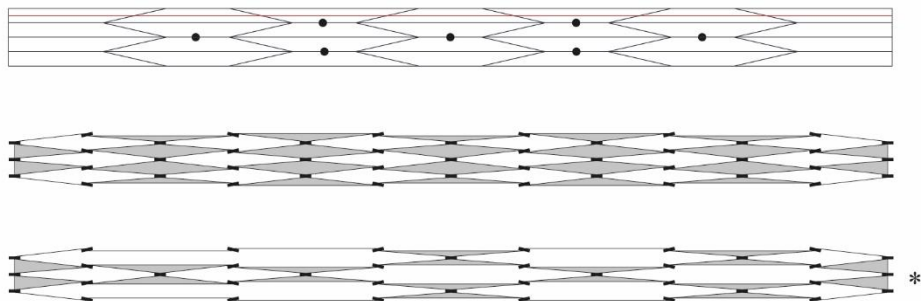


## Single Centered Patterns and Kinematic Diagrams

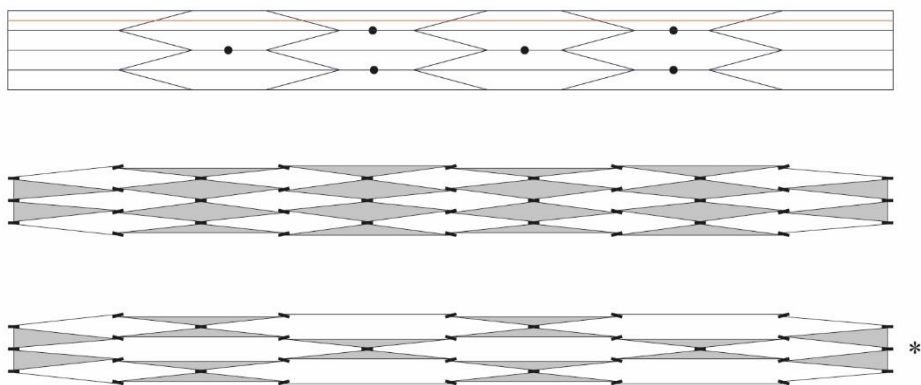
Trapezoidal pattern 4 Rows

● removed joints  
\* modified kinematic diagram

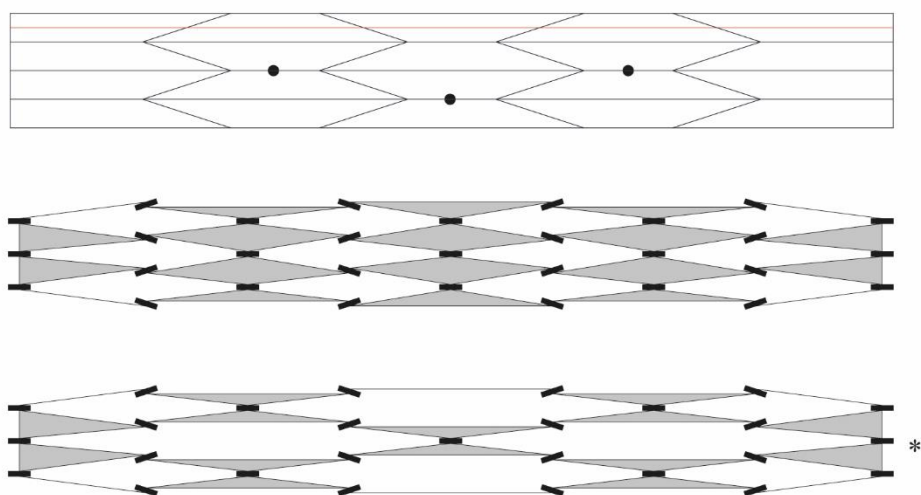
n:7



n:6

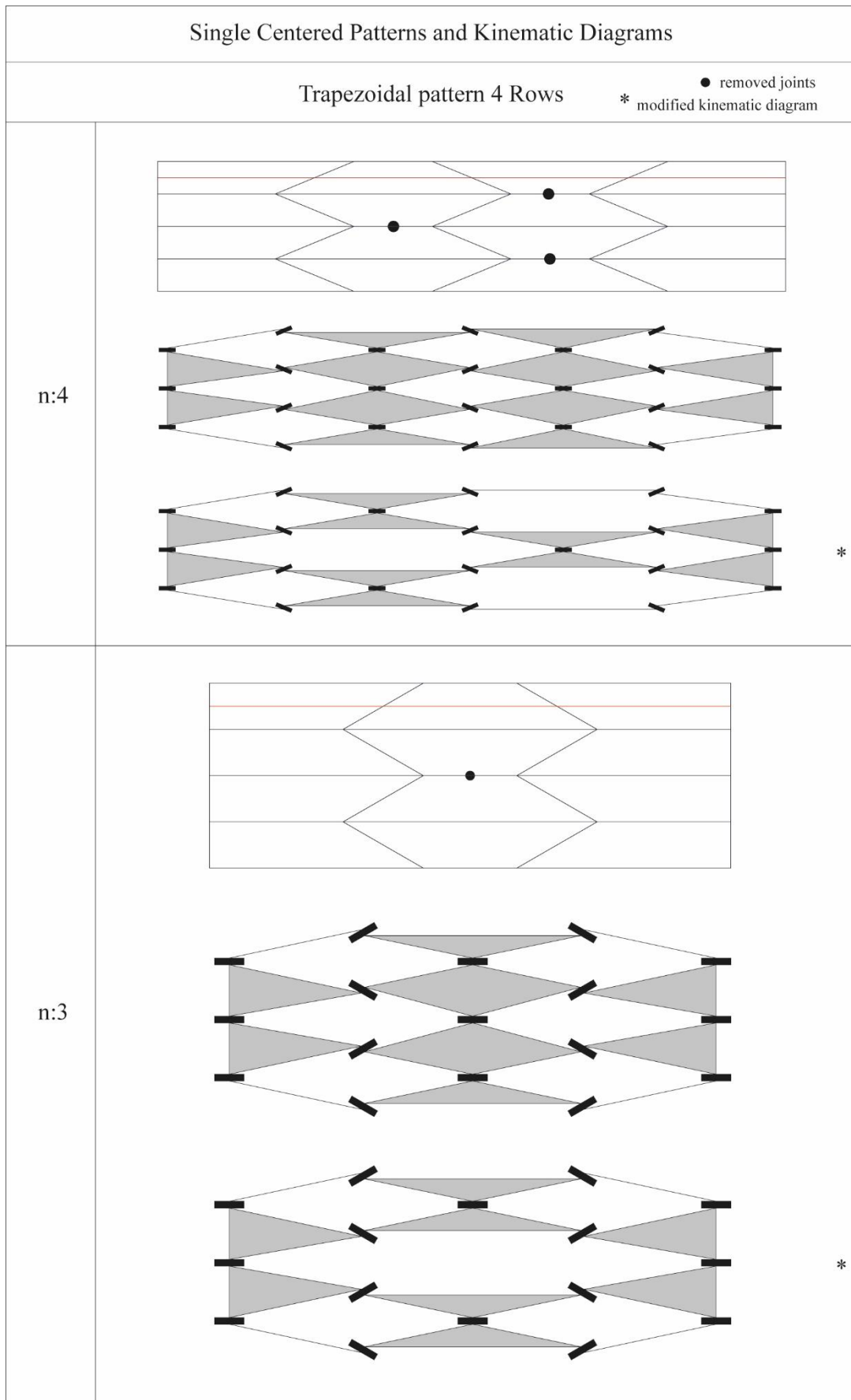


n:5



**(cont. on the next page)**

(cont.)

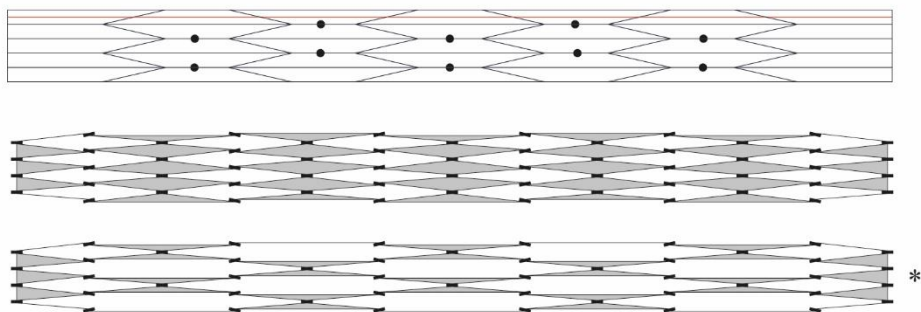


# Single Centered Patterns and Kinematic Diagrams

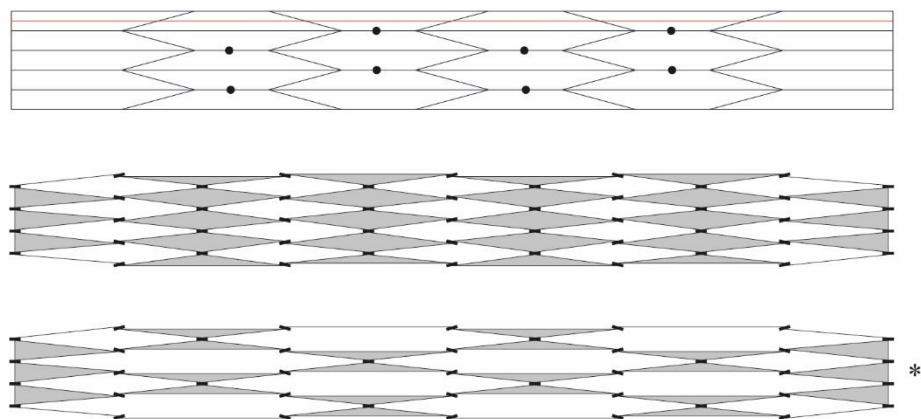
## Trapezoidal pattern 5 Rows

● removed joints  
\* modified kinematic diagram

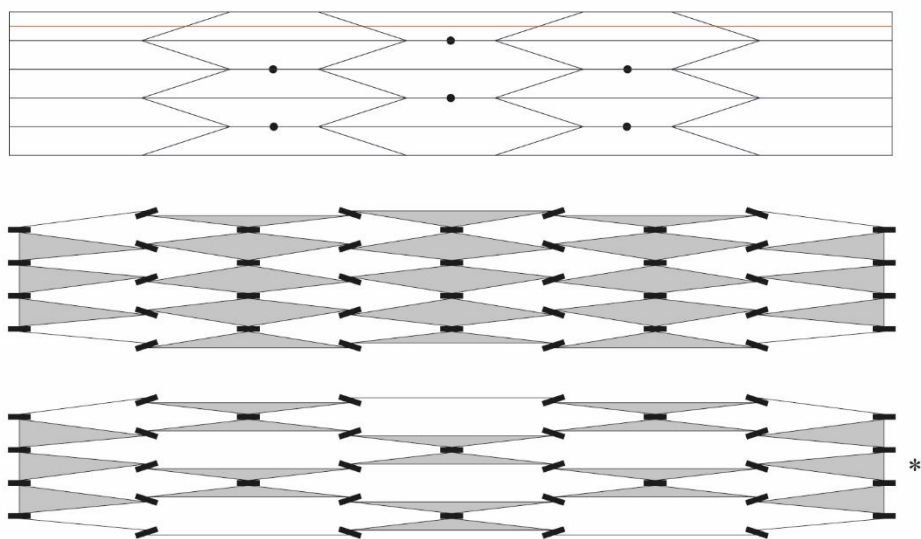
n:7



n:6

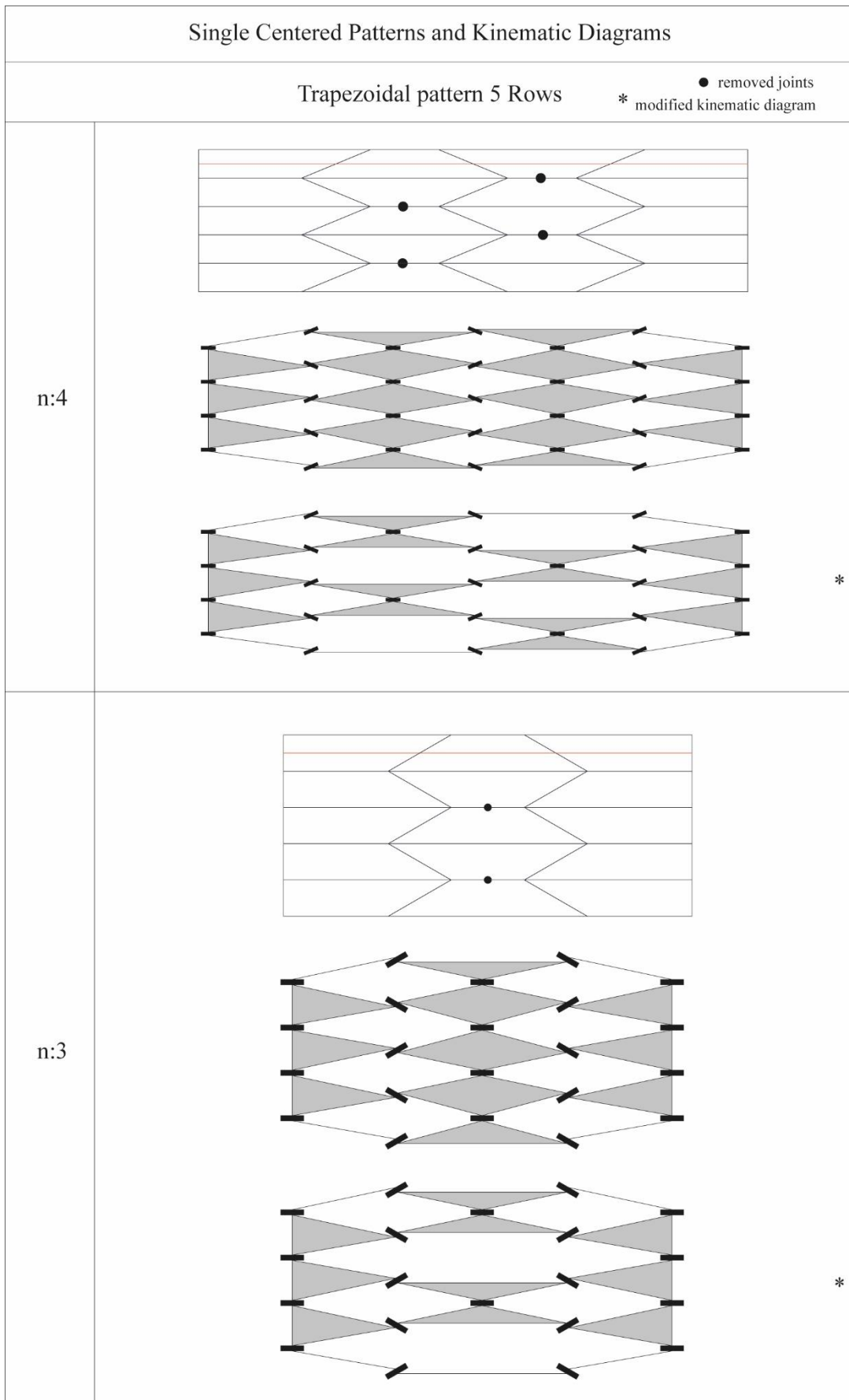


n:5



(cont. on the next page)

(cont.)





# APPENDIX C

## DOUBLE CENTERED RIGID ORIGAMI BARREL VAULT CALCULATION SHEET

Following image is a screen shots from the excel sheet prepared to calculate all the parameters to create a MV-Pattern by modifying three parameters: radius  $r$ , segment number  $n$ , and the distance between centers of the arcs  $a$ . The file have been provided within a DVD with the dissertation.

File name: “BarrelVault-DoubleCentered.xlsx”

	A	B	C	D	E	F	G	H	I	J	K	L	M	N	O	P	Q	R	S	T	
1																					
2																					
3																					
4	Type of Arch	Obtuse																			
5	$r$	$n$	$a$	$s$ (meter)	$\theta$	$b$	$A$	$B$	$C$	$D$	$\beta_1$	$\beta_2$	$\alpha_1$	$\alpha_2$	$\lambda$	$h_1$	$h_2$	$2h$	$n$ Total	$s$ Total	
6	4	3	2	1,743386	25,174163	2	75,52249	28,95502	77,41292	48,45789	154,8258	125,870813	12,58708	27,06459	77,41292	0,19464	0,445388	0,38928	6	10,46031	
7	▲	▲	▲																		
8	▼	▼	▼																		
9																					
10	Deployed configuration											Row #	Depth / Span / Height / Volume								
11	$\sigma$	$\mu_1$	$\mu_2$	$\lambda'$	$\delta_1$	$\delta_2$	$\theta d$	$rd$	$\beta_1 d$	$\beta_2 d$	$\lambda d$	Rn	Td1	S	H	V					
12	15	166,7698	164,9335	173,3849	3,3075382	7,533234	6,615076	15,10854	173,3849	164,9335	86,69246	10	3,7602	10,0980	1,2727	30,0719					
13	▲											▲									
14	▼											▼									
15																					
16	$\sigma = 90$ the final folded state																				
17	$\sigma = 0$ the initial state																				
18																					

## APPENDIX D

### DOUBLE CENTERED RIGID ORIGAMI BARREL VAULT PATTERN AND KINEMATIC DIAGRAMS

Following tables are a series of patterns and kinematic diagrams of a double centered rigid origami barrel vault. Patterns and kinematic diagrams are representatives of the following data tables:

- Table 3.20: Double centered triangular pattern mobility analysis with different number of segments and rows.
- Table 3.21: Double centered modified triangular pattern mobility analysis with different number of segments and rows.
- Table 3.22: Double centered trapezoidal pattern mobility analysis with different number of segments and rows.
- Table 3.23: Double centered modified triangular pattern mobility analysis with different number of segments and rows.

Both triangular patterns and trapezoidal patterns with different numbers of segments and different numbers of rows are presented in the following tables. For each cell a CP with a red line, as the pattern-generator, and a black dot to represent the joint that have been removed if a modification has been done to the mechanism. Again for each cell under the CP a kinematic diagram of the original pattern and if modified the modified kinematic diagram is drawn with an \* next to it.

## Double Centered Patterns and Kinematic Diagrams

### Triangular pattern 2 Rows

● removed joints  
\* modified kinematic diagram

<p>n:5 nr:10</p>	
<p>n:4 nr:8</p>	
<p>n:3 nr:6</p>	
<p>n:2 nr:4</p>	

Double Centered Patterns and Kinematic Diagrams	
Triangular pattern 3 Rows	
	<ul style="list-style-type: none"> <li>● removed joints</li> <li>* modified kinematic diagram</li> </ul>
n:5 nr:10	
n:4 nr:8	
n:3 nr:6	
n:2 nr:4	

## Double Centered Patterns and Kinematic Diagrams

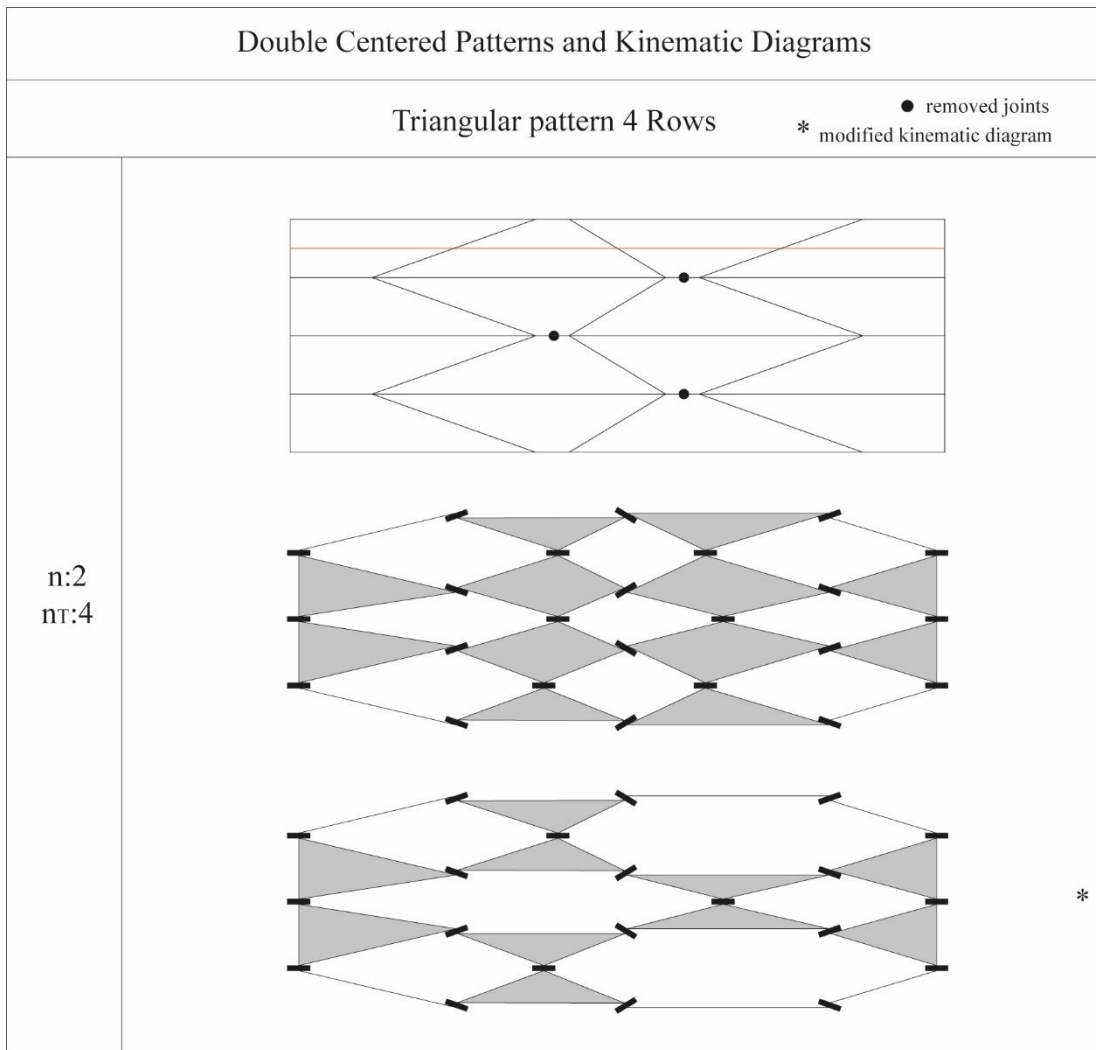
### Triangular pattern 4 Rows

● removed joints  
\* modified kinematic diagram

<p>n:5 nr:10</p>	
<p>n:4 nr:8</p>	
<p>n:3 nr:6</p>	

**(cont. on the next page)**

(cont.)



\*

## Double Centered Patterns and Kinematic Diagrams

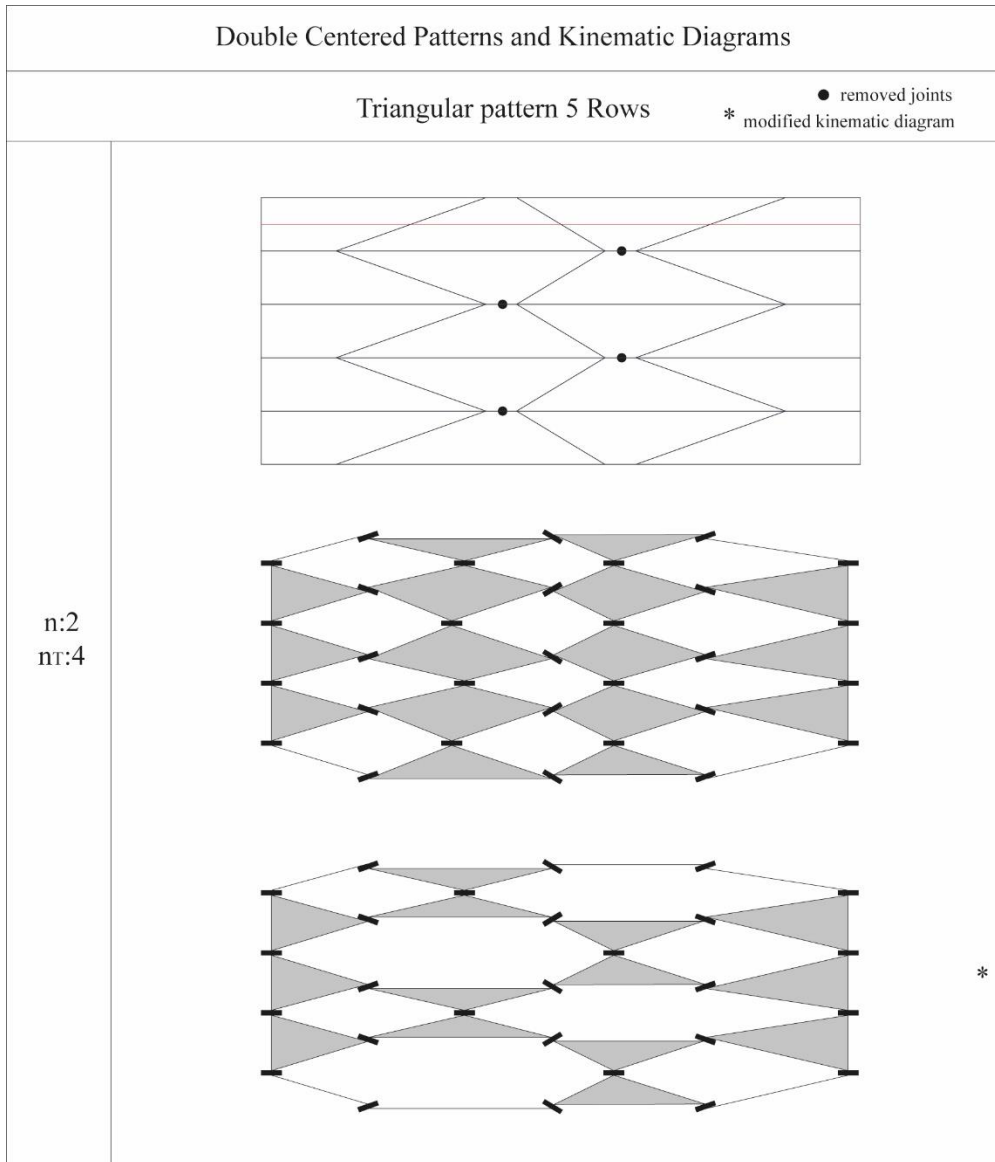
### Triangular pattern 5 Rows

● removed joints  
\* modified kinematic diagram

<p>n:5 nr:10</p>	
<p>n:4 nr:8</p>	
<p>n:3 nr:6</p>	

(cont. on the next page)

(cont.)



\*



Double Centered Patterns and Kinematic Diagrams	
Trapezoidal pattern 2 Rows	
	<ul style="list-style-type: none"> <li>● removed joints</li> <li>* modified kinematic diagram</li> </ul>
<p>n:5 nr:10</p>	
<p>n:4 nr:8</p>	
<p>n:3 nr:6</p>	
<p>n:2 nr:4</p>	

## Double Centered Patterns and Kinematic Diagrams

### Trapezoidal pattern 3 Rows

● removed joints  
\* modified kinematic diagram

<p>n:5 nr:10</p>	
<p>n:4 nr:8</p>	
<p>n:3 nr:6</p>	
<p>n:2 nr:4</p>	

## Double Centered Patterns and Kinematic Diagrams

### Trapezoidal pattern 4 Rows

● removed joints  
\* modified kinematic diagram

<p>n:5 nr:10</p>	
<p>n:4 nr:8</p>	
<p>n:3 nr:6</p>	
<p>n:2 nr:4</p>	

## Double Centered Patterns and Kinematic Diagrams

### Trapezoidal pattern 5 Rows

● removed joints  
\* modified kinematic diagram

<p>n:5 nr:10</p>	
<p>n:4 nr:8</p>	
<p>n:3 nr:6</p>	
<p>n:2 nr:4</p>	

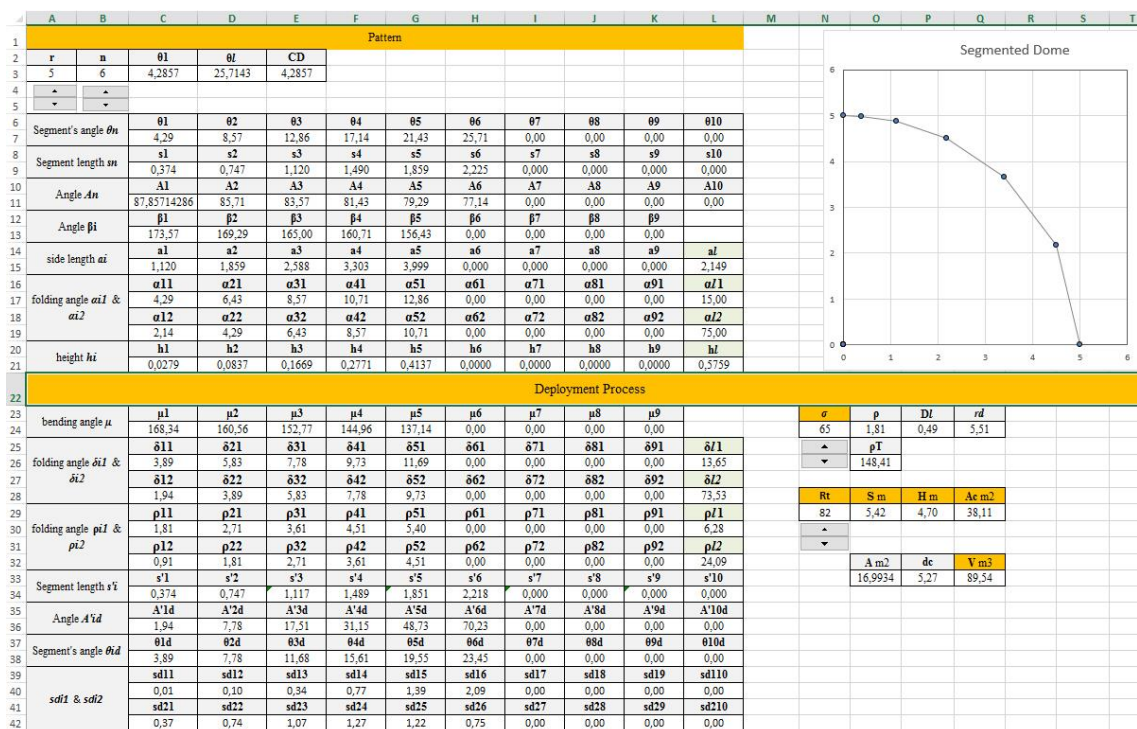
# APPENDIX E

## PSEUDO-DOME RIGID ORIGAMI CALCULATION SHEET (PATTERN)

Following image is a screen shots from the excel sheet prepared to calculate all the parameters to create a MV-Pattern by modifying two parameters: radius  $r$  and segment number  $n$ . The file have been provided within a DVD with the dissertation.

This calculation sheet allows a designer to create a pattern with any number of segment without a need to create a complementary triangle.

File name: “Dome-calculations-V1-Pattern.xlsx”



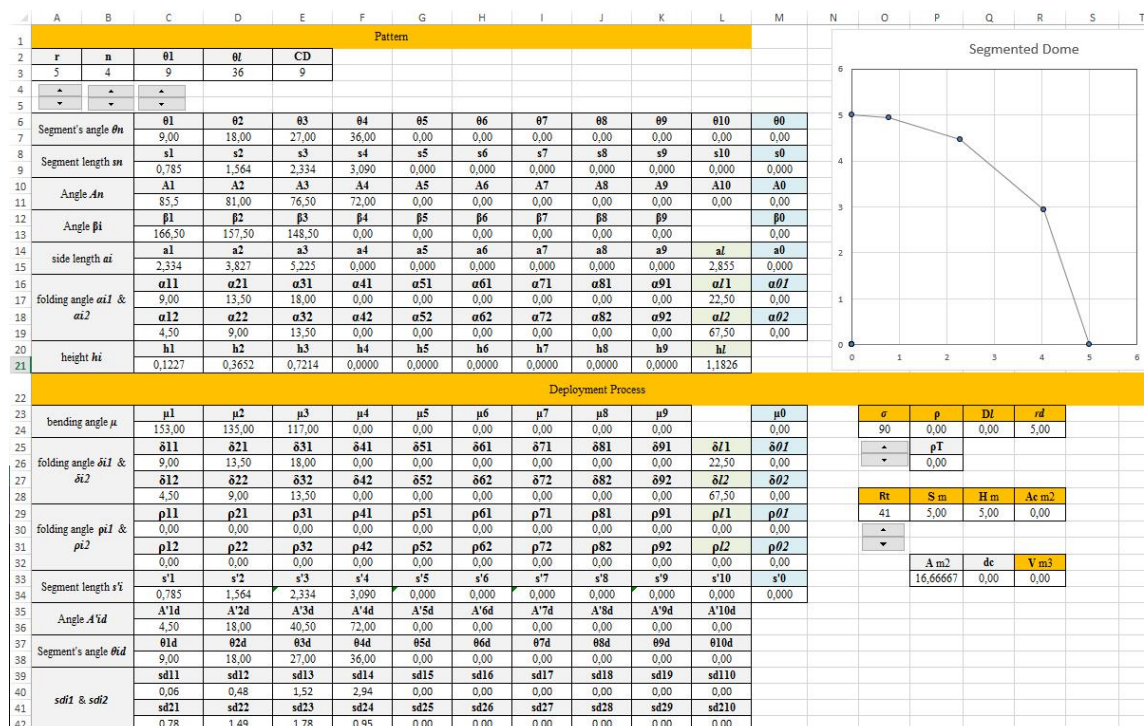
# APPENDIX F

## PSEUDO-DOME RIGID ORIGAMI CALCULATION SHEET (COMPLEMENTARY)

Following image is a screen shots from the excel sheet prepared to calculate all the parameters to create a MV-Pattern by modifying three parameters: radius  $r$ , segment number  $n$ , and first segment angle  $\theta_1$ . The file have been provided within a DVD with the dissertation.

This calculation sheet allows a designer to create a pattern with a complementary triangle. This sheet includes the calculations for the complementary triangle's parameters (column in blue).

File name: "Dome-calculations-V2-Complementary.xlsx"



## VITA

Andrée Sonad KARAVELİ KARTAL

### EDUCATION

- 2011-2017 \_\_\_\_\_ **PhD in Architecture**, Izmir Institute of Technology, Department of Architecture, Turkey  
**Thesis:** “Kinematic Design and Analysis of Deployable Vault and Pseudo-dome Structures Based on Origami Techniques”
- 2007-2009 \_\_\_\_\_ **Master of Architecture**, Ecole Polytechnique Fédérale de Lausanne, Department of Architecture, Switzerland  
**Thesis:** “People vs. Earthquakes”  
**Project:** “Temporary Tent Village for IDP’s (Internally Displaced People) at Zeytinburnu district of Istanbul, Turkey”
- 2000-2005 \_\_\_\_\_ **Bachelor of Architecture**, Yeditepe University, Department of Architecture, Turkey

### PROFESSIONAL EXPERIENCES

- 2014 – 2016 \_\_\_\_\_ Instructor, full-time, Gediz University  
2013 – 2014 \_\_\_\_\_ Instructor, part-time, Gediz University  
2011 – 2012 \_\_\_\_\_ Designer, Origami courses at İzmir H2B Sanat  
2006 – 2007 \_\_\_\_\_ Architect at MİAR Mimarlık (İstanbul)

### As Workshop Coordinator:

- 2016 \_\_\_\_\_ Parametric Design: Folded Plate Structures, GU, Izmir  
2015 \_\_\_\_\_ Origami Workshop at TOBB University, Ankara  
2014 \_\_\_\_\_ 8. Ulusal İç Mimarlık Öğrencileri Buluşması, İzmir  
2014 \_\_\_\_\_ CartogrEphesus, Workshop, Gediz University, İzmir  
2013 \_\_\_\_\_ Origami Workshop at IYTE University, İzmir  
2012 \_\_\_\_\_ Origami Workshop at IYTE University, İzmir  
2012 \_\_\_\_\_ Paper Doors / Kağıttan Kapılar, Mimarlar Odası İzmir Şubesi, Mimarlık haftası, İzmir

### PUBLICATIONS

- Maral Hüseyin, Akgün Yenal, Çınar Ali Kemal, Karaveli Andree Sonad (2015). *İzmir’deki Afet Sonrası Toplanma Ve Acil Barınma Alanları Üzerine Bir Değerlendirme*. 3.Türkiye Deprem Mühendisliği ve Sismoloji Konferansı (Tam metin bildiri)(Yayın No:2835526) • Yamalı Mustafa Sercan, Akgün Yenal, Karaveli Andree Sonad (2015). *Deprem Sonrası Acil Barınma Birimi Tasarımları Üzerine Bir Değerlendirme*. 3.Türkiye Deprem Mühendisliği ve Sismoloji Konferansı (Tam metin bildiri)(Yayın No: 2835522) • Karaveli Andree Sonad, Şenol Gülşen, Yavuz Nur (2015). *Temel Tasarım Stüdyosunda Bir Öğrenme Biçimi Olarak Öykünme: Biyomimesis*. Mimari Tasarım Araştırmaları Ulusal Sempozyumu, (Yayın No:2835517) • Karaveli Andree Sonad, Döşemeciler Ayçe (2015). *Mimari Geometri Dersinin Tasarım Dersleri ile Olan İlişkisinin Değerlendirilmesi*. Mimari Tasarım Araştırmaları Ulusal Sempozyumu, (Yayın No:2835516)